

THE DEVELOPMENT OF A NEW NON-METALLIC EXPLOSIVES INITIATOR

by

HENDRIK CORNELIUS BEZUIDENHOUT

Thesis submitted in fulfilment of the requirements for the degree

Doctor of Technology: Chemical Engineering

in the Faculty of Engineering

at the Cape Peninsula University of Technology

Supervisor: Professor S K Mukhopadhyay

**Cape Town
November 2017**

CPUT Copyright Information

The thesis may not be published either in part (in scholarly, scientific or technical journals), or as a whole (as a monograph), unless permission has been obtained from the University

DECLARATION

I, Hendrik Cornelius Bezuidenhout, declare that the contents of this thesis represent my own unaided work, and that the thesis has not previously been submitted for academic examination towards any qualification. Furthermore, it represents my own opinions and not necessarily those of the Cape Peninsula University of Technology.

Signed

Date

ABSTRACT

Explosives are used to achieve certain functions in diverse environments, including mining, civil construction, military operations, and demolition. Irrespective of the application, the basic principle of augmentation of energy applies. Energy in the form of heat and shock is released by an initiator. This energy is taken up by an intermediary charge, which in turn propagates to the main explosive charge. Ultimately the energy released from the main explosive charge performs the functions. Initiating systems make use of this exact principle within their own boundaries of confinement. The rate at which this energy transfer takes place as well as the magnitude of augmentation is to a great extent influenced by parameters such as the type of confinement, chemical composition and density of the explosives, as well as other environmental conditions.

Traditionally lead azide has been used as the primary explosive component in an initiating system. Pressure from international environmental agencies has discouraged the use of heavy metals in commercial products. Nano-porous silicon has been used together with an oxidiser to form an explosive mixture. The literature has shown that nano-porous silicon-based explosive formulations are sensitive enough to pick up from the energy released by the pyrotechnic composition. The reaction of such nano-porous silicon explosive compositions changes from a deflagration to a detonation. However, their ability to initiate the base charge of an initiating system has not yet been demonstrated. A nano-porous silicon/nitriminotetrazole-based explosive system was developed and characterised. A relative reactivity concept was developed and successfully used to further characterise the new nano-porous silicon explosive. The lead azide primary explosive replacement has been shown to be sensitive enough to pick up from the heat output generated by the delay composition and strong enough to reliably initiate the base charge explosive.

The performance of the base charge explosive is primarily a function of its density and the confinement it is used in. An explosive system was developed whereby the base explosive was coated with a polymer to give it compressible characteristics. A ballistic ball indentation evaluation method was developed and effectively applied to characterise explosive performance behaviour under various conditions, including density and confinement. Explosive pellets, pressed separately and at a higher density, have been shown to increase performance compared with explosives consolidated inside an aluminium casing.

Global initiatives require from the manufacturer or end user to track and trace initiating systems throughout their complete lifecycle. Radio frequency identification (RFID) has been identified as the system of choice to provide such track and trace capability. One of the biggest shortcomings of radio frequency systems is the ease with which the system can be

isolated or shielded, preventing the tag from communicating with a reader or programmer. Metallic environments contribute significantly to such conditions when using radio frequency systems. Hence, conventional metallic detonator casings prohibit tracking and tracing of the system.

Moving away from metallic confinement may compromise the detonation properties of initiating systems. A polymeric initiator casing was shown to be feasible by evaluating various polymers, using plate dent tests. Plate dent test results were interpreted by introducing an equation to determine detonation velocity from the explosive charge height and indentation diameter. The explosive reaction zone thickness was determined using explosive column height and applied in an adapted equation. The adapted equation was used to demonstrate the influence of casing mass on the reaction velocity of explosives utilised in a thin walled or in weak confinement.

Maximising explosive energy transfer was achieved by focusing the shock wave. This was demonstrated by encapsulating the secondary explosive base charge in a polymeric ribbed body. Optimal design of the shape was demonstrated experimentally and explained theoretically.

This study described the development of a non-metallic initiating system in its totality. The study concluded by demonstrating the modular design concept of the non-metallic, lead-free, initiating system with a track and trace capability.

ACKNOWLEDGEMENTS

I wish to thank:

- AEL Mining Services and CPUT for this opportunity.
- Mr Naziem George for his kind assistance with administrative requirements at CPUT.
- Dr Thilo van der Merwe and Messrs Andries Botha, Morris Bear, Robin Winslow, Francois de Bruyn, Harry van Biljon, Isaac Ramashapa, Tim Nel and Mrs Tondani Manyatse for their support and assistance.
- Prof. Samir Mukhopadhyay for his patience, support and mentorship throughout this journey.
- Dr Piet Halliday, for his support, insightful discussions and mentorship.
- My father, Mr Ben Bezuidenhout, and my late mother. Mrs Corrie Bezuidenhout, who invested in my academic journey; I shall always be thankful for this opportunity.
- My wife, Ezanda, and my sons Divan, SJ, and Drikus, for their sacrifice, support and understanding.
- My Lord Jesus Christ, for giving me the opportunity and strength to complete this study.

The financial assistance of the AEL Mining Services towards this research is acknowledged. Opinions expressed in this thesis and the conclusions arrived at, are those of the author, and are not necessarily to be attributed to AEL Mining Services.

DEDICATION

To my wife Ezanda, and my sons Divan, SJ, and Drikus

PUBLICATIONS and CONFERENCE PRESENTATIONS

Selected papers of this research project were published in the journals or presented at international conferences. Details are as follows:

Journal publications

Bezuidenhout, H.C. & Mukhopadhyay, S. 2013. High temperature reaction behaviour of nanoporous silicon based explosive formulations. *International Journal of Basic and Applied Sciences*, 2(4):381-386.

Bezuidenhout, H.C. & Mukhopadhyay, S. 2014. Determination of small-scale detonation pressure of explosives from crater size effects on spherical Indentation. *Journal of the Explosives Safety and Technology Society (Visfotak) India*, 8:36-40.

Bezuidenhout, H.C. & Mukhopadhyay, S. 2016. Nanoporous silicon based energetic formulations for use in explosives initiating system. *International Journal of Applied Engineering Research*, 11(21):10465-10471.

Bezuidenhout, H.C. & Mukhopadhyay, S. 2017. An interrelationship between reaction zone thickness and explosives column length derived using a polymer bonded explosives formulation. *Journal of Engineering and Applied Sciences*, 12(4):950-953.

Conference presentations

(Also published respectively in ISSN and ISBN proceedings)

*Bezuidenhout, H.C. & Mukhopadhyay, S. 2013. Thermal sensitivity of nano-porous silicon based explosive formulations. *Proceedings of the 44th International Annual Conference of ICT, Karlsruhe, Germany, 25–28 June*.

Bezuidenhout, H.C. & Mukhopadhyay, S. 2013. The development of a novel non-metallic initiator for explosives. *Proceedings of the 7th EFEE World Conference on Explosives and Blasting, Moscow, Russia, 15–17 September*.

*This paper was awarded one of the best papers at the conference

TABLE of CONTENTS

DECLARATION	ii
ABSTRACT	iii
ACKNOWLEDGEMENTS	v
DEDICATION	vi
PUBLICATIONS and CONFERENCE PRESENTATIONS	vii
TABLE of CONTENTS	viii
LIST of FIGURES	xiv
LIST of TABLES	xix
GLOSSARY	xxii
ACRONYMS and ABBREVIATIONS	xxiv

CHAPTER 1

INTRODUCTION	1
1.1 Background	1
1.2 Statement of Research Problem	4
1.3 Scope and Research Objectives	5
1.3.1 <i>Scope of study</i>	5
1.3.2 <i>Research objectives</i>	5
1.4 Experimental Design and Research Methodology	6
1.4.1 <i>Porous silicon-based explosive formulation development</i>	6
1.4.2 <i>Detonator design and development</i>	6
1.4.3 <i>Deflagration-to-detonation transition development</i>	7
1.5 Outline of the Thesis	7

CHAPTER 2

LITERATURE REVIEW	9
2.1 Historical Background to Explosive Research	9
2.2 Science of Explosives	12
2.2.1 <i>The means of confinement</i>	13
2.2.2 <i>Detonation velocity of explosives</i>	13
2.2.3 <i>Density of explosive material</i>	13
2.2.4 <i>Effect of diameter of the explosive material</i>	14
2.2.5 <i>Effect of initiation/ignition of the explosive material</i>	14
2.3 Functions of a Detonator and Relevant Recent Developments	14
2.4 Explosives Materials for Detonators	17
2.4.1 <i>Base charge explosive</i>	18
2.4.2 <i>Lead azide</i>	18
2.4.3 <i>Pentaerythritol tetranitrate (PETN)</i>	19
2.4.4 <i>Lead azide and PETN detonating system</i>	20
2.5 Limitations of Current Explosive Materials and Recent Developments	22
2.6 Novel Silicon-Based Explosive Materials	25

2.6.1	<i>Nano-porous silicon</i>	25
2.6.2	<i>Porous silicon-based explosive</i>	27
2.6.3	<i>Porous silicon-based initiating systems</i>	29
2.7	Radio Frequency Identification Tags	29
2.7.1	<i>Advantages and limitations of radio frequency identification and barcoding systems</i>	30
2.8	Summary	31

CHAPTER 3

PREPARATION AND EVALUATION OF NANO-POROUS SILICON AND TETRAZOLE SALTS FOR EXPLOSIVE FORMULATION

		33
3.1	Introduction	33
3.2	Process of Developing Nano-porous Silicon	33
3.2.1	<i>Mechanisms of silicon dissolution</i>	34
3.2.2	<i>Dissolution chemistry</i>	36
3.3	Nano-porous Silicon Sample Characteristics	38
3.3.1	<i>Storage effects on npSi</i>	42
3.3.2	<i>Oxidation effects on npSi</i>	43
3.4	Synthesis of Tetrazole Salts	46
3.4.1	<i>Preparation of 5-nitriminotetrazole salts</i>	47
3.4.2	<i>Preparation of 5-nitrotetrazole</i>	47
3.5	Analytical Results	48
3.6	Summary	51

CHAPTER 4

POROUS SILICON INITIATING AND PBX EXPLOSIVE FORMULATIONS DEVELOPMENT

		52
4.1	Introduction	52
4.2	Nano-Porous Silicon-Based Explosive Formulation Development	52
4.2.1	Balanced fuel- to-oxidiser ratio determination	54
4.2.2	Proposed methodology for relative reactivity	57
4.2.3	Determining the R_r of nano-porous silicon-based explosives compositions	60
4.2.4	Oxidiser-to-fuel ratio determination	62
4.2.5	The effect of oxidation of nano-porous silicon on the R_r of silicon-based explosive formulations	63
4.2.6	The effect of ageing of silicon-based explosive formulations	64
4.2.7	Effect of density on the thermal reactivity of the nano-porous silicon-based explosive formulations	64
4.2.8	Burning rate evaluation	65
4.2.9	Closed-vessel pressure test	66
4.2.10	Results: Nano-porous silicon-based formulation development	67

4.2.10.1	Results: Fuel-to-oxidiser ratio	67
4.2.10.2	Results: Effect of aged nano-porous silicon on the reactivity of npSi-based explosive formulations	69
4.2.10.3	Results: Effect of density on the reactivity of nano-porous silicon-based explosives	70
4.2.10.4	Results: Nano-porous silicon burning rate	71
4.2.10.5	Results: Closed pressure vessel test	71
4.2.10.6	Results: Closed pressure vessel test	74
4.2.11	<i>Nano-porous silicon-based explosive formulation development – Discussion</i>	76
4.3	Preparation of PETN and RDX-Based PBX Explosive Formulations	83
4.4	Test and Evaluation	89
4.4.1	<i>Small-scale gap test</i>	89
4.4.2	<i>Friction sensitivity test</i>	91
4.4.3	<i>Impact sensitivity test</i>	92
4.4.4	<i>Differential scanning calorimetry (DSC)</i>	94
4.4.5	<i>Results: PBX-based explosives formulation test and evaluation</i>	95
4.4.5.1	Results: SSG	95
4.4.5.2	Results: Friction sensitivity	96
4.4.5.3	Results: Impact sensitivity	97
4.4.5.4	Results: Differential scanning calorimetry	97
4.4.6	<i>PBX-based explosives formulation test and evaluation – Discussions</i>	98
4.5	Summary	99

CHAPTER 5

ADVANCES TOWARDS A LEAD-FREE SILICON-BASED EXPLOSIVES INITIATING SYSTEM

5.1	Introduction	101
5.2	Characterisation of Detonation Pressure in Small-Scale Applications	102
5.2.1	<i>Experimental design</i>	103
5.2.2	<i>Mathematical evaluation</i>	105
5.2.3	<i>Results</i>	108
5.2.4	<i>Postulated mathematical methodology – Results</i>	110
5.3	New Intermediary Detonation Transfer System	113
5.3.1	<i>Experimental approach</i>	114
5.3.2	<i>Results and analysis</i>	116
5.3.3	<i>Ballistic ball indentation test</i>	117
5.4	Detonator Base Charge Explosives	118
5.4.1	<i>Ballistic ball indentation test</i>	119
5.5	Summary	120

CHAPTER 6

NON-METALIC DETONATOR CASING DEVELOPMENTS	121
6.1 Introduction	121
6.2 Detonator Casing Design: Basic Criteria	123
6.2.1 <i>Materials evaluation</i>	123
6.2.1.1 Optimal explosives column length evaluations	123
I. <i>Scope</i>	124
II. <i>Analysis</i>	124
a) Method	124
b) results	126
c) Remarks	130
6.2.1.2 Explosives casing effects	130
I. <i>Analysis</i>	130
a) Method	130
b) Results	131
c) Remarks	134
6.3 Proposed Detonator Casing Design	134
6.3.1 <i>Shock tube holder</i>	135
6.3.2 <i>Main body</i>	135
6.3.3 <i>Shock tube connector clip</i>	135
6.3.4 <i>Booster casing</i>	136
6.4 Summary	136

CHAPTER 7

BOOSTER CASING DEVELOPMENT AND MATHEMATICAL DERIVATION	137
7.1 Introduction	137
7.2 Physics of Booster Casing Optimisation	138
7.3 Test Method Illustration of Shock Waves	139
7.3.1 <i>Shock wave simulation</i>	139
7.3.2 <i>Results</i>	141
7.3.3 <i>Large-scale shape evaluation</i>	143
7.3.4 <i>Results</i>	144
7.3.5 <i>New booster casing design – prototype</i>	147
7.3.6 <i>Performance evaluation of new casing design</i>	148
7.3.6.1 Sectional thickness of new booster casing	148
7.3.6.2 Indentation profile	151
7.3.7 <i>Mathematical derivation</i>	153
7.4 Discussion	158
7.5 Summary	159

CHAPTER 8

EVALUATION OF TENSILE PERFORMANCE AND TRACIBILITY OF NON-METALLIC CASING

	160	
8.1	Introduction	160
8.2	Test and Evaluation of the Proposed Design	161
8.2.1	<i>Detonator component tensile test</i>	161
8.2.1.1	Tensile tests conducted at different temperatures	161
8.2.1.2	Artificial ageing	163
8.2.1.3	Results	164
8.2.1.4	Discussion	168
8.3	Tracking and Tracing	168
8.3.1	<i>RFID detection testing</i>	169
8.3.1.1	Results	171
8.3.1.2	Discussion	172
8.4	Summary	172

CHAPTER 9

SUMMARY AND CONCLUSIONS

	173	
9.1	Summary	173
9.2	Concluding Remarks	176
9.3	Recommendations for Future Research	179

BIBLIOGRAPHY

	180
--	-----

APPENDIX 3A: npSi particle size distribution	191
APPENDIX 3B: HF specification	193
APPENDIX 3C: Methanol specification	194
APPENDIX 3D: Acetone specifications	195
APPENDIX 4A: Heat of formation of elements and bonds	196
APPENDIX 4B: Noise generation related to sample mass	197
APPENDIX 4C: Reactivity of npSi explosives manufactured from different oxidisers and various surface areas	198
APPENDIX 4D: SSG test results	200
APPENDIX 4E: Impact and friction sensitivity results of different PBX explosive formulations	201
APPENDIX 5A: Mathematical evaluation logic flow diagram	202
APPENDIX 5B: PETN indentation diameters at different densities	203
APPENDIX 7A: Result of 90° shock wave simulation	204
APPENDIX 7B: Results of 75° shock wave simulation	205
APPENDIX 7C: Results of 60° shock wave simulation	206

APPENDIX 7D: Results of 45° shock wave simulation	207
APPENDIX 7E: Results of 30° shock wave simulation	208
APPENDIX 7F: Large-scale plate dent test results – outside profile	209
APPENDIX 7G: Large-scale plate dent test results – inside profile	210
APPENDIX 7H: Pressure calculations	211
APPENDIX 8A: Shock tube holder design	214
APPENDIX 8B: Main body design	215
APPENDIX 8C: Shock tube connector clip design	216
APPENDIX 8D: Booster casing design	217
APPENDIX 8E: Actual pull-strength results – shock tube to shock tube holder	218
APPENDIX 8F: Actual pull-strength results – shock tube holder to body	219
APPENDIX 8G: Actual pull-strength results – body to base	220
APPENDIX 8H: Actual pull-strength results (aged) – shock tube to shock tube holder	221
APPENDIX 8I: Actual pull-strength results (aged) – shock tube holder to body	222
APPENDIX 8J: Actual pull-strength results (aged) – body to base	223

LIST of FIGURES

Figure 1.1: Empirical structure of a detonation train	2
Figure 2.1: Nobel's first detonator systems	10
Figure 2.2: A two-dimensional detonation reaction	12
Figure 2.3: A typical explosive detonator	16
Figure 2.4: Various detonator designs	16
Figure 2.5: Lead Azide	19
Figure 2.6: PETN	20
Figure 2.7: Nano-porous silicon	26
Figure 2.8: Nano-porous silicon under ultraviolet radiation	26
Figure 2.9: High-resolution SEM of pSi surface	27
Figure 3.1: Cross-sectional view of a lateral anodisation cell	34
Figure 3.2: Cross-sectional view of a conventional single tank cell	35
Figure 3.3: Schematic illustration of typical porous silicon morphologies. (a) n- (100) orientated wafer anodised in the dark, (b) n- (110) orientated wafer, (c) n- (100) orientated wafer with back side illumination, (d) p+ wafer with dilute ethanolic HF, (e) n+ wafer with dilute aqueous HF, and (f) p- with concentrated aqueous HF	35
Figure 3.4: Reaction model for the dissolution of p-Si in aqueous HF solution	36
Figure 3.5: Typical J-V curve of p+-Si in dilute aqueous HF solution. Porous silicon is obtainable for $J > J_{ep}$	37
Figure 3.6: Transmission Electron Microscope (TEM) image of a typical porous silicon particle	38
Figure 3.7: Scanning Electron Microscopy (SEM) image of npSi sample HDS - V001	39
Figure 3.8: SEM image of npSi sample HSD - V002	40
Figure 3.9: TEM image of npSi sample HDS-I002	40
Figure 3.10: SEM image of npSi sample HDS - I002	41
Figure 3.11: Atomic Force Microscopy (AFM) phase image of npSi sample HDS - I002	41
Figure 3.12: AFM valley image of npSi sample HDS - I002	42
Figure 3.13: Weight loss of approximately 1.5 g rotor-milled npSi powder after HF, methanol, IPA and acetone soaks in air (at room temperature)	43
Figure 3.14: Temperature dependent oxidation of npSi for an one hour process	45
Figure 3.15: Pore volume dependency on oxidation temperature	45
Figure 3.16: Synthesis of 5-aminotetrazole	47
Figure 3.17: Synthesis of 5-nitriminotetrazole	47
Figure 3.18: Synthesis of acid copper salt of 5-nitrotetrazole	48

Figure 3.19: IR spectra for 5-nitriminotetrazole and starting material	49
Figure 3.20: IR spectra of the two 5-nitrotetrazole salts	49
Figure 3.21: 5-Nitriminotetrazole crystallised from water	50
Figure 3.22: 5-Nitriminotetrazole crystallised from acetone	51
Figure 4.1: npSi-Based explosive formulation	53
Figure 4.2: Optical light microscope image of npSi-based explosive formulation	53
Figure 4.3: Hotplate set-up for the determination of relative reactivity	59
Figure 4.4: Si:NaClO ₄ mixture	60
Figure 4.5: Si:LiClO ₄ mixture	61
Figure 4.6: Si:Ba(ClO ₄) ₂ mixture	61
Figure 4.7: Si:PETN mixture	61
Figure 4.8: Si:NT mixture	61
Figure 4.9: Si:HNS mixture	62
Figure 4.10: Burning rate experimental set-up. Marker plate (a). High- speed camera (b). Bottom picture shows the method to ignite the test sample (c).	66
Figure 4.11: Schematic view of the pressure chamber	67
Figure 4.12: Closed vessel pressure test set-up	67
Figure 4.13: Schematic depiction of the relative reactivity of NT/Si mixtures with relation to density	71
Figure 4.14: Linear relation between SSA of porous silicon and burn rate	72
Figure 4.15: npSi/NaClO ₄ burn	73
Figure 4.16: npSi/Ba(ClO ₄) ₂ burn	73
Figure 4.17: npSi/PETN burn	73
Figure 4.18: npSi/NT burn	73
Figure 4.19: npSi/HNS burn	73
Figure 4.20: npSi/NT combined pressure test result	74
Figure 4.21: npSi/NT combined peak pressure result	74
Figure 4.22: npSi/NT combined pressures onset results	75
Figure 4.23: npSi/NT combined pressure results – linear portion of the pressure rise	75
Figure 4.24: Relative reactivity result comparison	77
Figure 4.25: Burning reaction mechanism	79
Figure 4.26: Cross-section of exposed area of burn	80
Figure 4.27: SP/npSi mixture reaction velocity as a function of density	81
Figure 4.28: Area determination under the onset point of pressure rise	82
Figure 4.29: Pressable PBX manufacturing process	86
Figure 4.30: Castable PBX manufacturing process	87
Figure 4.31: Small-scale gap test set-up	90

Figure 6.4: Experimental test set-up showing the 2D initiator (a), and the test explosives (b) on top of the aluminium witness block (c)	125
Figure 6.5: Indentation diameter as a function of explosives' height	127
Figure 6.6: Detonation velocity as a function of $1/(H_e/d_i)$ ratio of the explosives column	127
Figure 6.7: Detonation velocity plot from Equation 6.2 with experimental data	129
Figure 6.8: Calculated detonation velocity from Equation 6.4	130
Figure 6.9: RXKF pellets (red) visible inside different casings. Polymeric (a), copper (b) and aluminium confinement (c)	131
Figure 6.10: Indentation profile obtained for tests conducted with copper and aluminium confinement. The innermost profile represents no confinement	132
Figure 6.11: Combined profiles. Inner cone represents the reference, the two middle cones represent the polymeric indentation and aluminium indentation, and the outer cone represents the copper confinement	132
Figure 6.12: Shock tube and shock tube holder (red) assembly	135
Figure 6.13: Shock tube holder and main body assembly with delay element	135
Figure 6.14: Shock tube connector clip assembly	136
Figure 6.15: Booster casing assembly	136
Figure 7.1: Proposed non-metallic detonator design	137
Figure 7.2: Shock wave simulator test set-up	140
Figure 7.3: Typical high-speed video image interpretation	141
Figure 7.4: 400g booster inside ribbed sleeve – typical test set-up (front view)	143
Figure 7.5: 400g booster inside ribbed sleeve – typical test set-up (side view)	144
Figure 7.6: Typical witness plate result showing a grooved imprint	144
Figure 7.7: Typical witness plate result – side view. The top (a) forms the outside and the bottom (b) forms the inside profile of the witness plate	145
Figure 7.8: Plot obtained from apex polynomial data	145
Figure 7.9: Plot obtained from data measured from inside witness plate	146
Figure 7.10: New booster casing	147
Figure 7.11: New booster casing – sectioned	147
Figure 7.12: Booster casing indicating the position of measurements reported in Table 7.6	148
Figure 7.13: Filled booster casing on top of aluminium witness plate	149
Figure 7.14: Filled booster casing indentation profile	149
Figure 7.15: Reference RXKF charge on top of witness plate	149
Figure 7.16: Reference RXKF charge indentation profile	149
Figure 7.17: Sectioned booster casing showing thin and thick sections	150

Figure 7.18: Indentation profile results for various thicknesses of sleeves	150
Figure 7.19: Indentation profile set-up (a) and a typical result (b)	151
Figure 7.20: Wide angle depiction of the result. Reference result (a) and profile result (b)	151
Figure 7.21: Depiction of indentation measurements	152
Figure 7.22: Shock wave pressure variances through different materials	158
Figure 8.1: Typical ultrasonic weld interface	161
Figure 8.2: Typical set-up of clamped in position on tensile tester	162
Figure 8.3: Sample inside climatic chamber on tensile tester	162
Figure 8.4: Diurnal cycle as given in MIL-STD- 331C	163
Figure 8.5: Diurnal temperature profile used for conditioning of test samples	163
Figure 8.6: Test items inside climatic chamber	164
Figure 8.7: Shock tube (a) and shock tube holder (b) interface	164
Figure 8.8: Shock tube and shock tube holder interface failure	165
Figure 8.9: Shock tube holder (a) and main body (b) interface	165
Figure 8.10: Shock tube holder (a) and main body (b) interface failure	165
Figure 8.11: Main body (a) and booster (b) body interface	166
Figure 8.12: Main body (a) and booster body (b) interface failure	166
Figure 8.13: Motorola RFID scanner (a) and an RFID tag (b)	170
Figure 8.14: RFID tag inside aluminium shell positioned in the middle off 100 aluminium shells	170
Figure 8.15: RFID tags positioned inside the shock tube holder (a), body (b) and the clip (c)	170
Figure 8.16: 30 HDPE bodies containing 30 RFID tags	171
Figure 9.1: Graphical representation of the output of this research leading to the development of a new lead free and non-metallic detonator	175

LIST of TABLES

Table 2.1: Primary explosives' detonation velocities	17
Table 2.2: Secondary explosives' velocity of detonation comparison	18
Table 2.3: Primary explosives' characteristics	21
Table 2.4: Secondary explosives' characteristics	22
Table 2.5: Estimated heat of reactions	28
Table 2.6: Advantages of track and trace systems	30
Table 2.7: Disadvantages of track and trace systems	31
Table 3.1: Nano-porous silicon characteristics (sample from Vesta Sciences)	39
Table 3.2: Properties of oxidised npSi powders	44
Table 3.3: Experimentally determined IR frequencies with tentative vibration assignments	50
Table 4.1: Balanced stoichiometric ratio (fuel to oxidiser)	56
Table 4.2: Heat of reaction calculated from Equation 4.19	57
Table 4.3: Silicon to oxidiser ratios on mass balance	60
Table 4.4: Properties of oxidised porous silicon powder samples	63
Table 4.5: Explosive formulations used in ageing characterisation	64
Table 4.6: Nano-porous silicon formulations used in burning and power output characterisation	65
Table 4.7: Relative reactivity results obtained for Si/oxidiser mixtures	68
Table 4.8: The stoichiometric ratios with corresponding noise measurements	68
Table 4.9: The effect of different oxidiser-to-fuel ratios	69
Table 4.10: R_r results of npSi-based explosive formulations prepared from aged silicon	69
Table 4.11: R_r results of npSi-based explosive formulations – NT	70
Table 4.12: R_r results of npSi-based explosive formulations – SP	70
Table 4.13: Nano-porous silicon explosive formulations burn rate results (same Si)	72
Table 4.14: Nano-porous silicon explosive formulations burn rate results (same fuel)	72
Table 4.15: Area values obtained for different npSi explosive formulations	82
Table 4.16: Typical PBX formulations (a shortened list from Akhavan, 2011:13)	84
Table 4.17: PSD results of PETN and RDX used in PBX manufacturing	84
Table 4.18: Reference formulations	88
Table 4.19: Pressable PBX development formulations	88
Table 4.20: Castable PBX development formulations	89

Table 5.1: Indentation diameters of witness plate on charging PETN at different densities	108
Table 5.2: PETN density and related VoD according to the Urizar equation	110
Table 5.3: PETN detonation pressures related to VoD	110
Table 5.4: Postulated methodology results	110
Table 5.5: Correction factor related to density	111
Table 5.6: Corrected detonation pressures	113
Table 5.7: npSi Explosive formulation	114
Table 5.8: IDTS transfer test results – fuse head initiated	117
Table 5.9: IDTS transfer test results – delay element initiated	117
Table 5.10: IDTS transfer test results – shock tube initiated	117
Table 5.11: BMW 111-I formulation	119
Table 5.12: BBI results for composition BMW 111-I	119
Table 5.13: Corrected detonation pressures according to Equation 5.10	119
Table 6.1: Explosive column height evaluations – Properties	126
Table 6.2: Explosive column height evaluations – Results	126
Table 6.3: Calculated and measured VoD values from test data	129
Table 6.4: Material properties	131
Table 6.5: Polymeric confinement and indentation profile measurements	133
Table 6.6: Detonation velocity calculations with adapted confinement equation	134
Table 6.7: VoD verifications compared with Du	134
Table 7.1: Different shock wave simulator shapes	140
Table 7.2: 45° small-scale evaluation results	142
Table 7.3: 60° small-scale evaluation results	142
Table 7.4: 75° small-scale evaluation results	142
Table 7.5: Area results of apex curves	146
Table 7.6: Average booster-casing dimensions	148
Table 7.7: Indentation width / depth comparison	152
Table 7.8: Indentation profile compared with ribbed profile	152
Table 7.9: Observations from profile measurements	153
Table 7.10: EXPLO 5 characteristics for RXKF 9501	153
Table 8.1: Pull-out results – Shock tube and shock tube holder interface	166
Table 8.2: Pull-out results – Shock tube holder and main body interface	167
Table 8.3: Pull-out results – Main body and booster body interface	167
Table 8.4: Pull-out results – Shock tube and shock tube holder interface (aged)	167

Table 8.5: Pull-out results – Shock tube holder and main body interface (aged)	168
Table 8.6: Pull-out results – Main body and booster body interface (aged)	168
Table 8.7: RFID tag detection results	171
Table 9.1: Non-metallic assembly configuration	176

GLOSSARY

Terms	Definition/Explanation
Alchemist	Alchemy is an ancient tradition, the primary objective of which was the creation of the mythical 'philosopher's stone', which was said to be capable of turning base metals into gold or silver
Booster	Booster explosives are those components of the explosive train that function to transmit and augment the force and flame from the initiating explosive. They ensure the reliable initiation of the secondary explosive charge
Deflagration	In a deflagration reaction, the decomposition of the explosive material is propagated by a flame front, which moves slowly through the explosive material in contrast to detonation
Detonation train	A triggering sequence, also called an explosive train, is a sequence of events that culminates in the detonation of explosives
Detonation	This term is used to describe an explosive phenomenon whereby the decomposition reaction is propagated by the explosive shock wave traversing through the explosive material. The shock front is capable of passing through the high explosive material at great speeds, typically thousands of meters per second
Detonator	A detonator is a device used to trigger or initiate an explosive or explosive device. It is usually the first part in the detonation train
Explosion	An explosion is a rapid increase in volume and release of energy in an extreme manner, usually with the generation of high temperatures and the release of gases. An explosion creates a shock wave. If the shock wave is a supersonic detonation, then the source of the blast is called a 'high explosive'. Subsonic shock waves are created by low explosives through the slower burning process known as deflagration
Explosive	Any substance or device that can be made to produce a volume of rapidly expanding gas in an extremely brief period

High explosive	Explosive materials that tend to react by detonation
Low explosive	Explosive materials that tend to react by deflagration
Primary explosive	A primary explosive is an explosive that is sensitive to stimuli such as impact, friction, heat, or electrostatic sources of initiation
Propellants	A propellant is a material that produces pressurised gas that is utilised to achieve propulsion of a solid body
Pyrotechnics	Pyrotechnics is the science of using materials capable of undergoing self-contained and self-sustained exothermic chemical reactions for the production of heat, light, gas, smoke, and/or sound
Saltpetre	Sodium nitrate
Secondary explosive	Secondary explosives are explosives that are comparatively insensitive to stimuli such as heat, friction, and shock. They are mostly classified as high explosives, and are generally detonated with a primary explosive

ACRONYMS and ABBREVIATIONS

Acronyms/Abbreviations	Definition/Explanation
AFM	Atomic Force Microscopy
° C	degree celsius
atm	atmosphere
B.E.T.	Brunauer–Emmett–Teller
BBI	Ballistic Ball Indentation
cc	cubic centimetre
cc/g	cubic centimetre per gram
CJ	Chapman-Jouget
dB	decibel
DCHP	Dicyclohexyl phthalate
DDT	Deflagration-to-detonation transition
DDNP	diazodinitrophenol
DLA	dextrinated lead azide
DOA	Dioctyl adipate
DSC	Differential scanning calorimetry
EDX	Energy-dispersive X-ray
EPA	Environmental protection agency
EVA	Ethyl vinyl acetate
F	Fluoride
FTIR	Fourier transform infrared spectroscopy
g	gram
GaAs	Gallium arsenide
GAM	gelatin/azide/molybdenum disulfide
GaP	Gallium phosphate
H	Hydrogen
h	hour
HF	Hydrofluoric acid
HMX	Cyclo-tetramethylenetetranitramine
HNS	Hexanitrostilbene
HTPB	Hydroxy-terminated polybutadiene
IDTS	Intermediary detonating transfer system
IED	Instantaneous electric detonator
IML	Intrinsic Materials Laboratory
InP	Indium phosphate

J	Joule
Kel-F	chlorotrifluoroethylene–vinilidene fluoride
keV	kilo-electronvolt
kJ/mol	kilojoule per mole
LA	Lead azide
LMNR	lead 2-mononitroresorcinate
mA/cm ²	milliampere per square centimetre
mg	milligram
ml	millilitre
Mpa	megapascal
mΩ/cm	milliohm per centimetre
nm	nanometre
npSi	nano-porous silicon
NT	Nitriminotetrazole
NTO	Nitrotriazole - 5 - one
OH	Hydroxide
PBX	Plastic bonded explosive
PETN	Pentaerythritol tetranitrate
PS	Porous silicon
RDX	Cyclo-trimethylenetrinitramine
RFID	Radio frequency identification
rpm	revolutions per minute
s	Second
SDT	Shock-to-detonation transfer
SEM	Scanning Electron Microscopy
Si	Silicon
SiC	Silicon carbide
SiGe	Silicon-germanium
SLA	service lead azide
SP	Sodium perchlorate
SSA	specific surface area
SSGT	Small scale gap test
TATNB	triazido-trinitrobenzene
TEM	Transmission Electron Microscopy
TNT	Trinitrotoluene
V	Volt
VoD	Velocity of Detonation

CHAPTER 1

INTRODUCTION

1.1 Background

Chemicals have been used to produce heat, light, smoke, noise and motion for thousands of years, and this use most likely originated either in China or India. The need to produce and control this energy to fulfil a specific purpose eventually led to the creation of the science behind explosives. Explosive materials (also energetic materials) are materials that produce exothermic chemical reactions, generating gas and heat in a fraction of a second.

Developments in energetic material science continued to a point where more defined high explosives, propellants and pyrotechnics were created. Thomson Gale further classified these as blasting agents, primary explosives, low explosives and high explosives (*Gale Encyclopedia of Science*, 2001:5). Each area subsequently split into its own specialised field of applications, namely, for military operations, mining, civil engineering, construction and other uses.

Explosives are used to break or cause damage to their immediate surroundings, largely in a controlled manner. Shock waves produced by the rapid expansion of gases are one of the main causes of destruction following an explosion (Kent, 2003:116).

The total shock energy consists of energy contained in the shock front, in the detonation driving zone and in the reaction zone. A detonation front (or shock front) is intrinsically unstable and possesses a transient three-dimensional structure (Lee, 2008:11). Detonations with a sonic condition behind the reaction zone are called Chapman–Jouguet (CJ) detonations. The CJ theory bypasses certain details of the detonation structure and is accepted as a solution of to steady, one-dimensional conservation equations. Explosives rely on many factors to perform optimally to their intended design and/or function. Energetic materials are applied to attain a well-defined goal. The main explosive charge is usually applied to achieve this goal; however it all starts with the detonator and the subsequent augmentation of energy. The principle of energy enhancement in an explosive system is referred to as the augmentation of energy and is also known as the explosive train principle (Duguet, 2009:7). An empirical structure of a detonation train is described in Figure 1.1.

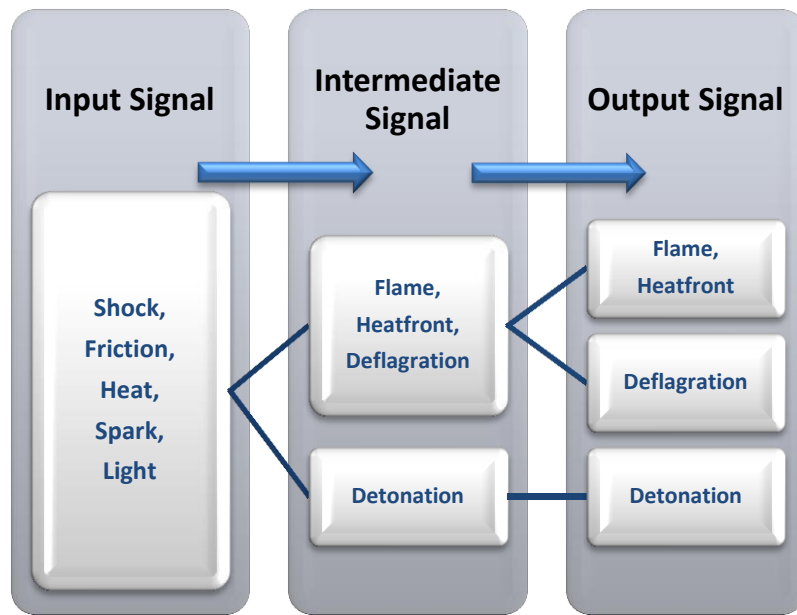


Figure 1.1: Empirical structure of a detonation train

An explosive detonator is an independent system that entails its own explosive train in an enclosed environment. An explosive detonator consists of a primary explosive charge and a secondary explosive charge. The detonator can also contain a pyrotechnic delay element. Mercury fulminate and gunpowder were packed into a copper cylinder, closed at one end, to develop the first detonator. This basic design is somewhat similar to what is still in use today. Mercury fulminate, since its discovery in the 16th century (Duguet, 2009:35), was the only initiating (or primary) explosive known until the last decade of the nineteenth century. In 1891, Theodor Curtius first prepared lead azide (LA) for explosive applications (Brown, 2010:187). LA eventually replaced mercury fulminate as the primary explosive in detonators.

LA is currently the primary explosive of choice, mainly because of its sensitivity that renders it highly susceptible to initiation when exposed to low energy levels. One of LA's greatest attributes is its ability to undergo a deflagration to detonation transition (DDT) in a fairly short timeframe. The sensitivity of LA to friction is one of its biggest disadvantages from a safety point of view. The introduction of LA into commercial detonator manufacturing resulted in an unacceptably high level of explosions during its production and use (Agrawal, 2010:77). Despite its friction sensitivity, LA is still used extensively today mainly owing to a lack of suitable alternatives. Pentaerythritol tetranitrate (PETN) is currently the explosive of choice as secondary charge in commercial detonators.

When applied as a base charge in detonators, PETN does not have many limitations. It is sensitive to reliably pick up from low-energy inputs and produce high-energy outputs (via detonation reaction). This sensitivity can be a concern during manufacturing and application, but incorporation of waxes in the manufacturing process is utilised successfully to control this problem (Brown, 2010:175). The thermal stability of PETN, although somewhat less than that of cyclo-trimethylenetrinitramine (RDX), is good, and PETN can be stored for several years in controlled environments.

Lead-based materials are catalogued in the environmental protection agency (EPA) toxic chemical list. They are regulated under the Clean Air Act as Title II Hazardous Air Pollutants and also classified as a pollutant under the Clear Water Act in the United States (Mehta et al., 2009:175). These regulatory aspects led many research projects to focus on and develop a primary explosive that could replace LA (from an environmental point of view).

In January 2002 the Faculty of Science and Engineering at the University of California (San Diego) issued a press release with the heading “Computer chips found to possess explosive properties useful for chemical analysis and nanoscale sensors” (*Science Daily*, 2002). Since the accidental preparation of exploding nano-porous silicon, its potential as an explosive ingredient in explosive formulations has been energetically pursued. Energetic materials are used in a number of critical defence components (Subramanian et al., 2009:2). The use of nano-porous silicon in commercial explosive environment has not been as extensively pursued as in the military environment.

Sailor patented a porous silicon-based explosive in 2004 (Sailor et al., 2004). This porous silicon-based explosive formulation consists of nano-porous silicon (npSi) and an oxidiser. The use of nano materials in explosive compositions also increases the sensitivity to external stimuli of the explosive compositions as reported by Lamy-Bracq et al. (2007:103). Such compositions are sensitive to friction and electrostatic discharge (Berger et al., 2006:91). This was validated by Subramanian et al. (2009:2).

Batchelor and Loni (2010:6) stated that the surface chemistry of the porous silicon was one of the most important parameters affecting the explosive nature of the material. Canham (1997c:44) reported that the ageing of porous silicon was noted as early as 1965, when the porous silicon was stored in ambient air for a prolonged period. The use of a polymer binder did not only assist in improving the sensitivity of the explosive formulations specifically towards friction and heat (Morgan et al., 2008:115), but also increased the shelf life of nano-porous silicon-based explosive formulations. This

finding relates to the sensitivity of the porous silicon explosive formulation and its shelf life. Current limitations of the nano-porous silicon-based explosive formulation are its sensitivity to external stimuli and poor shelf life.

On the 4th of April 2008, the European Directive on Identification & Traceability of Explosives came into effect. The ultimate research aim pertaining to this project is explicitly to look into the use of radio frequency identification (RFID) tags to achieve the above. Currently the incorporation of RFID tags into existing commercial detonating systems (component level) cannot be achieved. The reason for this is the interference generated by the metal components of the detonating systems to the signal used by the RFID antenna. A novel detonator design is needed to replace the traditional metal components. To achieve this target, a thorough understanding of the application of explosives is desirable.

Understanding detonation physics is vital in exploring the wider applications of explosives. The environment in which explosives are used can greatly affect their behaviour and hence their ability to react completely. Further to this is the chemical compatibility of ingredients even more so after ageing. Incompatibility between components can compromise functionality and safety of the system. The characteristics of the explosive formulation to be developed are intended to be determined in relation to the environment in which the new non-metallic detonator is likely to be applied. One of the main characteristics should be the velocity of detonation (VoD). This characteristic is an invaluable parameter for an explosive formulation that primarily dictates the intended application. Agrawal (2010:30) reported that the VoD of an organic explosive was also a function of the energy produced by its decomposition. The theoretical calculation of the VoD then became complex as most equations were formulated focusing on organic or inorganic mixtures and not combinations of the two.

1.2 Statement of Research Problem

A suitable replacement for LA used as an initiating explosive charge is still a challenge. Environmental concerns force this issue to be addressed. The successful development of a silicon-based explosive formulation is expected to provide a replacement for LA. The design and development of a detonator that has the ability to be tagged will also be a significant step forward in keeping track of detonators throughout their life cycles. This will prove vital not only in terms of traceability for security purposes, but also for inventory control in a manufacturing environment.

Establishing a suitable scientific knowledge base describing the detonation behaviour of explosives in a surrounding environment of non-metallic confinement is currently a requirement to ensure the optimised development of a non-metallic initiating system.

The main aims of the proposed study are therefore two-fold:

- Develop and evaluate a silicon-based explosive formulation to replace LA as the primary explosive component in an explosive initiator.
- Design, develop and evaluate a non-metallic detonator shell that will form the basis in which an RFID system can be incorporated.

1.3 Scope and Research Objectives

1.3.1 Scope of study

In order to establish the technology required for a non-metallic detonator, a project plan was developed. The research study focused on the following points:

- Literature study.
- Porous silicon-based explosive formulation development.
- Deflagration to detonation transition development and establishing the science behind it.
- Detonator design and development.

1.3.2 Research objectives

The following are the main research objectives:

- To conduct a literature survey to establish the status of current local and international nano-porous silicon developments and metal-free detonator developments.
- To determine the characteristics of a suitable nano-porous silicon to be used as part of an explosive formulation.
- To determine the physical, chemical and explosive characteristics of the silicon-based primary explosive formulation.
- To assess and validate the functionality of a silicon-based explosive formulation.
- To determine the physical and explosive characteristics of a plastic-bonded explosive (PBX) formulation that can be readily initiated with silicon-based explosive composition.
- To develop, evaluate and characterise an initiator body that is non-metallic and capable of housing a tagging and tracing function.
- To assess functionality of the non-metallic detonator design.

- To develop the detonation physics knowledge base addressing explosive behaviour in non-metallic environments.

1.4 Experimental Design and Research Methodology

1.4.1 Porous silicon-based explosive formulation development

Current international and local environmental issues have motivated scientists to abandon the use of heavy metals in industrial and related applications. Commercial detonators use heavy metals in their explosive formulations.

The intended development of porous silicon-based explosive focuses on characterising porous silicon and the development and characterisation of the silicon-based explosive formulation. The plan of this part of the research focuses on the following:

- Performing laboratory experimentation.
- Determining the chemical characteristics of the porous silicon-based explosive formulation.
- Determining the explosive characteristics of the porous silicon-based explosive formulations.
- Determining the effect of different environments on the detonation physics of an initiating explosive formulation.

On conclusion of this part of the study, it is expected that a nano-porous silicon-based primary explosive formulation will be developed and scientifically evaluated to serve as a replacement for LA.

1.4.2 Detonator design and development

This part of the study focuses on the design and development of a novel non-metallic detonator system that can reliably function according to its original design intent.

The development of a non-metallic detonator shell focuses on identifying and characterising polymeric materials as well as the performance characteristics of the non-metallic detonator shell when filled with various components. The characterisation of alternative materials can be done by laboratory experimentation.

The focus of this part of the research is to determine the physical characteristics of selected polymers needed to manufacture a suitable non-metallic detonator body.

On conclusion of this part of the study, it is expected that a non-metallic detonator shell will be developed that is easy to fill and produce reproducible functionality. The effects

of a non-metallic shell on the performance of the explosives are postulated with a possible scientific explanation. The effects of the non-metallic detonator casing on the behaviour of the explosive used are scientifically described.

1.4.3 Deflagration-to-detonation transition development

It is necessary to develop a deflagration-to-detonation transition system that functions reliably in a non-metallic environment.

The development of a deflagration-to-detonation transition system was mainly done with laboratory experimentation. The focus of this part of the research can be extended to:

- determine the effect of the casing material on the rate of detonation of the explosive material used;
- determine the most effective column diameter and length;
- determine the most effective nano-porous silicon to explosive ratio;
- evaluate the material performance when subjected to various pressures during consolidation of the explosive composition;
- determine the ability to reliably pick up energy from the timing delay; and
- determine the ability to reliably initiate the base explosive charge in the detonator.

On conclusion of this part of the study, a deflagration-to-detonation transition system is developed that will be easy to manufacture and produce consistent functionality. The detonation mechanisms thus developed is scientifically described involving physics of explosion.

1.5 Outline of the Thesis

The thesis is divided into nine chapters. Chapter 1 introduces the subject matter, scope of work and research objectives of the thesis. Chapter 2 provides a short history of explosives, describing their origins, applications and developments over the past decades. It further revisits relevant work on nano-porous silicon and selected explosives properties.

Chapter 3 describes the development of nano-porous silicon with characterisation results. This chapter also describes how the processes of ageing, storage and oxidation affect nano-porous silicon. The preparation of tetrazole salts is also presented here.

Chapter 4 describes the development and evaluation of new nano-porous silicon-based explosive formulations. Tetrazole salts (from Chapter 3) and other oxidisers are used to prepare mixtures with nano-porous silicon. In the second part of this chapter, the development of a PETN-based PBX explosive is described. A new test methodology to further characterise explosive formulations developed in this study is introduced here.

In Chapter 5 an explosive train is proposed involving the newly developed explosive formulations developed in Chapter 4. Indentation profiles of detonation tests conducted on witness blocks are analysed using a methodology developed in this study.

Chapter 6 focuses on developing a non-metallic detonator casing. Different polymeric materials are used to contain a PBX explosive charge. The influence of non-metallic confinement on the detonation velocity of the explosive is measured and analysed. Chapter 7 describes the optimisation of the non-metallic booster body. A theoretical model is used to describe the magnitude of shock waves through different media.

In Chapter 8 the effect of environmental conditions on the strength of the non-metallic body under different conditions is described. The compatibility between the non-metallic detonator body and a wireless RFID system is demonstrated.

The summary and conclusions from the research findings are reviewed in Chapter 9.

CHAPTER 2

LITERATURE REVIEW

2.1 Historical Background to Explosive Research

It is generally accepted that black powder was perhaps the first explosive mankind had used successfully. As early as 220 BC, an accident occurred when Chinese alchemists unintentionally made black powder while separating gold from silver, resulting in an explosion (Akahvan, 1998:1). Unfortunately, it is still unknown whether those alchemists ever realised that they had manufactured black powder. Greek fire was used in a battle in 668 A.D. (Explosives.org, 2009) and that might well be regarded as one of the first pyrotechnic mixtures other than black powder.

Black powder was used for hundreds of years in an uncontrolled ignition process. However, methods were gradually developed for controlled ignition. Since 1831, black powder was often ignited with a fuse developed by William Bickford (Helmenstine, 2013). The fuse was primarily manufactured from black powder itself and served the purpose of guiding the flame to the black powder charge in the hole. This procedure often required workers to manually light fuses with an open flame (Lindahall.org, 2013).

In 1846, the Italian scientist Ascanio Sobrero discovered nitroglycerine. In 1866, Alfred Nobel found a safer means of handling nitroglycerine in the form of dynamite (Nitroglycerin, 2013). The discovery of dynamite brought with it the invention of the first blasting cap. Alfred Nobel was the inventor of a mechanism to initiate (detonate) reliably dynamite. This was needed as black powder did not have the capability to initiate dynamite reliably.

Nobel first started to detonate the nitroglycerine using a small charge of black powder contained in a glass bulb or wooden cylinder. He used a mixture of gunpowder and mercury fulminate, or the fulminate on its own. These formulations were later packed into a copper cylinder (Brown, 2010:186). In 1865, mercury fulminate was not new. As part of the family of fulminates, Basil Valentine described gold or aurum fulminate in 1603 as:

...a powder that kindles as soon as it takes up very little heat or warmth, and does remarkable great damage when it explodes with such vehemence and might that no man would be able to restrain it (Brown, 2010:179).

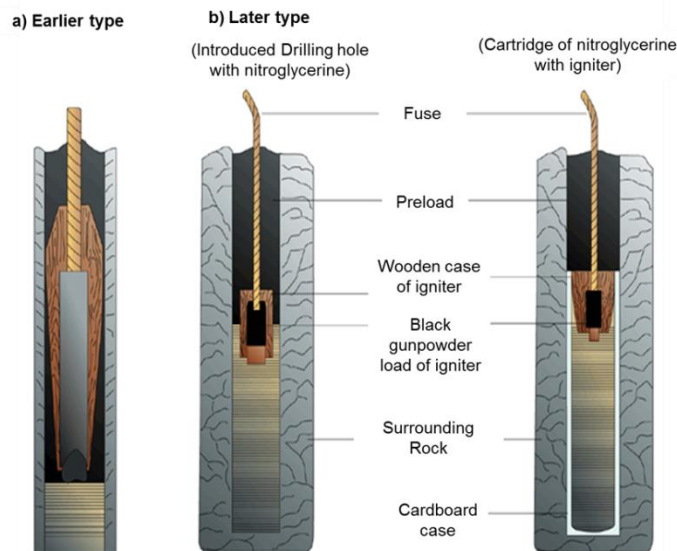


Figure 2.1: Nobel's first detonator systems (Zandipour, 2014)

The Swedish-German scientist Johann Kunkel von Löwenstern had known mercury fulminate from the 17th century (Klapötke, 2011:1). Fulminates were used in fireworks, toys and demonstrations of supposed magic. In 1800, Edward Howard reported on new fulminating mercury (Brown, 2010:1881). The application of fulminates leaned more towards the firearms industry. Mercury fulminate was used in flintlock guns but proved to be less successful because of its power and sensitivity. It was only when Alfred Nobel used mercury fulminate in his blasting that it found its first real practical application (Klapötke, 2011:1). Without significant modification, this device was used into the 1920's (Once Upon A Time, 2013), hence changing the means of initiating explosives forever.

Optimal initiation of explosives signifies the start of a process that eventually leads to the bulk of the energetic material releasing all of its potential energy. Optimal energy release is essential in obtaining the desired performance from the explosive used. Optimal energy is obtained by using a combination of explosives that varies in pick-up sensitivity and output power. This method or process is often referred to as an energetic train or detonation train. Mainly two types of energetic trains can be identified. The first comprise low explosive trains or pyrotechnic trains and the second high explosive trains, generally known as explosive trains. Both types of trains function on the principle of energy augmentation. The process mainly consists of an input, an intermediate and an output signal (Duguet, 2009:7). Up to the invention of the blasting cap, the energetic train was predominantly low explosive. This means that an open flame was used to ignite the intermediate part. This intermediate part produced a

controlled burning to ignite the bulk charge (black powder). The bulk black powder charge then reacted with a severity determined by its volume, confinement and chemical make-up.

The invention of nitroglycerine, and more specifically the invention of dynamite, established the capability of obtaining a detonation reaction when desired. The invention of the blasting cap opened the doors for late nineteenth-century explosives like TNT, picric acid, tetryl, pentaerythritol tetranitrate (PETN) and cyclo-trimethylenetrinitramine (RDX) to be used (Akahvan, 2011:20).

A blasting cap forms the first part in a high explosive train. The principal function of a blasting cap is to transform an input signal into a detonation output signal. Nobel's first blasting cap did just that. Blasting caps continuously developed not only to keep pace with the development of primary explosives, but also with the developments with regard to the input signal. Primary explosives saw significant progress in the late 19th century through to the 20th century, establishing many fulminates, azides, styphnates and tetrazoles. The most predominant primary explosive used today is lead azide. Lead azide was discovered in Germany in the late 19th century, and owing to its stability and ability to undergo an extremely rapid deflagration-to-detonation transition, it is still widely used today (Duguet, 2009:40).

It can be seen that irrespective of the input stimuli, the blasting cap still augments energy from a low input to substantially higher output energy. The type of initiating system used is greatly dependent on the specific application. Explosives applications and environments have changed over the decades, and with that the technology of explosives has changed as well. New explosive formulations have been developed to accommodate modern requirements. The bases of these requirements are still physical safety and environmental compatibility (less toxic). Mercury fulminate has been abandoned because of these two notable shortcomings: it has poor thermal stability (safety related), and it has toxic and corrosive properties (Duguet, 2009:37). Not only are the safety and environmental properties of explosives immensely important from a modern-day perspective, but also the waste generated from explosives manufacturing processes. In order to reduce, control and monitor explosive waste, environmental legislation has been implemented (Akahvan, 2011:25). Future explosive developments are expected to focus more on environmentally acceptable or 'greener' explosive compositions. This approach will not only apply to the final explosive product but also to its manufacturing process.

2.2 Science of Explosives

Explosives are used to break or cause damage to their immediate surroundings. Shock waves, produced by the rapid expansion of gases, are one of the main causes of destruction (Kent, 2003:116). This applies both to the military and commercial applications of explosives on their surroundings. The total shock energy consists of the energy contained in the shock front, detonation driving zone and the reaction zone as described in Figure 2.2.

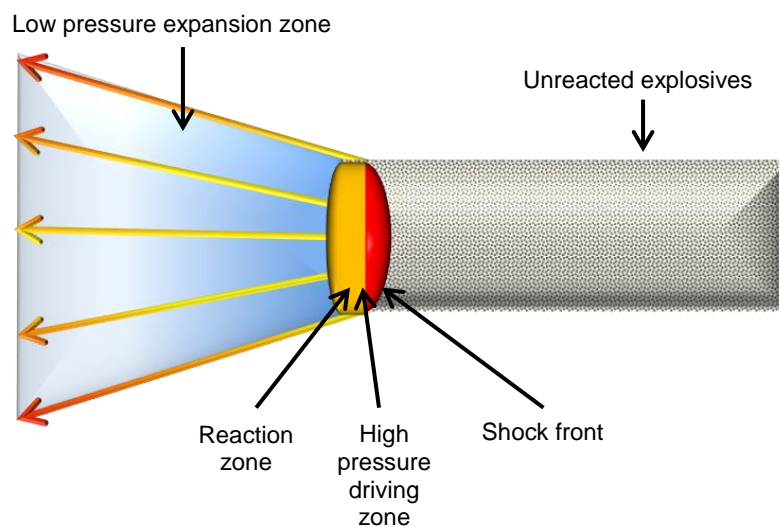


Figure 2.2: A two-dimensional detonation reaction

The detonation front (or shock front in Figure 2.2) is found to be intrinsically unstable and possesses a transient, three-dimensional structure (Lee, 2008:11). Detonations with a sonic condition behind them are called Chapman–Jouguet (CJ) detonations. The explosives used in current detonator systems produce CJ detonations. This also applies to larger explosive charges (or main charges).

When an explosive decomposes, the shock energy is used to break its immediate surroundings (creating fragments). This is achieved by reflection and super-positioning of such shock waves. Large gas volumes are also obtained during detonation and this energy is used to accelerate fragments. Explosive compositions are thus designed according to application in order to achieve a well-defined goal. Military explosives have a high breaking capability (brisance), thus a strong shock front. Commercial explosives produce higher gas volumes in order to achieve optimal ground movement.

Explosives rely on many factors to perform optimally to their intended design or function. The main explosive charge is usually applied to achieve this goal, but it all starts with the detonator and the subsequent augmentation of energy.

This applies to both military and commercial environments. Explosives rely on the rapidity of the reaction to perform their intended functions optimally. Although the rate of the reaction is primarily a function of the chemical make-up of the explosive, many external factors can also influence the rate at which an explosive reacts. Some of these factors include confinement, VoD, density, diameter of the explosive and the means of ignition.

2.2.1 The means of confinement

The detonation shock wave is transmitted more efficiently by a dense solid such as rock. It travels freely through the material, but the impulse which it imparts is not a type which, by itself, can propel heavy pieces of rock over a distance and thus do measureable work. Instead it produces intense compression for a very short time, and this tends to cause plastic and elastic flow in a homogeneous hard material. A brittle material will fail under intense compression, and an even tougher one will fail in tension when the initial compression phase of the wave is suddenly reversed by reflection. These extreme forces produce spalling and cracking effects in even the strongest materials. Gases are then able to expand and heave the broken mass in any direction (Bailey & Murry, 2000:29).

2.2.2 Detonation velocity of explosives

Because of the partition of energy requirement, the velocity of detonation (VoD) at which the detonation shock wave proceeds through a charge is an important parameter of the explosive material. The VoD of the explosive material can be predicted by calculation and/or measured experimentally (Bailey & Murray, 2000:29). The higher the VoD of the explosive, the higher the CJ pressure generated.

2.2.3 Density of explosive material

Since the detonation wave proceeds through the explosive, the energy which it releases within and behind itself will depend on the mass of the explosive traversed per unit area of the wave front. The more mass that is concentrated into a given volume of explosive, the more energy the wave front can release in order to sustain itself at high velocity. Provided the charge is of reasonable diameter and well confined, the velocity of detonation appears to be almost exactly proportional to the loading density or density of the explosive material in its particular means of application (Bailey & Murray, 2000:29).

2.2.4 Effect of diameter of the explosive material

The VoD falls below its maximum when the diameter of the charge is below a certain value, if the degree of confinement is also small. This diameter varies for different explosives, according to their sensitivity (Bailey & Murray, 2000:30). This can continue to a point where the VoD is so low that it cannot be sustained. The reaction subsequently dies. This is termed 'critical diameter'. The inverse argument also applies and is of great importance when initiating systems are designed. A sustainable detonation cannot be achieved when the diameter of the explosive column below the critical diameter of the specific explosive.

2.2.5 Effect of initiation/ignition of the explosive material

Explosive charges and initiating systems have been designed to ensure that the maximum intended effect of the explosives is achieved upon application. This can only be achieved when the explosives react at full and constant VoD. A detonator imparting an inadequate shock wave to the receptor charge will result in the receptor charge reacting at a velocity that is evidently lower than its potential VoD (Bailey & Murray, 2000:30).

Optimal initiation of an explosive can ensure the shortest reaction run-up in terms of distance and time and hence ensure optimal availability of the potential energy of the explosive formulation. Any explosive requires a certain time and distance for the chemical reaction to stabilise. A high explosive, for example, will first start to burn and then transform (jump) into a detonation reaction. By using the most efficient energy transfer the jump in reaction can be obtained in the shortest time and distance from the initiation point. The means of providing the first energy to the explosive is thus very important to ensure that the explosive reaches optimal performance in the shortest possible time from the start of the reaction.

The principle of augmentation of energy (explosive train) is again highlighted (Duguet, 2009:7). Since the development of explosives, this principle has not changed. Research and development focus on the development of new explosive formulations and improved methods of application.

2.3 Functions of a Detonator and Relevant Recent Developments

The earliest record of the use of gunpowder for blasting in a mine occurred in the *Proceedings of the Schemnitz Mine Tribunal* of 8 February 1627. The use of gunpowder in blasting progressed in three stages. The first was both laborious and hazardous and lasted until 1831. Holes were drilled, typically 0.6 m deep. The hole was

loaded with gunpowder and blocked off (tamped). A narrow channel of gunpowder was poured on the ground to a distance deemed safe by the miner. It was lit and the shot was fired. Many miners were killed using this method of blasting, including Thomas Epsley, an exponent of the art and the trainer of many miners in the use of this method (Brown, 2010:78).

In 1831 William Bickford invented safety fuse. This invention provided a better and much safer way to ignite gunpowder. Within the first few years after the use of safety fuse had been adopted, the number of blasting accidents had fallen by about 90% (Brown, 2010:79).

Detonators can have various forms and can contain several explosives formulations. The purpose of the detonator is to convert the input energy into detonation energy. The input energy can consist of many forms, for example: the flame energy from pyrotechnic composition (delay composition or fuse head), the kinetic energy from a stab initiator, or the combination of shock and flame as provided from a shock tube system. The main explosives components used inside a detonator are the primary explosive component and the output explosives (also referred to as the base charge). A typical detonator is shown in Figure 2.3 with different detonator configurations depicted in Figure 2.4.

The detonator has changed very little since the late 20th century in respect of the actual design and design intent. The ingredients, however, underwent considerable development for optimal performance. These developments are also driven by global environmental drives, e.g., moving away from heavy metals in explosives formulations. The deposition of lead post detonation is responsible for human toxicity and environmental contamination, especially in mines (Owen, 2006:9). Mercury contamination of soils and vegetation close to historic mercury fulminate production plants is also a common occurrence (Arbestain et al., 2009:1).

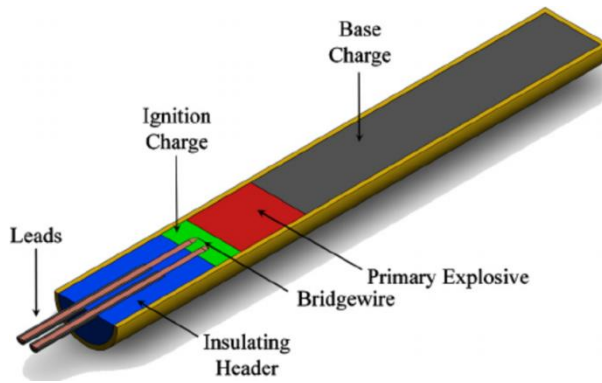
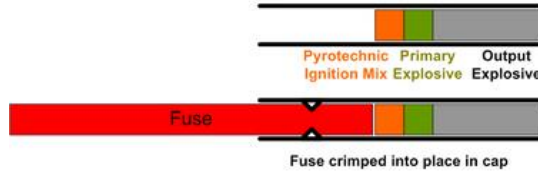
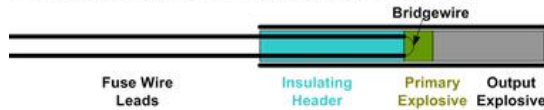


Figure 2.3: A typical explosive detonator (Parson et al., 2010)

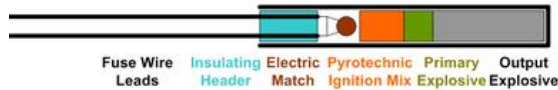
Pyrotechnic Fuse Type Blasting Cap



Solid Pack Electric Type Blasting Cap



Match or Fusehead Electric Type Blasting Cap



Exploding Bridgewire Type Blasting Cap



Slapper Type Blasting Cap

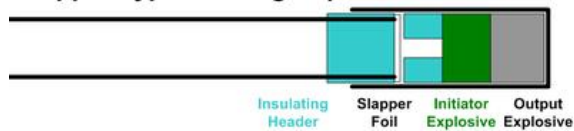


Figure 2.4: Various detonator designs (Wikipedia, 2011)

The late 19th and early 20th century saw the development of many novel and interesting explosives formulations. The development of explosives such as trinitrotoluene (TNT),

cyclo-trimethylenetrinitramine (RDX), and pentaerythritol tetranitrate (PETN), to name but a few, opened a whole new world of explosives and their applications. The development of primary explosives used inside a detonator also led to several novel explosives.

The development of primary explosives started with the discovery of gold fulminate in the 16th century. Its application was primarily in pyrotechnics, but more importantly it paved the way for the discovery of mercury fulminate. Since its discovery, mercury fulminate has been the only initiating explosive known. However, mercury fulminate was abandoned due to its toxicity in the 20th century (Duguet, 2009:37).

In 1891, Theodor Curtius first prepared lead azide (Brown, 2010:187). Lead azide eventually replaced mercury fulminate as the primary explosive of choice. In 1993, Bill Clinton (former president of the United States of America) issued a series of executive orders to reduce and eliminate where possible the procurement of hazardous substances and chemicals by federal facilities, directly implicating lead azide. Existing primary explosives include organic compounds, metastable interstitial composites and coordination complexes. Primary explosives such as tetracene, diazodinitrophenol (DDNP) and triazido-trinitrobenzene (TATNB) were developed, each with its own limitations (Huynh et al., 2006). Novel primary explosives like 5-nitrotetrazolato-N²-ferrate hierarchies were developed with great success (Huynh et.al., 2006).

2.4 Explosives Materials for Detonators

Primary explosives or primary high explosives are very sensitive materials and can easily be exploded by the application of heat, flame, spark, impact and friction. They are dangerous to handle and used in comparatively small quantities. Primary explosives are generally used in detonators, primers and percussion caps. Examples of sensitive explosives are lead azide, mercury fulminate and silver azide (Agrawal, 2010:6). Table 2.1 shows a comparison between selected primary explosives and their velocity of detonation (VoD).

Table 2.1: Primary explosives' detonation velocities

Explosive name	Density (g.cm ⁻³)	Detonation Velocity (VoD) (m.s ⁻¹)
Lead Azide	4.71	5180
Mercury Fulminate	4.42	4250
Lead styphnate	3.02	5200

2.4.1 Base charge explosive

Output explosives, more commonly known as base charge explosives, are used to increase the energy output of the detonator. Secondary explosives are used as the base charge in a detonator. Agrawal (2010:6) describes secondary high explosives as explosives that are relatively insensitive to both mechanical shock and flame but explode with greater violence when set off by an explosive shock obtained by detonating a small amount of primary explosive in contact with it. Some well-known secondary explosives include PETN, HMX, RDX and TNT.

Table 2.2: Secondary explosives' velocity of detonation comparison

Explosive name	Density (g.cm ⁻³)	Detonation Velocity (VoD) (m.s ⁻¹)
RDX	1.76	8750
HMX	1.90	9100
PETN	1.70	8400

Detonator systems intended to initiate secondary explosives (main explosive charges) cannot function properly if they do not contain both primary and secondary explosives components.

2.4.2 Lead azide

Mercury fulminate, lead 2-mononitroresorcinate (LMNR), lead azide and lead styphnate are simple inorganic salts. They are thermally stable to >200 °C, but their excessive sensitivity and release of toxic metals upon detonation have made their replacement desirable (Huynh et al., 2006).

Lead azide has a high ignition temperature and is today the most commonly used primary explosive. Lead azide is poisonous, slightly soluble in hot water and in alcohol. It is also highly soluble in a diluted solution of nitric or acetic acid in which a little sodium nitrate has been dissolved. It reacts with copper, zinc, cadmium or alloys containing such metals, forming an azide that is more sensitive than the original lead azide. Because lead azide does not react with aluminium, detonator capsules for lead azide are preferably made of this metal. The hygroscopicity of lead azide is very low. Water does not reduce its impact sensitivity, as is the case with mercury fulminate. Ammonium acetate and sodium dichromate are used to destroy small quantities of lead azide. Lead azide may be used where detonation is caused by flame or heat. Its colour varies from white to buff. Lead azide is widely used as an initiating explosive in high-explosive detonator devices. Lead azide, when protected from humidity, is completely stable in stowage (GlobalSecurity.org, 2006).

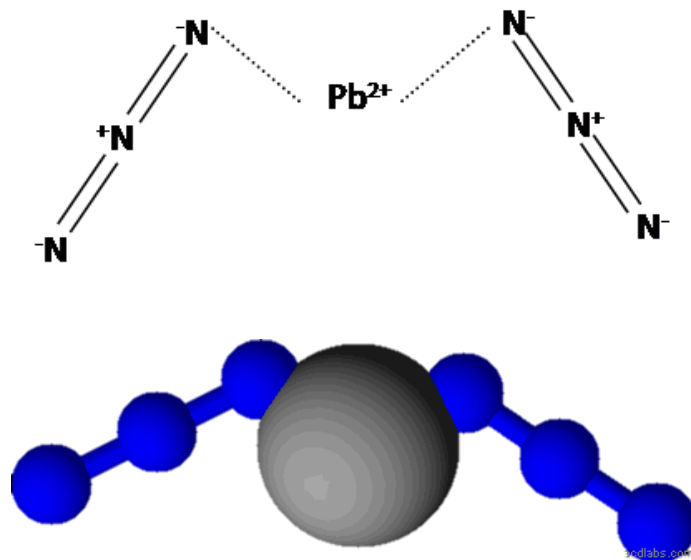


Figure 2.5: Lead Azide

2.4.3 Pentaerythritol tetranitrate (PETN)

PETN is often considered a benchmark explosive. Explosives that are more sensitive than PETN can be classified as primary explosives (Agrawal, 2010:6). PETN is used as a priming composition in detonators, a base charge in blasting caps and a core load for detonating fuse. It is more sensitive to shock and friction than TNT or tetryl, and is seldom used alone in large boosters. It is primarily used in booster and bursting charges of small calibre ammunition, in upper charges of detonators in some land mines and shells, and as the explosive core of detonating cord. One of the more well-known boosters utilising PETN is the pentolite booster. Pentolite is a mixture of PETN and TNT.

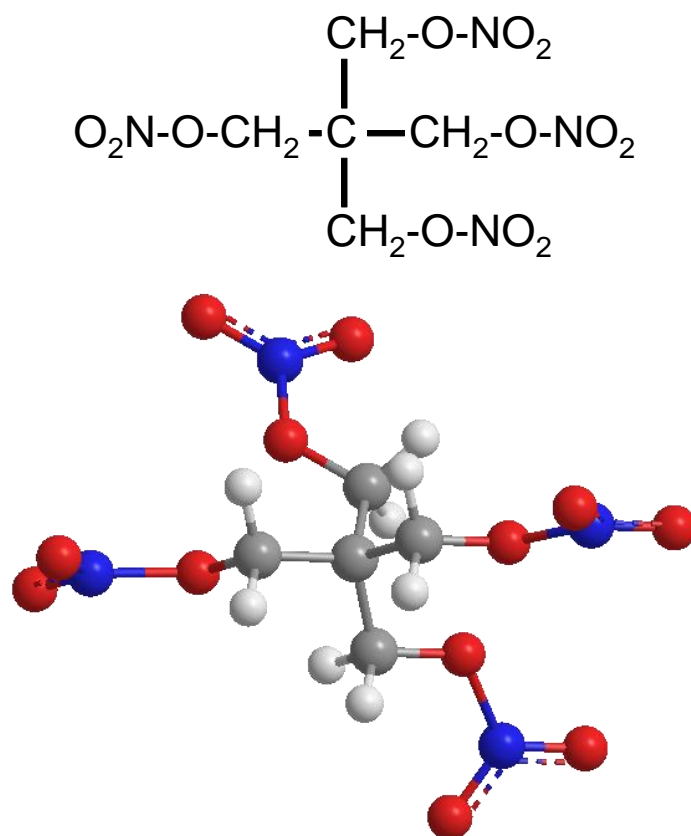


Figure 2.6: PETN

2.4.4 Lead azide and PETN detonating system

Lead azide and PETN are widely used in detonating systems. This preference can be ascribed to two reasons: its sensitivity and power output. In order for the detonating system to function optimally, the explosive of choice must react in a desired way to the input energy supplied. This is not the only characteristic that is required. The detonating system shall remain stable and functional for a time duration usually specified by the customer. Selecting a suitable explosive to be used in a detonating system is not a simple task. The following issues need to be considered:

- The environmental condition of the areas where the detonating system will be required to function.
- The time duration and storage conditions of the detonating system following manufacturing.
- The input energy that will be used to initiate the detonating system.
- The output energy needed by the detonating system.
- Environmental impacts.
- Safety requirements.

Lead azide is currently the primary explosive of choice for detonators. Its sensitivity to pick up from fairly low-energy sources and its ability to undergo a deflagration-to-detonation transition in a fairly short timeframe is one of its greatest attributes. Table 2.3 shows a brief comparison between different primary explosives and some of the criteria to be considered when choosing a primary explosive for the use in a detonating system.

Table 2.3: Primary explosives' characteristics

Primary explosives	VoD (m.s ⁻¹)	Density (g.cm ⁻³)	Friction Sensitivity	Ignition Temperature (°C)	Toxicity
Lead Azide	5180	4.71	Extremely sensitive	350	Toxic
Lead Styphnate	5200	3.02	Less than MF or LA	260-310	Toxic
Mercury Fulminate	4250	4.42	Extremely sensitive	160	Toxic
Diazodinitrophenol	7000	1.71	Sensitive	157	Toxic

Lead azide can also be prepared using four different methods. Agrawal (2010:77) distinguishes between service lead azide (SLA), dextrinated lead azide (DLA), improved lead azide and a gelatin/azide/molybdenum disulfide (GAM) form of azide. These variations of lead azide have been developed to produce a less sensitive form of lead azide.

Another main consideration is the compatibility of lead azide with other explosives. As the primary explosives component in a detonating system, lead azide is seldom used on its own. Combinations with other primary explosives and secondary explosives are often used. This can be done safely, as lead azide is compatible with almost all other explosives.

Lead azide's sensitivity to friction is one of its biggest disadvantages from a safety point of view. Introducing lead azide into commercial detonators resulted in unacceptably high levels of explosions during its manufacture and use (Agrawal, 2010:77). The development of SLA and DLA improved the sensitivity to friction of lead azide but it did not solve the problem completely. Despite its friction sensitivity, lead azide is still used today owing to the lack of an alternative energetic material. Environmental pressure is also on the rise and the lead content of lead azide makes it less desirable for use in an explosive composition.

PETN is currently the explosive of choice for the secondary charge in commercial detonators. Table 2.4 compares some of the properties of PETN with those of other secondary explosives. The same approach used in selecting a primary explosive is applied to selecting a secondary explosive for use in a detonating system. The secondary explosive must be sensitive enough to pick up from the power output provided by the primary explosive. The secondary explosive must then react and provide enough energy to carry the detonation reaction to the next step in the detonation system.

RDX is also a secondary explosive and is being used to replace PETN in many applications. RDX is more powerful than PETN and is also less sensitive than PETN (Agrawal, 2010:6). RDX is, however, more difficult to manufacture than PETN and also more difficult to acquire. PETN is easily initiated by LA and rapidly undergoes a deflagration-to-detonation transition.

Table 2.4: Secondary explosives' characteristics

Secondary explosives	VoD (m.s ⁻¹)	Density (g.cm ⁻³)	Detonation pressure (kbar)
PETN	8400	1.70	307
RDX	8800	1.80	338
HMX	9100	1.90	390
TNT	7000	1.60	190

PETN does not have many limiting properties. The thermal stability of PETN is somewhat less than that of RDX but this can be argued as being marginal. Its sensitivity is a concern during manufacturing and use, but incorporation of waxes in the manufacturing process is utilised successfully to control this problem (Brown, 2010:175). It is thus clear that lead azide and PETN remain the combination of choice when developing an initiating system.

2.5 Limitations of Current Explosive Materials and Recent Developments

Lead has been a part of human civilization for a long time and knowledge about its toxicity dates back to the early 1900's. Even though it was known to be toxic lead was introduced in gasoline in 1922. In 1965, Clair Patterson (a geochemist) brought attention to airborne lead changing the perception that only factory workers were susceptible to lead poisoning. The Clear Air Act was signed into law in 1970 (Fowler, 2008:1). Subsequently lead-based materials are catalogued on the Environmental Protection Agency (EPA) toxic chemical list and classified as pollutants under the Clear Water Act in the United States of America (Mehta et al., 2009:175). In 2008, the EPA

reduced air emission rules for lead requiring industries to reduce lead levels to $0.15 \mu\text{g}\cdot\text{m}^{-3}$. This is 10 times greater than earlier restrictions. Implementation plans were required by 2013, with a proposed compliance date of January 2017 (Fowler, 2008:3).

In 2015, Europe amended annex XVII to regulation (EC) No 1907/2006 of the European Parliament and of the Council on the Registration, Evaluation, Authorization and Restriction of Chemicals (REACH) (OJL., 2015:1). This regulation addresses commercial articles that contain lead. Articles containing more than 0.05% lead (by weigh) are affected by this regulation (Redshaw, 2015:1).

The South African Occupational Health and Safety Act, Act no. 85 of 1993, contains the national Lead Regulations, 2001. These regulations specify an occupational exposure limit of $0.15 \text{ mg}\cdot\text{m}^{-3}$ (Government Notice R236, 2002:2). Lead Azide has a molecular weight of $291.2 \text{ g}\cdot\text{mol}^{-1}$ of which 71.2% is lead (by mass). This led many research projects to develop a primary explosive that can replace LA (from an environmental point of view).

Efforts directed towards greener primary explosives led to the development of numerous explosive formulations. Explosive formulations included copper(I)5-nitrotrazolate (DBX-1) reported on by Fronabarger and Klapötke (Fronabarger et al., 2011:1; Klapötke, 2011:18). DBX-1 is thermally stable up to $325 \text{ }^\circ\text{C}$ and its impact sensitivity is comparable to that of lead azide (0.04 Joule (J) compared to 0.05 J respectively) (Klapötke, 2011:18). 1-Nitroquanyl-3-nitro-5-amino-1,2,4-triazole (ANTA-NQ) has an impact sensitivity of 46J and friction sensitivity of greater than 360 N (Chavez and Parrish, 2010:1). Although this explosive formulation is developed as a green explosive, it is rather insensitive and not suitable as a lead azide replacement. Sabatini and Oyler (2016:5) reported on numerous green primary explosives including potassium 4,6-dinitrobenzofurozan (KDNBF), potassium 1,1-dinitramino-5,5-bis(tetrazolate) (K_2DNABT) and 1,5-(dinitramino) tetrazole dipotassium salt. Most complexes are synthesised from numerous steps and are complex to purify. Other challenges include availability of raw materials (or building blocks), poor particle morphology, limited data pertaining to large scale manufacture and characterization (detonation behaviour in large scale application).

Knowledge pertaining to detonation physics is vital in understanding the application of explosives. The environment in which explosives are used can greatly affect their behaviour and hence their ability to produce energy to their optimal potential. The characteristics of the explosive formulation to be developed are determined in relation

to the environment it will be applied in (the new non-metallic detonator). The main characteristic is detonation velocity (VoD). This characteristic is one of the most important characteristics of an explosive formulation and mostly dictates its primary application.

Other factors influencing the VoD include the means and extent of confinement, diameter, and the density of the explosive charge. In an ideal detonation, both the detonation pressure and the detonation velocity are dependent on the initial density of the unreacted explosive (Cooper, 1996:287). The effect of confinement on the VoD of an explosive formulation is complex. Cooper (1996:281) stated that the confinement of an explosive charge helps to increase the VoD of the formulation bringing it closer to its ideal performance. Experimental data for this is sparse and has not been taken accurately across a wide range of set parameters (Souers et al., 2004:19). Available data also refers to experiments conducted with steel used as the means of confinement. The VoD of a cylindrical column of explosives changes if the diameter of the column changes. A limited amount of data relating to this is available, since the test set-up is rather expensive and time consuming (Cooper, 1996:297).

Ideal explosives generally show a slow drop in velocity proportional to the reciprocal of the charge radius ($1/R$ ($R =$ charge radius)). This reduction in velocity continues until failure occurs at a velocity typically about 5% below the infinite diameter (Haskins et al., 2006:385). The effect of column height instead of column diameter on the VoD of the developed base charge explosives is determined. This is applicable in both the intermediate and main charge development of the non-metallic detonator.

The position of the initiating system in relation to the acceptor charge also influences the energy transfer of the initiator in an effect referred to by Held (1989:153) as the corner-turning effect. Held described the detonation as a flow process. In a flow, pressure builds up higher in the direction of propagation than perpendicularly to it. The reaction velocity will increase with an increase in pressure. Therefore the reaction and detonation wave will propagate at a higher velocity in the direction of propagation than transversely to it. In detonator design this is important as the primary explosives component must be in line with the secondary explosives component. In the next step of the detonation train this is not always true. Here the detonator can be enclosed by explosives, and transfer of energy is both radial and axial. The energy on the radial axis needs to be enhanced to ensure optimal initiation of the intermediary charge or the main explosives charge. It is accepted that there is enough room for the main charge to initiate properly (optimal corner turning has been achieved).

Current knowledge gaps are identified in being an understanding of the detonation physics (as briefly described above) when applying explosives in non-metallic environments. Proper explosive characteristics of nano-porous silicon explosive formulations are also not available.

2.6 Novel Silicon-Based Explosive Materials

2.6.1 Nano-porous silicon

Porous silicon was discovered by Art Uhlir at Bell Laboratories in the mid 1950's. Nano-porous silicon was prepared by chance while trying to develop a means to electrochemically machine silicon wafers. It was found that under the appropriate conditions of applied current and solution composition, the silicon did not dissolve uniformly but instead fine holes were produced. Since this did not provide the desired effect, the results were reported in a Bell Laboratories technical note and the material was pretty much ignored (Sailor Research Group, 2003). This was until the press release statement by the University of California (San Diego);

Most people are familiar with silicon as material that's used in computer chips for circuits ... This is the same material but we're making it into a very finely divided form of silicon – a nanocrystal – that has such a high surface area that it burns very quickly. The faster the burn the bigger the bang (*Science Daily*, 2002).

Sailor, a professor of chemistry and biochemistry and the lead researcher in the project, further described that when a postdoctoral researcher working in his laboratory tried to cleave the wafer with a diamond scribe, it blew up in his face. “It was just a small explosion, like a cap going off in a cap gun...” (*Science Daily*, 2002).

Nano-porous silicon is a sponge-like form of silicon produced by chemical or electrochemical etching of bulk silicon. The silicon is classified according to pore sizes:

- macro: > 1 μm
- meso: 10 nm to 100 nm
- micro: < 5 nm

The porosities can be tailored from 10 to 90% (Subramanian & Santosh, 2008).

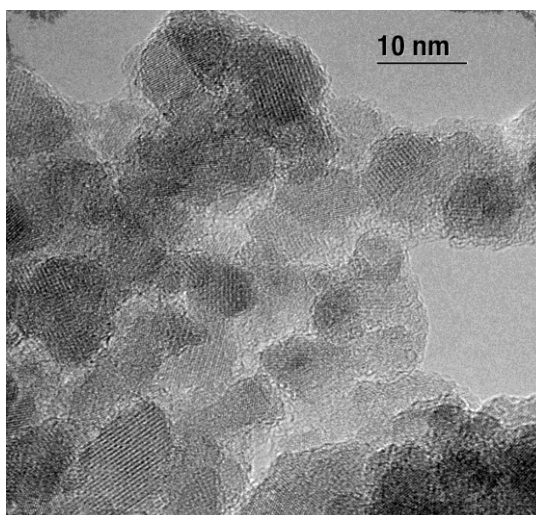


**Figure 2.7: Nano-porous silicon
(Subramanian & Santosh, 2008)**

Nano-porous silicon is luminescent under ultraviolet radiation. The manufacture of nano-porous silicon is on its own a delicate and complex process. Various processes have been developed, including chemical (Subramanian & Santosh, 2008), electrochemical (Subramanian & Santosh, 2008), wet chemical etching (Virginia Semiconductor, Inc., 2003), chemical vapour deposition (Gleason et al., 2006), isotropic silicon etching (White, 2007) and cryogenic reactive ion etching (Henry, et al., 2009). For manufacturing of energetic silicon only chemical and electrochemical etching techniques are used. Ervin et al. (2015:1) described an anchored electrode method for more controllable etching depths.



**Figure 2.8: Nano-porous silicon under ultraviolet radiation
(Subramanian & Santosh, 2008)**

2.6.2 Porous silicon-based explosive

Energetic materials are used in a number of critical defence components ranging from shaped charges, actuators and delay lines to detonators. US defence needs for more advanced energetic materials have been evolving rapidly in recent years. The need for increased mobility, enhanced range and intensity, reduced or modified signatures, reduced collateral damage, and the capability to destroy hardened and buried targets has increased demand for enhanced energetic materials (Subramanian et al., 2009). Sailor patented a porous silicon based explosive in 2004 (Sailor et al., 2004). The invention described the nature of the porous silicon-based explosives in conjunction with an oxidiser. Oxidisers in the invention were selected nitrates, perchlorate salts, selected fluoride salts, and selected solid-state explosives, namely, PETN, TNT and a metal azide (Sailor et al., 2004). Vesta Sciences used sodium perchlorate and iron oxide as oxidisers (Subramanian et al., 2009). Potassium periodate, Sodium metaperiodate and Iodopentoxide were also introduced by Abraham et al. (2016:179-188).

Properties obtained from mixtures described by Subramanian and Sailor seem satisfactory for an explosives formulation. The explosive compositions and nanoporous silicon were defined and categorised accordingly. Sailor primarily used Fourier transform infrared spectroscopy (FTIR), atomic emission spectroscopy and a flame test. Subramanian et al. (2009) described a more detailed analysis of the results. The particle size, nitric acid concentration, BET surface area and mean pore size were determined. The particles were also characterised using scanning electron microscopy (SEM), transmission electron microscopy (TEM) and X-ray diffraction.

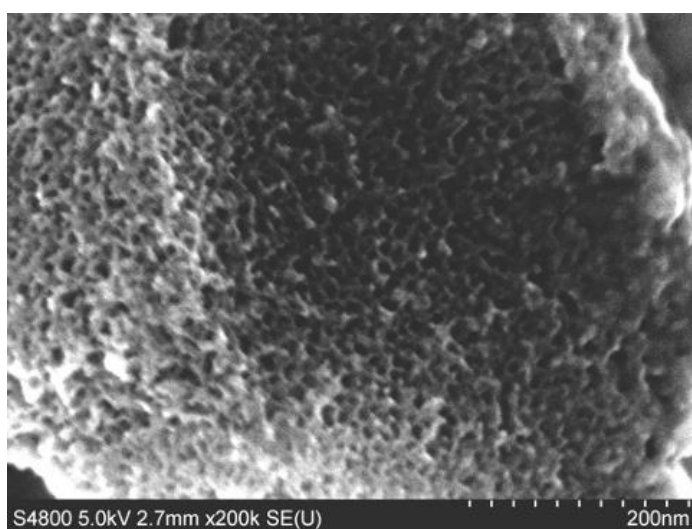


Figure 2.9: High-resolution SEM of pSi surface (Subramanian & Santosh, 2008)

The energetic compositions were characterised by the following tests: estimated heat of reaction, reaction rate of PSi with oxidisers and electrostatic discharge (Subramanian et al., 2009).

Table 2.5 shows the estimated heat of reaction results obtained by Subramanian et al (2009).

Sailor et al. (2004) and Subramanian et al. (2009) made no reference to the shelf life of the porous silicon-based explosives formulations. Bezuidenhout (2009:5) reported the development of a PETN-based nano-porous silicon explosive. During this study the shelf life of the nano-porous explosive composition was noted to be poor. Further analyses on freshly prepared samples exhibited explosives properties. However, the formulations did not function 24 hours later.

Table 2.5: Estimated heat of reactions

Reaction	ΔH_r (kJ.mol ⁻¹)	ΔH_r (kJ.g)
$\text{Si} + \text{O}_2 \rightarrow \text{SiO}_2$	-857	-15.2
$2\text{Si} + \text{NaClO}_4 \rightarrow 2\text{SiO}_2 + \text{NaCl}$	-1737	-10.4
$2\text{Si} + \text{KClO}_4 \rightarrow 2\text{SiO}_2 + \text{KCl}$	-1718	-9.4
$5\text{Si} + 4\text{KNO}_3 \rightarrow 5\text{SiO}_2 + 2\text{N}_2 + 2\text{K}_2\text{O}$	-3019	-6.1
$\text{Si} + (\text{C}_2\text{F}_4)_n \rightarrow \text{SiF}_4 + 2\text{C}$	-806	-6.2
$3\text{Si} + 2\text{Fe}_2\text{O}_3 \rightarrow 3\text{SiO}_2 + 4\text{Fe}$	-905	-2.2
$\text{Si} + 2\text{CuO} \rightarrow \text{SiO}_2 + 2\text{Cu}$	-567	-3.5
$\text{Si} + \text{Bi}_2\text{O}_3 \rightarrow \text{SiO}_2 + \text{Bi}$	-1423	-1.4

Batchelor and Loni (2010) stated that the surface chemistry of the porous silicon was one of the most important parameters that could have an effect on the explosive nature of the material. A gradual change in the hydride passivation to oxide passivation on air storage was likely to result in a decreased potency and might have impacted on how the material was further processed and/or stored (Batchelor & Loni, 2010).

Canham (1997c:44) reported the ageing of porous silicon when it was stored in ambient air for a prolonged period. There are, however, many techniques for changing the surface chemistry and minimising the rate of oxidation to control the ageing process (Batchelor & Loni, 2010).

2.6.3 Porous silicon-based initiating systems

Moving towards green initiating systems, nano-porous silicon was identified as the material that could provide a solution. Several studies involving energetic silicon have described the combustion behaviour of the material when used with different oxidisers. Du Plessis (2007) concluded that the filling of the pores was a function of the pore diameter and a filling factor that ranged from 40% to 70% for NaClO_4 (sodium perchlorate). Du Plessis further established an optimum pore size as being 3–4 nanometres (nm) to achieve the most effective nano-explosions. The combustion of porous silicon (Si) was also shown to be dependent on many factors that include porosity, pore volume, pore depth, and oxidiser ratios (Churaman et al., 2015; Piekiet al, 2015). Flame speed of explosive mixtures was found to be higher than $1500 \text{ m}\cdot\text{s}^{-1}$ for studies conducted involving on-chip porous silicon combustion. Reaction wave propagation was also shown to be influenced by the surface area of the nano-porous silicon (Parimi et al., 2015).

Energetic silicon was characterised and possible uses were outlined in the literature (Ramachandran et al., 2014). However demonstrating energetic silicon as an effective primary explosive replacement (specifically for lead azide) in larger applications has been inconclusive. Commercial initiators can take up to 160 mg of lead azide that is used to initiate a PETN base charge. The PETN base charge must in turn be strong enough to initiate at least a pentolite charge.

2.7 Radio Frequency Identification Tags

Tracing of explosives and related components are becoming an important part of inventory control. Explosive manufacturers, suppliers and end users are required to prove control over inventory and stock movement. This is to ensure that explosives cannot be obtained by unwanted persons. So the main drive is security. Radio frequency identification technology (RFID) is one of the biggest growing technologies with great potential in supply chain management (Knežević et al., 2015:35). RFID are successfully being used in:

- Class identification
- Location identification
- Transfer of further data
- Asset tracking
- Manufacturing
- Supply chain management
- Retailing
- Payment systems

- Security and access control
(Kaur et al., 2011:155)

RFID often refers to Ultra High Frequency (UHF) identification technology. This technology can be subdivided into active and passive systems. Passive systems refer to tags that, in their normal state, are not powered by external sources such as a battery (Asher, 2015:2). RFID readers are used to energize passive RFID systems. Active RFID systems, also called real-time location system) are constantly powered by an external source like a battery (Asher, 2015:4). It is not considered safe practise to have sources of energy like batteries close to explosives therefor active RFID systems are not considered in this study. Other trace and identification systems include barcoding.

2.7.1 Advantages and limitations of radio frequency identification and barcoding systems

Optimal and sustainable data acquisition and reporting is essential in track and trace systems. Adaptalift Hyster (Adaptalift Hyster, 2012:3) describes the advantages and disadvantages of RFID compared to barcoding systems. A comparative summary is given in Table 2.6 and Table 2.7

Table 2.6: Advantages of track and trace systems

Barcodes	RFID
Small and light	Can be read from a greater distance
Less expensive	Do not be positioned in line of sight
Material on which they are placed does not compromise the functionality	Read wright devices
Is a universal technology	High level of security
	Large data capacities
	Minimal human interaction
	Reusable and rugged

Table 2.7: Disadvantages of track and trace systems

Barcodes	RFID
Needs direct line of sight	More expensive
Scanner needs to be close to tag	Shielded when in liquid or surrounded by metal
Labour intensive	Reader collision can occur when two or more readers are used in close proximity of each other
Less security	Chips are readable/writeable and needs two separate machines
Easily damaged	
Damaged barcode cannot be scanned	

2.8 Summary

The research and development work conducted in the last 20 years of the history of explosives focused on the replacement of heavy metals in the chemical make-up of the primary explosives. Current focus is greener and safer primary explosive formulations. The actual performance requirements of a detonating system have not changed since its early development in the 19th century. The challenge thus remains to develop a novel explosives formulation that is greener to the environment and safer for humans.

The development and preparation of nano-porous silicon-based explosives formulation is a realistic development that can be applied as a replacement for a primary explosive like lead azide. The results obtained by Sailor et al. (2004) and Subramanian et al. (2009) are only selected proof that an explosive formulation can be manufactured from nano-porous silicon. By manipulating the pore volume and the surface area of the silicon particle, and by the selection of a suitable oxidiser, an explosive formulation to suit various needs in terms of power output and burn rates can be developed. In doing further research in this area, it is important to remember that explosive compositions from nano-porous silicon are also very sensitive to heat and friction (Subramanian et al., 2009). Although npSi explosive formulations can be manufactured characteristics like shelf life (when mixed with selected oxidisers) combined with high cost of manufacturing prevents npSi from being used in explosive formulations.

The construction of a detonating system has not changed much over the last few decades. Lead azide's sensitivity, its compatibility with other explosives and its stability make it a very good initiating explosive. Environmental pressures will contribute to the complete abolition of lead azide and termination of its use. New technology drives are already producing new generation initiating explosives to replace lead azide. PETN used as the secondary charge in a detonating system can ensure that the power output

of such detonating systems should be adequate for proper functioning. The sensitivity of PETN should ensure compatibility with new generation initiating explosives. The lifespan of LA as an explosive material may be short lived, but PETN will remain the secondary charge of initiator detonating systems well into the future.

A suitable replacement for lead azide (LA) as an initiating explosive charge is still a challenge. Environmental concerns force this issue to be addressed. The successful development of a silicon-based explosive formulation is expected to provide the ability to replace LA. Also the design and development of a detonator that has the ability to be tagged should be a significant step forward in keeping track of detonators throughout their life cycle. This could be vital not only in terms of traceability for security purposes, but also for inventory control. Establishing a suitable scientific knowledge base describing the detonation behaviour of explosives in a surrounding environment of non-metallic confinement is currently a requirement to ensure the optimised development of a non-metallic initiating system.

CHAPTER 3

PREPARATION AND EVALUATION OF NANO-POROUS SILICON AND TETRAZOLE SALTS FOR EXPLOSIVE FORMULATION

3.1 Introduction

Explosive compositions contain a mixture of oxygen and fuel components. Oxygen and fuel react primarily to produce heat and gas. Such mixtures, when initiated, can burn at various rates and are influenced by numerous factors such as type of chemicals used, the density of the products, mixture ratios, and confinement. Pyrotechnic compositions are typical examples of low explosives or deflagrating explosives. Silicon is well known for its use as a fuel in pyrotechnic compositions and more so for its use in pyrotechnic delay compositions. It is a lesser known material as an ingredient in typical detonating explosives. In this research, nano-porous silicon is a fuel that could be used to develop an explosive formulation when combined with selective oxidisers. A potential oxidiser is a tetrazole salt.

Tetrazoles have recently been explored as a possible replacement for lead azide. Tetrazoles are chemical compounds characterised by a doubly unsaturated five-membered ring containing four nitrogen atoms and one carbon atom (Matyas & Pachman, 2013). Nitrimitotetrazole was not only identified as a possible replacement for lead azide, but also as an oxidiser to be mixed with nano-porous silicon.

This chapter describes the preparation of npSi and selective characterisation thereof aimed at explosive applications. Ageing, storage, and oxidation effects on pore size and pore volume of the nano-porous silicon are examined. The manufacture of 5-nitrimitotetrazole is also described.

3.2 Process of Developing Nano-porous Silicon

In earlier studies porous silicon was mainly produced by anodisation in aqueous or ethanoic hydrofluoric acid (HF) solution (Allongue, 1997:3). Today, npSi can be manufactured utilising dissolution chemistry. Dissolution is the process by which a substance forms a solution in a solvent. For the dissolution of solids, the process of dissolution is the breakdown of the crystal lattice into individual ions, atoms or molecules and their transport into the system. The outcome of the process is governed by the thermodynamic energies involved rather than by the process of dissolution itself. Overall free energy must be negative for net dissolution to occur. The energies are controlled by the way in which different chemical bonds interact with those in the solvent (Sirius Analytical, 2017).

3.2.1 Mechanisms of silicon dissolution

Silicon spontaneously gives rise to well-defined pores with nanometre (nm) dimensions. Other materials such as SiC, Si_xGe_{1-x}, GaAs, GaP and InP can also be made porous (Allongue, 1997:3). Dissolution can be obtained by monitoring either the anodic current or the potential. In general, constant flow of current is preferable, as it allows for better control of the porosity and thickness as well as good reproducibility from batch to batch. The simplest cell which can be used to anodise silicon is shown in Figure 3.1.

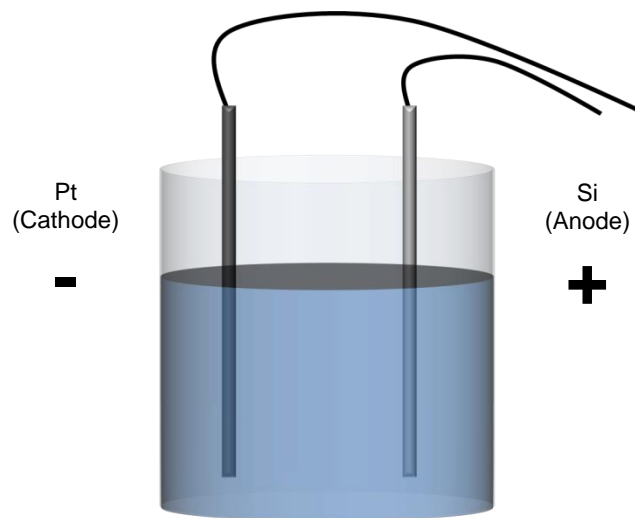


Figure 3.1: Cross-sectional view of a lateral anodisation cell (Adapted from Halimaoui, 1997:12)

The silicon wafer serves as the anode. The cathode can be made out of any HF-resistant conductive material. The cell body itself was made out of a material such as Teflon™. Since the entire silicon wafer serves as the anode, porous silicon (PS) is formed on any wafer surface in contact with the HF solution. This test set-up is simple but often it results in non-uniformity in both porosity and thickness of the resulting layer.

The second type of anodisation cell is the single-cell approach using reversible contact. In this type of cell a metal contact is made to the back of the wafer and sealed so that only the front end of the sample is exposed to the anodising electrolyte. Halimaoui (1997:12) noted that for silicon wafers with low resistivity (typically < few milliohm / centimetre ($\text{m}\Omega\cdot\text{cm}^{-1}$)), a good uniformity was obtained without the need for a metallic contact. For high-resistive silicon wafers (typically > few $\text{m}\Omega\cdot\text{cm}^{-1}$), a high-dose implantation ($\sim 10^{15} \text{ cm}^{-2}$ at 80 keV) of boron (for p-type) or phosphorus (for n-type silicon), on the back end, is required. This type of cell leads to PS layers of good

uniformity. This uniformity simplifies the interpretation of the current–voltage characteristic and offers good control of both thickness and porosity of the resulting layer.

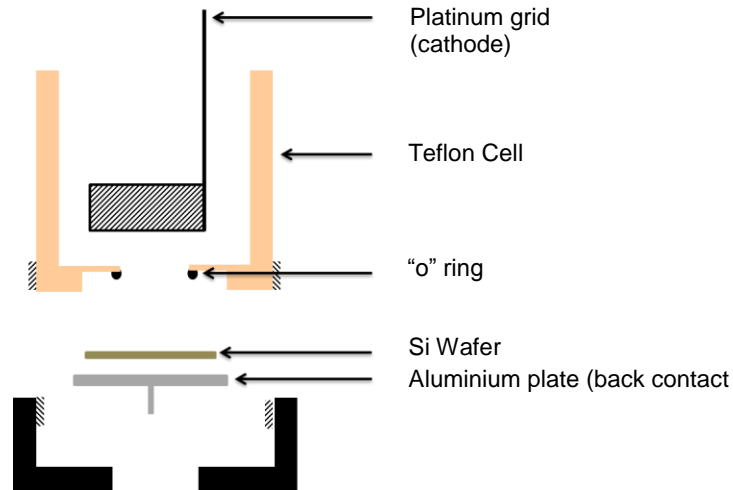


Figure 3.2: Cross-sectional view of a conventional single tank cell (Adapted from Halimaoui, 1997:13)

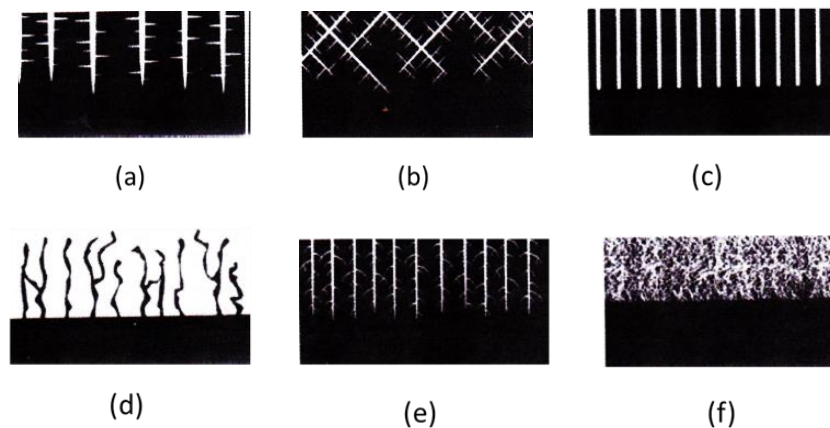


Figure 3.3: Schematic illustration of typical porous silicon morphologies. (a) n^- (100) orientated wafer anodised in the dark, (b) n^- (110) orientated wafer, (c) n^- (100) orientated wafer with back side illumination, (d) p^+ wafer with dilute ethanolic HF, (e) n^+ wafer with dilute aqueous HF, and (f) p^- with concentrated aqueous HF (Allongue,1997:3)

Anodic oxidation of crystalline Si under constant current in aqueous or ethanolic solutions of HF is possibly the most common porous silicon preparative method. An intrinsically easier but less frequently employed technique is the use of an open-circuit chemical stain-etch consisting essentially of HF, nitric acid and water.

3.2.2 Dissolution chemistry

The exact dissolution chemistry of silicon is still unclear but different mechanisms have been proposed (Halimaoui, 1997:13). Halimaoui (1997:14) reported the following overall reaction for the dissolution of silicon:



In the above equations, h^+ and e^- are the exchanged hole and electron respectively and λ is the number of charges exchanged during the elementary step. Mechanisms based on the same approach were often suggested in published literature. A variant for the dissolution mechanism based on a surface-bound oxidation scheme (with hole capture and subsequent electron injection, leading to the divalent silicon oxidation state) was proposed by Halimaoui (Halimaoui, 1997:14).

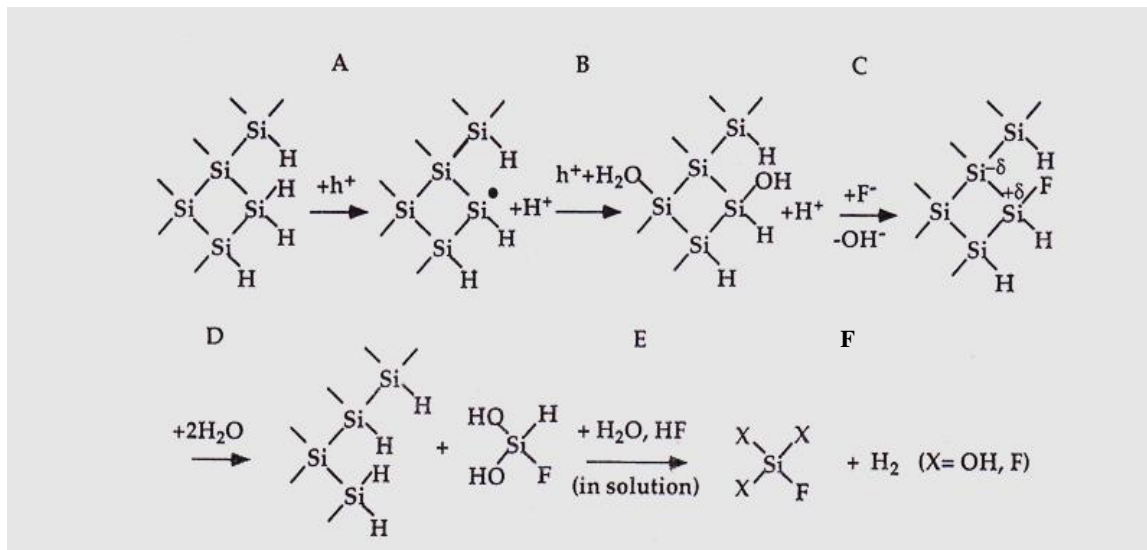


Figure 3.4: Reaction model for the dissolution of p-Si in aqueous HF solution (Allongue,1997:5)

On atomic scale, this model explains that the surface remains H-terminated as long as steps A–B remain slower than steps C–E. This can be achieved by keeping the rate of the hole supply below a certain limit ($J > J_{ep}$) as shown in Figure 3.5. For each Si atom dissolved, two holes are consumed in steps A and B, in association with a divalent reaction.

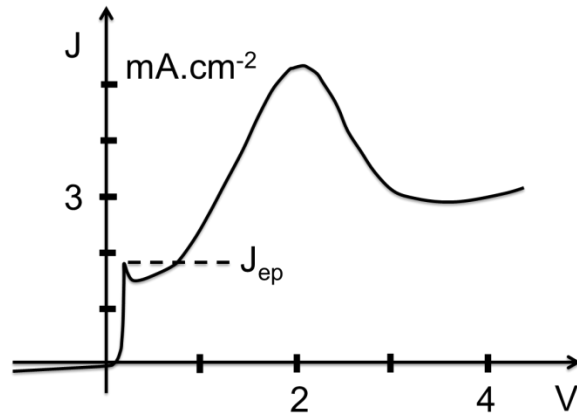
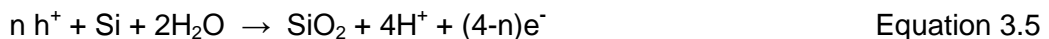


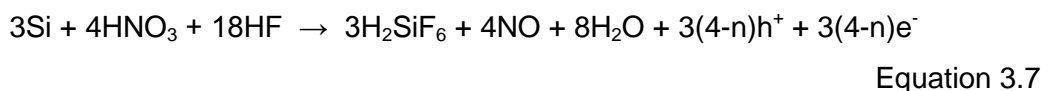
Figure 3.5: Typical J-V curve of p⁺-Si in dilute aqueous HF solution. Porous silicon is obtainable for J>J_{ep} (Adapted from Allongue,1997:3)

One molecule of hydrogen (step F) and two protons (steps B and C) are also generated on the surface. After the initial substitution steps, Si-H → Si-OH → Si-F un-dissociated HF and H₂O molecules chemically attack the polarised Si^{-δ}-Si^{+δ} back bonds. This leaves the hydrogen (H) atom attached to the Si^{-δ} atom on the surface (steps D–E in Figure 3.4). The final step occurs in the solution where the Si complex is further hydrolysed with production of molecular H₂ (step F). As the rate of the substitution S-H → SiOH increases, by increasing the rate of hole supply, the density of Si-OH bonds increases and becomes such that neighbouring groups start to condense into Si-O-Si bridges. This is the early stage of oxide formation.

As with the anodic oxidation of Si under bias, a key component of the stain-etch route to porous silicon formation is generation of holes. In most stain-etch methods employing HF and HNO₃, initially NO is produced which normally serves as a hole injector. Coffey (1997:23) reported the following reactions for the dissolution of stain etched silicon:



Over all the empirical reaction was then given as:



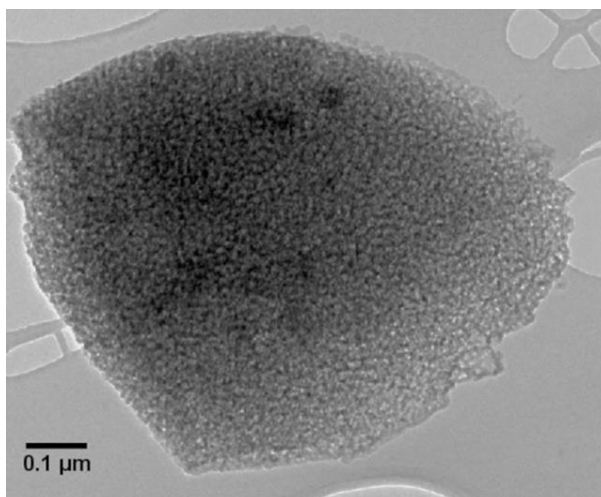


Figure 3.6: Transmission Electron Microscope (TEM) image of a typical porous silicon particle (Subramanian & Santosh, 2008)

3.3 Nano-porous Silicon Sample Characteristics

Many factors influence the performance and reliable functioning of explosive formulations. To manufacture safe and reliable explosive formulations, knowledge of the characteristics of the raw materials is vital. In this part of the research, the focus was on the characteristics of npSi used in explosives formulation and how the level of oxidation of the npSi could influence the reactivity of such formulations.

The samples used in this study were prepared using stain-etching as well as anodisation methods. Nano-porous silicon samples were sourced from Vesta Sciences and Intrinsic Materials. Samples varying in surface area, pore volume and pore size were obtained. Table 3.1 shows the material properties of the samples obtained from Vesta Sciences. These samples had a particle size distribution of $d_{10} = 1$, $d_{50} = 4$ and $d_{90} = 8$ (μm).

In Figures 3.7 and 3.8 different pore sizes are depicted.

Table 3.1: Nano-porous silicon characteristics (sample from Vesta Sciences)

Sample	Surface area (m ² .g ⁻¹)	Pore volume (cm ³ .g ⁻¹)	Pore size (nm)
HDS – V001	116	0.25	7.1
HDS – V002	110	0.23	6.6
HDS – V003	112	0.23	6.6
HDS – V004	116	0.22	6.2
HDS – V005	107	0.21	6.2
HDS – V006	133	0.28	6.5
HDS – V007	130	0.27	5.6
HDS – V008	176	0.39	7.0
HDS – V009	180	0.39	6.8
HDS – V010	176	0.34	6.2
HDS – V011	136	0.23	5.9

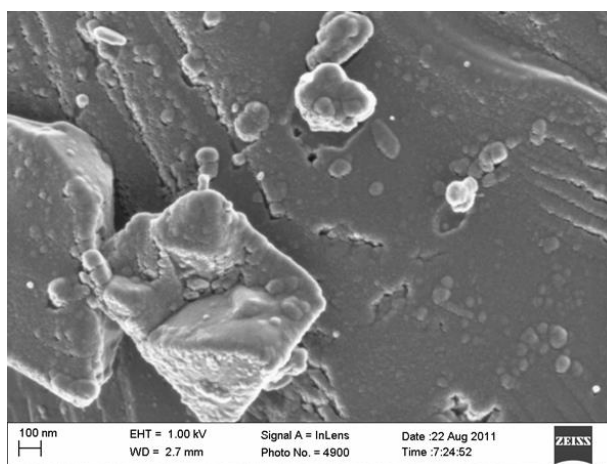


Figure 3.7: Scanning Electron Microscopy (SEM) image of npSi sample HDS - V001

To determine the influence of the level of oxidation on the reactivity of porous silicon-based explosive formulations, specially prepared silicon samples were used. Intrinsic Materials prepared porous silicon membranes from 6-inch silicon substrates (0.005 milliohm per centimetre (mΩ.cm⁻¹) to 0.02 mΩ.cm⁻¹ resistivity) by electrochemical anodisation using hydrofluoric acid / methanol electrolyte. The membranes, when dried, were subsequently ball-milled in ambient conditions using zirconia grinding

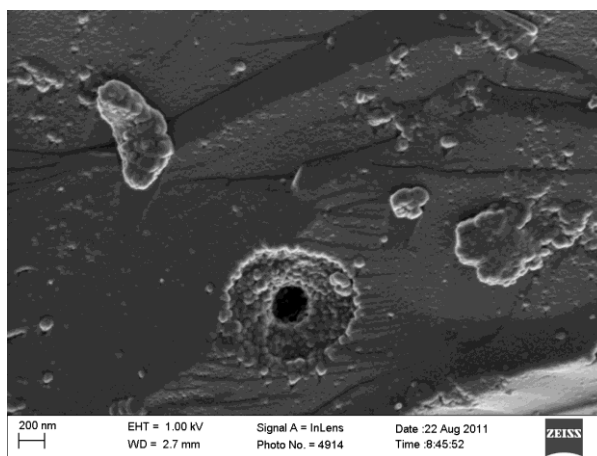


Figure 3.8: SEM image of npSi sample HSD - V002

media, at 300 rpm for 3 minutes, to yield a particle size distribution with $d_{10} = 4 \mu\text{m}$, $d_{50} = 24 \mu\text{m}$, $d_{90} = 86 \mu\text{m}$ (Appendix 3A). An additional batch of aged npSi powder was used for comparative studies. This was rotor-milled to yield a desirable size distribution with $d_{10} = 2 \mu\text{m}$, $d_{50} = 15 \mu\text{m}$, $d_{90} = 34 \mu\text{m}$ (Appendix 3A) and stored in a jar for 14 months. Chemical reagents used were as specified in Appendices 3B to 3D. Thermal oxidation of powders was carried out in an unpressurised air environment, using an oven with borosilicate glassware. Porosity of a nano-porous silicon sample is shown in Figure 3.9. Different surface roughness is notable when comparing Figure 3.7 with Figure 3.10.

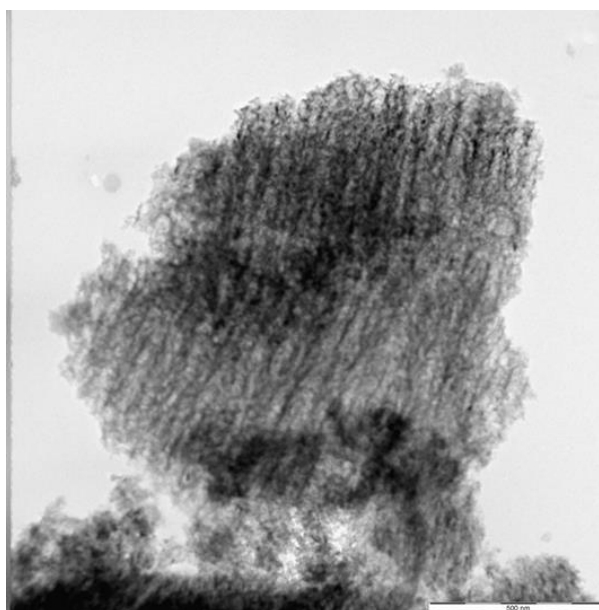


Figure 3.9: TEM image of npSi sample HDS-I002

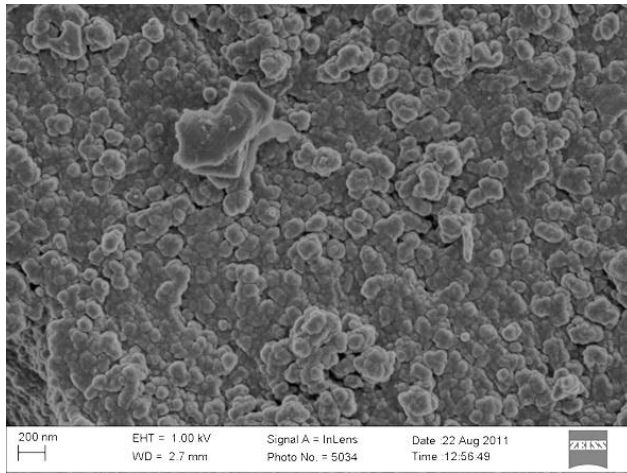


Figure 3.10: SEM image of npSi sample HDS - I002

The surface of the nano-porous silicon is shown in Figures 3.11 and 3.12.

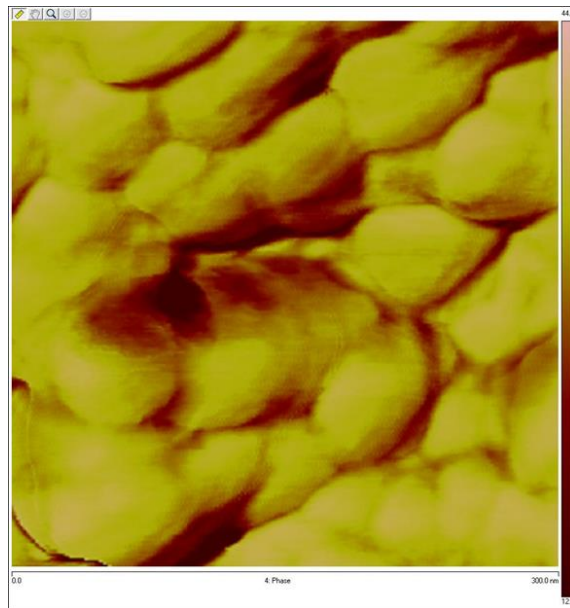


Figure 3.11: Atomic Force Microscopy (AFM) phase image of npSi sample HDS - I002

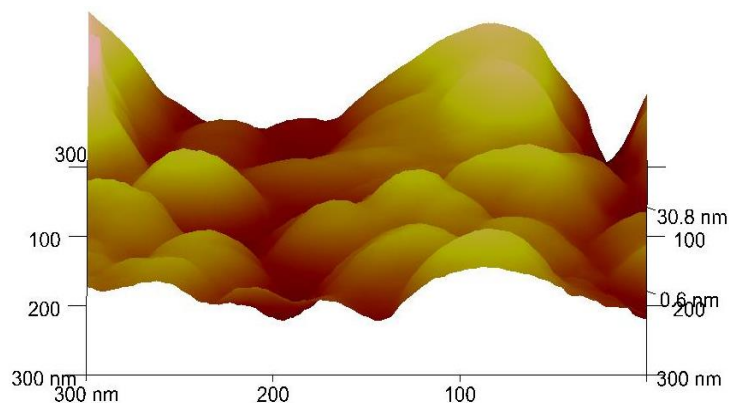


Figure 3.12: AFM valley image of npSi sample HDS - I002

The ball-milling process is known to oxidise npSi when carried out in air. This, in combination with the destructive nature of milling, has the effect of reducing pore volume. In order to determine effects associated primarily with a controlled degree of thermal oxidation (and natural ageing in air), the milled powders were washed in methanol-hydrofluoric acid to first remove the milling-induced oxide, thereby leaving a fresh hydride-passivated internal pore wall structure. To maintain this ‘clean’ surface, it was imperative that the npSi did not subsequently come into contact with air or aqueous solutions. Also, for safe handling, the hydrofluoric acid had to be completely removed from the pores. Consequently, an etch-rinse procedure was used to ensure that the npSi became ‘clean’ (wet) and free of hydrofluoric acid, for both storage/transport and use as a starting material for thermal oxidation. npSi batches of up to 8 g were manufactured using the following procedure:

- (a) Pre-wet milled npSi powder with 20 ml methanol.
- (b) Add 100 ml of 10% aqueous hydrofluoric acid.
- (c) Filter-off solution after 5 minutes (PTFE Buchner arrangement).
- (d) Five-minute soak-rinse with 100 ml methanol, twice (filtering off solution each time).
- (e) Final 5-minute soak-rinse with 100 ml iso-propyl alcohol (IPA).
- (f) Aliquot damp powder into batches for storage and drying/oxidation.

3.3.1 Storage effects on npSi

The IPA-damped powder scheduled for storage, sample HDS-I001, was immediately transferred to a 50 ml poly-ethylene/propylene container with screw-top lid, the

container then being filled with 40 ml acetone. The thread of the container was covered with several layers of Parafilm® before the lid was securely tightened. After attaching the lid, an outer seal was made with additional layers of Parafilm® held tightly in place with Sellotape®. The integrity of the seal was tested over a couple of days, with neither visible leakage nor smell of acetone being encountered. The small container was then put inside a larger container and back-filled with mica, the secondary container also being sealed internally and externally with Parafilm® and Sellotape®. The reduction in weight of the damp powder was a good indicator of how much solvent remained in the pores. This is shown in Figure 3.13 (for the rotor-milled npSi powder (QNA3538) subjected to the same HF wash/solvent-soak process then air dried from an acetone slurry (in a 7 cm diameter Petri dish)). The linear decrease up to 110 minutes relates to the bulk acetone evaporation, with the subsequent non-linear decrease being attributed to acetone evaporating from within the pores of the npSi. Complete drying, in air, took up to 4 hours (forwards-extrapolated) for this sample size (Figure 3.13). Weight loss of approximately 1.5 g rotor-milled npSi powder after HF, methanol, IPA and acetone soaks in air (at room temperature) was observed.

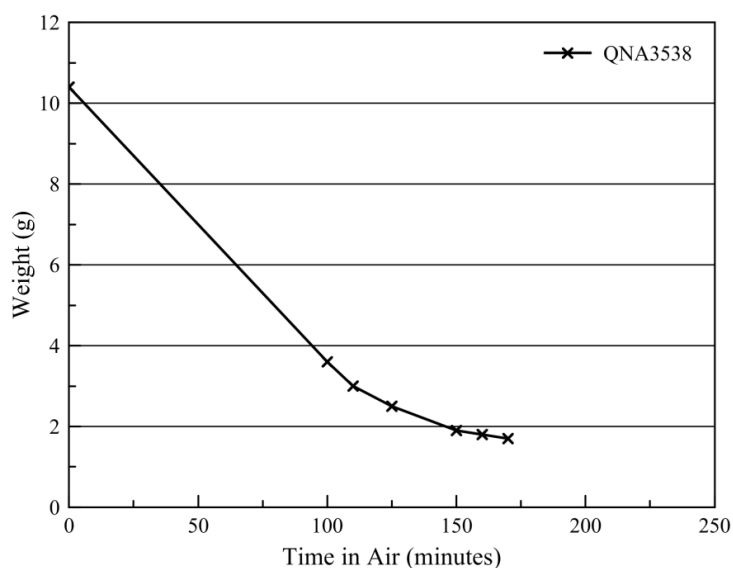


Figure 3.13: Weight loss of approximately 1.5 g rotor-milled npSi powder after HF, methanol, IPA and acetone soaks in air (at room temperature) (Adapted from Loni & Canham, 2011:4)

3.3.2 Oxidation effects on npSi

The isopropyl alcohol-damp powder scheduled for oxidation was dried under vacuum at 70 °C for 1.5 hours, with a further 2 days under vacuum at room temperature. On exposure to ambient air, the dried powder was split into 3 batches for immediate weighing and oxidation. Oxidation temperatures were chosen (for a fixed time of 1

hour) based on preliminary trials aimed at quantifying the weight increase. The weight increase was gained through oxidation. The degree of oxidation was defined by the value 'x' in silicon oxide (SiO_x). Gravimetric values are in accord with expectations based on internal work at Intrinsic Materials Laboratory, while values obtained by energy-dispersive X-ray (EDX) analysis were higher (see Table 3.2).

Table 3.2: Properties of oxidised npSi powders

Sample	Surface area (m ² .g ⁻¹)	Pore volume (cm ³ .g ⁻¹)	Weight % O (EDX)
HDS – I001	305	0.982	Not measured
HDS – I002	305	0.982	1.3
HDS – I003	290	0.918	5.9
HDS – I004	245	0.772	23.3

This higher value can be explained through unintentional oxidisation or artificial ageing of the (oxidised) npSi by the ion beam during analysis, although atmospheric impregnation is a more likely factor. EDX analysis was conducted three weeks (HDS-I002, HDS-I003 and HDS-I004) and one week (QNA3538HF) after being exposed to thermal oxidation. During this time, the samples, rendered hydrophilic, would have chemisorbed moisture from the atmosphere (with higher oxidation temperatures resulting in more hydrophilic material). This was in accord with the observation that the weight of the npSi sample (oxidised at 300 °C) after HF-washing/rinsing (QNA3538HF(300) (Figure 3.14)) increased by approximately 2% over a one-week period. Chemisorbed moisture might not be totally removed during EDX sample preparation/analysis – this could, however, explain in part why the values were higher than those calculated from gravimetric data for essentially 'fresh' samples. To test this hypothesis, EDX was carried out on Davisil® LC250, a commercially available porous silica (SiO₂). Analysis indicated a 3 wt% excess of oxygen (equivalent to SiO₂); this correlated with the certificate of analysis figure of 3.3% for 'weight loss on drying' (1.8% being oxygen from desorbed H₂O). It can be noted that only Si and O were present in the oxidised npSi, with no evidence of fluorine (or residual HF) typically observed in as-anodised/aged npSi. The lack of fluorine can be attributed to the soaking/rinsing process used before oxidation. Figure 3.14 shows the expected trend in the evolution of the oxidation process, with the temperature range extended (temperature-dependent oxidation of pSi for a one-hour process).

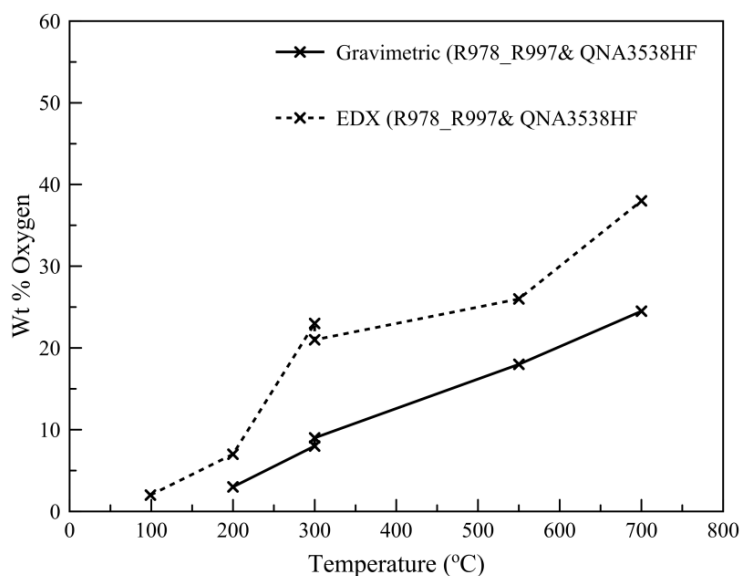


Figure 3.14: Temperature dependent oxidation of npSi for an one hour process (Loni & Canham, 2011:6)

The maximum theoretical value of 53.3 wt% oxygen, for SiO₂, can only be achieved after very high temperature processing (> 900 °C) – this is confirmed by the data trends. Figure 3.15 shows the reduction in pore volume of HF-washed npSi after oxidation, for both ball-milled and rotor-milled npSi – this reduction should be considered when formulating aged or milled powders with PETN, as different payloads would result. ‘Fresh’ hydride-passivated npSi stored in acetone would gradually oxidise, once dried and exposed to air.

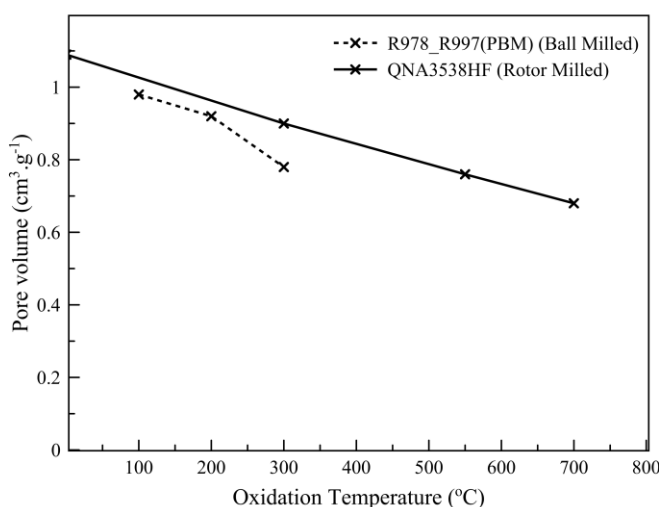


Figure 3.15: Pore volume dependency on oxidation temperature (Loni & Canham, 2011:6)

Although the pore volume of the fresh hydride-passivated ball-milled sample (R978/R997PBM) was not included in Table 3.2, backwards extrapolation would indicate approximately 1 ml.g^{-1} was to be expected for this (equivalent to a porosity of 70% before oxidation). The pore volume before washing in HF (R978/R997 PBM) was somewhat lower at 0.768 ml.g^{-1} ; this was indicative of the degree of oxidation induced by the milling process. These values were in accordance with the measurements carried out on the rotor-milled and naturally-aged npSi batch (QNA3538, stored for 14 months), where the pore volume was increased from 0.742 ml.g^{-1} before HF washing to 1.074 ml.g^{-1} after HF washing – the increase being attributed to a combination of oxide removal and chemical leaching of the npSi powder.

The surface chemistry of the porous silicon is one of the most important parameters that can have an effect on the explosive nature of the material. A gradual change from hydride to oxide passivation on air storage may result in decreased potency and may have some bearing on how the material is further processed and/or stored. Related to this is the use of simple chemical washing procedures to remove residual elements, which can also change the internal surface chemistry and impart improved stability against oxidation. The degree of thermal oxidation of the npSi powders may have an adverse effect on the 'explosivity'. However, in the present study, the reactivity of npSi powder stored for 14 months (rotor-milled batch QNA3538, with native/milling-induced oxide) was compared with the same powder after HF-washing, solvent soaks and air-drying, by propelling small aliquots (10 mg) into 69% nitric acid – a crude screening test used previously for stain-etched powders. The fresh sample ignited almost immediately and the 'aged' sample ignited to the same degree, after a marginally longer initiation time. This was encouraging. It demonstrated that npSi maintained high reactivity even after prolonged storage and with milling-induced oxide passivation.

3.4 Synthesis of Tetrazole Salts

In this section, preparation and evaluation of tetrazole salts (primary explosives formulations) are described. They were synthesised at AEL Mining Services experimental laboratories. Tetrazole in its free state does not have the characteristics of a primary explosive. Owing to its acidic nature, tetrazoles easily form metallic salts. A large number of these salts (or derivatives) have explosives properties and fall into the category of primary explosives. In this study, 5-nitriminotetrazole and 5-nitrotetrazole were synthesised from 5-aminotetrazole. Aminotetrazole was synthesised in accordance with the synthetic scheme outlined in Figure 3.16.

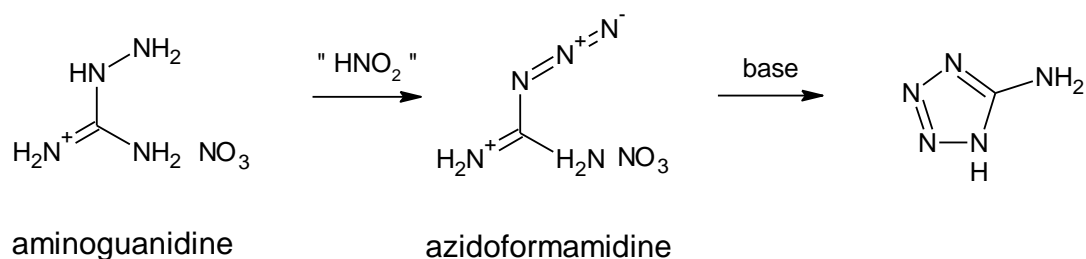


Figure 3.16: Synthesis of 5-aminotetrazole

3.4.1 Preparation of 5-nitriminotetrazole salts

5-Aminotetrazole was nitrated using nitric acid (96%) (Figure 3.17). The reaction was quenched via the addition of ice-cold water. The volume of the solution was reduced in situ and the resulting product purified via crystallisation. The product thus obtained was the nitramine, 5-nitriminotetrazole. Nitriminotetrazole was recrystallised from water to obtain a coarse material.

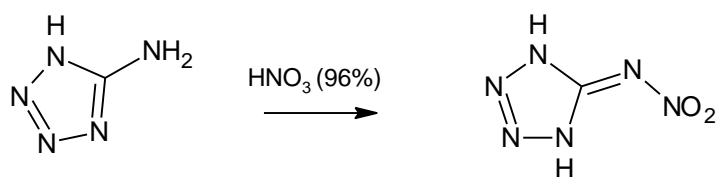


Figure 3.17: Synthesis of 5-nitriminotetrazole

3.4.2 Preparation of 5-nitrotetrazole

Nitro groups ($-\text{NO}_2$) are more electron withdrawing than the nitramine groups ($=\text{N}-\text{NO}_2$), hence a tetrazole containing nitro groups should be more sensitive than a tetrazole that does not have nitro groups. The more sensitive 5-nitrotetrazole was synthesised from 5-aminotetrazole with the aid of sodium nitrite, copper sulphate and nitric acid (70%). Synthesis proceeded via a diazotetrazole intermediate which was believed to explode from the slightest stimulus when its concentration exceeded 2% in solution. The reaction is given in Figure 3.18.

The product was isolated as the acid copper salt of nitrotetrazole, a 1:1 mixture of the copper salt and nitrotetrazole. This product is very sensitive and normally converted to the more stable sodium salt. The average yield of the final product ranges between 45 and 55%, based on the starting 5-aminotetrazole. This product is insoluble in most solvents and all attempts to recrystallise it, failed.

Conversion to the sodium salt of 5-nitrotetrazole was done with the use of sodium hydroxide. The sodium salt was soluble in acetone and hence recrystallized.

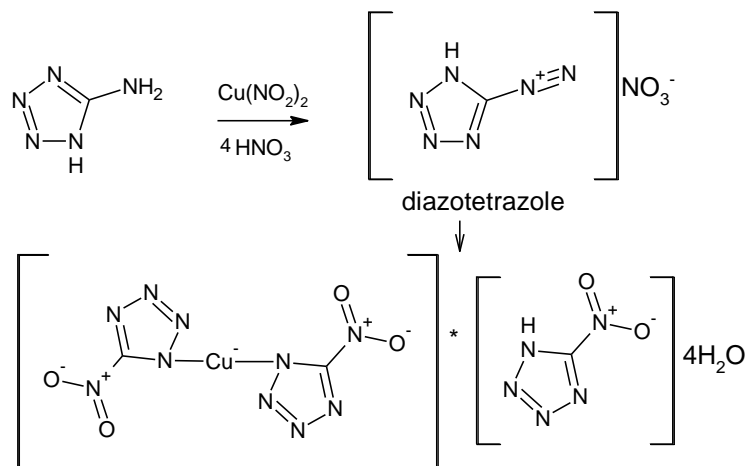


Figure 3.18: Synthesis of acid copper salt of 5-nitrotetrazole

The yield obtained following this method of preparation was between 80 and 83% (calculated on mass of the input raw materials).

3.5 Analytical Results

Infrared spectroscopy was performed on the nitriminotetrazole as well as on the nitrotetrazole (sodium salt). The nitriminotetrazole was compared with aminotetrazole and the two nitrotetrazole salts (sodium and copper) were compared (Figures 3.19 and 3.20).

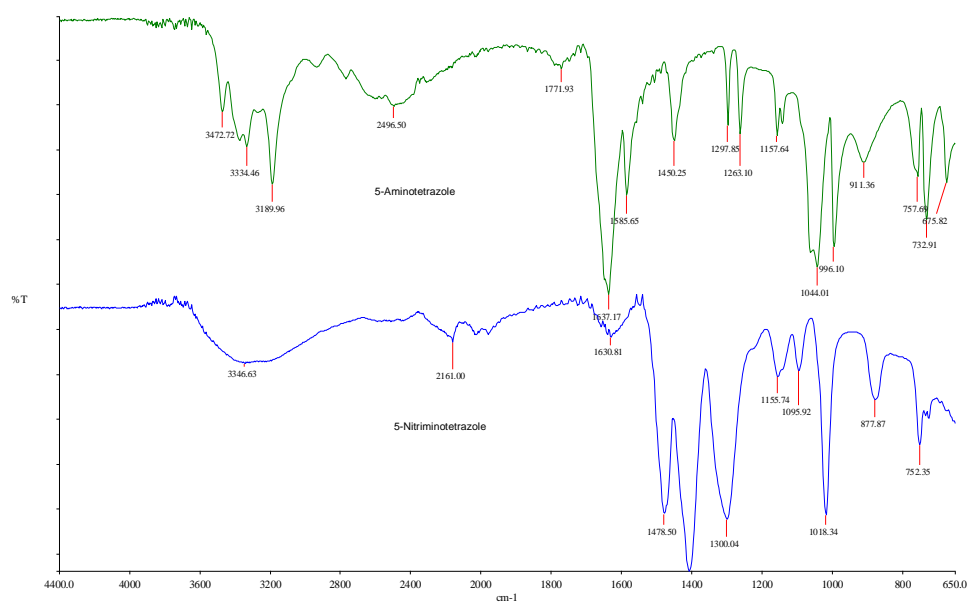


Figure 3.19: IR spectra for 5-nitriminetetrazole and starting material

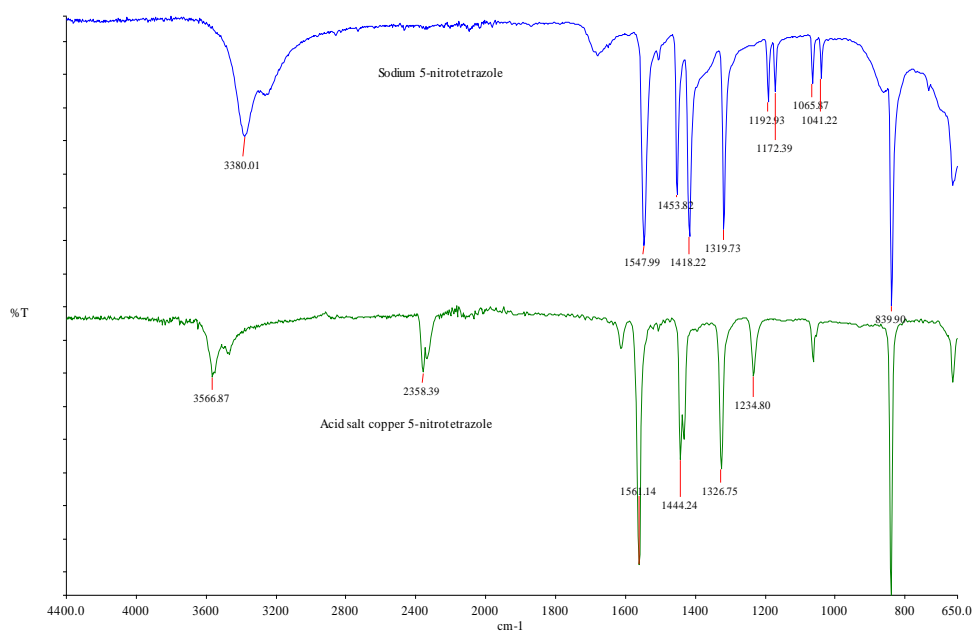


Figure 3.20: IR spectra of the two 5-nitrotetrazole salts

Klapötke et. al. (2009:S9) reported assignments of the peaks as shown in Table 3.3.

Table 3.3: Experimentally determined IR frequencies with tentative vibration assignments

	ν (calc., cm^{-1})*	ν (exp., cm^{-1})	Vibration assignment*
1	669	675	$\gamma(\text{NO}_2+\text{NT-ring}+\text{Tz-ring})$
2	727	732	$\gamma(\text{N6}+\text{N7}+\text{N8})$
3	765	757, 752	$\gamma(\text{NO}_2+\text{NT-ring})$
4	825	877	$\delta(\text{NO}_2)$
5	1020	911, 996, 1018	$\delta(\text{C3}+\text{N9}+\text{N8})_{\text{Tz-ring}}$
6	1048	1044	$\delta(\text{N4}+\text{N5}+\text{C1})_{\text{NT-ring}}$
7	1086	1095	$\nu_{\text{as}}(\text{N-N})_{\text{NT-ring}}+\omega(\text{CH}_2)$
8	1163	1155, 1157	$\nu(\text{N7-N8})_{\text{Tz-ring}}+\gamma_{\text{sym}}(\text{CH}_2)$
9	1120	1263	$\nu(\text{N4-N5})+\omega(\text{CH}_2)$
10	1279	1297	$\gamma(\text{CH}_2)$
11	1313	1300	$\nu(\text{N2-N3}+\text{C1-N2})$
12	1316	1319, 1326	$\nu_{\text{sym}}(\text{NO}_2)+\nu(\text{C1-N5})$
13	1415	1418	$\nu(\text{C2-C3})_{\text{Tz-ring}}$
14	1451	1444, 1450, 1453, 1478	$\nu(\text{C-N}+\text{N-N})_{\text{NT-ring}}$
15	1590	1547, 1561, 1585	$\nu_{\text{as}}(\text{NO}_2)$
16	3026	3189	$\nu_{\text{as}}(\text{CH}_2)$

Vibrational mode assignment: ν = stretching, δ = in-plane bending, γ = out-of-plane bending, ω = in plane rocking, as – asymmetric and sym = symmetric.

*(Klapötke et al., 2009:S1)

Visual inspection of nitriminotetrazole also showed a distinctive difference in the physical structure of recrystallized nitriminotetrazole when recrystallized from water and acetone. Nitriminotetrazole was recrystallized from water to obtain a coarse material. Figures 3.21 and 3.22 show the differences in crystal structure and size of nitriminotetrazole crystallised from water and acetone respectively.

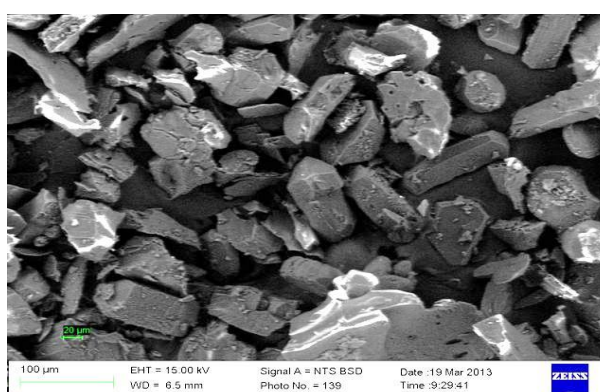


Figure 3.21: 5-Nitriminotetrazole crystallised from water

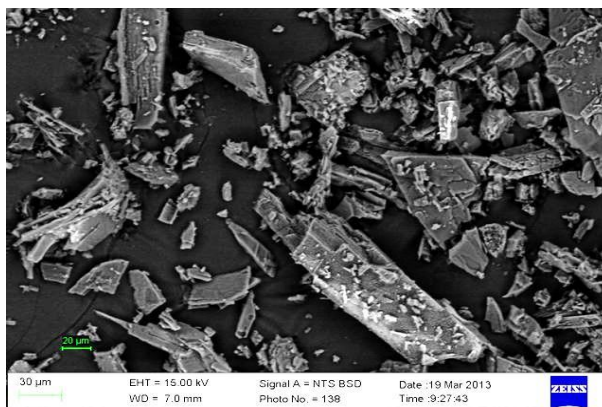


Figure 3.22: 5-Nitriminotetrazole crystallised from acetone

Slow evaporation crystallisation technique was used to for both the water and acetone solutions. Since water took longer to evaporate than the acetone. The quicker evaporating acetone might have caused nucleation of the nitriminotetrazole to occur. This is probably the reason for the nitriminotetrazole recrystallized from acetone to be finer than the tetrazole crystallised from water.

3.6 Summary

This chapter reviewed the manufacture of nano-porous silicon by means of dissolution chemistry. Through the dissolution process, various nano-porous silicon samples were prepared varying in pore volume, surface area and pore size. Section 3.3.1 showed the effect of storage on nano-porous silicon. Additionally, Section 3.3.2 demonstrated how the degree of oxidation influences the surface area and pore volume of the nano-porous silicon. Nano-porous silicon's inclination to oxidise at different temperatures has also been shown. Section 3.3 showed that the pore volume of nano-porous silicon decreased when the percentage of oxidation of the Si increased.

Section 3.4 demonstrated the synthesis of 5-nitriminotetrazole. Nitrotetrazole salts proved a challenge to manufacture and laboratory scale testing was stopped for safety reasons. Owing to constant crystal structure and shape as well as ease of manufacture, nitriminotetrazole recrystallized from water was selected as an oxidiser in nano-porous silicon-based explosive formulations. This is covered in the next chapter.

CHAPTER 4

POROUS SILICON INITIATING AND PBX EXPLOSIVE FORMULATIONS DEVELOPMENT

4.1 Introduction

The structural development of npSi-based explosive compositions was actively pursued after their explosive properties were discovered. npSi explosives formulations appeared to have provided an acceptable alternative to lead azide as a primary explosive in current initiating systems. Si explosives formulations can be more environmentally friendly and do not require a complicated and expensive infrastructure to manufacture. Despite the aforementioned advantages, large-scale application of npSi in commercial explosives formulations has not been extensively pursued, unlike in military applications. Section 4.2 in this chapter describes energetic formulations utilising nano-porous silicon that has different pore volumes and surface areas. Developments in the optimal stoichiometric oxidiser / fuel ratios, and the effects of oxidation and ageing of the npSi on the reactivity, are also presented. Selected nano-porous silicon explosives formulations are tested in order to identify the energetic formulation that exhibits the best explosive characteristics. 5-Nitriminotetrazole (NT) is also evaluated as an oxidiser. Once the nano-porous silicon explosive formulations have been developed and suitably characterised, an acceptable polymer-bonded explosive (PBX) base charge is developed (Section 4.3). This is needed to produce a base charge formulation that can readily be initiated.

4.2 Nano-Porous Silicon-Based Explosive Formulation Development

Explosive formulations were prepared by mixing selective oxidisers with the nano-porous silicon. Saturated solutions of the selected oxidiser were made by dissolving the oxidiser in dry, high-purity acetone. Hygroscopic oxidisers were dried under vacuum at 50 degrees Celsius ($^{\circ}\text{C}$) for 24 hours to ensure that they were dry before being used to prepare the aforementioned solution. The solvent containing the oxidiser was added to the porous silicon in such a manner that the selective mixtures of different oxidiser-to-fuel ratios could finally be obtained. The mixtures were dried in an oven under a vacuum (0.7 mega pascal (MPa)) for 3 hours at 55 $^{\circ}\text{C}$. After drying, the powder was removed from the oven and wetted again with an organic solvent. As the solvent evaporated it was refined simultaneously by mechanically using a dry bone spatula. The refining continued until a homogeneous fine powder was obtained. After refining, the formulations were dried again in an oven to ensure that all the solvent was removed from the powder. The powder was subsequently stored in a desiccator until it was used.



Figure 4.1: npSi-Based explosive formulation

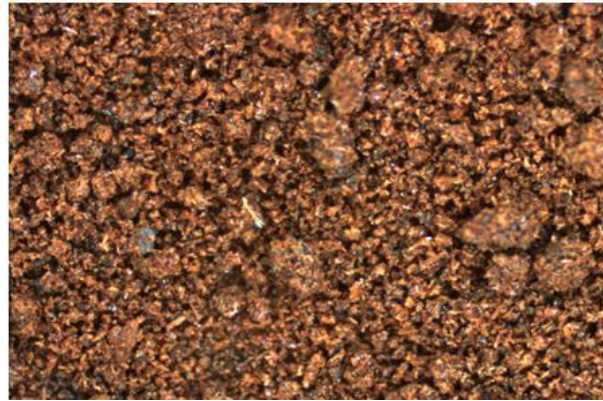


Figure 4.2: Optical light microscope image of npSi-based explosive formulation

Different oxidisers were used in the development of a nano-porous silicon-based explosive formulation. The different oxidisers contribute different sensitivities with regard to impact friction and heat of subsequent explosive formulations. The development of a npSi-based explosives formulation was done around determining the following:

- i. Stoichiometric fuel-to-oxidiser ratio.
- ii. Relative reactivity of nano-porous silicon.
- iii. Optimal oxidiser-to-fuel ratio.
- iv. Effect of oxidation of npSi on the reactivity of silicon-based explosive formulations.
- v. Effect of ageing of npSi-based explosive formulations.
- vi. Effect of density on the reactivity of npSi explosive formulations.
- vii. Burning rate of npSi explosive formulations in powder form.
- viii. Pressure of npSi explosive formulations in closed vessel pressure test.

4.2.1 Balanced fuel- to-oxidiser ratio determination

Cooper (1996:20) stated that if one mole of methane for every two moles of oxygen was present, there would still be fuel remaining at the end of the reaction. Since that extra fuel would not have burned, it would not have contributed to the production of heat, but would have added to the total combined weight. Therefore, even though the heat evolved by the reaction would remain the same, the heat evolved per unit weight of the reaction would be lower. The fuel-to-oxidiser ratio (stoichiometric ratio) is thus required to be balanced precisely.

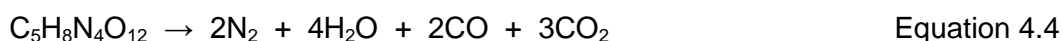
Lithium perchlorate (LiClO_4), barium perchlorate ($\text{Ba}(\text{ClO}_4)_2$), sodium perchlorate (NaClO_4), PETN ($\text{C}_5\text{H}_8\text{N}_4\text{O}_{12}$), nitriminotetrazole ($\text{CH}_2\text{N}_6\text{O}_2$) (hereafter (NT)) and hexanitrostilbene ($\text{C}_{14}\text{H}_6\text{N}_6\text{O}_{12}$ or HNS) were selected as oxidisers to be mixed with nano-porous silicon. The expected reactions with some of the oxidisers are given below.



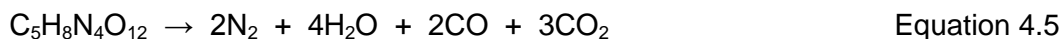
The reactions for PETN, NT and HNS are more complex. Explosives consisting of carbon (C), hydrogen (H), nitrogen (N) and oxygen (O) are referred to CHNO explosives. When CHNO explosives react, the reactant molecule is broken down into its individual atomic components. These atoms then recombine to form the final products of the reaction. Cooper (1996:118) stated that in all cases, the reaction hierarchy of the products formed could be estimated by using the following rule:

- i. All the N form N_2 .
- ii. All the hydrogen is burned to H_2O .
- iii. Any oxygen left after H_2O formation burns to CO .
- iv. Any oxygen left after CO formation burns to CO_2 .
- v. Any oxygen remaining forms O_2 .
- vi. Traces of NO_x are always formed.

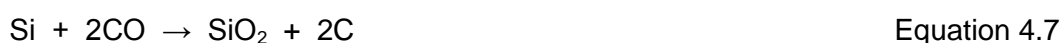
Following these rules the reaction of PETN can be given as



When Si is mixed with PETN, the silicon does not react with the PETN in the reaction zone of the reaction. The Si reacts with the reaction products (H₂O, CO and CO₂) formed during the detonation process and in the expansion zone of the reaction. The reaction of Si with PETN can be written as:



The Si then reacts to form:



The balanced equation of final reaction can thus be written as:



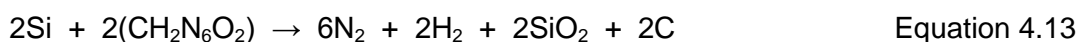
Similarly the reaction of NT with Si can be given as:



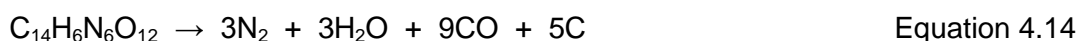
Then Si reacts to form:



The balanced equation can hence be written as:



Similarly the reaction of Hexanitrostilbene (HNS) with Si can be given as:



The Si reacts to form:



The balanced equation can therefore be written as:



Note: Equations 4.9, 4.13 and 4.17 are complete reactions excluding reactions with atmospheric gases.

The stoichiometric ratio for different npSi to selective oxidiser is shown in Table 4.1.

Table 4.1: Balanced stoichiometric ratio (fuel to oxidiser)

Fuel	Oxidiser	Balanced stoichiometric ratio
Si	NaClO ₄	2:1
Si	LiClO ₄	2:1
Si	Ba(ClO ₄) ₂	4:1
Si	C ₅ H ₈ N ₄ O ₁₂	6:1
Si	CH ₂ N ₆ O ₂	2:2
Si	C ₁₄ H ₆ N ₆ O ₁₂	6:1

Chemical reactions occur where one or more chemical species changes its molecular configuration to a different one. A difference in internal energy between the starting and ending chemical states can, therefore, be assumed, based on the changes in chemical bonds. Cooper (1996:118) stated that absolute enthalpy could not be determined for a substance, and therefore only changes or differences in the quantity could be dealt with. To simplify calculations of heat of reaction and make those more consistent, a standard state to which all changes in enthalpy for chemical reactions was referenced and was arbitrarily defined. The standard state used for most engineering calculations is defined as 25 °C and 1 atm pressure conditions.

The calculation device used to reference heat of reaction to the standard state is the heat of formation (ΔH_f^0). The heat of formation can be considered a special case of the heat of reaction (Cooper, 1996:118). It is the heat of reaction or enthalpy change involved in making a particular compound or molecule from its elements, where both the elements and the final compound are at standard state conditions.

The heat of formation for the elements and products shown in Equations 4.1 to 4.18 is listed in the table in Appendix 4A.

From the ΔH_f^0 , the enthalpy change involved in a chemical reaction at standard state can be determined. The heat of reaction (ΔH_r^0) at standard state is equal to the difference between the standard heats of formation of the reaction products and the standard heats of formation of the reactants. ΔH_r^0 is obtained by Equation 4.19 given by Cooper (1996:124):

$$\Delta H_r^0 = \sum \Delta H_f^0 \text{ products} - \sum \Delta H_f^0 \text{ reactants} \quad \text{Equation 4.18}$$

A positive value indicates the product has greater enthalpy (endothermic reaction), whereas a negative value indicates the reactants have greater enthalpy (exothermic reaction).

Table 4.2: Heat of reaction calculated from Equation 4.19

no	Mixture	Reaction products	ΔH_r^0 (kJ.mol ⁻¹)
1	2Si + NaClO ₄	2SiO ₂ + NaCl	-1848.4
2	2Si + LiClO ₄	2SiO ₂ + LiCl	-1847.8
3	4Si + Ba(ClO ₄) ₂	4SiO ₂ + BaCl ₂	-3691.6
4	C ₅ H ₈ N ₄ O ₁₂	2N ₂ + 4H ₂ O + 2CO + 3CO ₂	-2651.0
4.1	2Si + 4H ₂ O	2SiO ₂ + 4H ₂	-854.2
4.2	Si + 2CO	SiO ₂ + 2C	-689.7
4.3	3Si + 3CO ₂	3SiO ₂ + 3C	-1551.6
4.4	6Si + C ₅ H ₈ N ₄ O ₁₂	2N ₂ + 4H ₂ + 6SiO ₂ + 5C	-5710.5*
5	2(CH ₂ N ₆ O ₂)	6N ₂ + 2H ₂ O + 2CO	-926.6
5.1	Si + 2H ₂ O	SiO ₂ + 2H ₂	-427.1
5.2	Si + 2CO	SiO ₂ + 2C	-689.7
5.3	2Si + 2(CH ₂ N ₆ O ₂)	6N ₂ + 2H ₂ + 2SiO ₂ + 2C	-2043.4*
6	C ₁₄ H ₆ N ₆ O ₁₂	3N ₂ + 3H ₂ O + 4CO ₂ + CO + 9C	-2428.6
6.1	1.5Si + 3H ₂ O	1.5SiO ₂ + 3H ₂	-640.65
6.2	4.5Si + 9CO	4.5SiO ₂ + 9C	-3103.65
6.3	6Si + C ₁₄ H ₆ N ₆ O ₁₂	3N ₂ + 3H ₂ + 6SiO ₂ + 5C	-6226.9*

*Total change in enthalpy for complete reaction. This change in enthalpy does not occur at once but is generated in stages.

From Table 4.2 it can be deduced that the organic oxidisers have the highest heat of reaction and can be expected to burn generating greater heat energy.

4.2.2 Proposed methodology for relative reactivity

To better compare the difference in reactivity of the nano-porous silicon-based explosive formulations, a relation was developed between the noise generated by the

reaction and the measured time to reaction. This new test method was developed to further characterise the npSi-based explosive formulations. The method was presented at the Institute of Chemical Technology (ICT) in Germany in 2013 and published in the conference proceedings. The postulated argument is based on the understanding that the louder the noise produced, the more brisant the explosive formulation is assumed to be. The heat sensitivity of the formulation is a function of the time it took the formulation to react upon exposure to specific thermal stimuli. A quick reaction is indicative of a more heat-sensitive formulation. The rational relative reactivity of formulation that produced a loud noise and a long time to reaction cannot be higher when it is compared with a formulation that produced a loud noise and a short time to reaction. This problem was overcome by increasing the difference between the noise and time values in the equation. The noise was increased by power 10 (δ), and the inverse of the time (α) measurement was used. It is important to note that the magnitude of the noise is not related to the laps in time. R_r is accepted as an approximation from a function of sound and time. This gave Equation 4.19 which is in its current form unit less.

$$R_r \sim \delta^{10} \left(\frac{1}{\alpha} \right) \quad \text{Equation 4.19}$$

Different mixtures were evaluated by exposing the samples to heat. A laboratory hotplate was modified to produce the heat for this set of experiments. The hotplate was modified in such a manner so that the temperature could be controlled to be within a tolerance of ± 1.0 °C. The modified hotplate was calibrated to determine the temperature on a specific, pre-selected position on the hotplate. This was done to ensure that all the samples were exposed to a similar rate of temperature change. These temperature measurements were collected by measuring the temperature inside an aluminium cup in 5-second time intervals. The temperature of the hotplate was 400 °C.

A sample of the formulation to be evaluated was put in a specific position on the heat source. A noise meter (decibel meter) was positioned 150 millimetres (mm) horizontally from the sample and 140 mm above the sample. The time taken for a reaction to occur was measured using a standard, calibrated stopwatch. This time was the time measured from the moment the sample was placed on the hotplate to the time the reaction was completed. This test set-up allowed for the measurement of the noise level and the time taken for a reaction to occur. Figure 4.3 shows the test set-up.

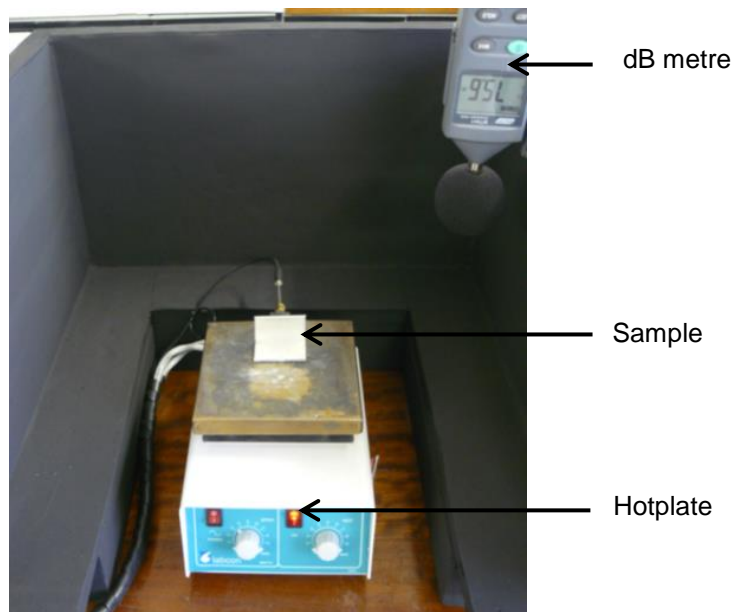


Figure 4.3: Hotplate set-up for the determination of relative reactivity

Variables that could influence the results include sample mass, Si-to-oxidiser ratio and rate of temperature change. These variables were controlled by:

- keeping the rate of temperature change as constant as possible,
- predetermining the Si-to-oxidiser ratio and keeping this ratio constant, and
- determining the influence of sample mass on the magnitude of the noise reading (Appendix 4B).

The optimum sample mass that showed the least effect on the noise reading was determined (Appendix 4B). A sample mass of between 0.030 gram (g) and 0.040 g was used for the samples tested.

The responses obtained were scientifically defined by the following three factors: the time to reaction, the temperature at the reaction, and the noise level of the reaction. Time measured, for a reaction to occur, can be indicative of the sensitivity of the formulation towards heat. Temperature at reaction refers to the temperature at which a reaction is noted. Noise level can be related to sound over pressure (Szendrei, 2010:1). The sound over pressure can be related to the over-pressure generated by the reaction.

4.2.3 Determining the R_r of nano-porous silicon-based explosive compositions

Sodium perchlorate, barium perchlorate, lithium perchlorate, PETN, NT and HNS were mixed with nano-porous silicon in stoichiometric ratios. The nano-porous silicon sample HDS-V008 (with an SSA of $176 \text{ m}^2 \cdot \text{g}^{-1}$ and a pore volume of $0.39 \text{ cm}^3 \cdot \text{g}^{-1}$ (Table 3.1 in the previous section)) was used for all samples. Table 4.3 shows the mass-to-mass ratio between the porous silicon and the oxidiser.

Table 4.3: Silicon to oxidiser ratios on mass balance

	Ratio Si:Oxidiser	Si Theoretical (g)	Oxidiser Theoretical (g)	Si actual (g)	Oxidiser Actual (g)
NaClO₄	1:0.50	1.5	3.2761	$1.5069^{\pm 0.0009}$	$3.2665^{\pm 0.0012}$
LiClO₄	1:0.50	1.5	2.8487	$1.5016^{\pm 0.0010}$	$2.8423^{\pm 0.0009}$
Ba(ClO₄)₂	1:0.25	1.5	4.4970	$1.5022^{\pm 0.0014}$	$4.4893^{\pm 0.0010}$
PETN	1:0.16	1.5	2.8139	$1.5011^{\pm 0.0008}$	$2.8132^{\pm 0.0014}$
NT	1:1.00	1.5	6.9617	$1.5016^{\pm 0.0011}$	$6.9581^{\pm 0.0013}$
HNS	1:0.16	1.5	4.0164	$1.5004^{\pm 0.0012}$	$4.0079^{\pm 0.0014}$

The mixtures were evaluated using the method described in Paragraph 4.2.2. A Zeiss optical microscope was used to obtain pictures of the different mixtures. The mixtures are depicted below.

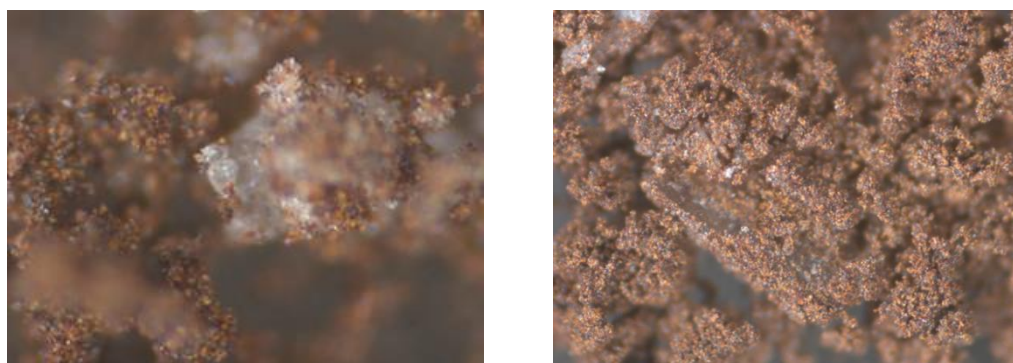


Figure 4.4: Si:NaClO₄ mixture

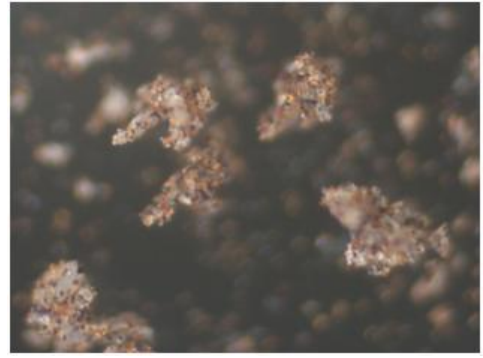
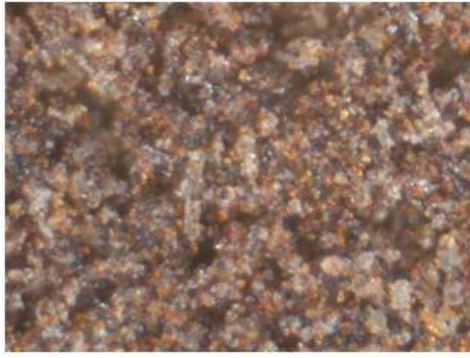


Figure 4.5: Si:LiClO₄ mixture

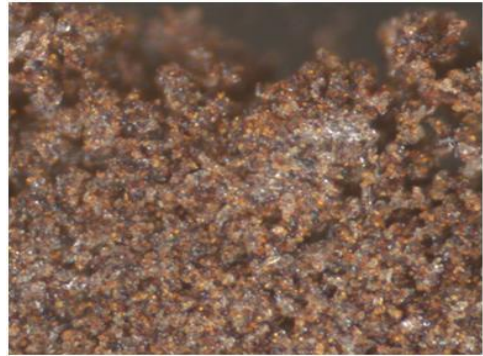
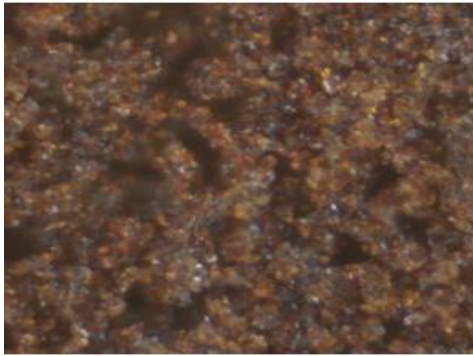


Figure 4.6: Si:Ba(ClO₄)₂ mixture

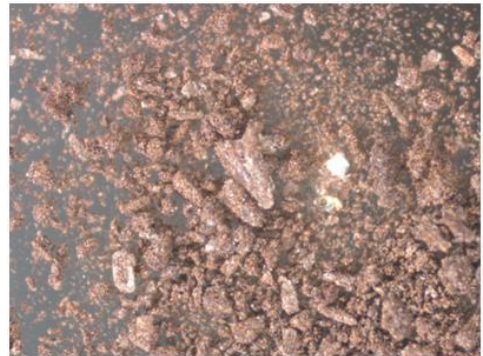
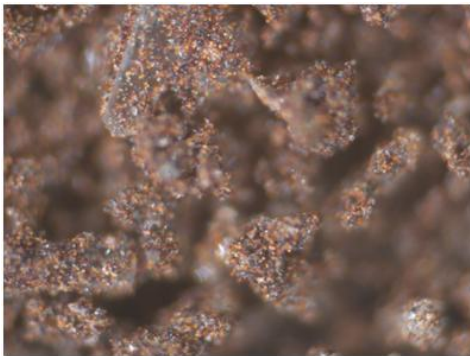


Figure 4.7: Si:PETN mixture

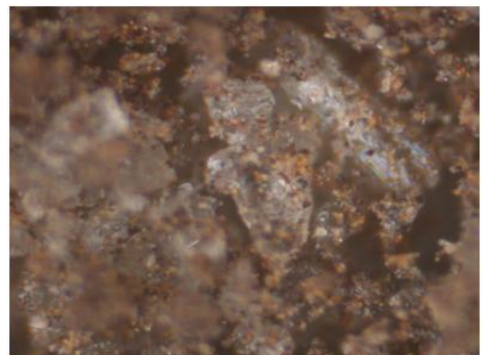


Figure 4.8: Si:NT mixture

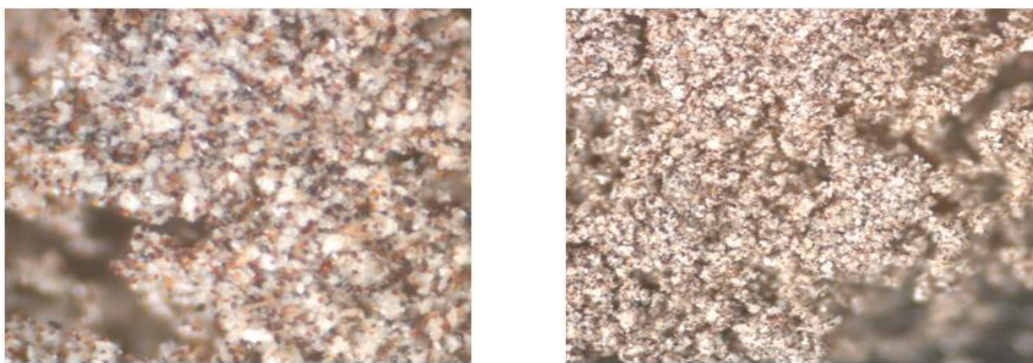


Figure 4.9: Si:HNS mixture

Figures 4.4 to 4.9 show that large quantities of the oxidiser crystallised outside the pores of nano-porous silicon.

4.2.4 Oxidiser-to-fuel ratio determination

An optimal reaction characteristic is not necessarily related to a complete reaction mechanism. In order to obtain all the potential energy stored in a chemical composition, the need for a complete reaction is vital. When developing an explosive composition, other factors such as speed at which the decomposition reaction occurs may be more significant than a complete reaction (from a thermo-dynamic perspective). On revisiting the explosive train principle, it can be understood that before developing an explosive formulation, it is vital to understand where and how (in the explosive train) the potential explosive formulation will be used. In replacing lead azide as a primary explosive composition, two things need to be kept in mind: a) ignition sensitivity or how easily the composition can be initiated, and b) power output (whether the explosive power generated upon reaction will be strong enough to initiate the next explosive in the chain).

In this section, nano-porous silicon with varying specific surface areas was mixed with different oxidisers (in different ratios). To measure the difference in reaction, the noise generated by the reaction was measured. The rationale behind this argument is nested in the science of sound waves and compression of air. Quicker decomposition reactions (high reaction rates) result in higher noise levels. The ratio of oxidiser to fuel that will give the fastest decomposition reaction as related to the sound generated was determined. Sodium perchlorate, barium perchlorate, lithium perchlorate, and PETN were used as oxidisers and nano-porous silicon samples with specific surface areas of 141, 175, 192 and 480 $\text{m}^2\cdot\text{g}^{-1}$ were used as the fuel.

The mixtures were evaluated using the method described in Section 4.2.2 with the amendment that only noise measurements were taken.

4.2.5 The effect of oxidation of nano-porous silicon on the R_r of silicon-based explosive formulations

Nano-porous silicon starts to oxidise from the moment it is prepared. This part of the study shows the effect of oxidised porous silicon when used to manufacture nano-porous silicon-based explosive formulations. Porous silicon membranes were prepared from six-inch silicon substrates by electrochemical anodisation using HF-methanol electrolyte. The thermal oxidation of powders was carried out in normal air, using an oven with borosilicate glassware. The temperature and exposure time were varied, in order to obtain nano-porous silicon samples that were at different states of oxidation. The properties of the artificially aged nano-porous silicon are given in Table 4.4.

Table 4.4: Properties of oxidised porous silicon powder samples

Sample	Surface area ($\text{m}^2 \cdot \text{g}^{-1}$)	Wt% O (EDX)
HDS – I001	305	-
HDS – I002	305	1.3
HDS – I003	290	5.9
HDS – I004	245	23.3

Explosive formulations were prepared by mixing selective oxidisers with the nano-porous silicon. Sodium perchlorate (NaClO_4) and pentaerythritol tetranitrate (PETN) were selected as oxidisers. Saturated solutions of the selected oxidisers were prepared by dissolving the oxidiser in dry, high purity acetone. Sodium perchlorate was dried under vacuum at 50 °C for 24 hours to ensure that it was dry before being used to prepare the aforementioned solution. The solvent containing the oxidizer was added to the porous silicon in such a manner that the selective mixtures of different oxidiser-to-fuel ratios could finally be obtained. The mixtures were air dried (through evaporation) while being refined mechanically using a dry bone spatula. Refining continued until a homogeneous fine powder was obtained. After refining, the formulations were dried in an oven under a vacuum (0.7 mega Pascal (MPa)) for 3 hours at 55 °C.

The mixtures were evaluated using the method described in Section 4.2.2.

4.2.6 The effect of ageing of silicon-based explosive formulations

The effect of ageing on the reaction behaviour of silicon-based explosives is related to the oxidation of the mixture. In the previous section, the effect of oxidised silicon on the reactivity of silicon-based explosive formulation was addressed. In this section the effect of ageing of the formulation is shown through determining the relative reactivity of the aged formulations.

To determine the reactivity of aged nano-porous silicon explosive formulations, two different oxidisers were used to manufacture eight different explosive formulations. These formulations were prepared as described earlier using sodium perchlorate (SP) and nitriminotetrazole (NT) as oxidisers. The samples were stored in a desiccator for a period of one year and tested at different time intervals. The formulations evaluated are given in Table 4.5.

Table 4.5: Explosive formulations used in ageing characterisation

Formulation	Oxidiser	Binder (%weight)	NT* (% weight)	Oxidiser-to-porous silicon ratio
T1	NT	Wax (18%)	-	3 : 1
T2	NT	Nitrocellulose (NC) (11%)	-	3 : 1
T3	NT	-	-	3 : 1
T4	NT	Wax (5%)	75%	3 : 1
N1	SP	Wax (18%)	-	1.4 : 1
N2	SP	NC (11%)	-	1.4 : 1
N3	SP	-	-	1.4 : 1
N4	SP	Wax (5%)	75%	1.4 : 1

*Additional NT was added to the nano-porous silicon-based explosive formulation

The mixtures were evaluated using the method described in Section 4.2.2.

4.2.7 Effect of density on the thermal reactivity of the nano-porous silicon-based explosive formulations

Only NT was used as oxidiser to prepare the nano-porous silicon-based explosives formulation. The oxidiser-to-fuel ratio used was 3 : 1 on mass balance. The selected explosive increment was consolidated using a hand press. Samples of the explosive formulation were consolidated at the following densities (gram / cubic centimetre ($\text{g}\cdot\text{cm}^{-3}$)), 0.71, 1.99, 2.07, 2.11, 2.22, 2.25, 2.52 and 2.60.

The mixtures were evaluated using the method described in Section 4.2.2.

In Sections 4.2.1 to 4.2.7 of this chapter, the preparation of a nano-porous silicon-based explosive formulation was discussed with the focus on establishing an energetic composition. In the next section, the selection of energetic Si formulations is narrowed down to the final formulation proposed as a lead azide replacement.

4.2.8 Burning rate evaluation

Nano-porous silicon-based explosive formulations were prepared using different oxidisers and nano-porous silicon possessing different surface areas. These formulations are given in Table 4.6. The oxidiser-to-fuel ratio used was aimed to be approximately 3 : 1 on mass balance. Actual values are shown in Table 4.6.

Table 4.6: Nano-porous silicon formulations used in burning and power output characterisation

No.	Oxidiser	npSi Sample	npSi Surface Area (m ² .g ⁻¹)	Si ^{actual} (g)	Oxidiser Actual (g)	Si : Oxidiser ratio
1	NaClO ₄	HDS - V009	180.00	1.5069 ^{±0.0012}	3.2665 ^{±0.0011}	1:2.20
2	Ba(ClO ₄) ₂	HDS - V009	180.00	1.5022 ^{±0.0010}	4.4893 ^{±0.0012}	1:3.00
3	PETN	HDS - V009	180.00	1.5011 ^{±0.0009}	2.8132 ^{±0.0014}	1:1.90
4	NT	HDS - V009	180.00	1.5016 ^{±0.0011}	4.0079 ^{±0.0013}	1:2.70
5	HNS	HDS - V009	180.00	1.5004 ^{±0.0010}	4.6306 ^{±0.0011}	1:3.00
6	NT	HDS – I002	305.00	1.5028 ^{±0.0014}	4.0083 ^{±0.0009}	1:2.65
7	NT	HDS – I003	290.00	1.5017 ^{±0.0012}	4.0075 ^{±0.0012}	1:2.65
8	NT	HDS - V004	116.00	1.5021 ^{±0.0011}	4.0071 ^{±0.0010}	1:2.65
9	NT	HDS - V009	180.00	1.5019 ^{±0.0013}	4.0081 ^{±0.0010}	1:2.65
10	NT	Nano Si*	0.17	1.5019 ^{±0.0011}	4.0081 ^{±0.0009}	1:2.65

Nano silicon obtained from Intrinsic materials to be used as reference.

Formulations No. 1 to 5 in Table 4.6 were used in this experiment. The nano-porous silicon-based explosive formulations were prepared as described in Section 4.2.2. The powder was poured onto a marker plate in a slot that was 5 mm wide and 5 mm deep with a total length of 150 mm. The markers on the marker plate were positioned 20 mm apart (this is measured as being the distance between the markers). A FASTEC IMAGING™ TroubleShooter™ high-speed video camera was used to capture the burning event. Timing between markers was determined using the frames per second data obtained from high speed imaging. An open flame was used to ignite the selected composition.

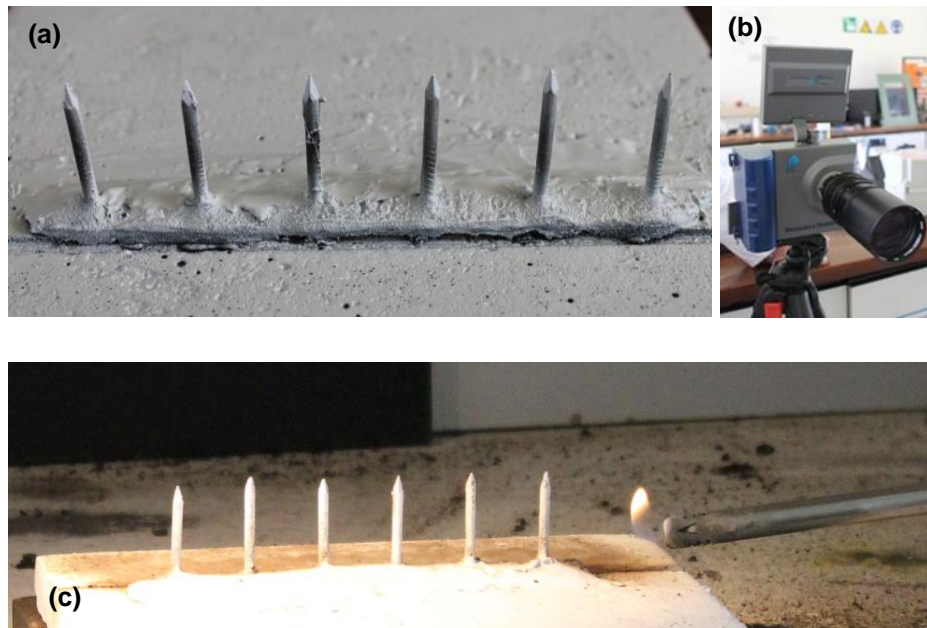


Figure 4.10: Burning rate experimental set-up. Marker plate (a). High- speed camera (b). Bottom picture shows the method to ignite the test sample (c).

4.2.9 Closed-vessel pressure test

The closed-vessel pressure test was conducted to determine the pressure profile of an npSi / tetrazole explosive formulation. The explosive formulations No. 6 to 10 in Table 4.6 were used in this evaluation.

A pressure vessel was connected to a power supply to ignite the sample. A pressure sensor was connected to a data-capturing unit. The sample was ignited and the pressure data was logged (Figures 4.11 and 4.12).

The pressure vessel had a sample chamber of 20 cm³. One (1) g of the explosive formulation was poured over a high-resistance Ni/Cr wire inside the pressure vessel. The pressure vessel was closed tightly to prevent any pressure from being lost.

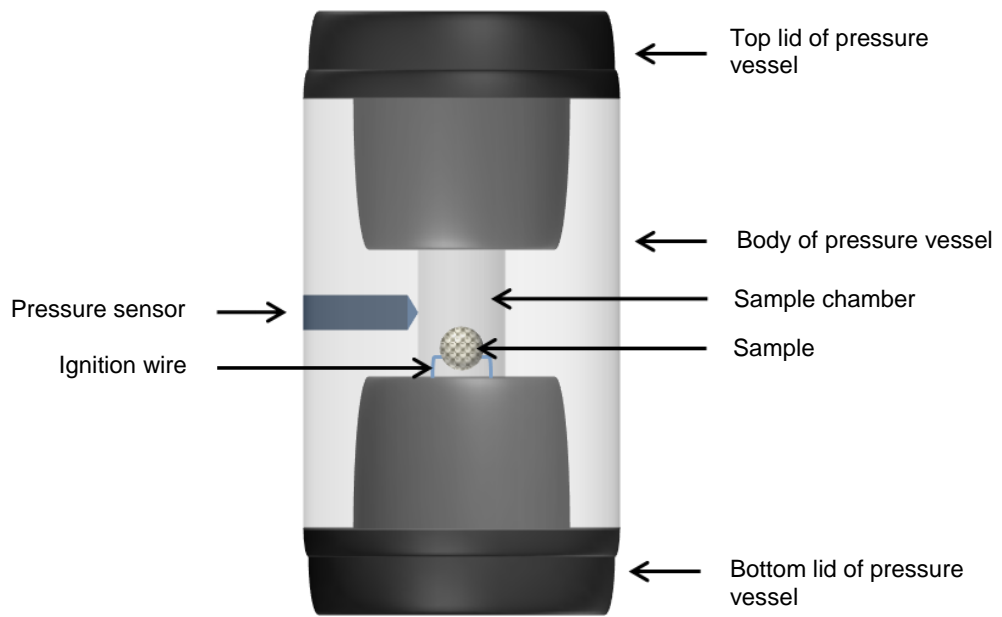


Figure 4.11: Schematic view of the pressure chamber

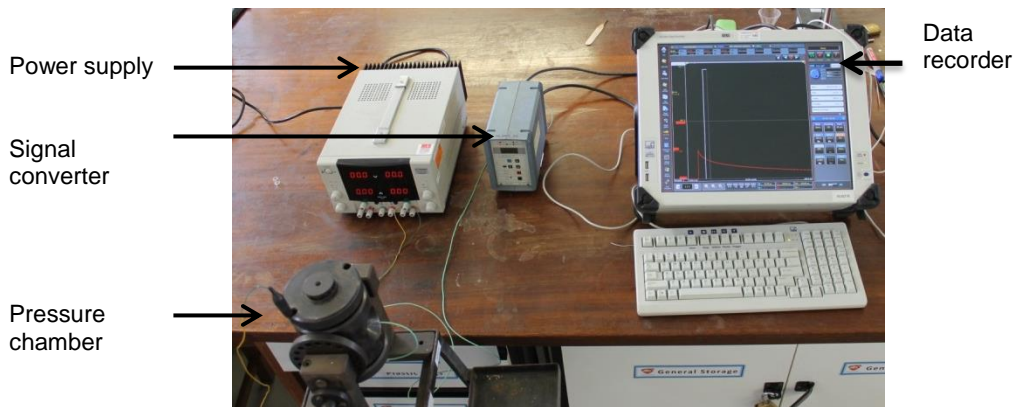


Figure 4.12: Closed vessel pressure test set-up

4.2.10 Results: Nano-porous silicon-based formulation development

The results of Sections 4.2.1 to 4.2.9 are reported in this section.

4.2.10.1 Results: Fuel-to-oxidiser ratio

The relative reactivity results of nano-porous silicon-based explosive formulations prepared to be stoichiometrically balanced (Table 4.1). Si sample HDS – V008 was used. Results are shown below.

Table 4.7: Relative reactivity results obtained for Si/oxidiser mixtures

	Si:NaClO ₄	Si:LiClO ₄	Si:Ba(ClO ₄) ₂	Si:PETN	Si:NT	Si:HNS
	R _r x10 ¹⁹	R _r x10 ¹⁹	R _r x10 ¹⁸	R _r x10 ¹⁷	R _r x10 ¹⁸	R _r x10 ¹⁶
Average	2.57	2.29	7.44	2.30	1.99	4.06
Min	1.79	0.01	1.48	1.56	1.32	2.38
Max	3.06	6.85	13.40	3.86	3.15	6.88
Standard deviation	0.37	2.29	4.83	0.70	0.55	1.44

The results of the tests conducted on explosives formulations prepared using npSi with different surface areas are shown in Table 4.7. Three distinctive types of reactions were observed. The reactions observed varied from a sublimation reaction (cook-off without notable flame), a deflagration reaction, and an explosion reaction. The noise associated with a deflagration reaction was $60 \geq 90$ dB. Noise levels above 90 dB are assigned to an explosion. Noise levels measured with corresponding ratios are shown in table 4.8.

In reflecting on the results obtained in the previous section, the effect of different oxidisers used with the same nano-porous silicon fuel is significant. Considered that the mixtures were stoichiometrically prepared, some of the results were disappointing. This can easily be explained when mixtures prepared using oxidisers like PETN and NT are outperformed by the mixtures prepared from oxidisers like sodium perchlorate. In this section Ba(ClO₄)₂ showed a high standard deviation. This is ascribed to inconsistent reaction behaviour of the mixture that was also observed the burning rate evaluations described in section 4.2.10.5.

Table 4.8: The stoichiometric ratios with corresponding noise measurements

No.	Formulation	Stoichiometric ratio	Noise (dB)
1	Si:Ba(ClO ₄) ₂	1:0.25	101.30 ^{±1.20}
2	Si:LiClO ₄	1:0.50	97.85 ^{±2.14}
3	Si:PETN	1:0.16	62.40 ^{±2.01}
4	Si:SP	1:0.50	113.40 ^{±2.59}

More detailed results are presented in Appendix 4C.

Table 4.9 reports the results obtained that were above 90 dB.

Table 4.9: The effect of different oxidiser-to-fuel ratios

PSi Sample	Surface Area (m ² .g ⁻¹)	Ratio Si : Oxidiser						
		1:2.5	1:1.6	1:1.2	1:0.8	1:0.4	1:0.2	1:0.1
		Oxidiser that produced high noise level (dB)						
Vesta 20081120	192	-	<i>Ba(ClO₂)₄</i>	Ba(ClO ₂) ₄ <i>SP</i>	Ba(ClO ₂) ₄ PETN <i>SP</i>	Ba(ClO ₂) ₄ <i>PETN</i> <i>SP</i>	PETN <i>SP</i>	-
Intrinsiq T4/S6	141	-	-	Ba(ClO ₂) ₄ <i>SP</i>	Ba(ClO ₂) ₄ <i>SP</i>	Ba(ClO ₂) ₄ <i>SP</i>	-	-
Intrinsiq T4/S8	480	LiClO ₄	Ba(ClO ₂) ₄ <i>LiClO₄</i>	<i>Ba(ClO₂)₄</i> LiClO ₄ <i>PETN</i> <i>SP</i>	Ba(ClO ₂) ₄ LiClO ₄ PETN <i>SP</i>	Ba(ClO ₂) ₄ LiClO ₄ <i>SP</i>		-
Intrinsiq JM/S1	176	-	-	Ba(ClO ₂) ₄	Ba(ClO ₂) ₄ LiClO ₄ <i>SP</i>	<i>Ba(ClO₂)₄</i> <i>LiClO₄</i> <i>SP</i>	Ba(ClO ₂) ₄ LiClO ₄	-
Intrinsiq BM/S1	176	-	-	Ba(ClO ₂) ₄	<i>Ba(ClO₂)₄</i> <i>SP</i>	Ba(ClO ₂) ₄ <i>LiClO₄</i> <i>SP</i>	Ba(ClO ₂) ₄ LiClO ₄ <i>SP</i>	-

Note: The Silicon samples used for this experiment were obtained from Intrinsiq materials with one sample obtained from Vesta Sciences. The original nomenclature was used as received from the suppliers and is not similar to the Si samples mentioned earlier. Values in bold italics represent the loudest noise measured for the specific npSi/oxidiser mixture.

4.2.10.2 Results: Effect of aged nano-porous silicon on the reactivity of npSi-based explosive formulations

The relative reactivity results obtained from the evaluation conducted on the nano-porous silicon explosive formulations prepared using the aged nano-porous silicon are given in Table 4.10.

Table 4.10: R_r results of npSi-based explosive formulations prepared from aged silicon

Sample	PETN-based nano-porous silicon explosives formulation				SP-based nano-porous silicon explosives formulation			
	Time (s)	Noise (dB)	R _r x10 ¹⁷	R _r STD. dev x10 ¹⁷	Time (s)	Noise (dB)	R _r x10 ¹⁹	R _r STD. dev x10 ¹⁷
HDS – I001	3.22 ^{±0.51}	62.00 ^{±2.31}	2.60	0.36	11.90 ^{±0.95}	105.60 ^{±1.20}	1.45	7.77
HDS – I002	4.48 ^{±0.62}	107.26 ^{±1.20}	449.00	1.70	9.19 ^{±0.81}	104.68 ^{±1.29}	1.72	18.75
HDS – I003	6.06 ^{±0.42}	62.00 ^{±2.96}	1.38	0.19	12.07 ^{±1.02}	107.10 ^{±1.01}	1.65	20.91
HDS – I004	9.07 ^{±0.89}	62.00 ^{±2.15}	0.93	0.11	NR	NR	NR	NR

NR denotes no reaction

4.2.10.3 Results: R_r of aged nano-porous silicon-based explosive formulations

Relative reactivity results of the ageing evaluation of nano-porous silicon-based explosive formulations are shown in Tables 4.11 (NT used as oxidiser) and 4.12 (SP used as oxidiser).

Table 4.11: R_r results of npSi-based explosive formulations – NT

	NT formulations from Table 4.5							
	T1	STD.dev.	T2	STD.dev.	T3	STD.dev.	T4	STD.dev.
Days	$R_r \times 10^{17}$	$R_r \times 10^{17}$	$R_r \times 10^{17}$	$R_r \times 10^{17}$	$R_r \times 10^{17}$	$R_r \times 10^{17}$	$R_r \times 10^{17}$	$R_r \times 10^{17}$
0	1.86	0.56	13.70	2.61	33.70	11.62	14.44	1.52
5	1.42	0.58	16.70	3.95	28.50	4.74	8.41	1.69
24	1.03	0.11	2.72	0.56	20.60	1.62	4.30	0.27
31	0.69	0.08	7.92	1.07	12.90	1.7	4.13	1.4
45	1.20	0.33	5.79	0.55	18.20	5.75	4.08	0.36
75	0.18	0.01	2.82	0.20	8.06	1.78	2.10	1.05
380	0.15	0.02	0.25	0.08	0.45	0.16	5.62	1.84

Table 4.12: R_r results of npSi-based explosive formulations – SP

	SP formulations from Table 4.5							
	N1	STD.dev.	N2	STD.dev.	N3	STD.dev.	N4	STD.dev.
Days	$R_r \times 10^{17}$	$R_r \times 10^{17}$	$R_r \times 10^{17}$	$R_r \times 10^{17}$	$R_r \times 10^{17}$	$R_r \times 10^{17}$	$R_r \times 10^{17}$	$R_r \times 10^{17}$
0	3.35	0.59	183.00	59.80	124.00	36.20	9.00	0.98
5	1.08	0.12	346.00	25.98	77.80	11.2	11.20	2.80
24	0.43	0.05	156.00	28.78	1.89	0.29	3.04	0.47
31	0.31	0.08	62.90	11.52	NR	NR	3.42	0.27
45	0.40	0.05	5.14	0.39	NR	NR	3.34	0.28
75	NR	NR	0.65	0.13	NR	NR	1.29	0.14
380	NR	NR	NR	NR	NR	NR	2.77	0.38

NR denotes no reaction

4.2.10.4 Results: Effect of density on the reactivity of nano-porous silicon-based explosives

The results obtained are depicted in Figure 4.13.

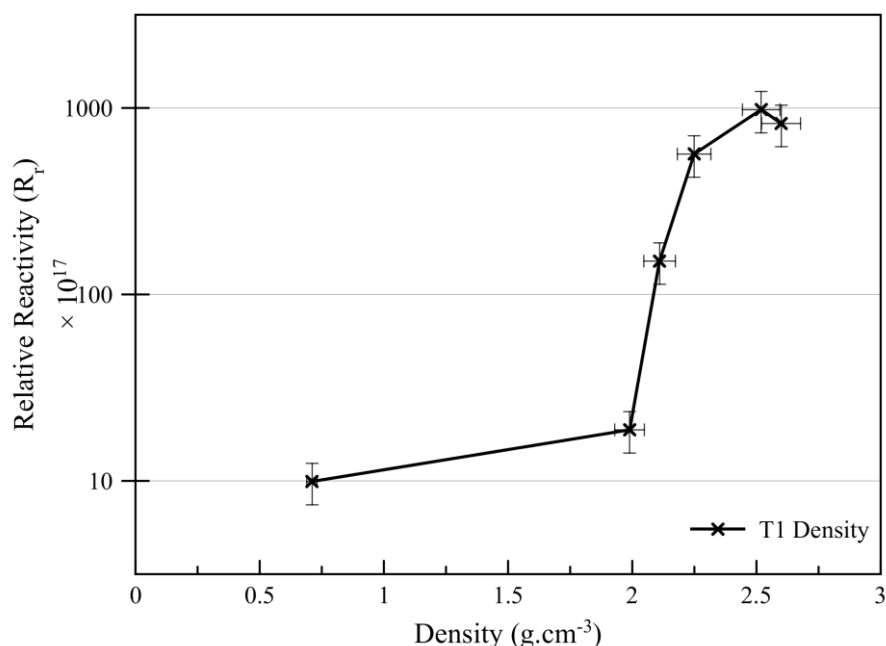


Figure 4.13: Schematic depiction of the relative reactivity of NT/Si mixtures with relation to density

4.2.10.5 Results: Nano-porous silicon burning rate

Upon ignition, the nano-porous silicon explosive formulation starts to burn. This is a controlled burn and the reaction does not build up to detonation. The low density (in this case pouring density) of $0.5 \text{ g.cm}^{-3} \pm 0.1$ and lack of confinement are considered to be contributing factors to this.

Firstly, the burn rate of nano-porous silicon explosives formulations, consisting of the same porous silicon (fuel) but with different oxidisers, was determined. Secondly, the burn rate of nano-porous silicon explosives formulations, consisting of different porous silicon (fuel) but with the same oxidiser (nitrotetrazole) was determined. The results obtained are shown in Tables 4.13 and 4.14 respectively.

Table 4.13: Nano-porous silicon explosive formulations burn rate results (same Si)

No.	Oxidiser	npSi Sample	npSi Surface Area (m ² .g ⁻¹)	Burn speed (m.s ⁻¹)
1	NaClO ₄	HDS – V008	180	0.519 ^{±0.061}
2	Ba(ClO ₄) ₂	HDS – V008	180	NR
3	PETN	HDS – V008	180	0.016 ^{±0.052}
4	NT	HDS – V008	180	0.845 ^{±0.081}
5	HNS	HDS – V008	180	0.891 ^{±0.099}

Table 4.14: Nano-porous silicon explosive formulations burn rate results (same fuel)

No.	Oxidiser	npSi Sample	npSi Surface Area (m ² .g ⁻¹)	Burn speed (m.s ⁻¹)
1	NT	HDS – I002	305.00	2.930 ^{±0.0367}
2	NT	HDS – I003	290.00	2.118 ^{±0.265}
3	NT	HDS – V004	116.00	1.426 ^{±0.178}
4	NT	HDS – V008	180.00	1.865 ^{±0.233}
5	NT	Nano Si	0.17	0.642 ^{±0.008}

When the results are plotted, we can find a linear relation of specific surface area to burning velocity.

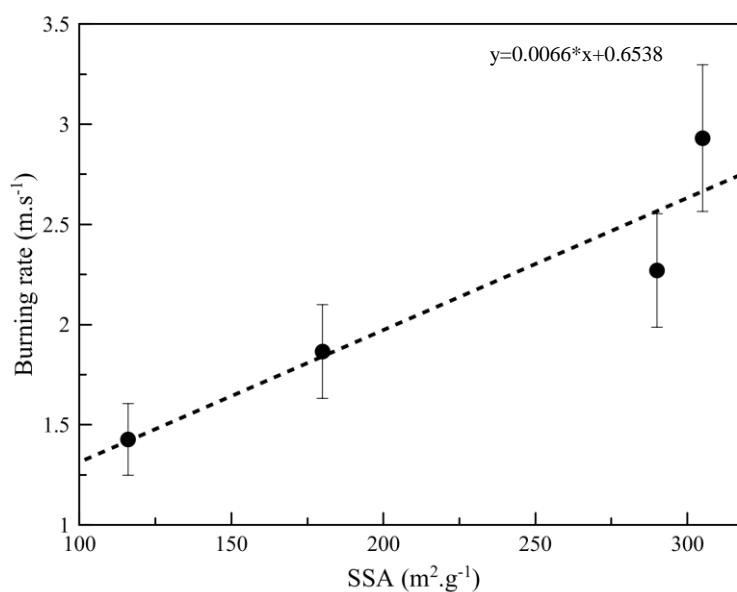


Figure 4.14: Linear relation between SSA of porous silicon and burn rate



Figure 4.15: npSi/NaClO₄ burn



Figure 4.16: npSi/Ba(ClO₄)₂ burn



Figure 4.17: npSi/PETN burn



Figure 4.18: npSi/NT burn



Figure 4.19: npSi/HNS burn

4.2.10.6 Results: Closed pressure vessel test

The results obtained from the pressure test are given below.

Figure 4.20 shows the combined pressure test results for the different formulations evaluated. In this figure, the numbers shown as P_{Si} 1 to P_{Si} 5 represent the formulations 1 to 5 in Table 4.14.

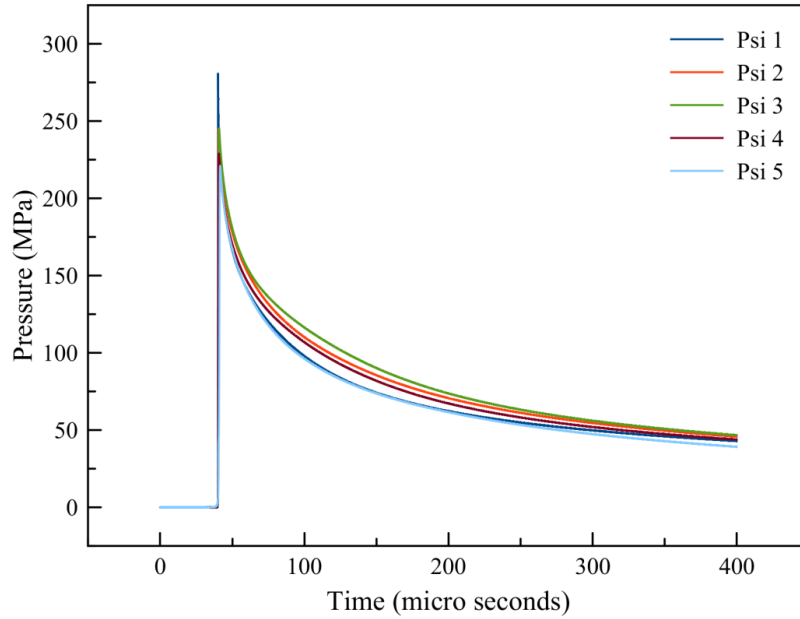


Figure 4.20: npSi/NT combined pressure test result

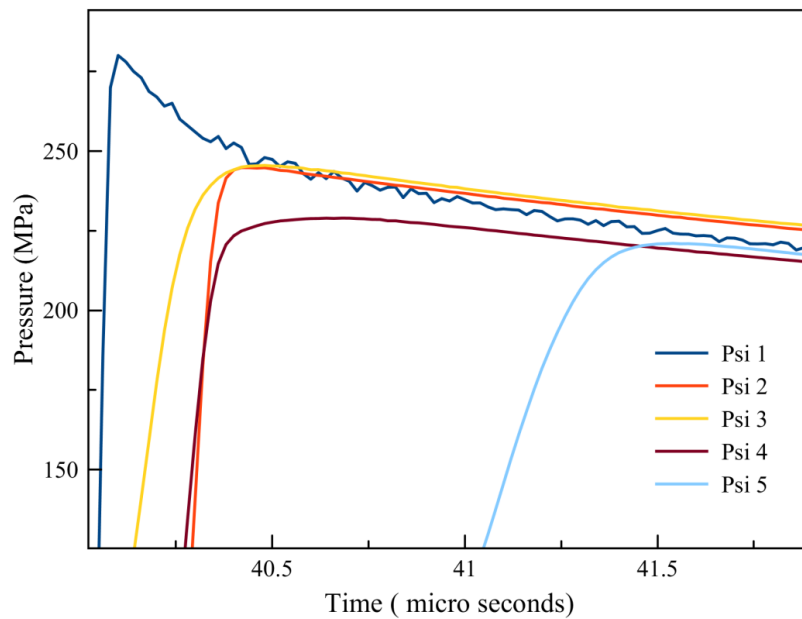


Figure 4.21: npSi/NT combined peak pressure result

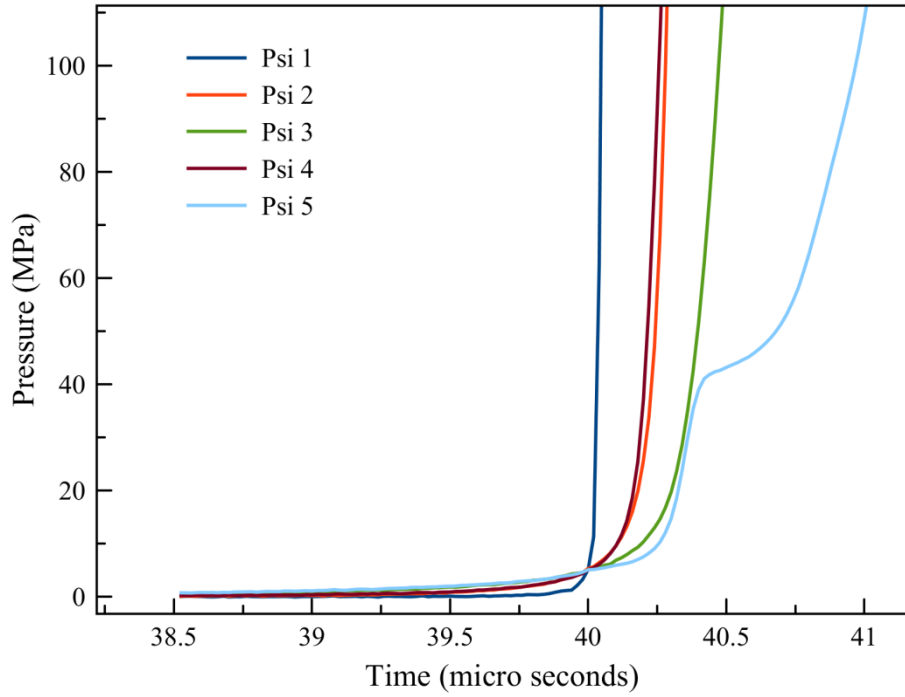


Figure 4.22: npSi/NT combined pressures onset results

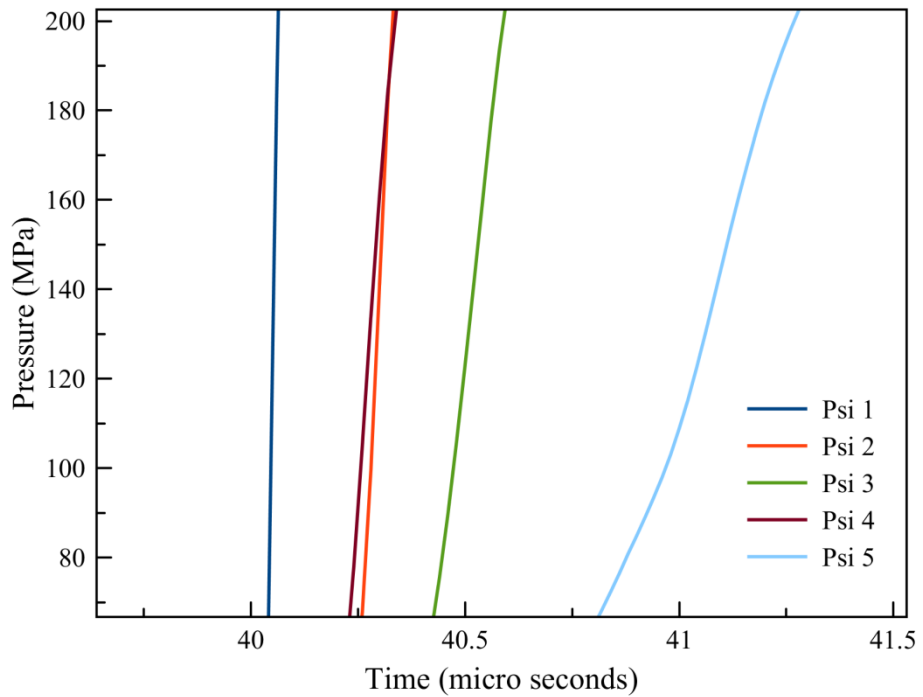


Figure 4.23: npSi/NT combined pressure results – linear portion of the pressure rise

4.2.11 Nano-porous silicon-based explosive formulation development – Discussion

Optical microscopy shows that the oxidiser forms large crystals coated with the nano-porous silicon. It is questionable whether there is actually any oxidiser encapsulated in the nano-pores of the silicon. Large needle-like crystals are undesirable when preparing explosive formulations. Such crystals are usually highly sensitive to stimuli like impact and friction. The incorporation of grit into explosive formulations also poses a potential risk. In general, grit refers to unwanted or foreign objects that can contaminate explosive formulations. Examples of grit can be dust or soil that is in contact with the explosives. The impact and friction sensitivity of explosives is likely to increase when grit is present. In the formulations, the nano-porous silicon can pose a potential risk as it may act not only as a fuel but also as grit in the explosive formulation. The combination of grit and a sensitive crystal structure can render some of these formulations unsafe for processing and field application.

On observing the reactions, two types of characteristic explosives behaviour were noted. These are described as pyrotechnic and explosive behaviour respectively. As per Cooper's (1996:34) explanation, pyrotechnics are porous; hence the convective heat transfer due to hot gas permutation into the reactant material mixed ahead of the reaction zone becomes important. In the case of sodium perchlorate mixtures, similar behaviour is predominantly taking place. The larger the surface area of the nano-porous silicon used, the higher the intensity of the noise (hence the faster the reaction becomes). In the case of pyrotechnic mixtures, the reaction rate is not only affected by pressure, density and temperature but also by porosity, particle size, purity, homogeneity and stoichiometry. From Figures 4.4 to 4.9 it can be seen that the crystal formation on the silicon as well as the crystal structure is inconsistent. The difference in behaviour noted can relate to the differences in particle size, purity, homogeneity and porosity.

Combining different oxidisers with nano-porous silicon influences the reactivity of the formulation. Explosive compositions used as oxidisers (PETN, HNS and NT) performed significantly differently from the inorganic oxidisers used. This was not only visually noticeable but is also supported by the results shown in Table 4.7.

Stoichiometric mixtures of nano-porous silicon and sodium perchlorate are shown to be significantly more reactive than mixtures of nano-porous silicon and PETN, NT and HNS respectively. This is also demonstrated in Figure 4.24. When the standard deviations of the R_r results are compared, it is noticeable that the mixtures containing

explosives as oxidisers perform less consistently compared with the mixtures prepared using the inorganic oxidisers.

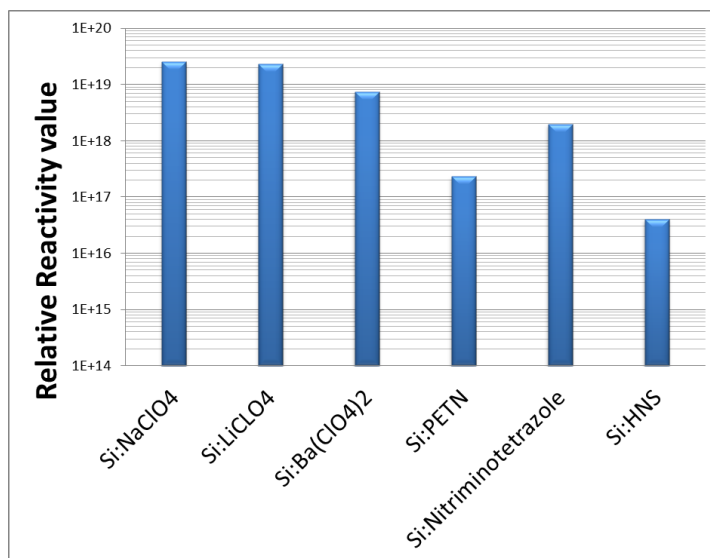


Figure 4.24: Relative reactivity result comparison

Explosives' characteristics can be seen where organic explosives (PETN, HNS and NT) are used as oxidiser. A different mechanism can be responsible for the decomposition of organic explosives. Here the silicon can act as a conductor of heat if used in the right ratio. If heat is put into a small local volume of reactive material, the material starts to decompose. The higher the temperature, the faster the decomposition reaction proceeds. As the temperature in this small volume is generated, heat is transferred (through conducting the heat) to the surrounding material. If the heat is not produced fast enough by the reaction in this small volume, it can be transferred to the adjacent wall material. It cools down and the reaction gets progressively slower until the reaction reaches a point where it is likely to stop. If the reaction in the small volume produces heat faster than it can be transferred to the adjacent material, then the smaller volume heats up or increases in temperature progressively. This increase in temperature speeds up the reaction rate and consequently heat is produced even faster (resulting in a self-sustaining reaction). In the reaction of the organic explosives-based mixtures, the organic explosives (PETN) react faster when silicon with a higher surface area is used (Table 4.9).

Using the hotspot theory, this reaction behaviour can be explained to be a function of the transfer of heat. In the right ratio, the Si acts as a conductor of heat; the lower volume heats up or increases in temperature and transfers heat to the organic explosives. The organic explosives start to burn and transfer this heat to adjacent Si

and organic explosives particles. This reaction repeats itself whilst increasing in speed. At a certain point the reaction becomes self-sustainable to such an extent that only the organic explosives react by detonation. If the ratio is wrong, the silicon acts as a semiconductor, taking up heat much faster than it can transfer it to its immediate surroundings. This in turn prevents the organic explosives jumping from deflagration to detonation. This is more noticeably from the density evaluations conducted and shown in Table 4.13. When considering density in his argument the silicon contact with the explosives increases in intimacy as the density increases. Heat is then transferred more effectively to the explosive. The explosive starts to react and heats the silicon in front of it. The reaction increase in speed until a deflagration to detonation is achieved.

The level of oxidation of the nano-porous silicon also affects the reactivity of the nano-porous silicon-based explosive formulations. Canham (1997c:44) reported that that porous silicon films underwent pronounced 'ageing' when stored in ambient air for a prolonged period of time (refer to Section 3.3.2). The speed and the extent to which the oxidation of the silicon occurs depends upon many factors such as intensity of light, level of humidity and level of highly oxidising airborne species. Results shown in Table 4.10 demonstrate the influence of pre-oxidised nano-porous silicon on the reactivity of the explosives formulation.

Formulations T1 to T4 and N1 to N4 were used to show the change in reactivity over time. The relative reactivity results (Table 4.11) indicate a distinct difference in reactivity when T1 is compared with T2, T3 and T4. Difference in reactivity was also noted when N1 was compared with N2, N3 and N4. Nano-porous silicon-based explosives formulations, where sodium perchlorate was used as the oxidiser, show a rapid decline in reactivity (Table 4.12). Formulations N3 (no binder) were non-responsive after 24 days. In an attempt to extend the shelf life of formulations N1 and N2, different binders were used (nitrocellulose and synthetic wax). The results obtained indicate no significant increase in the shelf life of these formulations (Table 4.12). Formulation N4 showed a significant decline in reactivity over 380 days but not a complete deprivation of reactivity. Nano-porous silicon-based explosives formulations where NT was used as the oxidiser show a rapid decline in reactivity (Table 4.11). The same binders were used in a similar attempt to extend the shelf life of formulations T1 and T2. Formulation T4 showed a significant decline in reactivity after 75 days. The reactivity thereafter steadily increased again over the remainder of the 380 days. Overall the nano-porous silicon explosive formulations prepared with NT tested to be more stable over time compared with SP mixtures.

Increasing the density of the nano-porous silicon explosive formulation (T1) resulted in an increase in the reactivity of the formulation. This increase in reactivity is seen from a density of 2.2 g.cm^{-3} . The increase in reactivity is achieved through both a decrease in the reaction time and an increase in the noise level of the reaction obtained from the test. NT / Si mixtures react faster when the mixture is at a state of higher density. Using the hotspot theory, this reaction behaviour can be explained to be a function of the transfer of heat. In the right ratio the Si acts as a conductor of heat; the small volume heats up or increases in temperature and the heat is transferred to the NT / Si. The NT / Si starts to burn and transfers this heat to adjacent Si and NT particles. This reaction repeats itself whilst increasing in speed. At a certain point the reaction becomes self-sustainable to such an extent that only the NT reacts by detonation.

Burn rate changes were noted for the different oxidisers used. Pour density (that varied between 0.97 and 1.05 g.cm^{-3} for all the samples tested), as well as the intimate contact between the fuel and oxidiser that is used, influence the burn rate. A burning reaction is a reaction where the burn front propagates into the unreacted material in many ways and as a combination of these. Heat is conducted through the particles and the particles ignite when the activation energy requirements are met. Hot gas pushed into the unreacted material can act as a mechanism to pre-heat the particles and in combination with the heat conducted can cause ignition. Radiated heat can cause ignition if the unreacted material is opaque to such an extent where radiation is not obscured. In the samples used here this mechanism is unlikely, as none of the samples were opaque. Particle size (as exposed surface area) can influence the rate of reaction in a manner where the burn rate increases as the surface area increases.

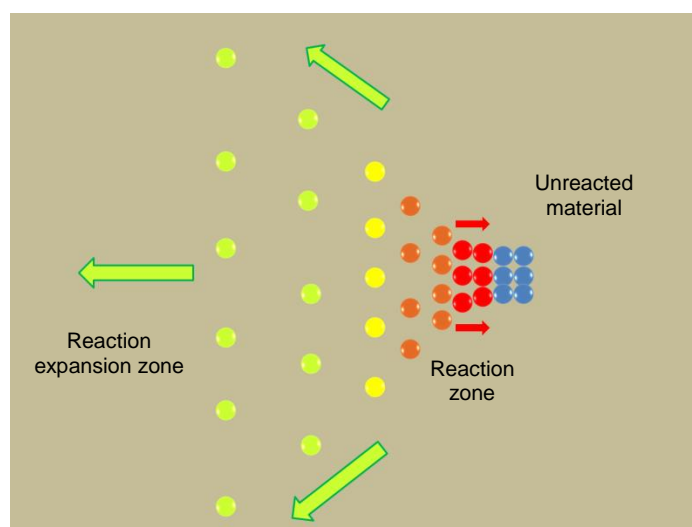


Figure 4.25: Burning reaction mechanism

In the data presented in Table 4.13 it is seen that there is a significant difference in burning speed. A 'No Result' (NR) is reported for the barium perchlorate mixture. The reason for this is that no self-sustainable burn reaction was observed when the formulation was ignited. The mixture did however burn as seen in Figure 4.16. A possible reason ascribed to this is that the material particles were not in close contact with one another to ensure forward propagation of the reaction. More energy is required than what was available. It was however noted that the barium perchlorate did burn through the complete column when assisted by an external heat source.

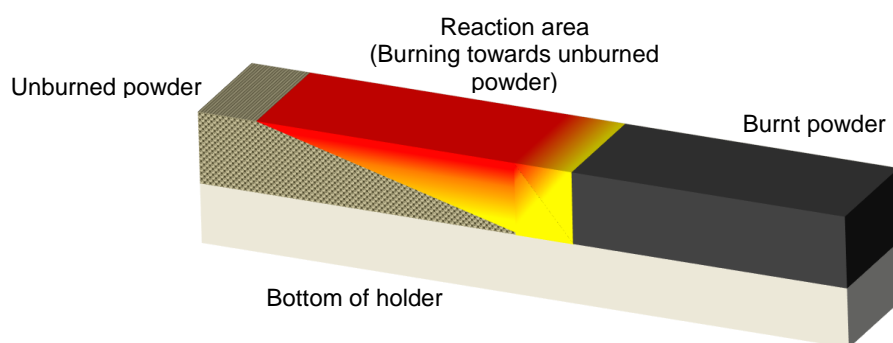


Figure 4.26: Cross-section of exposed area of burn

The exposed burn length (measured length at the base of the flame) was 36.2 mm and with a width of 5 mm gave an exposed surface area of 175 mm². When comparing Figures 4.15, 4.17, 4.18 and 4.19, it shows the exposed burn area for these formulations to be greater than that shown for the barium perchlorate mixture. A sustainable burn was achieved for these formulations. The SP mixture burned fast enough on the surface so that it reached the end of the line while the beginning of the line was still burning. This is indicative of a very fast-burning mixture.

Figure 4.27 shows a linear decline in the reaction rate of SP/npSi mixtures with an increase in density. Figure 4.13 show that tetrazole-based npSi explosive formulations undergo a progressive increase in R_r when the density increases. npSi / tetrazole mixtures are therefore selected as the explosive formulation of choice in the further development of a non-metallic explosives initiator.

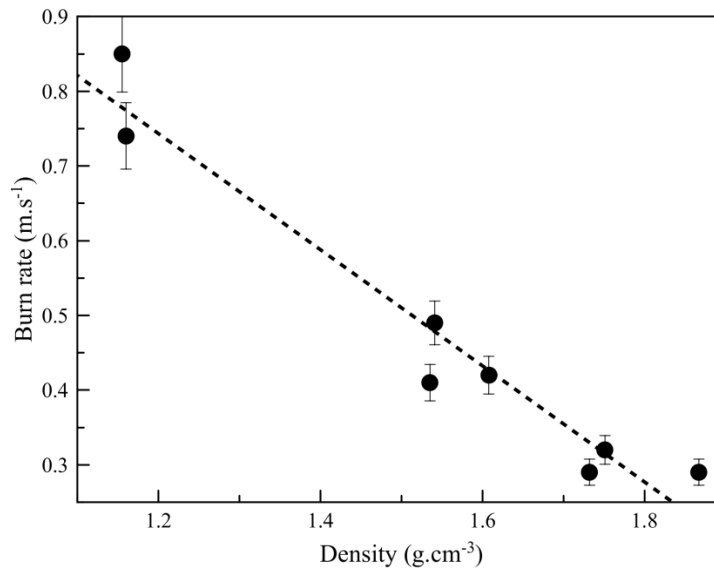


Figure 4.27: SP/npSi mixture reaction velocity as a function of density

This section has shown that the burning rate of porous silicon-based explosive formulations increases when the SSA of the silicon increases. Because intimacy of contact between the oxidiser and the fuel can increase the reaction rate, the oxidiser does enter the nano-sized pores of the nano-porous silicon. If this did not happen, an increase in the reaction rate with an increase in SSA would not have been evident.

Figure 4.20 shows the combined pressure profile of the npSi/NT mixtures combusting in a closed pressure vessel. From this result a pressure profile showing a steep rise in pressure and a slow decrease in pressure can be observed. If this is broken down into the different peak pressures, dissimilar areas under the curve are notable. Figure 4.22 enlarges the onset point of the pressure rise. This is the point or area where the ignition of the powder occurs. Mainly three events happen in this area. First the ignition wire heats up, then the powder starts to ignite, and lastly the powder burns. These events are difficult to see on the pressure data presented here. What is visible is the rate of transition. This is the area where the first rise occurs and the beginning of the linear portion of pressure rise. In Figure 4.28 this is the area between the pressure data (black), the point where the pressure starts to rise (point where the blue and black line separate) and the linear portion of pressure rises (green line) (point where the blue and black line cross).

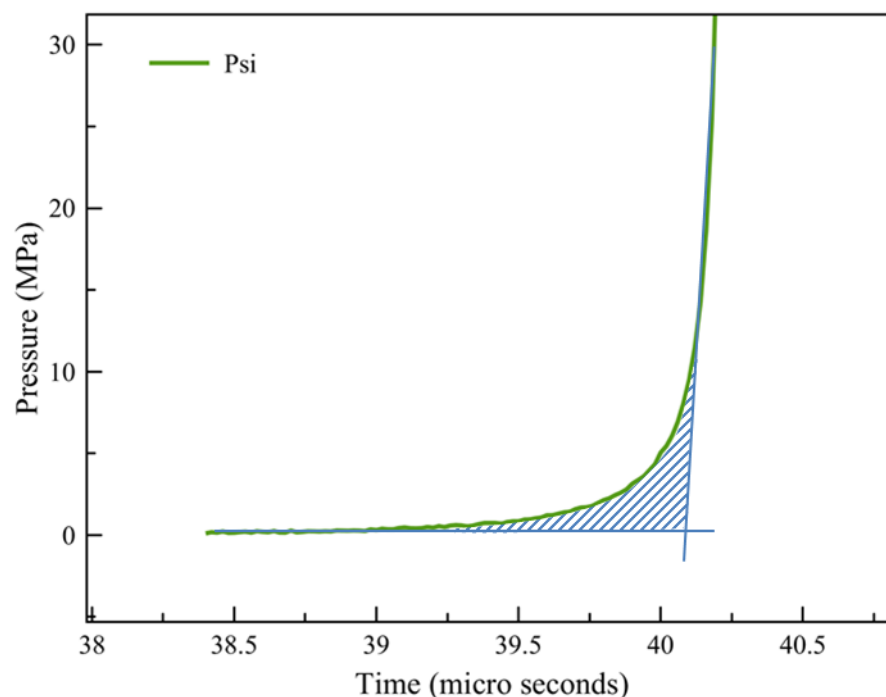


Figure 4.28: Area determination under the onset point of pressure rise

The area under the respective data points was determined with the help of a data processing program called GRAPH (version 4.4.2). The calculated areas are given in Table 4.15.

Table 4.15: Area values obtained for different npSi explosive formulations

No.	Oxidiser	npSi Sample	npSi Area ($\text{m}^2 \cdot \text{g}^{-1}$)	Area under the graph (Pa.s)
1	NT	HDS – I002	305.00	0.38
2	NT	HDS – I003	290.00	3.30
3	NT	HDS – V004	116.00	6.44
4	NT	HDS – V008	180.00	3.96
5	NT	Nano Si	0.17	12.65

From the data it is seen that the npSi explosive formulation where silicon with the higher surface area was used produced the smaller area under the data points. From the burning velocity results it is seen that a higher SSA (for the porous silicon) induces a higher burn rate. A possible explanation can be that the smaller surface area under the data points is indicative of a faster reaction compared with formulations that

showed a higher area under the data points. Hence a faster burning reaction could be indicative of a sensitive npSi/NT explosive formulation that requires less input energy to start burning (activation energy).

This section reviewed the manufacturing of nano-porous silicon explosive formulations and their characteristics. Various oxidisers were used in combination with various samples of Si. The effects of SSA of the npSi, initial state of oxidation of the Si used to prepare the mixtures, the effect of different oxidisers, and the effect of density on the reactivity of various formulations were shown. A novel test method, relative reactivity (R_r), was developed in this study and provided a means of creating a comparative platform used to compare the different formulations tested.

The R_r for NT is higher than PETN and HNS. Nano-porous silicon explosives formulations prepared with NT were also shown to have a longer shelf life than perchlorate oxidisers. Unconfined burn rate results also showed nano-porous silicon mixed with NT to be faster than other oxidisers (although slightly to HNS mixtures with npSi). From the results presented in this section, npSi/NT (1 : 3) formulations prepared with nano-porous silicon having an SSA of $180 \text{ m}^2.\text{g}^{-1}$ is used in the development of a non-metallic explosive initiator.

The next section describes the development of PBX formulations.

4.3 Preparation of PETN and RDX-Based PBX Explosive Formulations

PBX is explosives material in which explosive powder is bound together using small quantities of polymer (plastic) and a small percentage of additives such as plasticisers and antioxidants (flowing agents can also be added). PBXs were originally developed to reduce the sensitivity of explosive crystals by embedding the explosive crystals in a rubber-like polymeric matrix. The first PBX composition was developed at the Los Alamos Scientific Laboratories in the United States of America in 1952. The composition consisted of cyclo-trimethylenetrinitramine (RDX) crystals embedded in plasticised polystyrene. (Akhavan, 2011:13). Some of typical examples of PBX formulations are given in Table 4.16.

Table 4.16: Typical PBX formulations (a shortened list from Akhavan, 2011:13)

Explosive	Binder and Plasticiser
HMX, RDX	Acetyl-formyl-2,2 dinitropropanol (DNPAF) and polyurethane
HMX, RDX, NTO	Cariflex (thermoplastic elastomer)
HMX, RDX, HNS	Hydroxy-terminated polybutadiene
HMX, RDX	Hydroxy-terminated polyester
HMX, RDX, PETN	Kraton (block copolymer of styrene and ethylene-butylene)
HMX, RDX, PETN	Teflon (polytetrafluoroethylene)
HMX, RDX, HNS, PETN, NTO	Kel-F (polychlorotrifluoroethylene)
PETN, RDX	Nylon (polyamide)

The type of polymer binder and the formulation of PBX determine the properties of the explosive product. PBX can be produced as granules for pressing, but can also be made to have a putty-like consistency that enables the materials to be cast. The explosive formulation must be sensitive enough to pick up from the energy generated by the deflagration-to-detonation transition (DDT) system (described in Chapter 4). Furthermore it should be strong enough to initiate a main explosive charge. Both castable and pressable PBX formulations were initially explored.

In this study PETN and selectively RDX were used as the main explosive component in the PBX formulations prepared. Particle size distribution (PSD) of all explosives was done before commencing with the manufacturing process. The PSD was measured using a Malvern Mastersizer with iso-propanol as the dispersant and the stirrer speed set at 2100 rpm. The results obtained are presented below.

Table 4.17: PSD results of PETN and RDX used in PBX manufacturing

Explosives	Batch No.	d ₁₀	d ₅₀	d ₉₀	Span
Coarse PETN	PETN-01	217.308	301.577	417.826	0.665
Fine PETN	RPETN-01	52.492	116.737	223.523	1.465
RDX	RRDX	102.902	218.995	390.964	1.316

The following process was used to prepare a pressable PBX:

A slurry was prepared by adding the selected explosive to demineralised water and stirring it at a speed of 500 revolutions per minute (rpm). The batch was heated to 65 °C over a water bath while stirring. The selected binder was dissolved in a suitable solvent and added slowly to the explosive slurry. Stirring speed was increased to 700 rpm whilst maintaining the temperature of the slurry at 65 °C. These parameters were maintained for 20 minutes to drive off the solvent. Time allowed for the solvent to evaporate was adapted according to the type of solvent used. A cool-down period was introduced next by turning off the heat and the stirrer. The slurry, now consisting of water and larger granules, was allowed to cool down until a temperature of 30 °C was reached. The granules were retrieved by means of normal filtration and washed several times with water. Granules were then dried in an oven at 70 °C for 24 hours (the time allocated to dry in the oven was adapted according to binder and plasticiser systems used).

To prepare a castable PBX, the following process was used:

A binder was dissolved in a solvent. The explosive filler matrix was prepared from the selected explosive formulation and graphite. The dry ingredients were added to the binder matrix and stirred until a homogeneous mixture was obtained. The viscosity of the mixture was adapted until a flow rate was obtained that suited the casting process. Subsequently the mixture was cast into the desired shapes and cured in an oven at 70 °C. The curing time is a function of the binder system used.

A schematic description of both processes is shown in Figure 4.29 and Figure 4.30.

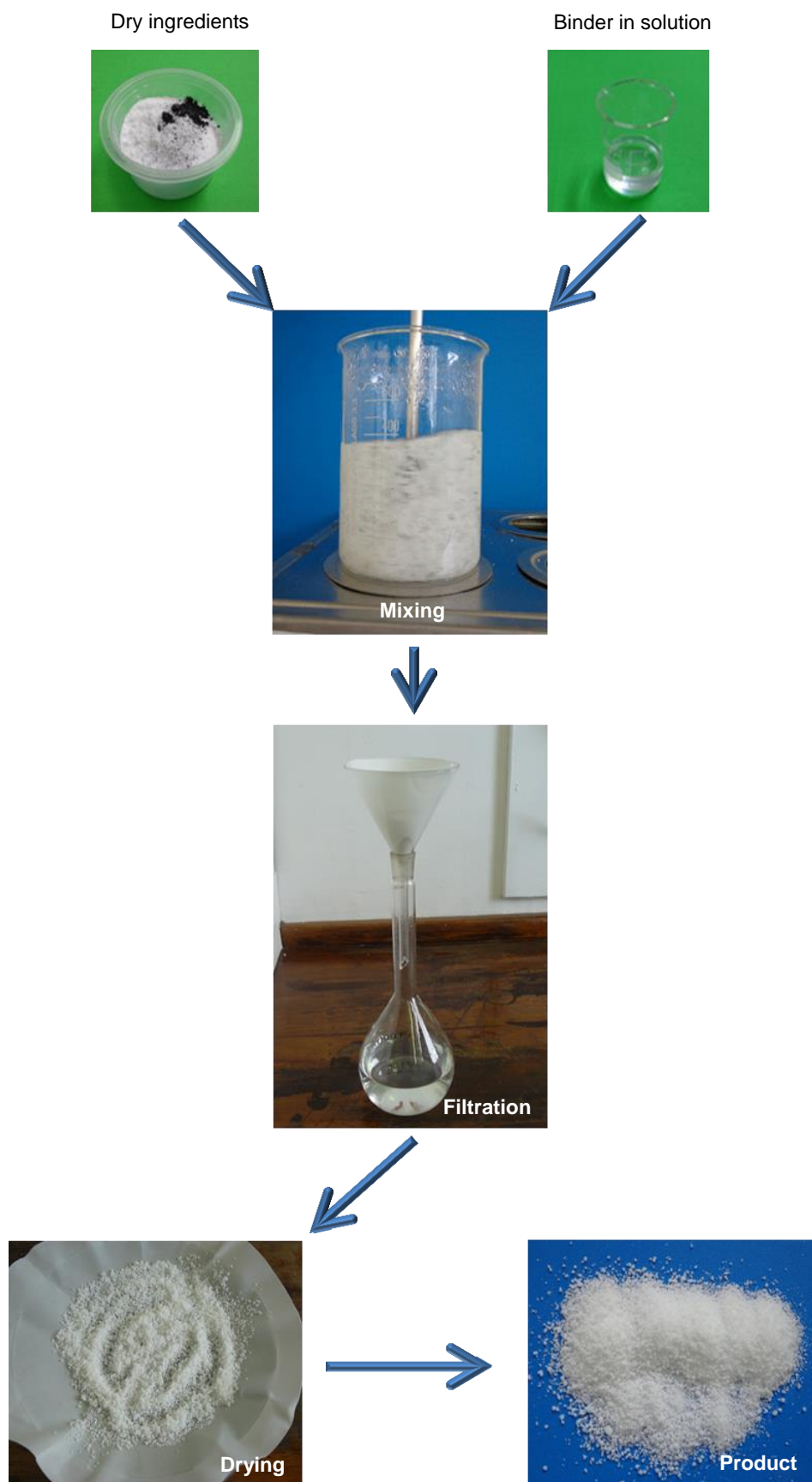


Figure 4.29: Pressable PBX manufacturing process

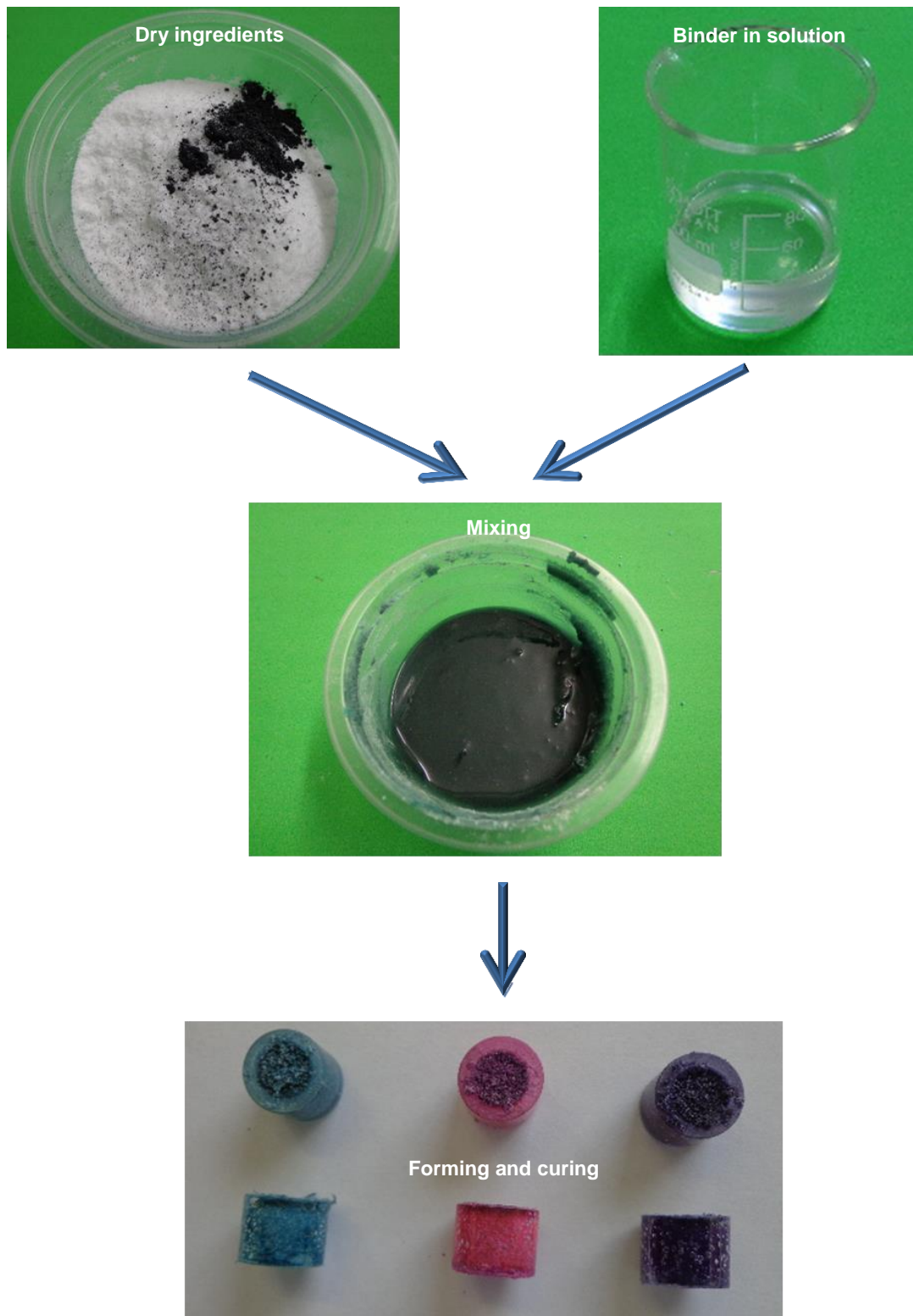


Figure 4.30: Castable PBX manufacturing process

Various castable and pressable explosive formulations were designed and manufactured. Explosive particle size, binders and plasticisers were varied in order to change the shock sensitivity of the formulation. Colour agents were added for identification purposes.

Table 4.18: Reference formulations

	Name	Description	Colour	Formulation
1	PETN	Coarse PETN	White	PETN powder
2	RXKF 9501	RDX 95% / density 1.51 g.cm ⁻³	White	RDX 95%, KEL-F 5%
3	Tetrazole	5-nitriminotetrazole	Pale yellow	Tetrazole powder
4	Cu tetrazole	Copper tetrazole	Blue/green powder	Copper tetrazole powder

Table 4.19: Pressable PBX development formulations

	Name	Description	Colour	Formulation
1	BMW 101	Coarse RDX	Violet	RDX 94.5%, Kraton 5%, Graphite 0.5%
2	BMW 111 - A	Coarse PETN	Malachite green	PETN 94.5%, Kraton 5%, Graphite 0.5%
3	BMW 111 - B	Coarse PETN 70% / Fine PETN 30%	Malachite green	PETN 94.5%, Kraton 5%, Graphite 0.5%
4	BMW 111 - C	Coarse PETN 30% / Fine PETN 70%	Malachite green	PETN 94.5%, Kraton 5%, Graphite 0.5%
5	BMW 111 - D	Fine PETN	Malachite green	PETN 94.5%, Kraton 5%, Graphite 0.5%
6	BMW 111-E	Coarse PETN 95% / Fine PETN 5%	Rodamine B pink	PETN 95%, Kraton 4.5%, Graphite 0.5%
7	BMW 111-F	Coarse PETN 90% / Fine PETN 10%	Rodamine B pink	PETN 95%, Kraton 4.5%, Graphite 0.5%
8	BMW 111-G	Coarse PETN	Rodamine B pink	PETN 90%, Kraton 10%, Graphite 0.5%
9	BMW 111-H	Coarse PETN 95% / Fine PETN 5%	Rodamine B pink	PETN 90%, Kraton 10%, Graphite 0.5%
10	BMW 111-I	Coarse PETN	Malachite green	PETN 97.5%, Kraton 2.5%, Graphite 0.5%
11	BMW 111-J	Coarse PETN 95% / Fine PETN 5%	Malachite green	PETN 97.5%, Kraton 2.5%, Graphite 0.5%
12	BMW 130	PETN 60 / RDX 40%	Rodamine B pink	RDX/PETN 94.5%, Kraton 5%, Graphite 0.5%
13	BMW 212	Coarse PETN	White	PETN 95%, EVA 5%, DCHP 0.5%
14	BMW 211-A	Coarse PETN 95% / Fine PETN 5%	Malachite green	PETN 95%, EVA 4.5%, Graphite 0.5%
15	BMW 211-B	Coarse PETN 90% / Fine PETN 10%	Malachite green	PETN 95%, EVA 4.5%, Graphite 0.5%

Table 4.20: Castable PBX development formulations

	Name	Description	Colour	Formulation
1	THR 211	THR 211 at density 1.55g/cc	Malachite green	PETN 95%, EVA 4.5%, Graphite 0.5%
2	THR 211	Coarse PETN	Malachite green	PETN 94.5%, EVA 5%, Graphite 0.5%
3	THR211A	Coarse PETN 95% / Fine PETN 5%	Malachite green	PETN 95%, EVA 4.5%, Graphite 0.5%
4	THR211B	Coarse PETN 90% / Fine PETN 10%	Malachite green	PETN 95%, EVA 4.5%, Graphite 0.5%
5	THR211C	Coarse PETN	Malachite green	PETN 90%, EVA 9.5%, Graphite 0.5%
6	THR211D	Coarse PETN 95% / Fine PETN 5%	Malachite green	PETN 90%, EVA 9.5%, Graphite 0.5%
7	THR211E	Coarse PETN	Malachite green	PETN 97.5%, EVA 2.0%, Graphite 0.5%
8	THR211F	Coarse PETN 95% / Fine PETN 5%	Malachite green	PETN 97.5%, EVA 2.0%, Graphite 0.5%
9	THR 212	Coarse PETN	Malachite green	PETN 95%, EVA 4.5%, DCHP 0.5%
10	THR 280	Coarse PETN 70% / Fine Cu TET 30%	Light green	Explosives 95%, EVA 5%, (binder % questionable) no lecitin
11	THR 287 - A	Coarse PETN 70% / Fine Cu TET 30%	Light green	Explosives 95%, EVA 5%, lecitin
12	THR 287 - B	Coarse PETN 50% / Fine Cu TET 50%	Light green	Explosives 95%, EVA 5%, lecitin
13	THR 287 - C	Coarse PETN 30% / Fine Cu TET 70%	Light green	Explosives 95%, EVA 5%, lecitin
14	THR 313	PETN wax calcium stearate	White	PETN 95%, wax 4.5%, calcium stearate 0.5%
15	THR 416	PETN, HTPB, DOA, Graphite	Grey	PETN 90%, HTPB 4.75%, DOA 4.75%, Graphite 0.5%

4.4 Test and Evaluation

These explosive formulations were developed to be compatible with the power output of the DDT system that was developed (can be initiated with the DDT system). The explosive formulations developed were subjected to the small-scale gap test in order to determine the shock sensitivity of the formulations compared with that of PETN and nitriminotetrazole.

4.4.1 Small-scale gap test

Shock initiation tests or gap tests seek to determine the effects of different materials imposed between a detonating standard donor explosive and a receptor explosive. Gap tests are not intended to be reliability tests (Zukas & Walters, 1998:291) although they do give an indication of what conditions might be required to ensure a reliable transmission of a detonation pulse. Gap tests determine the differences between

sensitiveness and sensitivity. Shock sensitiveness tests are intended to predict the hazards from the unintentional detonation of one explosive when exposed to the shock from another detonating explosive. These tests are true sympathetic detonation tests, since the stimulus is pure shock from the donor to the acceptor through the gap, which screens out fragments.

There were a number of different gap tests: in all of them a fixed charge (donor) was fired into a thickness of inert material that was in contact with the sample of the test explosives (acceptor). In all of the tests the thickness of the gap material was varied so that the tests were conducted in which the acceptor did/did not detonate (go/no-go approach). To conduct the gap tests, the donor and gap spacers were standardised. The different gap tests were built around different donor explosives and gap spacer material.

The set-up for the gap test conducted in this study used a 2D detonator as the donor charge and 10 mm x 10 mm stainless steel cards with varying thickness. The 2D detonators contained 25 mg PETN as base charge and 150 mg LA as primary explosive charge. The acceptor charges were prepared to fit inside a polypropylene tube (8 mm inside diameter, 2 mm wall thickness and 10 mm high). An aluminium witness block was used to report any detonation (go) reaction of the acceptor explosives. A 12 mm x 12 mm square tube was used as a centring piece. The test set-up is shown in Figure 4.31.

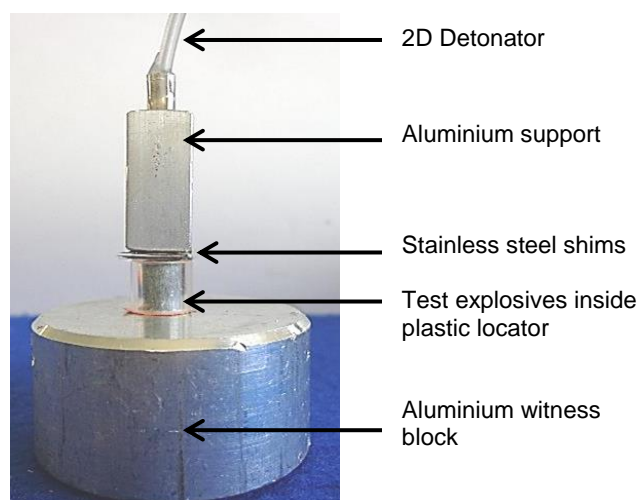


Figure 4.31: Small-scale gap test set-up

4.4.2 Friction sensitivity test

Throughout the life cycle of explosives the danger exists of their being subjected to friction. This can pose great danger, especially during the manufacturing process and when the explosive is being handled. The Julius Peters friction sensitivity apparatus is used to determine the friction sensitivity value of the explosive.

RSA-MIL-STD-154 describes the friction sensitivity test as follows:

A sample of the explosive formulation is placed on top of a porcelain plate, perpendicular to the surface roughness of the plate. A porcelain pin is secured onto the top arm of the apparatus. The porcelain plate is then secured to the bottom arm of the apparatus. The top arm is then lowered so that the porcelain pin rests on the explosive sample on the porcelain plate. A weight is then positioned on a pre-selected position on the top arm of the apparatus. This gives a certain force to be applied to the explosive sample. The porcelain plate is then moved in a single back-and-forth motion. Any type of reaction is noted, e.g. smoke, smell, noise and sparks. If a reaction occurs, the weight and/or the position of the weight are adjusted until no reaction is obtained for six consecutive repetitions.

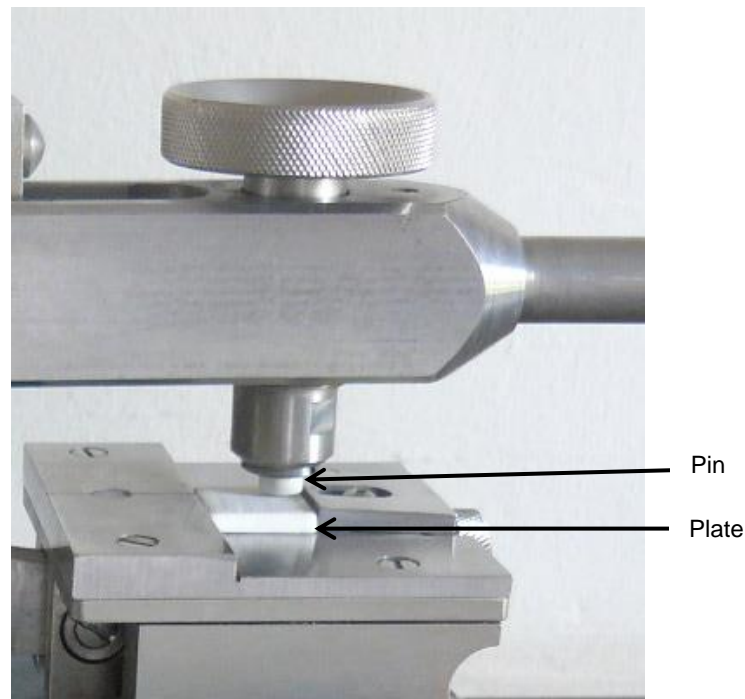


Figure 4.32: Porcelain plate and pin set-up

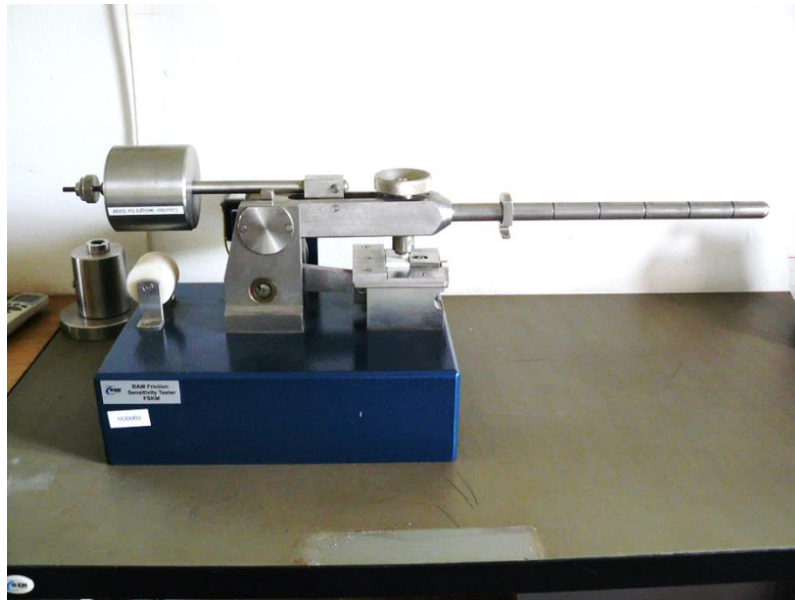


Figure 4.33: Friction sensitivity apparatus

4.4.3 Impact sensitivity test

The impact sensitivity test value of an explosive gives an indication of the mechanical energy needed to initiate an explosive. To determine the impact sensitivity value of an explosive the Julius Peters impact sensitivity apparatus is used.

RSA-MIL-STD-154 describes the impact sensitivity test as follows:

A 40 mg sample of the explosive is placed between two rollers. The rollers are kept in position by a collar. The unit containing the explosive sample is then positioned on top of a witness block. A selected mass (1 kg, 2.5 kg, 5 kg, 10 kg or 20 kg) is dropped from a predetermined height onto the unit containing the explosive sample. The witness block is then examined for a pass or fail reaction. If the explosive sample reacted, a pass reaction is noted, if no reaction is observed, a fail reaction is noted. The height of the weight is then adjusted according to each reaction obtained for the previously tested sample. The adjustment is done using a logarithmic scale. The height is adjusted upward if a fail reaction is obtained and downward for a pass reaction. This procedure is repeated for thirty samples. The 50% ignition height can now be calculated by using the following formula:

$$I = y + d \left[\frac{A}{N} \right] \pm 0.5 \quad \text{Equation 4.20}$$

+ When N = Total negative

- When N = Total positive

50% ignition height = 10^1 = mm or kg.m

y = the logarithm of the lowest height where the frequency is the lowest.

d = the difference of the logarithms of the consecutive heights.

N = the total number of repetitions of the event with the lowest frequency.

A = the sum of the products $i.n_i$. (i = numeric value given to every level where the lowest frequency occurred. The lowest level is given the value 0 and the next level is given the value 1, etc. n_i = the number of repetitions of the event with the lowest frequency on every level.)

I = the mean of the variant (the log. of the height).

From the 50% ignition height the Figure of Insensitivity (F of I) can be calculated by the following formula:

$$F \text{ of } I = \frac{\text{Height (unknown)}}{\text{Height of RDX}} \times 80$$

Equation 4.21

Height = 50% ignition height.



Figure 4.34: Julius Peters impact sensitivity apparatus

The results obtained when using Equation 4.21 are comparative values and must not be seen as absolute values.



Figure 4.35: Collar and roller set-up

4.4.4 Differential scanning calorimetry (DSC)

During heating of an explosive formulation, interaction occurs between the different components of the formulation. This interaction can make the explosive formulation unstable. To establish if the explosive is safe for handling, the thermal properties of the explosive formulation when subjected to normal processing temperatures must be known.

The DSC (PerkinElmer DSC 8500) was used to determine the melting and decomposition temperatures of explosive formulations. The endothermic and exothermic peaks obtained provide an indication of the stability of the explosive formulation.

RSA-MIL-STD-154 describes the DSC test as follows:

The DSC maintains the sample and reference material isothermal to each other by the application of electrical energy. The samples are heated at a linear rate (5 °C/min) and a curve of heat flow as a function of temperature is obtained. Any thermal event occurring in the sample is given as a peak from the DSC base line.



Figure 4.36: PerkinElmer DSC 8500 apparatus

4.4.5 Results: PBX-based explosives formulation test and evaluation

4.4.5.1 Results: SSGT

The small-scale gap test (SSGT) results are shown in Figure 4.37 and 4.38. Actual results are presented in Appendix 4D.

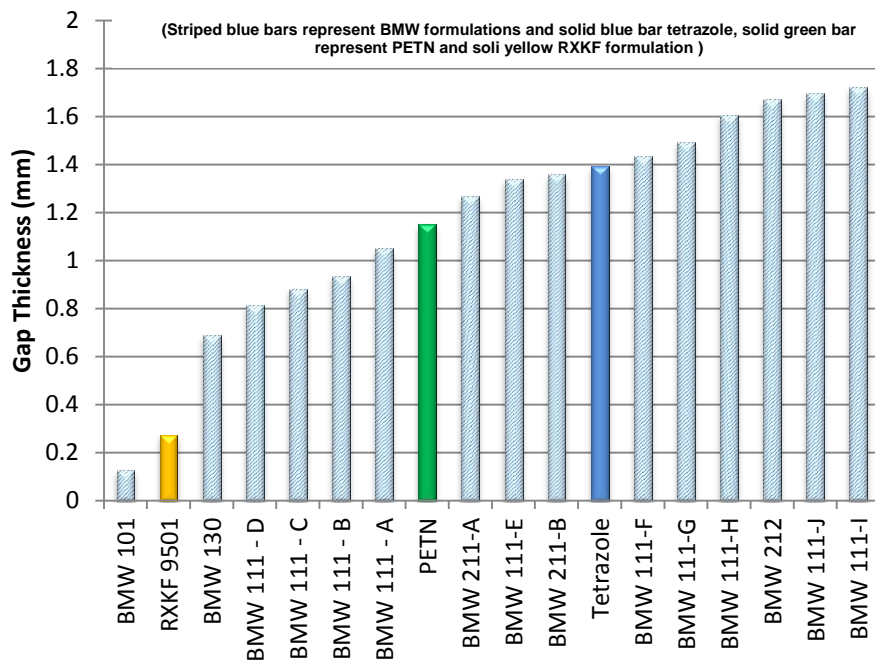


Figure 4.37: Pressable PBX formulations – SSGT results

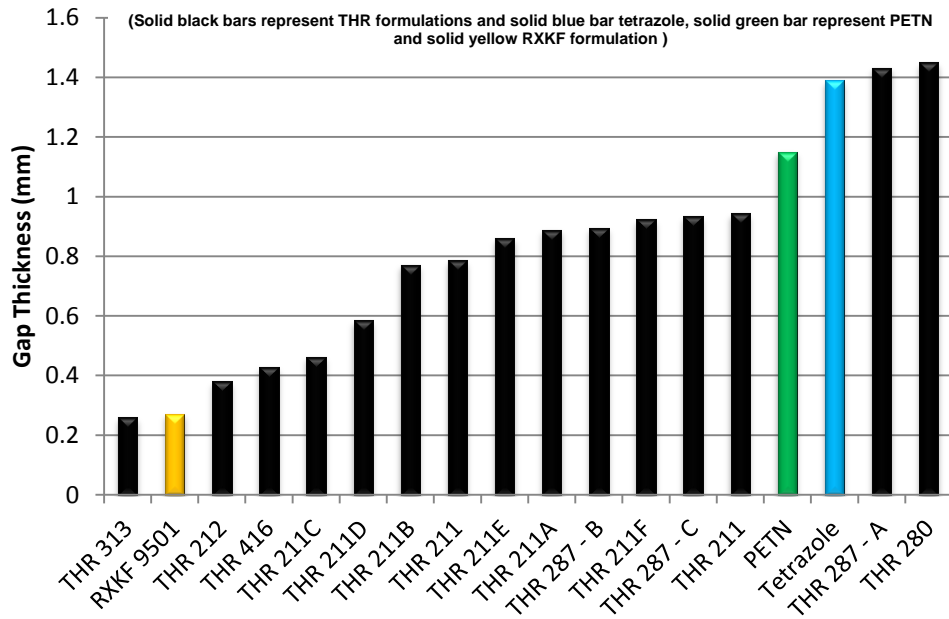


Figure 4.38: Castable PBX formulations – SSGT results

4.4.5.2 Results: Friction sensitivity

The friction sensitivity results are shown in Figure 4.39.

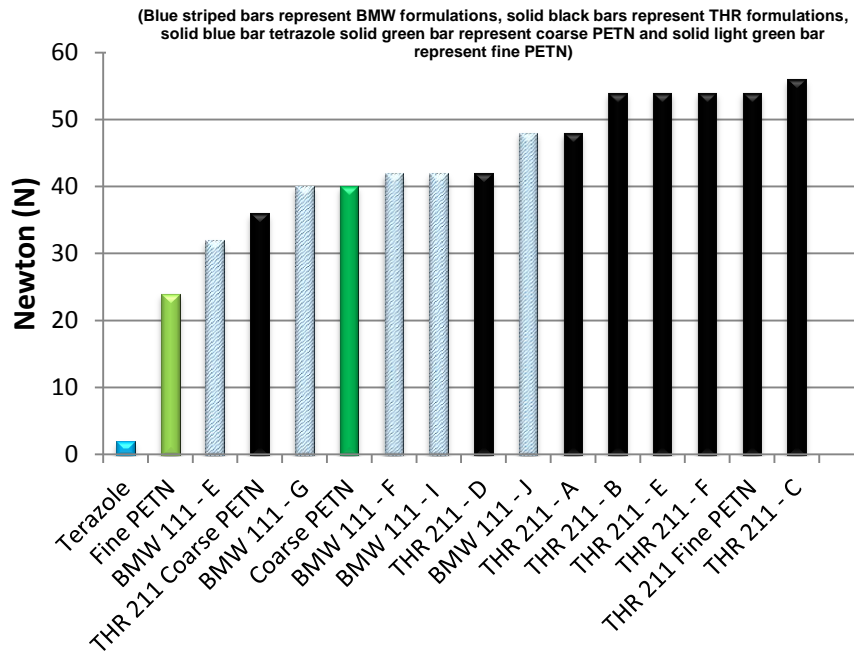


Figure 4.39: Friction sensitivity results

Striped bars represent the pressable PBX formulations and black bars represent the castable PBX formulations

4.4.5.3 Results: Impact sensitivity

The impact sensitivity results are shown in Figure 4.40

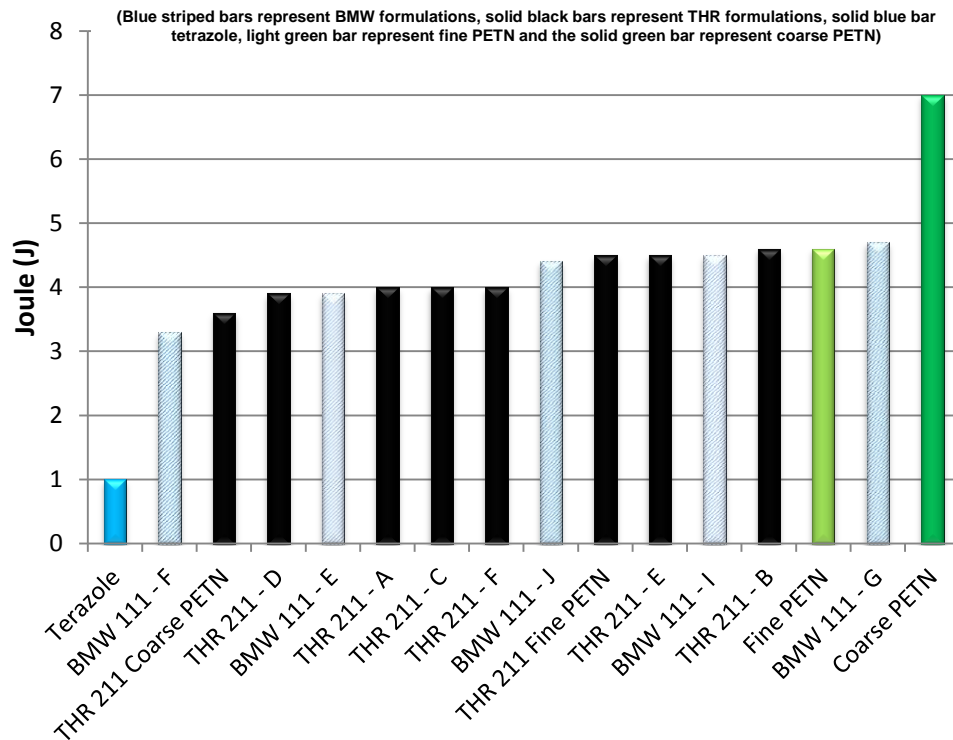


Figure 4.40: Impact sensitivity results
Striped bars represent the pressable PBX formulations and black bars represent the castable PBX formulations

Impact and friction sensitivity results are tabulated in Appendix 4E.

4.4.5.4 Results: Differential scanning calorimetry

DSC results for PETN are shown in Figure 4.41. Results for BMW 111-I and THR 211-F are shown in Figures 4.42 and 4.43.

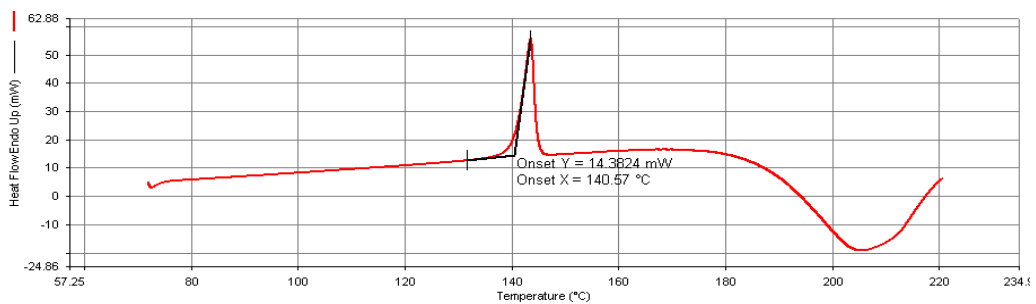


Figure 4.41: DSC results for PETN

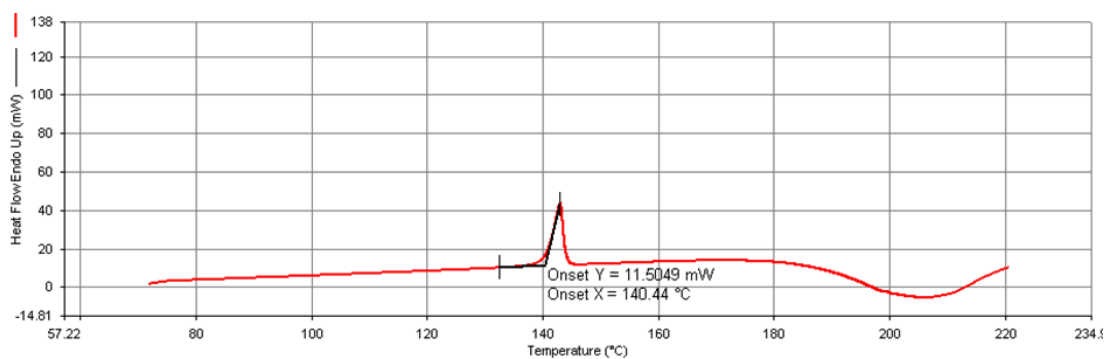


Figure 4.42: DSC results for BMW 111-I

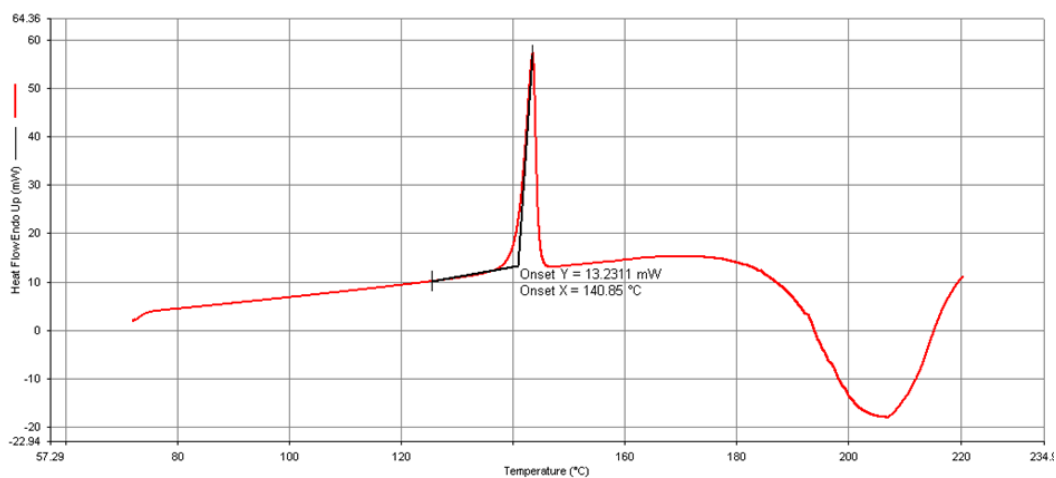


Figure 4.43: DSC results for THR 211-F

4.4.6 PBX-based explosives formulation test and evaluation – Discussions

The small-scale gap test (SSGT) results show an increase in sensitiveness with an increase in PETN particle size. PBX explosive formulations using coarse PETN have a higher sensitivity than explosive formulations using fine PETN particle. Where combinations of particle sizes are used, the same trend is noted. The higher the load percentage of coarse PETN particles in the powder, the more sensitive the formulation is.

Friction sensitiveness result demonstrate a tendency of formulations to be more sensitive as the particle size of the PETN decreases. Tetrazole formulation evaluated is shown to be very sensitive to friction and this is expected.

Impact sensitiveness result show formulations containing coarse PETN to be significantly less sensitive compared with formulations containing fine PETN. Tetrazole again proved to be the more sensitive formulation. The previous three paragraphs also

showed a decrease in binder content resulting in an increase in impact and friction sensitivity. In an attempt to increase the shock sensitivity of PETN, a formulation was prepared mixing PETN with copper tetrazole (THR 287 series of PBX formulations). In the small- scale gap test formulation, THR 280 tested for the most shock sensitive castable PBX formulation. Considering the data of Figures 4.37 and 4.38, pressable PBX formulations (and more specifically the BMW 111 series) tested the most sensitive to shock sensitivity (Figure 4.44). When evaluating the pressable formulations, explosive pellets were pressed with the powders. The pellets were pressed in such a manner to produce a density of 1.55 g.cm^{-3} .

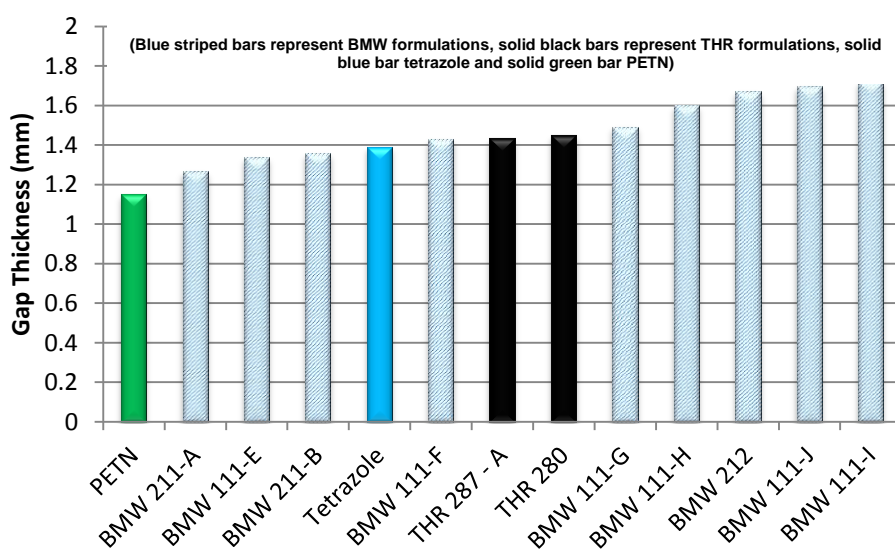


Figure 4.44: Summary of PBX shock sensitivity data

From Figure 4.40, formulation BMW 111 – I is 47.56% more sensitive than PETN and 22.00% more sensitive than the tetrazole formulation tested. Increasing the shock sensitivity of a formulation will ensure improved reliability when used in combination with the developed DDT. It is however vital that such a formulation is still safe to handle. In Figures 4.39 and 4.40, a notable change in the impact and friction sensitivity values of the formulation is seen.

DSC results presented in Figures 4.41 to 4.43 show almost no changes in the onset points of the explosive tested. This is indicative of no changes in the chemical make-up of PETN when formulations were prepared. The formulations can be considered as being stable (ingredients can be seen as being compatible with one another).

4.5 Summary

In this chapter, nano-porous silicon-based explosive formulations were prepared and evaluated. Relative reactivity was introduced as an effective test method to measure

the reactive behaviour of energetic formulations. Pore properties, surface area and type of oxidiser influence the reaction behaviour of npSi explosive formulations. From the results presented, 5-nitriminotetrazole was identified as the oxidiser to be used in combination with npSi. npSi/NT (1 : 3) formulations prepared with nano-porous silicon having an SSA of $180 \text{ m}^2.\text{g}^{-1}$ could be used as a lead-free initiating explosive in the development of a non-metallic explosive initiator.

The development of a PBX that is suitable to be initiated by a shock-to-detonation transfer (SDT) system was achieved. Various PETN-based PBX formulations were prepared and evaluated. From the work presented in this chapter, formulation BMW 111-I has been identified for use in non-metallic initiators, mainly for its pick-up sensitivity.

Chapter 5 describes the development of an explosives initiating system utilising npSi/NT (1 : 3) formulations in combination with PBX explosive formulation BMW111-I.

CHAPTER 5

ADVANCES TOWARDS A LEAD-FREE SILICON-BASED EXPLOSIVES INITIATING SYSTEM

5.1 Introduction

Explosive formulations are designed to perform specific functions. These functions are defined by the intended area of application and desired expectations. In Chapters 3 and 4 the development of new explosive formulations, intended as primary explosive replacement as well as new base charge, was discussed. Explosives are seldom used in application as single components because of sensitivity differences and energy output requirements. In this chapter, the explosives developed and described in previous chapters are combined to function as an explosive system intended to initiate a main explosive charge.

The principle of energy augmentation is applied. In an explosive system the input signal can take different forms:

- Electric power producing heat by Joule effect or sparks, sometimes together with a shock wave in the device itself.
- A heat source or flame.
- Mechanical action, shock or friction, generating heat.
- Shock wave.

In the case of an initiator, this input signal is generally non-pyrotechnic in nature. Mechanical action in the form of percussion, piercing or rubbing, and electrical action could be used to start a detonation reaction. The resultant output signal produced by an initiator can then be:

- a flame resulting from a combustion (or deflagration) reaction,
- a strong detonation shock wave capable of producing the detonation of high explosives.

In this development a similar approach is followed in an attempt to increase the energy of the new initiating system. In the assumed design the new primary explosives developed to replace the conventional lead azide formulation should be sensitive enough to start a high-velocity decomposition reaction (detonation) from the heat generated by the pyrotechnic delay formulation. The new base charge should be sensitive enough to pick up from the output signal generated by the new primary explosive charge and be strong enough to initiate a commercial secondary explosive charge.

In order to develop an effective detonation system, an important characteristic, VoD, needs to be measured. Many techniques can determine VoD; however, measurement over a small distance (10 mm or less) remains a challenge. This chapter furthermore describes a methodology developed as part of the research study to determine explosive characteristics of various formulations in small-scale applications.

5.2 Characterisation of Detonation Pressure in Small-Scale Applications

For many years, small-scale tests have been used to determine explosive characteristics, even though these results were largely qualitative. Explosive power and detonation pressure are two key performance characteristics that define the reactive behaviour of explosives. Explosive performance of an energetic material can be influenced by numerous factors which include particle size, density, morphology and the shape of the explosives charge. When these factors are combined with the variations induced by the experimental test set-up, it is probable that accuracy and repeatability may often be compromised. Experimental evidence for detonation in confined geometry can be the depth and shape of the dent created on a lead witness plate (Cooper, 1996:77). Plate dent tests are commonly used to compare the performance of different energetic materials. The Floret test is an example of a plate dent test and measures the dent produced on a copper witness plate as a result of a detonating explosive (Gagliardi et al., 2005). The depth and shape of the cavity produced on the witness plate are considered to be a semi-quantitative measure of the explosive energy and detonation-spreading divergence characteristics respectively. Further developments of the Floret test led to more quantitative results. One of these methods focuses on indentations created by an acceptor explosive and entails a complex data-acquisition methodology. Similarly the lead plate test produces qualitative experimental evidence for the detonation reaction through the depth and shape of the dent created on a lead plate (Redner, 2010). The depth of the indentation on the lead plate (resulting from the shock wave) can be related to the pressure of the detonation. The width of the cavity at half depth can be interpreted as a function of the detonation wave spreading (Gagliardi et al., 2005). Indentation depth and width can thus be correlated with the energy output of the energetic material.

In materials science, continuous indentation tests permit the amount of penetration of an indenter into a material to be measured. This penetration is a function of an applied load and is commonly used to measure the elastic moduli of materials (Thiruvengadathan et al., 2010:248). A characteristic feature of these indentation experiments is the development of a plastic zone created in the witness plate or block.

Thus combining the theory around the continuous indentation test and explosive indentation test can better describe the indentation profile obtained by the detonating explosives.

5.2.1 Experimental design

Initiators consisting of metallic shells were prepared to contain different explosive formulations for analysis. Explosive mass was kept constant at 400 milligrams (mg). After the explosive formulations were dosed into the shells, the explosive materials were consolidated at different pressure intervals in order to obtain different explosive densities. Copper shells were used as the standard carrier into which the explosive formulations were dosed before being consolidated (Figure 5.1). A second initiator was positioned on top of the test explosive charge. The second initiator is used to initiate the test explosive. This test configuration is shown in Figure 5.1.

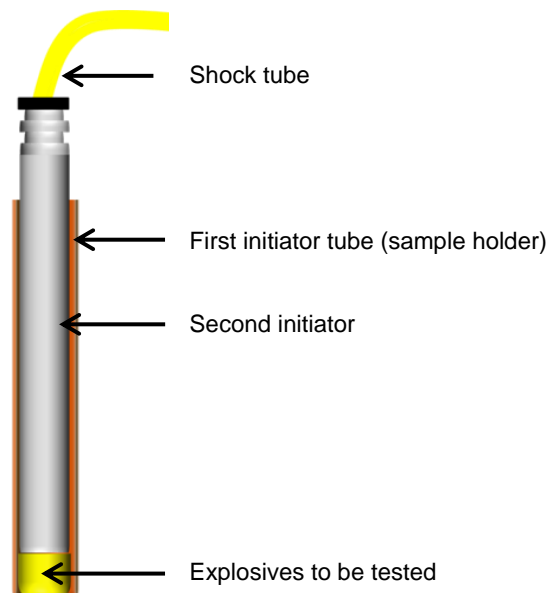


Figure 5.1: Initiator set-up showing the explosives to be tested and the initiating detonator

The filled initiator was then positioned on top of a 10 mm hardened sphere. This sphere was machined to have a flat surface with a diameter similar to the outside diameter of the initiator. The 10 mm sphere and initiator were then positioned on top of an aluminium witness block. Aluminium grade 6082 was used as the material of choice for the witness block.

In order to ensure that the initiator and sphere were perpendicular to the witness block, the initiator and sphere were positioned inside a plastic holder. Figure 5.2 shows the complete experimental set-up for conducting the ball indentation tests.

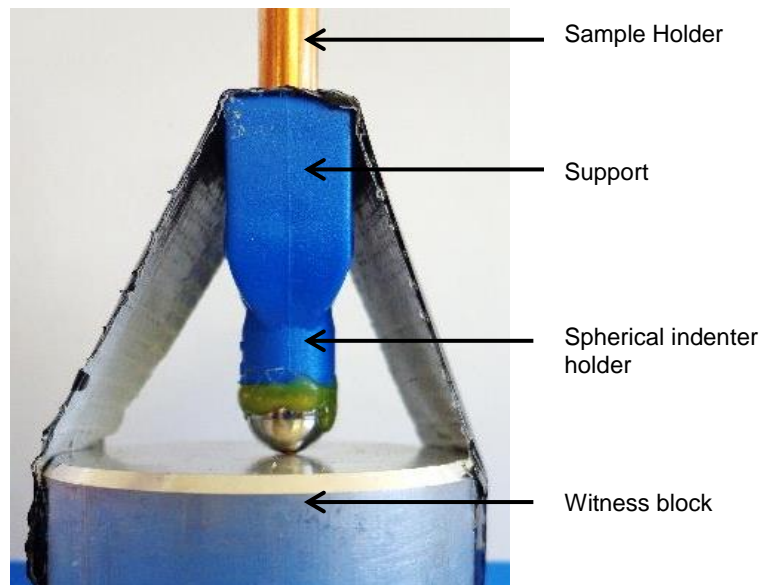


Figure 5.2: Typical ball indentation set-up

The diameters of the indentations obtained during the ball indentation test were measured using an optical light microscope. Barbato and Desogus (1986:145) referred to optical methods used to measure the indentations obtained when performing the Vickers and Brinell tests (indentation tests performed to measure hardness characteristics of materials). They concluded that the effects arising from using different optical microscopes were not taken into account and thus questioned the accuracy of measurements taken (Barbato & Desogus, 1986:145). A multiple of variables was present in the test set-up used in this evaluation. The mass of explosive, the height of the explosive after consolidation, and the density were all measured to two decimal point accuracy. Considering these parameters, the use of an optical light microscope to measure indentation diameter was accepted as an appropriate means to measure indentation depth.

Brinell observed that the mean indentation pressure generally increased during penetration whereas the ratio of force-to-surface area of the indentation was nearly constant. This proportionality coefficient depends on the work hardening of the material giving negative values (sinking-in type impressions) for materials with high work hardening (Richmond et al., 1974:75). The work hardening effect would thus be visible in the profile of the impressions obtained. Raised lip impressions were obtained for all the tests conducted (Figure 5.3) in this work.

Assuming that work hardening did not occur in this test and that indentation pressure generally increased with penetration, other possible effects that could influence the indentation profile were considered to be negligible. These possible influences were considered having no effect on the indentation profile.

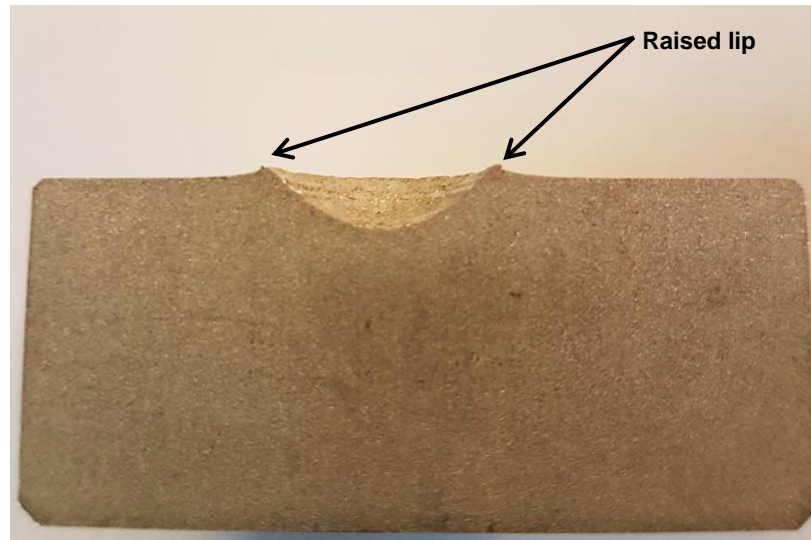


Figure 5.3: Raised lip indentation indicating no work hardening of witness block

5.2.2 Mathematical evaluation

The methodology described in this section was developed to determine the detonation pressure of PETN by measuring sphere indentation profiles on aluminium witness blocks. PETN was selected as the set standard because most of its detonation characteristics are well described in literature. The logic flow followed is given in Appendix 5A.

Experiments performed resulted in indentations being obtained on aluminium witness blocks. After measuring the diameters of these indentations and analysing the data, no realistic relation could be found between the depth of the indentation and the measured diameter. The elastic behaviour of the witness block could be the most probable explanation for this discrepancy in the indentation diameter / depth relation. In this study the diameter of the indentation was taken as the most accurate dimension instead of the indentation depth. However realising the significance of indentation depth, it was postulated that $h = f(s)$ (Figure 5.4). From the measured diameter the theoretical indentation depth (hereafter theoretical height) was determined. The theoretical height (h) was calculated using Equation 5.1 (Figure 5.4).

$$h = \frac{s}{2} \tan \frac{\alpha}{4}$$

Equation 5.1

where (s) is the measured indentation diameter and (a) the top angle formed by the triangle created by (s), the bottom length and the two sides being equal to the radius of the indenter.

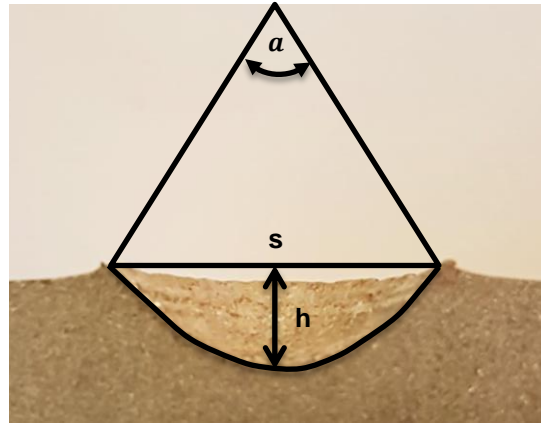


Figure 5.4: Schematic description of Equation 5.1

The theoretical height (h) calculated could be argued to be the height of the segment of a circle. This approach allowed for the elastic deformation of the witness block and a more realistic height could be determined.

Using the theoretical height (h) and the measured diameter (s) of the indentation, the contact area (φ) was calculated. The contact area denoted the area of contact between the indenter (sphere) and the indentee (witness block) at maximum depth (theoretical height (h)).

The indentation was three-dimensional and assumed the profile of a segment of a sphere. The contact area was the area of the segment of a sphere minus the area of the circle (top of the segment of the sphere). In Equation 5.2, (φ) denotes the calculated contact area, (h) is the theoretical height, and (r) the radius of the measured diameter (s).

$$\varphi = 2\pi sh - \pi r^2 \qquad \text{Equation 5.2}$$

The indentation on a witness block could be formed when applying energy for a certain period of time. The amount of energy and the dwell time of the sustained energy could

contribute to the depth of the indentation observed. During a detonation process, energy retention is normally a function of the geometry and environment of application of the explosive in question. Different models existed that could be used to allow for energy losses due to lack of confinement as well as other factors. The cylindrical charge driving plate principle is a Gurney model used to determine the velocity of a fragment accelerated from the end of a cylindrical charge as described by Cooper (1996:391). Other models outlined velocity predictions of fragments accelerated from unconfined and confined explosives charges (Johansson & Persson, 1970:105). The Gurney model was the first step in determining the fragment velocity and subsequently the time of reaction. However, the Gurney model produced questionable fragment velocities rendering it unfeasible for the purpose of this evaluation.

Johansson and Persson (1970:106) reported that the detonation front of the receptor charge (in this case the test explosive charge) was likely to emanate from the interior of the charge, retaining a distance from the outer surface of the charge. This distance would, however, be a critical value dependent on the explosive and charge diameter. In the experimental set-up for this study, the charge diameter was approximately three times the critical diameter of the explosive used and the initiating explosive was of such significant mass that the transfer of initiation would happen almost instantaneously. Based on this argument, it was claimed that the test explosive reacted fully. Hence the duration of the reaction time (t_r), could be assumed to be equal to the duration of the detonation reaction of the test explosive. The time (t_r) of reaction, was then calculated using the theoretical velocity of detonation (V_{oD_t}) with the actual (measured) height (h_e) of the explosive column (Equation 5.3).

$$t = \frac{h_e}{V_{oD_t}} \quad \text{Equation 5.3}$$

Using Newton's motion equations, acceleration (ω), was determined. The displacement into the witness block, the theoretical height determined earlier (h), (t_r) was the time taken for the reaction of the explosive to complete. (v) was the initial velocity of the indenter and taken as nil (assuming the metal sphere was stationary upon application of the detonation energy). The sphere changed from a stationary position to a position where it travelled at a maximum velocity in the witness block. Hereafter it decelerated again until it reached a point where it no longer had moved. The acceleration (ω) determined was thus a normalised acceleration over a specific time (t) and distance (h).

$$h = vt + \frac{1}{2}\omega t^2 \quad \text{Equation 5.4}$$

The force (F) that was applied during the detonation could be determined by:

$$F = M\omega \quad \text{Equation 5.5}$$

(M) was the mass of the sphere in kg, (ω) was the acceleration obtained from equation 5.4. The detonation pressure (P) in Pascal was determined by Equation 5.6.

$$P = \frac{F}{\phi} \quad \text{Equation 5.6}$$

5.2.3 Results

PETN charges of different densities were prepared and fired on a witness plate. Densities of the PETN were calculated using mass of the PETN divided by the volume the PETN occupies. The indentation diameters of 35 repetitions of different densities evaluated were measured. Actual results obtained are shown in Appendix 5B. The average results obtained are given in Table 5.1.

Table 5.1: Indentation diameters of witness plate on charging PETN at different densities

Density (g.cm ⁻³)	Indentation diameter (mm)
1.03 ^{±0.02}	5.50 ^{±0.04}
1.21 ^{±0.02}	5.64 ^{±0.09}
1.30 ^{±0.04}	5.87 ^{±0.06}
1.33 ^{±0.04}	5.92 ^{±0.08}
1.51 ^{±0.04}	6.23 ^{±0.10}
1.66 ^{±0.05}	6.42 ^{±0.08}

Density ranges of 1.10 to 1.60 g.cm⁻³ were intended but measured densities after filling varied as shown in Table 5.1. A linear relationship between indentation diameter and density was observed (Figure 5.5).

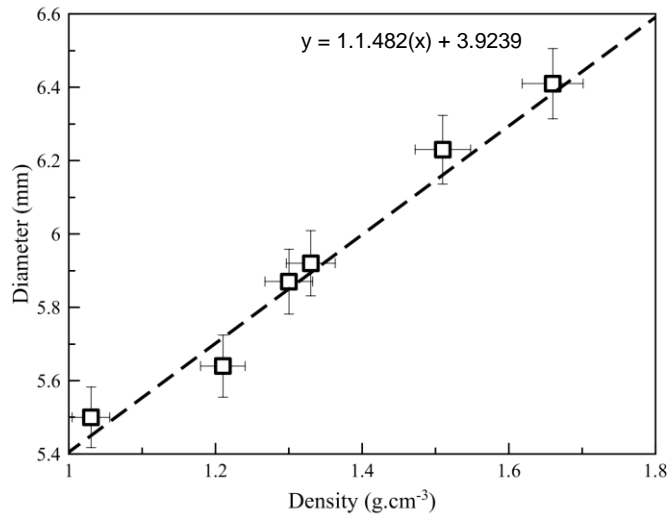


Figure 5.5: Indentation diameter as a function of explosives density

To determine the VoD at selected density the Urizar equation (Equation 5.7 (Cooper, 1996:77)) was used.

$$VoD = 1.5 + \rho \left(\frac{VoD_{TMD} - 1.5}{\rho_{TMD}} \right) \quad \text{Equation 5.7}$$

This gave theoretical VoD at the different densities. Theoretical maximum density (TMD) and related detonation velocity were obtained from Cooper (1996:79). The theoretical maximum density for PETN is 1.78 g.cm⁻³ and the related VoD is 8.59 km.s⁻¹. Theoretical VoDs were calculated and are given in Table 5.2. The data had shown a linear relationship between density and VoD. This VoD was used to determine the related detonation pressure according to Equation 5.8 as described by Cooper (1996).

$$P_{cj} = \frac{(\rho) VoD^2}{4} \quad \text{Equation 5.8}$$

The related detonation pressures are shown in Table 5.3. This data is used later as reference to describe the Ballistic Ball Indentation (BBI) model.

Table 5.2: PETN density and related VoD according to the Urizar equation

Density (g.cm ⁻³)	VoD (km.s ⁻¹) (Calc.)
1.03 ^{±0.02}	5.60
1.21 ^{±0.02}	6.32
1.30 ^{±0.04}	6.68
1.33 ^{±0.04}	6.80
1.51 ^{±0.04}	7.52
1.66 ^{±0.05}	8.11

Table 5.3: PETN detonation pressures related to VoD

Density (g.cm ⁻³)	VoD (km.s ⁻¹) From Urizer eq.	Detonation pressure (GPa) (Calc.)
1.03 ^{±0.02}	5.60	8.08
1.21 ^{±0.02}	6.32	12.08
1.30 ^{±0.04}	6.68	14.49
1.33 ^{±0.04}	6.80	15.36
1.51 ^{±0.04}	7.52	21.32
1.66 ^{±0.05}	8.11	27.31

5.2.4 Postulated mathematical methodology – Results

Indentations obtained on aluminium witness blocks were measured using an optical light microscope (Zeiss Discovery). The indentation diameters were used in Equations 5.1 to 5.6 in order to reach a pressure. Results are shown in Table 5.4.

Table 5.4: Postulated methodology results

Density (g.cm ⁻³)	Height (m) x 10 ⁻³	Contact area (calc.) (m ²) x 10 ⁻⁵	Time (s) (calc.) x 10 ⁻²	Deceleration (calc.) (m.s ⁻¹)	Force (N) (calc.)	Pressure (Pa) x 10 ³ (calc.)
1.03 ^{±0.02}	0.824 ^{±0.02}	2.8	0.195	433.66	1.64	57.9
1.21 ^{±0.02}	0.871 ^{±0.02}	3.1	0.154	733.45	2.79	90.3
1.30 ^{±0.04}	0.952 ^{±0.02}	3.5	0.137	1017.62	3.87	110.1
1.33 ^{±0.04}	0.970 ^{±0.02}	3.6	0.132	1121.95	4.26	118.1
1.51 ^{±0.04}	1.080 ^{±0.02}	4.3	0.103	2047.46	7.78	182.5
1.66 ^{±0.05}	1.164 ^{±0.02}	4.7	0.083	3349.59	12.72	271.4

When determining the pressure given by Equation 5.6, it was found that it differed from the theoretical detonation pressure given by Equation 5.8. The reasons for this could be ascribed to many factors. The profile of the ball was seen to have the biggest influence in creating a crater or indentation in the witness block. Another area of concern was the actual indentation. It was not clear how much material had deformed and how much influence the elastic region of the plate had on the actual profile that was measured. Deformation of the ball was also to be expected. From this it was evident that energy loss due to experimental process was inevitable. In order to compensate for this, a more holistic approach was adopted instead of scrutinising every parameter.

First, the theoretical detonation pressure was divided by the pressure obtained from the experimental indentation diameter and by doing so a correction factor was obtained for each PETN sample at different density that was evaluated. The results are shown in Table 5.5.

Table 5.5: Correction factor related to density

Density (g.cm ⁻³)	Experimental pressure (MPa)	Theoretical pressure (P _{ci}) (GPa)	Correction factor X 10 ⁻⁶
1.66 ^{±0.05}	0.271 ^{±0.025}	27.31	9.9383
1.51 ^{±0.04}	0.183 ^{±0.019}	21.32	8.5630
1.33 ^{±0.04}	0.118 ^{±0.014}	15.36	7.6886
1.30 ^{±0.04}	0.110 ^{±0.012}	14.49	7.5979
1.21 ^{±0.02}	0.090 ^{±0.019}	12.08	7.4733
1.03 ^{±0.02}	0.058 ^{±0.015}	8.08	7.1583

This data was plotted and the polynomial function (γ) (Equation 5.9) was determined using a graphing program (GRAPH version 4.4.2).

$$BBI_{cf} = (3.6752 * 10^{-6} * x^2) - (4.1080 * 10^{-5} * x) + 0.000122 \quad \text{Equation 5.9}$$

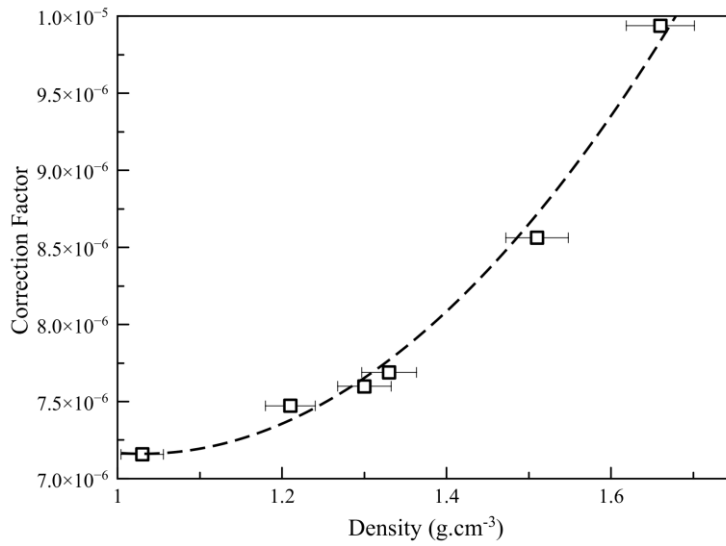


Figure 5.6: Correction factor as a function of density

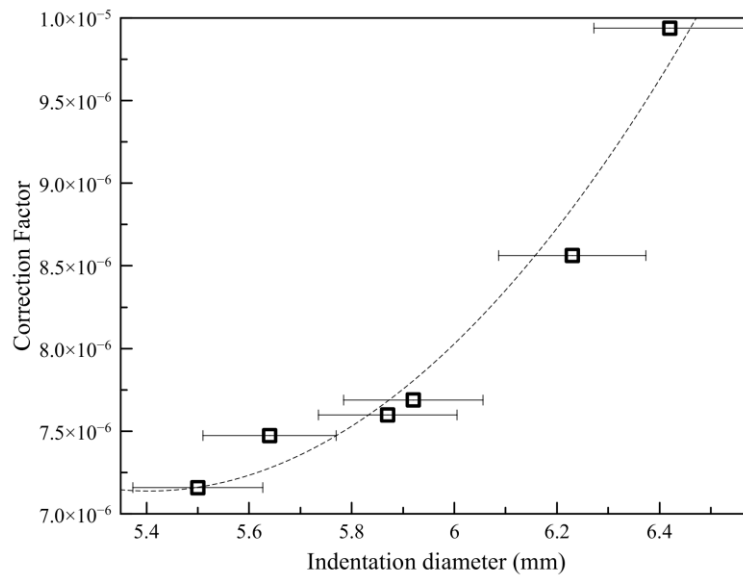


Figure 5.7: Correction factor as a function of indentation diameter

Equation 5.6 was rewritten to include the correction factor as Equation 5.10 and can now be used to determine the detonation pressure (CJ pressure) of PETN experimental indentation diameter.

$$P = \frac{F}{\varphi} / \gamma$$

Equation 5.10

where

$$F = M\omega$$

$$\varphi = 2\pi sh - \pi r^2$$

$$\gamma = (3.6752 * 10^{-6} * x^2) - (4.1080 * 10^{-5} * x) + 0.000122$$

(x = the indentation diameter)

Table 5.6: Corrected detonation pressures

Density (g.cm ⁻³)	Experimental pressure (MPa)	Theoretical pressure P _{cj} (GPa)	Corrected pressure (GPa)	% Deviation from theoretical pressure
1.66 ^{±0.05}	0.271 ^{±0.025}	27.31	27.85	1.94
1.51 ^{±0.04}	0.183 ^{±0.019}	21.32	20.94	1.76
1.33 ^{±0.04}	0.118 ^{±0.014}	15.36	15.52	1.03
1.30 ^{±0.04}	0.110 ^{±0.012}	14.49	14.69	1.36
1.21 ^{±0.02}	0.090 ^{±0.019}	12.08	12.51	3.44
1.03 ^{±0.02}	0.058 ^{±0.015}	8.08	8.00	0.99

A method has been successfully developed in this study to determine selected detonation parameters of new and existing explosives formulations.

5.3 New Intermediary Detonation Transfer System

Development of an intermediary detonating transfer system (IDTS) has been designed in this study to replace the conventional lead azide-containing detonator systems. A 2D detonator was used as reference since this was one of the smallest commercial detonators. The 2D detonator nominally contains 150 mg lead azide and 22 mg PETN in an aluminium shell.

Nano-porous Si-based explosive compositions in combination with nitriminotetrazole were used as main explosive components for this system. The aim of this IDTS was to reliably initiate a secondary explosive system used as base charge in the novel non-metallic initiating system.

It is important to highlight here that in Chapters 3 and 4 the development and evaluation of different lead-free explosives formulations were described. Chapter 5 builds on various results progressing towards a lead-free initiating system. Table 5.7 gives the npSi explosive formulation used in this part of the development.

Table 5.7: npSi Explosive formulation

	Description
Development name	STX101 (Silicon Tetrazole Explosives 101)
Formulation	npSi / nitriminotetrazole
SSA of npSi ($\text{m}^2\cdot\text{g}^{-1}$)	180
Ratio (Oxidiser Fuel)	1:3
Relative Reactivity (R_r)	9.93×10^{17}
Relative reactivity at a density of $3.0 \text{ g}\cdot\text{cm}^{-3}$	983.0×10^{17}

5.3.1 Experimental approach

The IDTS consisted of a non-metallic casing filled with explosive formulation composition STX101 at different densities. This was combined with nitriminotetrazole explosive formulations. The aim of this experiment was to determine if the newly developed IDTS could reliably initiate an RDX-based polymeric explosive (RXKF).

The sample holder contained three increments of explosives. The first increment was STX101, followed by two increments of nitriminotetrazole. The explosives were filled into a plastic body PA6/PA66 that was cross-linked with irradiation (PTS-creamide-A/B). The filling geometry is outlined in Figure 5.8.

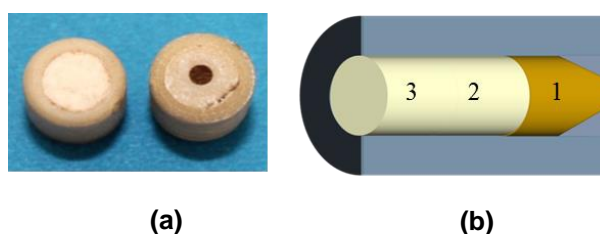


Figure 5.8: IDTS filling geometry (a) – STX101 first increment (b-1) and nitriminotetrazole the bottom two increments (b-2 and b-3)

The filled casing containing the explosives was then placed on top of an RXKF explosive charge. The IDTS in this set-up was the donor charge and the RXKF was the acceptor charge. The combined configuration was placed on an aluminium witness plate (Figure 5.9). The IDTS was placed inside a polymeric body to assist with ignition from different energy sources. The IDTS was initiated with input energies provided by:

- Fusehead
- Pyrotechnic delay element
- Shock tube

Angled aluminium was used for this to witness both the bottom output and side output of the explosive configuration.

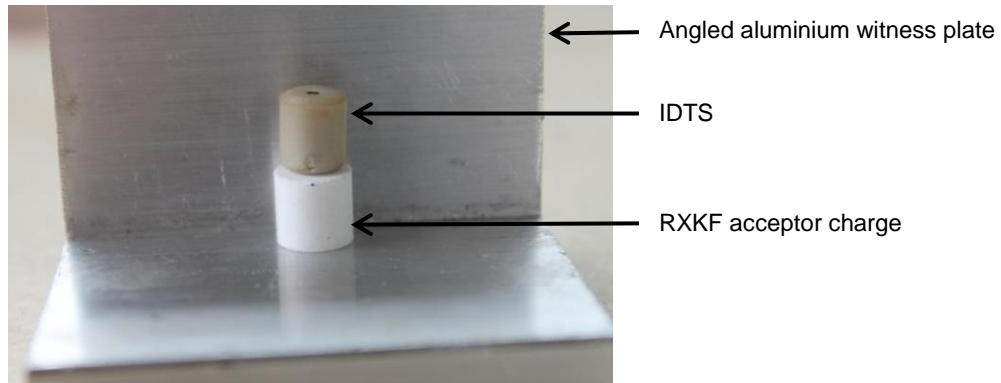


Figure 5.9: Initiation transfer test set-up showing the RXKF acceptor (bottom) and IDTS at the top

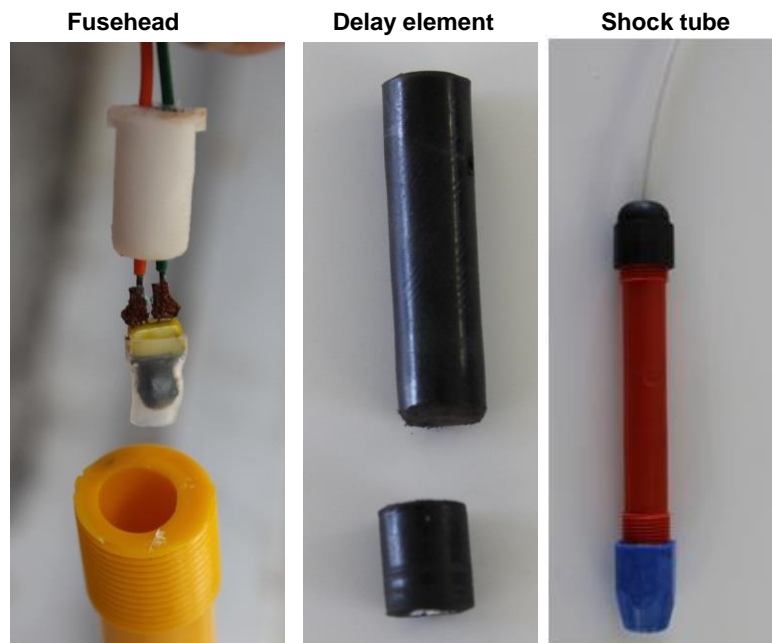


Figure 5.10: IDTS methods of initiation (Fusehead – left; Delay element – middle; shock tube – right)

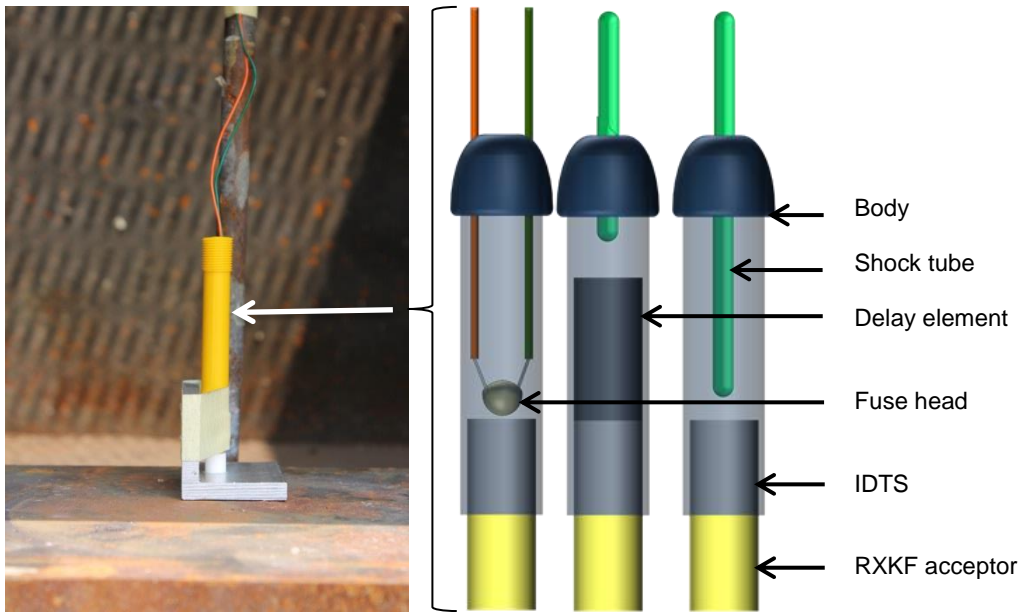
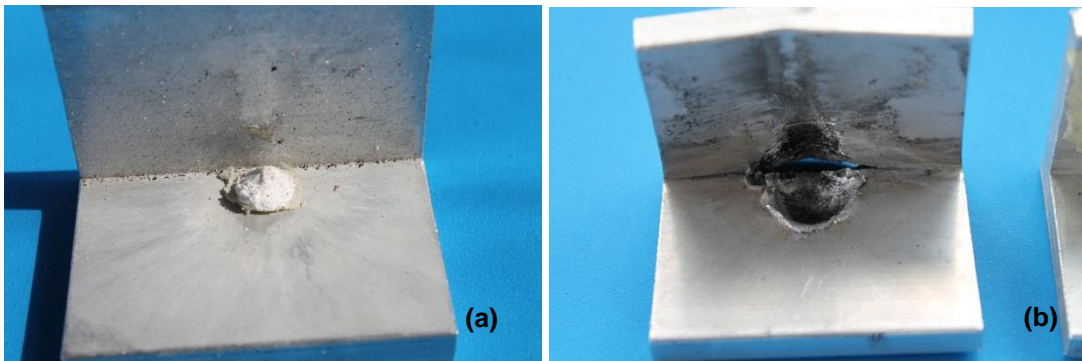


Figure 5.11: Typical set-up of a complete transfer test

5.3.2 Results and analysis

Results obtained are shown in Table 5.8. For the transfer system to pass the test, a clear indentation on the witness plate was established as a reference point.



**Figure 5.12: Transfer test results
A typical fail result (a) and a typical pass result (b)**

Table 5.8: IDTS transfer test results – fuse head initiated

Tests	Explosive increment	Density (g.cm ⁻³)	Explosives mass (g)	No. of repetitions	Pass %
1	STX101	1.00 – 1.09	0.041 – 0.042	10	0
	Tetrazole 1	1.90 – 2.00	0.075 – 0.080		
	Tetrazole 2	1.40 – 1.50	0.013 – 0.014		
2	STX101	1.45 – 1.55	0.040 – 0.041	10	30
	Tetrazole 1	1.70 – 1.80	0.074 – 0.075		
	Tetrazole 2	1.60 – 1.70	0.034 – 0.035		
3	STX101	1.50 – 1.60	0.023 – 0.024	10	100
	Tetrazole 1	1.45 – 1.50	0.075 – 0.076		
	Tetrazole 2	2.10 – 2.20	0.050 – 0.060		

Table 5.9: IDTS transfer test results – delay element initiated

Tests	Explosive increment	Density (g.cm ⁻³)	Explosives mass (g)	No. of repetitions	Pass %
1	STX101	1.00 – 1.09	0.041 – 0.042	10	0
	Tetrazole 1	1.90 – 2.00	0.075 – 0.080		
	Tetrazole 2	1.40 – 1.50	0.013 – 0.014		
2	STX101	1.45 – 1.55	0.040 – 0.041	10	10
	Tetrazole 1	1.70 – 1.80	0.074 – 0.075		
	Tetrazole 2	1.60 – 1.70	0.034 – 0.035		
3	STX101	1.50 – 1.60	0.023 – 0.024	10	100
	Tetrazole 1	1.45 – 1.50	0.075 – 0.076		
	Tetrazole 2	2.10 – 2.20	0.050 – 0.060		

Table 5.10: IDTS transfer test results – shock tube initiated

Tests	Explosive increment	Density (g.cm ⁻³)	Explosives mass (g)	No. of repetitions	Pass %
1	STX101	1.00 – 1.09	0.041 – 0.042	10	0
	Tetrazole 1	1.90 – 2.00	0.075 – 0.080		
	Tetrazole 2	1.40 – 1.50	0.013 – 0.014		
2	STX101	1.45 – 1.55	0.040 – 0.041	10	0
	Tetrazole 1	1.70 – 1.80	0.074 – 0.075		
	Tetrazole 2	1.60 – 1.70	0.034 – 0.035		
3	STX101	1.50 – 1.60	0.023 – 0.024	10	100
	Tetrazole 1	1.45 – 1.50	0.075 – 0.076		
	Tetrazole 2	2.10 – 2.20	0.050 – 0.060		

5.3.3 Ballistic ball indentation test

Determining detonation characteristics in small-scale environments is challenging and somewhat difficult to achieve without comprehensive equipment. The method described in Section 5.2 aimed at providing a means to determine selected explosive

characteristics by a small-scale test method. This method, however, was limited for the tests conducted with the IDTS and a 2D detonator, as the explosive mass of the two samples differed. Indentations were obtained and diameters were measured.

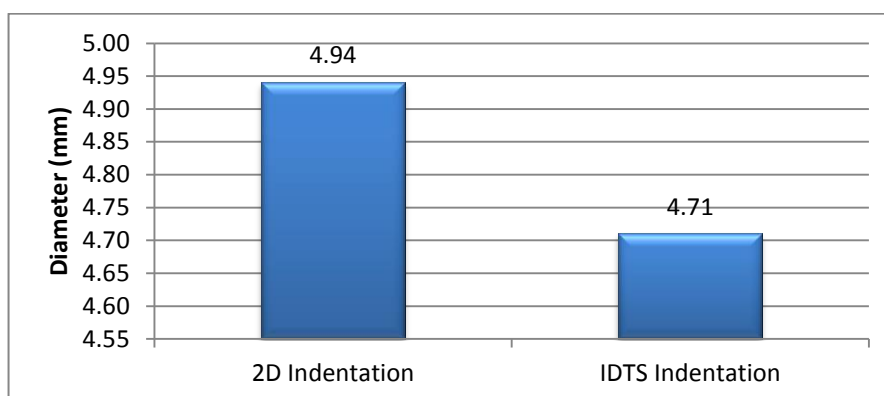


Figure 5.13: 2D and IDTS comparative indentation diameters

The indentation diameters obtained were measured and compared. The indentation diameters had shown a difference of 4.65%, which certainly could be significant. When the explosive masses were compared, a total of 0.150 g for the IDTS and a total of 0.172 g for the 2D detonator were obtained. This translated to a 12.8% difference in explosive mass.

IDTS constructed of npSi-based explosive formulation and nitriminotetrazole proved to generate adequate energy output with regard to detonation pressure to reliably initiate an RXKF base charge. STX101 consistently picked up from different energy inputs, and reliably initiated an acceptor charge even though it had 12.8% less explosive than the comparative 2D system. The newly designed IDTS can thus be utilised as a pick-up charge in an initiating system.

5.4 Detonator Base Charge Explosives

Formulation BMW 111-I, as discussed in Chapter 4, was used in this evaluation. The formulation was pressed at different densities and evaluated with the BBI test developed in this study. Chapter 4 had shown that this formulation was less sensitive to friction and impact than the original PETN used as base charge in traditional initiating systems. It also had shown improved pick-up sensitivity when compared with PETN.

Table 5.11: BMW 111-I formulation

	Description
Development name	BMW 111-I
Formulation	PETN 97.5 % Kraton 2.5 % Graphite 0.5 %
Identification	Malachite green

5.4.1 Ballistic ball indentation test

A similar experimental set-up explained in Section 5.2 was used. Indentations obtained on aluminium witness blocks were measured, using an optical light microscope (Zeiss Discovery). The indentation diameters obtained were used in Equations 5.1 to 5.6 in order to calculate a pressure. Results are shown in Table 5.12.

Table 5.12: BBI results for composition BMW 111-I

Density	Height	Contact area	Time	Deceleration	Force	Pressure
(g.cm ⁻³)	(m) x 10 ⁻³	(m ²) (calc.) x 10 ⁻⁵	(s) (calc.) x 10 ⁻²	(m.s ⁻¹) (calc.)	(N) (calc)	(Pa) (calc.) x 10 ³
1.05 ^{±0.02}	0.783 ^{±0.036}	2.6	0.213	345.80	1.31	49.68
1.31 ^{±0.04}	0.915 ^{±0.035}	3.3	0.144	877.25	3.33	100.52
1.53 ^{±0.04}	1.026 ^{±0.058}	3.9	0.109	1722.83	6.55	16.72
1.69 ^{±0.05}	1.103 ^{±0.077}	4.3	0.091	2666.81	10.13	23.37

Equation 5.10 was subsequently used to determine the detonation pressure (CJ pressure) of composition BMW 111-I by obtaining its indentation diameter. Results are shown in Table 5.13.

Table 5.13: Corrected detonation pressures according to Equation 5.10

Density	Experimental pressure	Corrected pressure
(g.cm ⁻³)	(MPa)	(GPa)
1.05 ^{±0.02}	0.050 ^{±0.015}	6.73
1.31 ^{±0.04}	0.100 ^{±0.012}	13.73
1.53 ^{±0.04}	0.167 ^{±0.015}	20.75
1.69 ^{±0.05}	0.233 ^{±0.025}	26.21

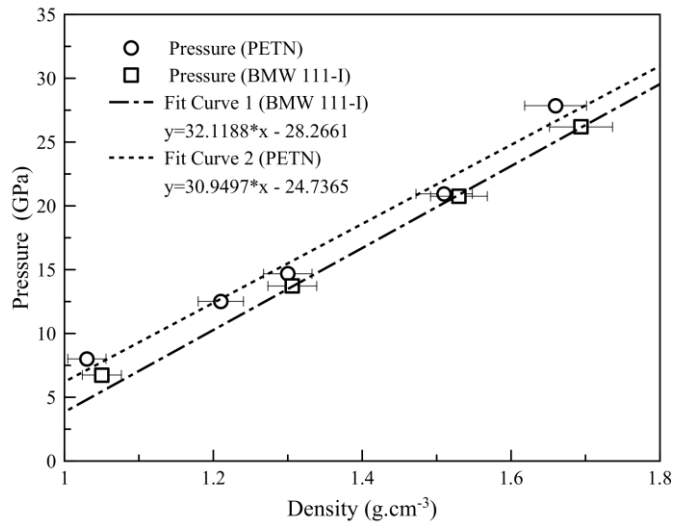


Figure 5.14: Detonation pressures (calculated) for PETN and composition BMW 111-I according to BBI

It is clear from Figure 5.14 that composition BMW 111-I has a lower detonation pressure than PETN. The use of inert binder systems does affect the detonation velocity and detonation pressure negatively. Although the detonation pressure is lower for BMW 111-I compared with PETN, the difference is not that significant. On an average, a difference of 8.3% was calculated.

5.5 Summary

The BBI methodology described in Section 5.2 showed good results in this application. This paves the way to calculate other explosives characteristics such as detonation velocity at different diameters as well as the influence of the casing material on the rate of reaction. This will be addressed in the next chapter.

Explosive formulations described in Chapter 4 were used to construct a detonation transfer system. IDTS constructed of npSi-based explosive formulation and nitriminotetrazole were shown to produce similar output energy upon detonation as the 2D detonator (according to the BBI test). The newly designed IDTS can effectively initiate a plastic bonded base charge and can therefore be used as a pick-up charge in an initiating system.

Chapter 5 has shown that STX101 and BMW111-I can be used to construct an effective explosives train. This explosives train is to be used in a non-metallic casing.

In Chapter 6 non-metallic casing developments are discussed.

CHAPTER 6

NON-METALIC DETONATOR CASING DEVELOPMENTS

6.1 Introduction

Aluminium and copper shells are traditionally used as casing materials in detonator design. These materials are used in shell casing design for ease of manufacturing, material cost, compatibility with detonator assembly technology, and to a lesser extent for confinement.

Typical construction of an aluminium shock tube detonator is shown in Figure 6.1. Two configurations are normally used, namely, an out-hole detonator and an in-hole detonator. When used together, a detonating system is formed. In-hole detonators are used to initiate explosives inside a blast hole in mining operations. Out-hole detonators are used to initiate the shock tube lines connecting different blast holes. A generic detonator system consists of an out-hole detonator that is connected by a piece of shock tube (can vary in length) to an in-hole detonator (Figure 6.2). The out-hole detonator is responsible for conveying the signal (flame and shock) in the shock tube to the next detonator system. This is done by connecting shock tubes (acceptor shock tubes) to the out-hole detonator in a clip specifically designed to hold both the acceptor shock tubes as well as the out-hole detonator. A number of shock tube systems are connected to a single out-hole detonator.

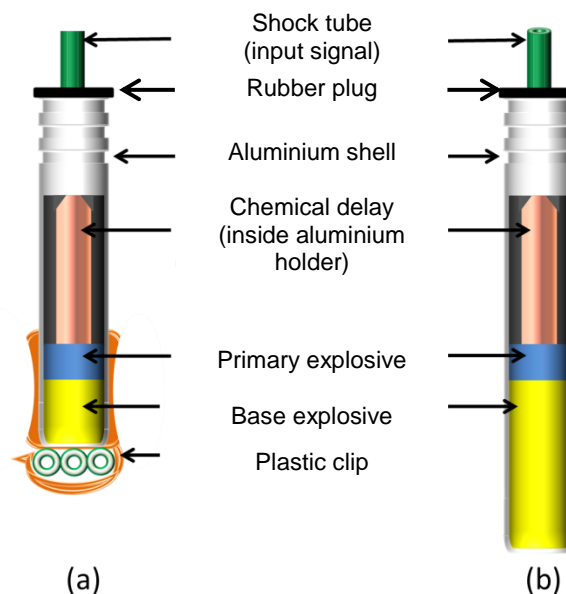


Figure 6.1: Schematic diagram of conventional aluminium shock tube detonator systems. Detonator (a) shows an in-hole detonator and (b) an out-hole detonator

The detonator system functions as follows: An initial shock tube lead-in is initiated with a detonator. Heat and shock are generated by the reacting HMX/Al inside the shock tube. This energy then propagates into a detonator that is connected to the end of the shock tube lead-in line. This detonator is connected to the first detonator system of the blast between the out-hole and in-hole detonators. When the lead-in detonator detonates, it initiates the shock tube of the first system. The energy is carried to the first set of in-hole detonators and simultaneously to the first set of out-hole detonators. Out-hole detonators have a shorter time delay than in-hole detonators to prevent the primary blast from damaging the shock tube blast line. Proper blast design and an effective blast is thus reliant on the functional reliability of the detonators used.

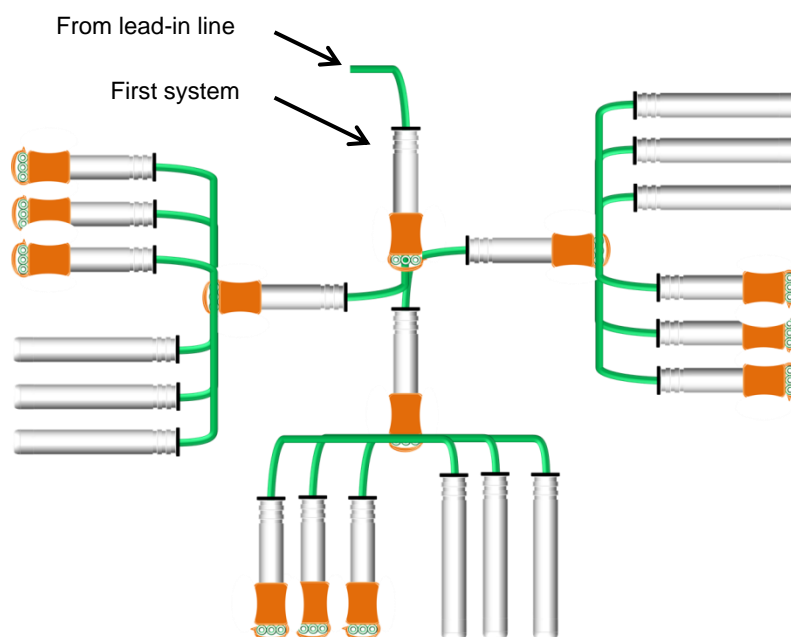


Figure 6.2: A typical detonator system as applied in a mining explosion

Detonator design is built on a solid foundation based on knowledge of explosives and required behavioural characteristics. Explosives' characteristics are influenced by their chemical properties, physical properties and immediate surroundings, e.g., casing or encapsulation. These characteristics influence the reaction velocity of the explosive (velocity of detonation (VoD)) and ultimately the detonation pressure. Cooper (1996:69) show a momentum equation that predicts the Chapman–Jouguet pressure (P_{cj}) of most explosives within an accuracy of 7%. This momentum equation factors in VoD (D) and density (ρ_o) to determine P_{cj} .

$$P_{cj} = \frac{\rho_o D^2}{4}$$

Equation 6.1

The density and diameter of the explosive charge influence VoD and detonation pressure. An effective detonator design is the optimal combination of density and diameter of the explosives charge (considering the effect that confinement or casing the explosive charge is used in has on these parameters).

In this chapter an alternative non-metallic casing design has been proposed. Various tests were performed to determine and evaluate selected casing characteristics. An axial ribbed-shaped design was used to influence the detonation wave characteristics to induce optimally initiation of the main explosive charge.

6.2 Detonator Casing Design: Basic Criteria

Each component in the detonator design has specific functions. The detonator shell provides containment, the rubber plug provides sealing, the shock tube provides the input energy, pyrotechnic mixtures provide the chemical delay and the explosives provide the output energy. An alternative non-metallic design must exhibit the same features. The following components are required to be evaluated / modified in optimising casing design:

- Shock tube holder
- Main body
- Shock tube connector clip
- Booster casing

6.2.1 Materials evaluation

Materials can influence the performance behaviour of explosives. Steel confinement increases the velocity of detonation and is well described in literature (Cooper, 1996; Souers, 1997). Confinement effects using non-metallic materials appear to be less intense. Explosive behaviour can be manipulated by its environment. An understanding of explosive behaviour as a function of length and VoD fluctuations when confined with aluminium, copper, and selected polymeric materials was reached. The results obtained enabled the project to choose a suitable material for construction.

6.2.1.1 Optimal explosives column length evaluations

Explosives require a certain distance to reach stable detonation. Such distance is influenced by the diameter and the density of the explosive charge. Additional to this, the reaction zone length of explosive formulations also influence this distance. The relationship between detonation velocity, diameter of the charge, and reaction zone length as defined by Equation 6.1, was first described by Eyring (1980:2358). Reaction zone length (α) refers to the thickness of the layer in which the chemical reaction takes place. The reaction zone length is obtained by plotting the detonation velocity of

unconfined explosives charges (D_u) against the explosive cylinder's inverse radius ($y=1/R_0$) in mm^{-1} as described by Souers et al. (2004:19). Further to this, Souers et al. (2004:19) stated that this plot became the standard display of the size effects with specific reference to diameter. Cooper (1996:280) added that the detonation velocity asymptotically approached a constant value as the diameter of the explosives charge (d) became larger. This could continue until an ideal detonation velocity or infinite diameter detonation velocity (D_∞) was obtained.

$$\frac{D_u}{D_\infty} = 1 - \alpha \frac{1}{d} \quad \text{Equation 6.2}$$

The reaction zone length is required to determine the effect of confinement on the velocity of detonation of a confined explosives charge (this is described in the next section of this chapter). It is however difficult to determine the reaction zone thickness from experimental data obtained by the diameter relation because of manufacturing challenges. These include manufacturing of explosive pellets of various diameters, varying from very small to extremely large (to a point where stable and repeatable detonation velocity is obtained). An alternative approach is required to determine the reaction zone length as the capability to manufacture explosives at various diameters is lacking.

I. **Scope**

The purpose of this section is not to evaluate differences in witness materials' response when exposed to the energy generated by the reacting explosives, hence material properties are not part of this evaluation. Witness block material is kept constant and the profiles obtained are accepted to be influenced by the energy fluctuations of the explosives column only. Along with these constraints, explosive pellets with a diameter of 7.88 mm were used. This diameter was chosen as this is sufficiently above the critical diameter of the explosives formulation ($4.0 \text{ mm} < \text{critical diameter} > 5.0 \text{ mm}$) identified for this study (Johansson & Persson, 1970:107; Dobratz, 1985:8-17). Although the critical diameter is not known, pre-work towards this study showed reliable detonation in column thicknesses as low as 2 mm, hence the literature value of 4–5 mm was accepted. Moreover, this diameter could be achieved from existing tooling and was largely compatible with available manufacturing capability.

II. **Analysis**

a) **Method**

To determine the influence of explosive column length on the indentation profile on the aluminium witness block, seven different charge lengths were tested. Identifying the optimal means of initiation was crucial, as this would influence run-up distance to

optimal detonation velocity at specific explosives' column length (D_h) in the particular geometry. When working in small diameters with length over diameter ratios <1 , it was important to ensure that the initiator used did not contribute to the indentation obtained in the witness block. Pre-work conducted identified a detonator with low explosive content as the optimal initiator to be used for this type of evaluation. This detonator contained 0.03 g of pentaerythritol tetranitrate (PETN) and 0.160 g of lead azide. The experimental set-up entailed cylindrical RXKF explosives charges, varying in length from 1.99 mm to 30.03 mm, tested on aluminium witness blocks. Each charge was placed vertically in the centre of an aluminium block. A detonator was placed on top of the explosive charge. Post-test, the indentation diameters (d_i) and indentation depths (l_d) of the profiles were measured. A similar set-up was used to measure (D_u) in conjunction with the break wire method to detect time intervals.

Figures 6.3 and 6.4 show the test configuration and the average properties of the different configurations are shown in Table 6.1.

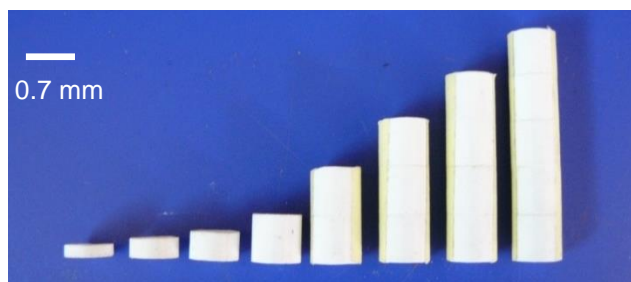


Figure 6.3: Different explosives' charge lengths that were evaluated

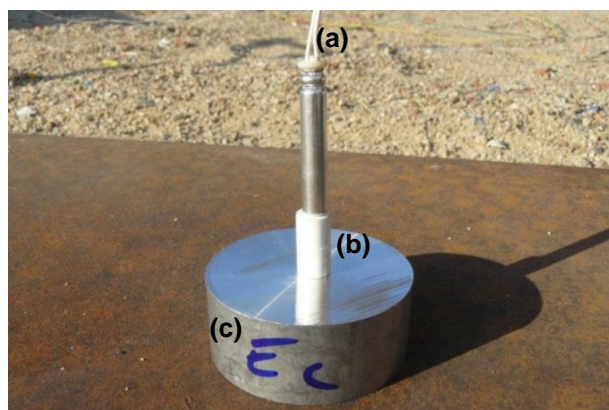


Figure 6.4: Experimental test set-up showing the 2D initiator (a), and the test explosives (b) on top of the aluminium witness block (c)

Table 6.1: Explosive column height evaluations – Properties

Explosive RXKF					
Sample	Height	Diameter	Mass	Density	l/d
	(mm)	(mm)	(mg)	(g.cm ⁻³)	ratio
A	1.99 ^{±0.40}	7.88 ^{±0.05}	161.02 ^{±3.24}	1.66 ^{±0.01}	0.25
B	3.01 ^{±0.21}	7.88 ^{±0.05}	243.55 ^{±16.99}	1.66 ^{±0.01}	0.38
C	4.25 ^{±0.15}	7.88 ^{±0.05}	343.62 ^{±11.88}	1.66 ^{±0.01}	0.54
D	7.51 ^{±0.05}	7.88 ^{±0.05}	607.40 ^{±3.77}	1.66 ^{±0.01}	0.95
E	15.02 ^{±0.08}	7.88 ^{±0.05}	1215.35 ^{±6.48}	1.66 ^{±0.01}	1.91
F	22.59 ^{±0.06}	7.88 ^{±0.05}	1827.87 ^{±4.85}	1.66 ^{±0.01}	2.87
G	30.03 ^{±0.08}	7.88 ^{±0.05}	2429.61 ^{±6.20}	1.66 ^{±0.01}	3.81

b) Results

Indentation diameter results obtained as well as the indentation depth results are shown in Table 6.2.

Table 6.2: Explosive column height evaluations – Results

Sample	l/d ratio	Indentation depth (mm)	Indentation Diameter (mm)
A	0.25	1.34 ^{±0.16}	10.27 ^{±0.29}
B	0.38	1.39 ^{±0.16}	10.74 ^{±0.50}
C	0.54	1.81 ^{±0.16}	12.14 ^{±0.14}
D	0.95	2.42 ^{±0.07}	13.34 ^{±0.22}
E	1.91	2.92 ^{±0.09}	14.21 ^{±0.16}
F	2.87	3.06 ^{±0.23}	14.26 ^{±0.16}
G	3.81	3.06 ^{±0.19}	14.65 ^{±0.16}

The indentation profile was caused by the power of the explosives which was related to the detonation velocity of the explosives. It was argued that the detonation velocity asymptotically approached a constant value as the height of the explosive column became longer. As the indentation depth and diameter approached a constant profile, constant power output of the explosive was accepted. From a constant power output a constant detonation velocity can thus be anticipated. As is the case with detonation velocity related to infinite diameter (D_{∞}), the same argument applied to detonation velocity at infinite height. Table 6.2 has shown that indentation diameter and indentation depth approach a constant value at l/d ratios that are >1. A plot of d_i/H_e

(Figure 6.5) shows that the indentation diameter approaches linearity for explosive column heights greater than 15mm (or l/d ratios that are >1).

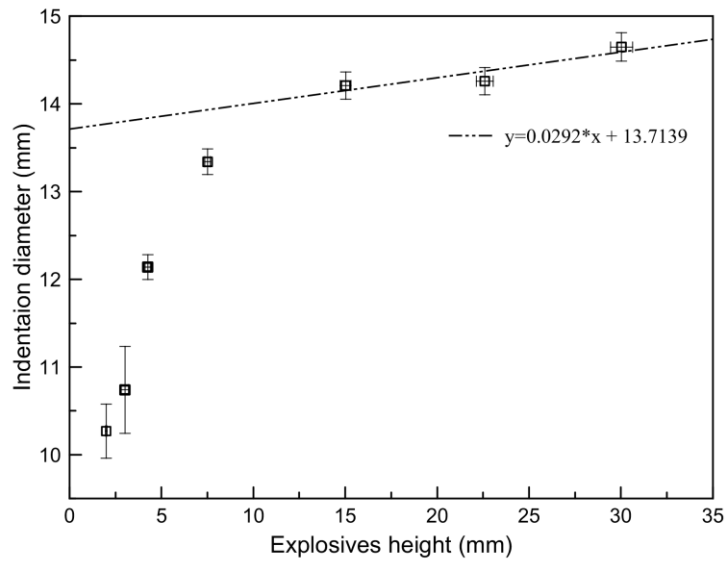


Figure 6.5: Indentation diameter as a function of explosives' height

At the linear section (Figure 6.5) the detonation velocity is by and large constant for the specific density, hence in this region it can be expected that the reaction zone length should be constant. The slope of the linear section of the indentation vs explosives column height plot can not be accepted as a function of the reaction zone length (as this is purely indentation data).

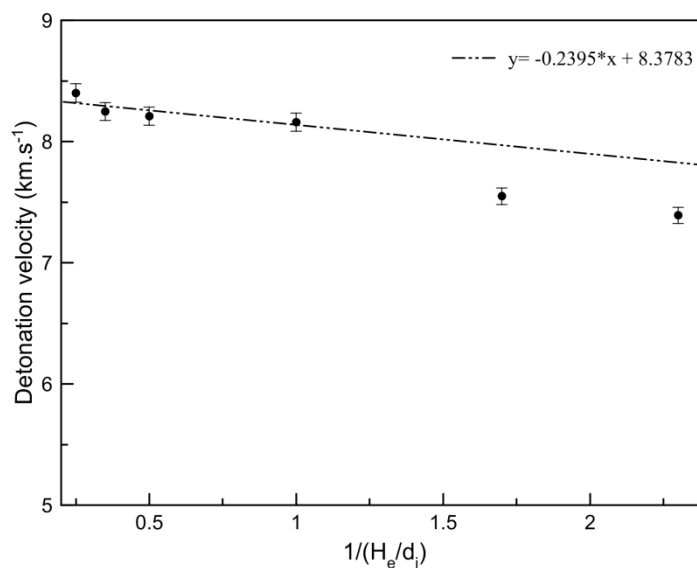


Figure 6.6: Detonation velocity as a function of $1/(H_e/d_i)$ ratio of the explosives column

Detonation velocity vs $1/(H_e/d_i)$ plot (Figure 6.6) also shows a linear section (where the detonation velocity approaches steady state) and the slope of this section is likely to be a function of the reaction zone length. The new value for (α) , now (α_h) , is determined to be 0.2395. Souers (1999:7) reported a reaction zone thickness of 0.22 mm for RDX at a density of 1.67 g.cm^{-3} . Infinite diameter detonation velocity (D_∞) in this approach was adopted to be equal to the detonation velocity at the theoretical maximum density (D_{TMD}). This was also verified by cross-calculating detonation velocities from literature data. D_{TMD} for the explosives composition used in this evaluation (RXKF) was 8.635 km.s^{-1} with a corresponding theoretical maximum density (ρ_{TMD}) of 1.82 g.cm^{-3} . Using the Urizar equation (Equation 6.3), (D_u) was calculated to be 8.359 km.s^{-1} for a column with a density of 1.66 g.cm^{-3} .

$$D_u = 5.50 + \rho \left(\frac{D_\infty - 5.50}{\rho_{TMD}} \right) \quad \text{Equation 6.3}$$

This correlated well with the actual measured detonation velocity average of 8.373 km.s^{-1} . Since this work is conducted at a specific diameter and detonation velocity has been measured, Equation 6.2 can therefore be used to calculate (α) . A value of 0.2391 is obtained for (α) . This value for (α) , compared very well with (α_h) , described earlier as being 0.2395.

From Equation 6.2, using (α) , the detonation velocity for other diameters can be plotted. When (α_h) is used and values in Equation 6.2 are replaced with height instead of diameter, a slight jump in the curve is observed (Figure 6.7; “VoD from Equation 6.2”) compared with “VoD from new (l/d)”. The plot with values obtained from Equation 6.2 shows slightly higher values. However corresponding data with the new reaction zone thickness can be considered comparable to the reaction zone thickness determined from explosive column diameter values. Equation 6.2 cannot be used for values with $l/d < 1$ (Figure 6.7).

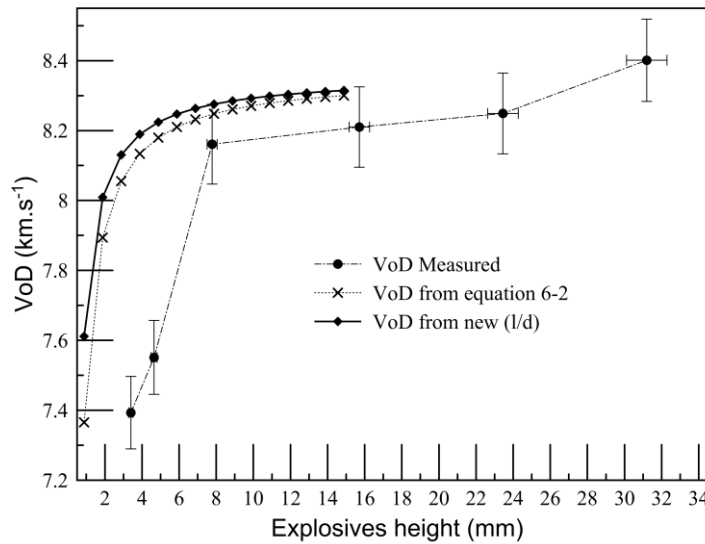


Figure 6.7: Detonation velocity plot from Equation 6.2 with experimental data

Using the data from Table 6.1, an empirical relationship has been derived describing (D_h) to indentation depth (Equation 6.4).

$$\left[\frac{D_h}{d_i}\right]^{-1} = 0.1061 * (\ln H_e) + 1.3901 \quad \text{Equation 6.4}$$

This equation describes the detonation velocity at column length for $H_e/d_i < 1$ and also for $H_e/d_i > 1$. In Equation 6.4, the following variables are catered for: the detonation velocity at height, the explosives' height and the indentation diameter obtained from experimental data. Results obtained from Equation 6.4 are shown in Table 6.3.

Table 6.3: Calculated and measured VoD values from test data

H_e	d_i	H_e/d	Explosives column density measured	H_e For Detonation velocity measurements	D_h Calculated From Eq. 6-4	D_h measured
(mm)	(mm)		(g.cm ⁻³)	(mm)	(km.s ⁻¹)	(km.s ⁻¹)
1.99 ^{±0.40}	10.27 ^{±0.29}	0.25			7.019	
3.01 ^{±0.21}	10.74 ^{±0.50}	0.38	1.66 ^{±0.01}	3.40	7.127	7.393 ^{±0.106}
4.25 ^{±0.15}	12.14 ^{±0.14}	0.54	1.66 ^{±0.01}	4.65	7.865	7.551 ^{±0.135}
7.51 ^{±0.05}	13.34 ^{±0.22}	0.95	1.67 ^{±0.01}	7.78	8.317	8.161 ^{±0.096}
15.02 ^{±0.08}	14.21 ^{±0.16}	1.91	1.66 ^{±0.01}	15.71	8.471	8.210 ^{±0.121}
22.59 ^{±0.06}	14.26 ^{±0.16}	2.87	1.67 ^{±0.01}	23.45	8.287	8.249 ^{±0.118}
30.03 ^{±0.08}	14.65 ^{±0.16}	3.85	1.67 ^{±0.01}	31.2	8.362	8.401 ^{±0.109}

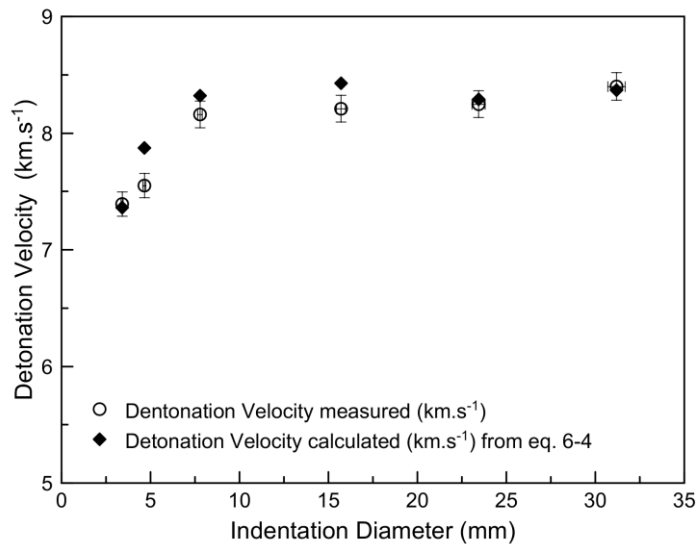


Figure 6.8: Calculated detonation velocity from Equation 6.4

c) Remarks

Data presented in Table 6.3 show a steady-state increase in indentation diameter as well as indentation depth with an increase in length over diameter ratio. It is shown that the indentation depth difference decreases when the length over diameter ratio approaches 1. The results presented show that the optimal power output is obtained when the explosive used has an l/d ratio that is greater than 1. Further to this, a method describing the reaction zone length has been successfully developed and demonstrated in this section.

6.2.1.2 Explosives casing effects

Explosives' characteristics can be influenced by their shape and environment of application. This section aims at describing the influence of polymeric confinement on the detonation velocity of RXKF explosives.

I. Analysis

a) Method

Explosive column diameter and density were kept constant. Three RXKF explosives pellets were used in each test (2.2 g). Copper IED detonators were used to initiate the RXKF explosives columns.

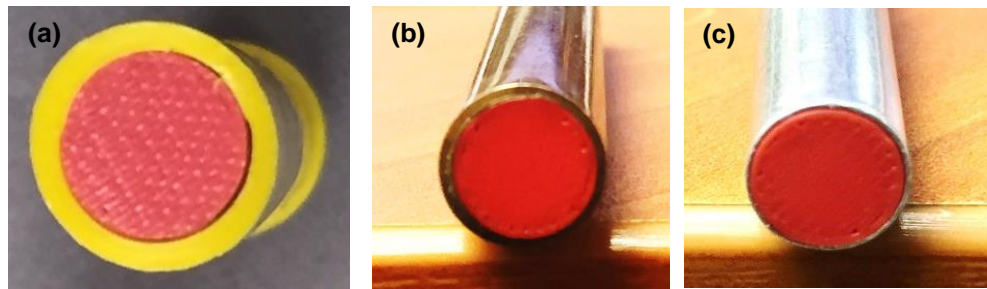


Figure 6.9: RXKF pellets (red) visible inside different casings. Polymeric (a), copper (b) and aluminium confinement (c)

Different materials were used for this evaluation. Table 6.4 gives the list of materials evaluated and the properties of the materials.

Table 6.4: Material properties

	Colour code	Material	Base material	Density	Hardness Shore D	Tensile modulus	
						Tensile strength at yield	Flexural modulus
				(g.cm ⁻³)	Units	(MPa)	(MPa)
1	Orange	PPBF970MO	Polypropylene	0.905	89 Rockwell	27.0	1500
2	Grey	HDPEC2760 + 5% tafmer	High-density polyethylene	-	-	-	-
3	Blue	PBT	Polybutylene terephthalate	1.340	-	56.6–60.0	1930 – 3000
4	Black	PEEK IXEF 1022	Polyether ether ketone	1.640	90	280.0	20 000
5	Clear	PP	Polypropylene	0.905	-	31.0–37.2	1140 – 1550
6	Gold	PPC740 25 RNA	Polypropylene	0.900	58	20.0	900
7	Yellow	HDPE	High-density polyethylene	0.959	-	22.1–31.0	1080

b) Results

Plotting the data in two dimensions gave clear differences in not only the depth but also the width of the indentations. This is clearly demonstrated in Figure 6.10.

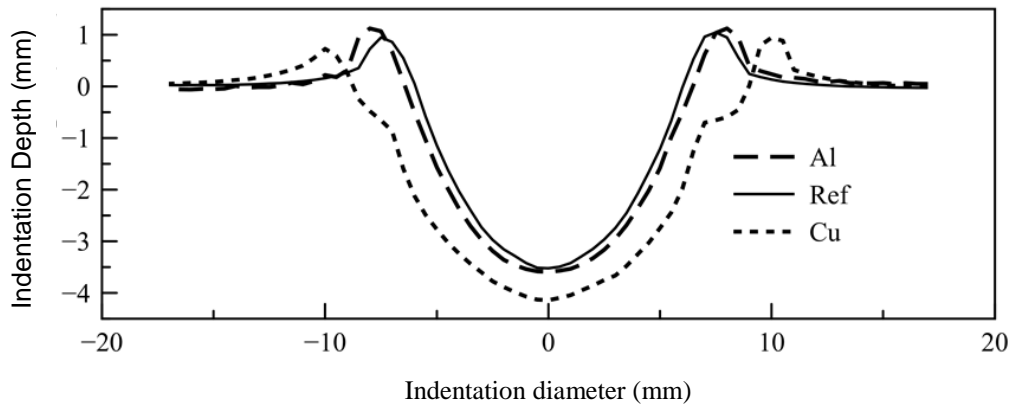


Figure 6.10: Indentation profile obtained for tests conducted with copper and aluminium confinement. The innermost profile represents no confinement

The indentation diameter results obtained and indentation depth results for the tests conducted with thin aluminium, copper and different polymeric confinement, are shown in Figure 6.11. The polymeric results reported in Figure 6.11 are the mean of the indentation results reported in Table 6.5.

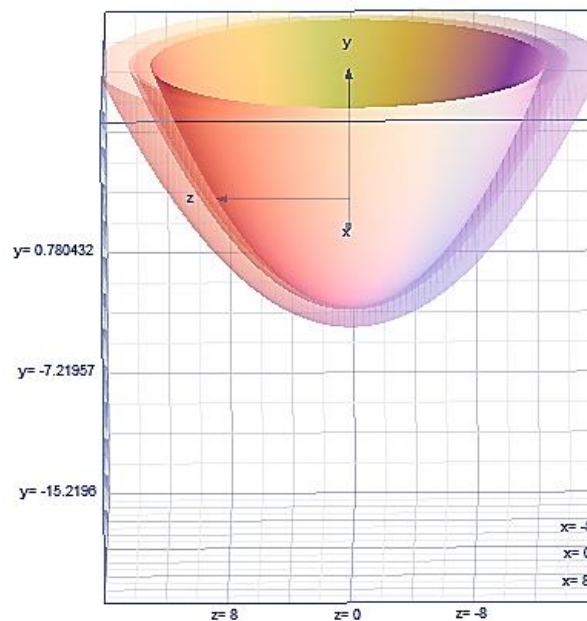


Figure 6.11: Combined profiles. Inner cone represents the reference, the two middle cones represent the polymeric indentation and aluminium indentation, and the outer cone represents the copper confinement

(The two cones in the middle are barely visible. Close inspection focusing on the left of Figure 6.11 best exposes the two cones.)

Table 6.5: Polymeric confinement and indentation profile measurements

Sample	Wall thickness	Indentation depth (measured)	Indentation diameter max (measured)	Indentation diameter extrapolated without shoulder	Modelled Indentation diameter	% Variance (extrapolated vs modelled)
	(mm)	(mm)	(mm)	(mm)	(mm)	
PP BF970MO	2.51 ^{±0.02}	3.41 ^{±0.19}	15.70 ^{±0.21}	13.00	13.27	2.035
HDPE	2.38 ^{±0.03}	3.28 ^{±0.17}	15.38 ^{±0.18}	13.02	13.27	1.880
PP	2.61 ^{±0.01}	3.45 ^{±0.17}	15.89 ^{±0.19}	13.14	13.27	0.980
HDPE C2760 + 5% tafmer	2.30 ^{±0.02}	3.41 ^{±0.18}	15.63 ^{±0.18}	12.96	13.27	2.336
PBT	2.47 ^{±0.02}	3.37 ^{±0.19}	16.40 ^{±0.22}	13.36	13.27	0.674
PEEK IXEF 1022	2.67 ^{±0.01}	3.16 ^{±0.17}	16.91 ^{±0.16}	14.36	13.27	7.591
PP C740 25 RNA	2.37 ^{±0.01}	3.41 ^{±0.19}	15.68 ^{±0.17}	12.78	13.27	3.692

The indentation diameters reported in Table 6.5 have shown a slight difference between the different polymeric confinements used. With the data from Table 6.5, the detonation velocity when confined can be calculated using Equation 6.5.

$$\frac{D_c}{D_\infty} = 1 - 8.7 \left(\frac{W_e}{W_c} \right) \left(\frac{a}{d} \right)^2 \quad \text{Equation 6.5}$$

With (D_c) being the VoD of the confined explosives charge, (D_∞) is the VoD at infinite diameter, (W_e) is the explosives mass, (W_c) is the mass of the casing, (a) is the reaction zone length, and (d) is the explosives charge diameter. Equation 6.5, however, produced inconsistent detonation velocity (under confinement) results. Equation 6.5 was adapted (by dividing the weight of explosives by 10) to give Equation 6.6 in an attempt to obtain a method for determining VoDs for explosives enclosed in thin-walled casings.

$$\frac{D_c}{D_\infty} = 1 - 8.7 \left(\frac{W_e/10}{W_c} \right) \left(\frac{a}{d} \right)^2 \quad \text{Equation 6.6}$$

Results obtained when using Equation 6.6 to calculate (D_c) are given in Table 6.6. Results were also verified with actual measurements involving selected materials. These results are shown in Table 6.7.

Table 6.6: Detonation velocity calculations with adapted confinement equation 6.6

Material	W_e (g)	W_c (g)	α_h	constant	d (mm)	D_∞ (km.s ⁻¹)	D_c (km.s ⁻¹)
PP	1.833 ^{±0.021}	0.763 ^{±0.015}	0.2395	8.7	0.788 ^{±0.010}	8.635	8.468
PBT	1.833 ^{±0.021}	1.068 ^{±0.012}	0.2395	8.7	0.788 ^{±0.010}	8.635	8.516
PP BF970MO	1.833 ^{±0.021}	0.733 ^{±0.018}	0.2395	8.7	0.788 ^{±0.010}	8.635	8.461
HDPE C2760 + 5% additive	1.833 ^{±0.021}	0.712 ^{±0.051}	0.2395	8.7	0.788 ^{±0.010}	8.635	8.456
PEEK IXEF 1022	1.833 ^{±0.021}	1.441 ^{±0.026}	0.2395	8.7	0.788 ^{±0.010}	8.635	8.547
HDPE	1.833 ^{±0.021}	0.738 ^{±0.031}	0.2395	8.7	0.788 ^{±0.010}	8.635	8.463
PP C740 25 RNA	1.833 ^{±0.021}	0.692 ^{±0.017}	0.2395	8.7	0.788 ^{±0.010}	8.635	8.451
Aluminium	1.833 ^{±0.021}	0.313 ^{±0.037}	0.2395	8.7	0.788 ^{±0.010}	8.635	8.229
Copper	1.833 ^{±0.021}	3.026 ^{±0.042}	0.2395	8.7	0.788 ^{±0.010}	8.635	8.593

Table 6.7: VoD verifications compared with D_u

Material	D_c calculated (km.s ⁻¹)	D_∞ (km.s ⁻¹)	D_u measured (km.s ⁻¹)	D_c measured (km.s ⁻¹)
PP	8.468	8.635	8.231 ^{±0.11}	-
PBT	8.516	8.635	8.231 ^{±0.11}	8.415 ^{±0.085}
PP BF970MO	8.461	8.635	8.231 ^{±0.11}	8.384 ^{±0.092}
HDPE C2760 + 5% additive	8.456	8.635	8.231 ^{±0.11}	-
PEEK IXEF 1022	8.547	8.635	8.231 ^{±0.11}	8.427 ^{±0.114}
HDPE	8.463	8.635	8.231 ^{±0.11}	-
PP C740 25 RNA	8.451	8.635	8.231 ^{±0.11}	-
Copper	8.593	8.635	8.231 ^{±0.11}	8.629 ^{±0.067}

D_u – VoD of unconfined explosives

c) Remarks

This study has shown an alternative method to determine reaction zone thickness in calculating the detonation reaction velocity. The standard equation to calculate the detonation reaction velocity under confinement (Equation 6.5) proved to be less effective for polymeric materials' confinement. Equation 6.5 was adapted to derive Equation 6.6. Results obtained with this approach are comparable with actual measurements.

6.3 Proposed Detonator Casing Design

The proposed design consists of various components. Shock tube holder, main body, shock tube clip and booster body are the main components of the proposed non-metallic detonator design.

6.3.1 Shock tube holder

The shock tube holder's main function is to provide an interface where the incoming shock tube can be secured to the main body. This is achieved by securing the shock tube to the shock tube holder.

A shock tube is inserted into the 4.17 mm diameter channel opening. The shock tube is inserted into the channel until the tapered channel prevents the shock tube from entering the channel further. A 15 mm free space is built into the design to allow full transfer of the shock tube energy to the delay component.

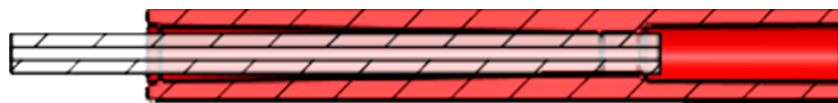


Figure 6.12: Shock tube and shock tube holder (red) assembly

6.3.2 Main body

The main body holds the chemical delay element. The shock tube holder containing the shock tube is used to secure the delay element into the main body. Ribs were positioned on the outside of the main body to increase the mechanical properties of the body.

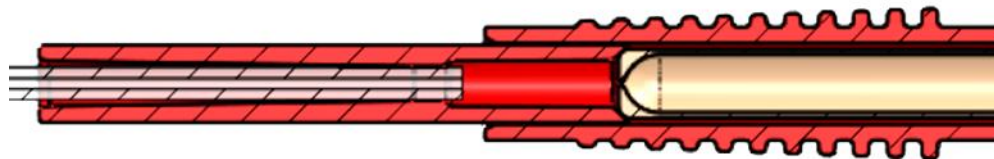


Figure 6.13: Shock tube holder and main body assembly with delay element

6.3.3 Shock tube connector clip

A shock tube connector housing is used to connect acceptor shock tubes to the detonator. Explosives pellets are positioned inside the housing. Acceptor shock tubes are then placed around the explosive pellets on the outside of the clip. When the explosives detonate, the energy released by the detonating explosive initiates the acceptor shock tubes.

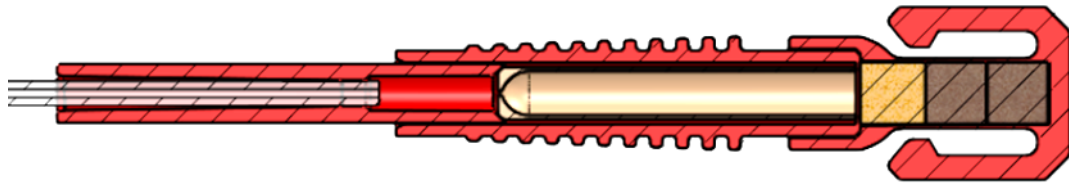


Figure 6.14: Shock tube connector clip assembly

6.3.4 Booster casing

The booster body contains the explosive charge that intends to initiate the large quantity of explosive that is intended to do the work in a typical blasting operation.

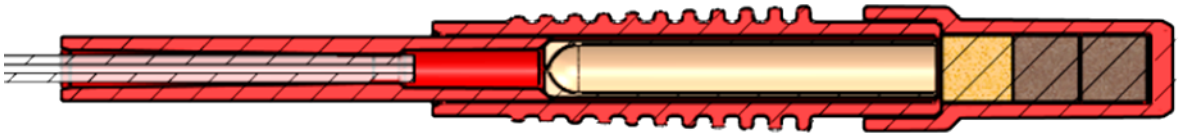


Figure 6.15: Booster casing assembly

6.4 Summary

This chapter showed that a non-metallic casing can be used in the construction of an initiating system. The influence of the casing on the detonation velocity of the explosive base charge was shown to be negligible in comparison with more conventional aluminium casing. An equation predicting detonation velocity was shown to be ineffective when applied to thin-walled confinement. This equation was adapted to be applicable to light confinement and produced results that correlated well with actual VoD measurements.

The initiating system described here showed a workable explosive train encapsulated in a non-metallic casing. The next chapter demonstrates the mechanical integrity of the casing. Optimisation of the booster casing is also described in Chapter 7.

CHAPTER 7

BOOSTER CASING DEVELOPMENT AND MATHEMATICAL DERIVATION

7.1 Introduction

A shock tube holder, main body, shock tube clip and booster casing are the main components of the proposed non-metallic detonator design as discussed in Chapter 6.

Each component has specific functions as described below:

- The shock tube holder's main function is to provide an interface where the incoming shock tube can be secured to the main body.
- The main casing contains the pyrotechnic delay element.
- A shock tube connector housing is used to connect acceptor shock tubes to the detonator.
- The booster casing contains the explosive charge that will initiate the large quantity of explosives intended to do the work in a typical blasting operation.

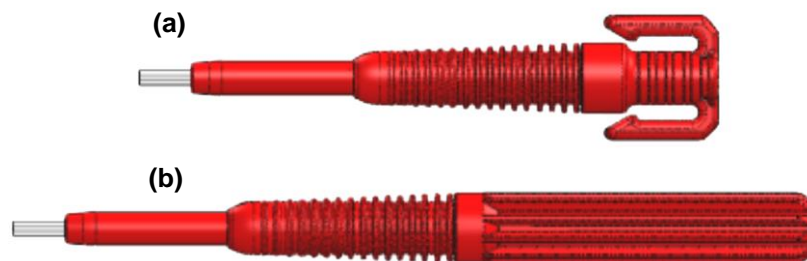


Figure 7.1: Proposed non-metallic detonator design (out-hole detonator (a) and down-hole detonator (b))

The functionality of an initiating system relies on many factors, including the following:

- A primary explosive composition that can be initiated reliably by the energy introduced by a shock tube and can transfer the low-energy input signal to a higher output signal (described in Chapters 3 and 4).
- A secondary charge that can be initiated reliably with the primary explosive composition and deliver a high-energy output (Chapters 4 and 5).
- An explosive train that can consistently deliver high energy under low-confinement conditions as described in Chapter 6.
- A casing design that is strong in order to withstand stringent environmental and handling conditions.

The booster casing in the planned design is an important part of the non-metallic initiating system. Conventional systems make use of a detonator that initiates boosters.

Boosters in turn initiate the main explosives charge. The non-metallic casing design incorporates the booster as a secured section of the initiating system. It is also important that the initiating system is not too large. A rib design is used here not only to add physical strength to the booster tube, but also to attempt energy enhancement through shock focusing.

This chapter describes how the rib design was optimised to produce the most effective blast energy.

7.2 Physics of Booster Casing Optimisation

Detonating explosives produce large quantities of gas and heat. These quantities of gas and heat form over an extremely short time frame and expand very rapidly. Air is compressed at the edge of the gas perimeter and a compression wave is formed. This is often referred to as blast waves and the energy associated with blast waves is used to perform work on neighbouring surroundings. In this chapter, an attempt has been made to develop a comprehensive understanding of blast energy being focused with the use of external geometric changes. The behavioural characteristics of the blast wave are explained based on a set of experiments.

Needham defined a blast wave as a shock wave that can decay immediately after the peak is reached (Needham, 2010:3). This decay occurs in all variables, including pressure, density and material velocity. The rate of decay is, in general, different for each of the parameters. Blast damage by explosives then occurs when the air driven by the explosives moving at high speed engulfs an object and mechanically interacts with it. Zukas and Walters (1998:10) described this process further. The blast wave is a steep pressure rise (shock wave) followed by an exponential decay of pressure. An actual blast wave has a negative pressure region behind it, where the pressure is less than the atmospheric pressure. The negative pressure region does less damage than the positive part. Blast waves interact with the object and the object experiences a force proportional to the square of the air velocity, the object area, and the drag coefficient. If the force is larger than the friction force between the object and the earth, the object will move; if it is less, then the object will remain stationary. The law of physics states that the momentum change is equal to the time integral of the net force. The criterion for damage to the object is either the total distance it moves or the maximum velocity it attains. In either case, there is a minimum impulse or a minimum pressure that causes motion that exceeds the damage limit. Another class of object that may be damaged by the blast is one that is fixed and that deflects elastically, and finally, plastically when it is stressed by the blast wave. Here the criterion for damage is

the deflection of the system. When the total duration of the pressure wave is short, compared with the vibration time of the system, the load is called impulse loading and the momentum is transferred to the casing before it moves appreciably. When the loading pulse is long compared with the natural vibration time of the system, the deflection depends on the peak pressure (Zukas & Walters, 1998:11).

The following approach was used to best identify the optimal design of the shape to focus the shock wave:

- Develop a shock wave simulator, evaluate different shapes and identify a few options to be used for further evaluations.
- Build prototype casings with selected shapes and evaluate with explosives on large scale.
- Explore a prototype booster design considering manufacturing constraints.
- Evaluate the prototype booster design.
- Obtain mathematical evaluation of shaped effect.

7.3 Test Method Illustration of Shock Waves

7.3.1 Shock wave simulation

To obtain video graphic or even photographic evidence of shock waves is an art in itself and very difficult to achieve without the right equipment. It is further acknowledged that a shock wave is a sound wave. An experimental set-up was tailored for this study to show the interaction of shock waves without the use of expensive equipment. The experimental set-up consisted of a water bath, strong light, a high-speed video camera, a 'hammer' and an anvil. The anvil was placed inside the water bath and then struck only once with the hammer. The resulting waves were captured with the high-speed camera and analysed.

The water bath was 60 mm high and filled with water to a level of 25 mm. Shock wave simulators were manufactured from mild steel to have different angles as shown in Table 7.1. One shock wave simulator was positioned inside the water bath opposite the light source. A 1000 W light was used as a light source. A high-speed camera was used to film the resultant waves at 1000 frames per second. A purpose-built hammer was used to strike the anvil once (with the same force). The test was repeated ten times with the same anvil.

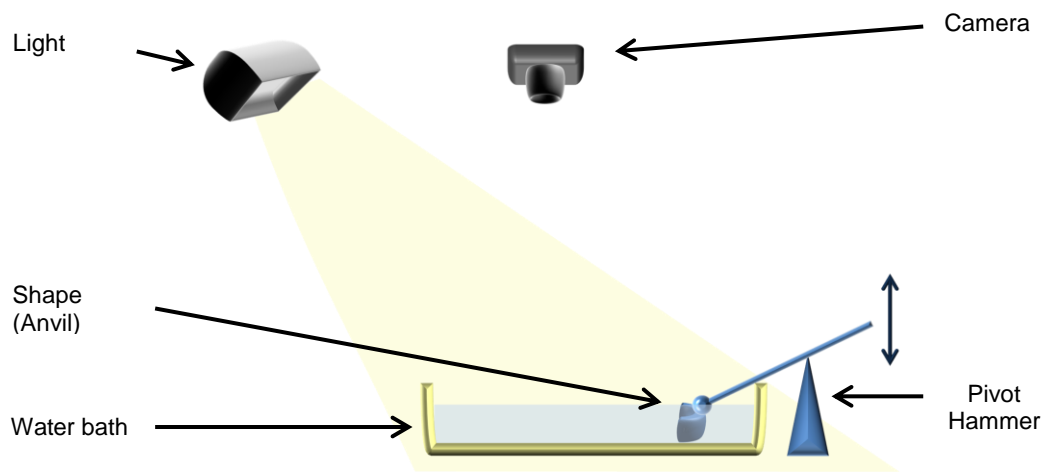




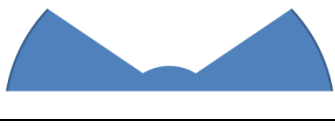
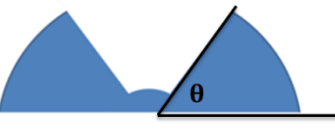
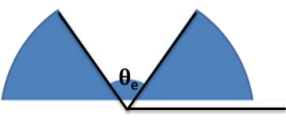


Figure 7.2: Shock wave simulator test set-up

Table 7.1: Different shock wave simulator shapes

Shape	Angle (θ)	Extrapolated inside angle (θ_e)
	90°	90°
	75°	30°
	60°	60°
	45°	90°
	30°	120°
	Position of angle	

7.3.2 Results

The high-speed video graphic results are shown in Appendices 7A to 7E. All the shapes evaluated produced distinct wave profiles. Constructive and destructive interference can clearly be observed as light and dark areas on the videos. The positive interference is obtained at the edge of the light areas and negative interference is visible at the bottom of the dark areas. This is derived from the position of the light and the camera. At a given point in time the resultant shape of the waves adopts a shape that closely resembles the reciprocal of the original shape.

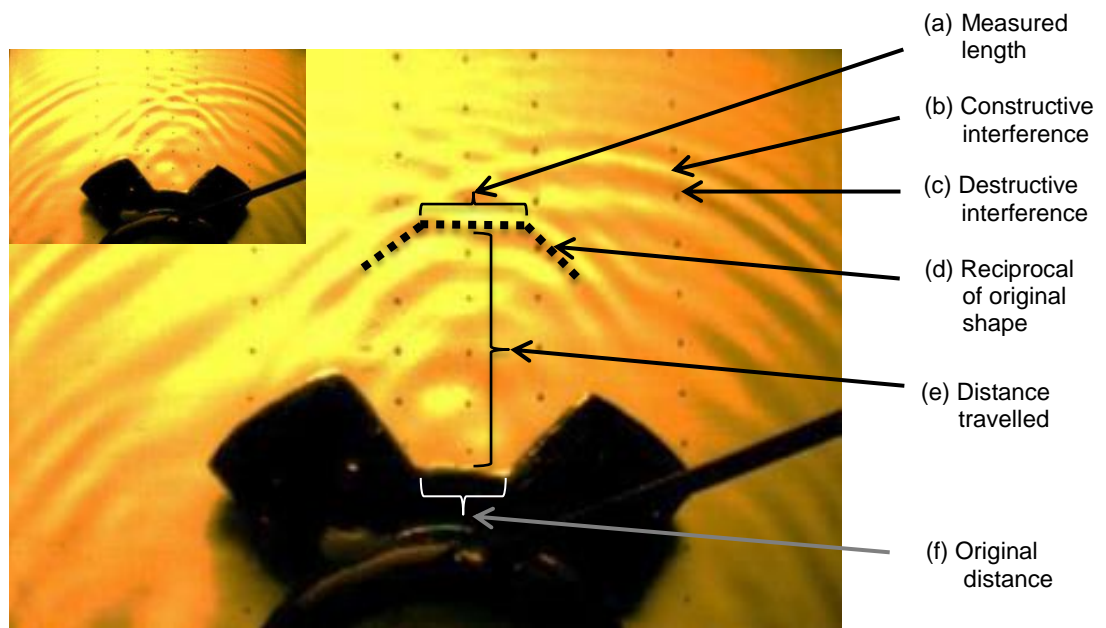


Figure 7.3: Typical high-speed video image interpretation

Visually the best wave profiles produced by the different angles were measured. The distance the wave travelled and the distance of the front plane of the wave were measured. The ratio reference in Tables 7.2 to 7.4 refers to the difference in length between the original bottom section of the shape and the wave at the specific distance. Results for 45°, 60° and 75° shapes are given in Tables 7.2 to 7.4.

Table 7.2: 45° small-scale evaluation results

Position	Frames	Time at 1000 FPS	Distance travelled	Distance with scaling factor	Distance travelled cumulative	Measured length	Scaled length	Ratio Ref.: length
		(s)	(mm)	(mm)	(mm)	(mm)	(mm)	(mm)
a	166	0.00	0.00	0.00	0.00	24.00	13.76	0.67
b	186	0.02	11.50	6.59	6.59	31.00	17.78	0.86
c	206	0.04	11.00	6.31	12.90	36.00	20.64	1.00
d	226	0.06	8.50	4.87	17.76	41.00	23.51	1.14
e	246	0.08	8.00	4.59	22.36	45.00	25.80	1.25
f	266	0.10	7.00	4.01	26.38	47.00	26.95	1.31

Table 7.3: 60° small-scale evaluation results

Position	Frames	Time at 1000 FPS	Distance travelled	Distance with scaling factor	Distance travelled cumulative	Measured length	Scaled length	Ratio Ref.: length
		(s)	(mm)	(mm)	(mm)	(mm)	(mm)	(mm)
a	176	0.00	0.00	0.00	0.00	69.00	39.56	1.98
b	196	0.02	8.00	4.56	4.56	75.00	43.01	2.16
c	217	0.04	10.00	5.70	10.26	85.00	48.74	2.44
d	247	0.07	12.000	6.84	17.09	102.00	58.49	2.93

Table 7.4: 75° small-scale evaluation results

Position	Frames	Time at 1000 FPS	Distance travelled	Distance with scaling factor	Distance travelled cumulative	Measured length	Scaled length	Ratio Ref.: length
		(s)	(mm)	(mm)	(mm)	(mm)	(mm)	(mm)
a	164	0.00	0.00	0.00	0.00	60.00	34.40	1.69
b	184	0.02	10.00	5.81	5.81	75.00	43.01	2.12
c	204	0.04	8.00	4.65	10.45	85.00	48.74	2.40
d	224	0.06	10.00	5.81	16.26	90.00	51.61	2.54

Since the original energy input is the same for all the tests (shapes evaluated), it can be accepted that the initial wave velocities are similar. From the high-speed images, a plane wave is seen forming behind the original wave. This plane wave is a result of

shock focusing and a sharp pressure increase where waves meet is anticipated (as described in Section 2.7). Since the shape of the wave is now flatter, the pressure can act on the target over a bigger area. The length of the front is a function of the angle and the distance from the original shape. Hence the criteria used in this section are the length of the plane section of the wave ((a) in Figure 7.3) and the distance ((e) in Figure 7.3) it formed from the point of origin ((f) in Figure 7.3). The results presented here (Tables 7.2 to 7.4) show the 60° angle to produce the most effective (longest) plane wave in the shortest distance the wave formed from the original shape. The 75° angle produced similar results; however the length of the plane section was slightly shorter compared with that of the 60° angle. The overall results were very close and it was considered premature to eliminate any of the shapes evaluated at this stage of the study. All the shapes were used in the next part of the study.

7.3.3 Large-scale shape evaluation

From the wave profiles obtained: 75°, 60° and 45° were further evaluated in this section. Sleeves containing grooves with the chosen angles were fabricated using a 3D printer. The angled channels were spaced on the outside of the sleeves and along the long axis of the sleeve. The sleeves were then placed on the side of a 400 g Pentolite booster. A typical 400 g booster is approximately 130 mm long with a diameter of 54 mm.

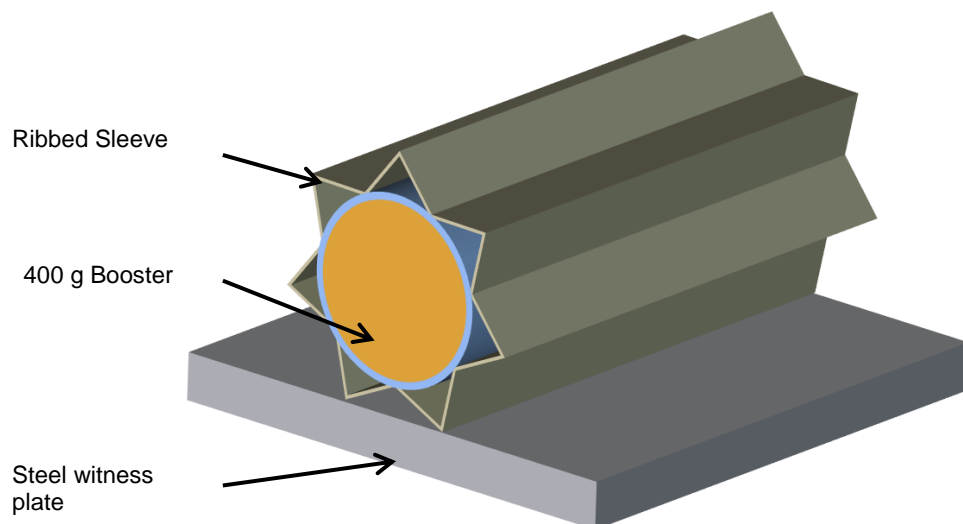


Figure 7.4: 400g booster inside ribbed sleeve – typical test set-up (front view)

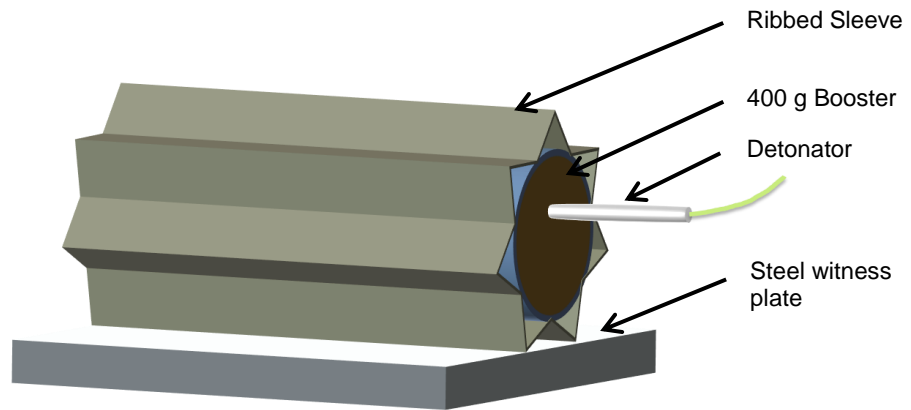


Figure 7.5: 400g booster inside ribbed sleeve – typical test set-up (side view)

The booster was initiated using an 8D detonator placed in the middle of the open side of the cylindrical casing. This resulted in the primary shock wave travelling horizontally over the witness plate. The focusing effect of the shock wave can be less compared with the focusing of a shock wave when the wave travels perpendicularly to the witness plate.

7.3.4 Results

Both the inside and outside profiles of the witness plates were measured using a height gauge. Measurements were taken across the largest bulge that was visually identifiable. Measurements were taken starting 20 mm from the side of the witness plate (this was taken as '0' or the zero point). The second value was then taken 40 mm from the side of the plate. This was the actual first value. Measurements were then taken at 5 mm intervals.



Figure 7.6: Typical witness plate result showing a grooved imprint

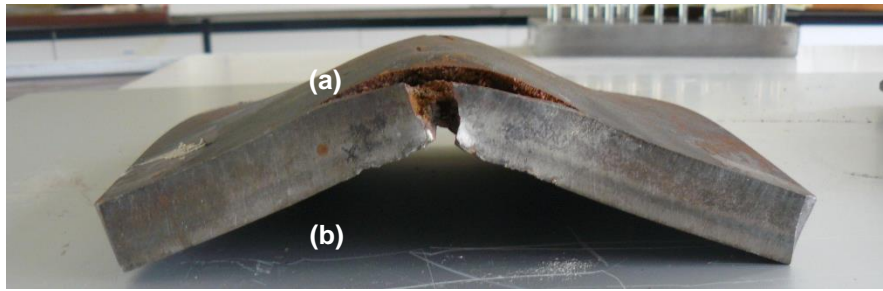


Figure 7.7: Typical witness plate result – side view. The top (a) forms the outside and the bottom (b) forms the inside profile of the witness plate

Actual measurements are shown in Appendix 7F. The angles shown here as well as in the appendices refer to the inside angle of the shape that was evaluated.

Two measurements were taken on either side of the maximum height measured. This was done to obtain the curvature at apex. Polynomial functions were obtained for each using a graphing program (GRAPH 4.0). The equation plot is given in Figure 7.8.

Booster:	$-0.0076(x^2) + 1.0512(x) - 9.8011$	Equation 7.1
45 °:	$-0.0062(x^2) + 0.8746(x) - 5.8847$	Equation 7.2
60 °:	$-0.0063(x^2) + 0.8775(x) - 5.6811$	Equation 7.3
75 °:	$-0.0063(x^2) + 0.8949(x) - 5.9747$	Equation 7.4

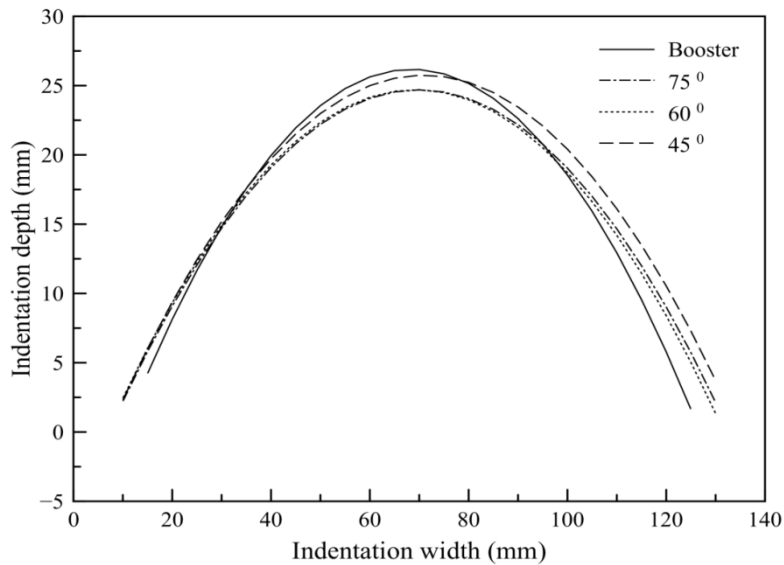


Figure 7.8: Plot obtained from apex polynomial data

The area underneath each graph was determined using the GRAPH program and is shown in Table 7.5.

Table 7.5: Area results of apex curves

Angle	Area (mm ²)
45°	2154
60°	2037
75°	2044
Booster	2038

Material flow properties dictate that under high temperature and pressure, more material flow will be observed on the inside than on the outside. The inside profile and outside profile thus differ from each other. Figure 7.9 shows the plotted data obtained from the measurements made on the indentation side of the witness plate. The actual measurements are given in Appendix 7G.

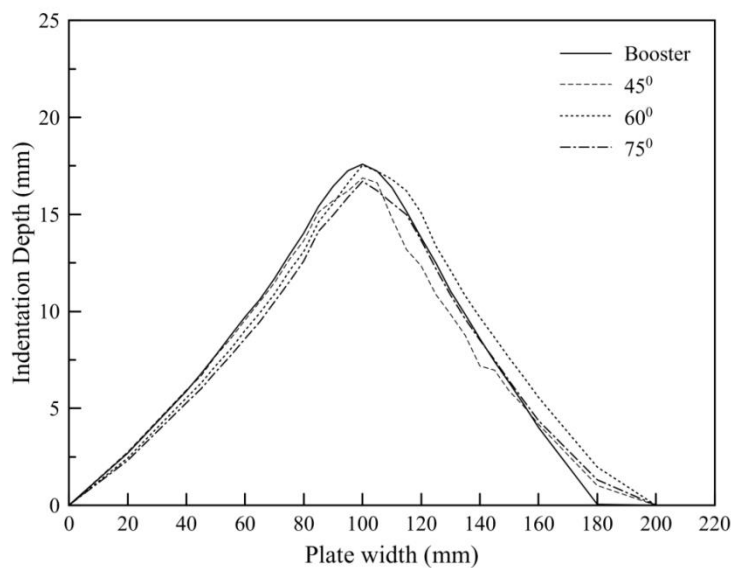


Figure 7.9: Plot obtained from data measured from inside witness plate

The indentation profiles depicted in Figure 7.9 show minor differences between the shapes evaluated. Indentation depths are similar, with the 60° shape producing the deepest indentation. The reference shot is the deepest of all the shapes evaluated.

From the results obtained from both the inside and the outside measurements of the different shapes evaluated, the behaviour identified on a mild steel witness plate can be considered to be the same. Of all the factors that can influence this shape, the main contributor is the material of the shape. In this case polymeric material was used in the

3D printing of the different shapes. These results were not considered during the design of the first prototype booster casing.

7.3.5 New booster casing design – prototype

Considering the results of the qualitative shock wave simulator, a prototype mould was manufactured to produce a booster casing for the non-metallic initiating system. The input data was to design a non-metallic casing with a wave-shaping profile of 60° forming channels parallel to the long axis of the body. Given the geometry and material properties, the prototype mould produced a product with a 75° angle. The shock wave simulation data showed this angle to be acceptable in the design.



Figure 7.10: New booster casing

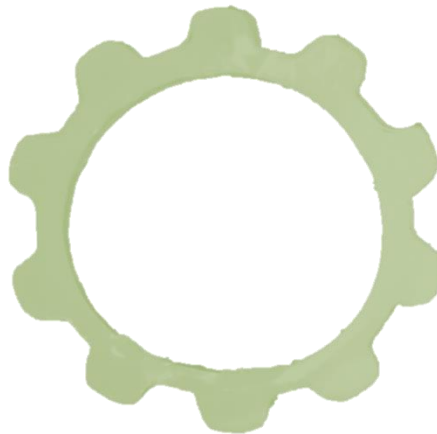


Figure 7.11: New booster casing – sectioned

Table 7.6: Average booster-casing dimensions

Position	Description	
A	Average distance between top of ribs (mm)	2.09
B	Average width of top ribs (mm)	1.33
C	Average width of bottom gap (mm)	1.17
D	Average height of rib (mm)	0.78
E	Average angle ($^{\circ}$)	126.79
F	Total rib thickness (mm)	1.59

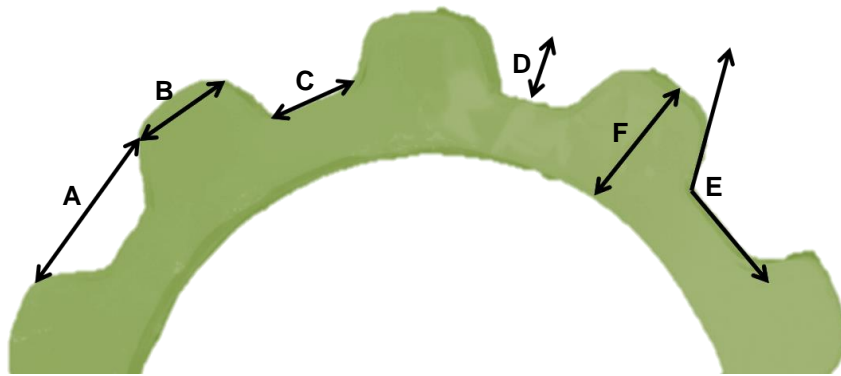


Figure 7.12: Booster casing indicating the position of measurements reported in Table 7.6

7.3.6 Performance evaluation of new casing design

The new booster casing was evaluated by loading the booster cup with RDX/Kelf (RXKF) explosive pellets. RXKF pellets weighed 0.66 g each and had a density of 1.66 g.cm^{-3} . The filled booster casing (9 RXKF pellets) was positioned on top of an aluminium witness block (Aluminium 2024). A standard IED (instantaneous electric detonator) was used to initiate the booster pellets.

7.3.6.1 Sectional thickness of new booster casing

A depth gauge was used to measure the indentation depth profiles obtained from the booster casing with the profile as well as the reference not encapsulated.



Figure 7.13: Filled booster casing on top of aluminium witness plate

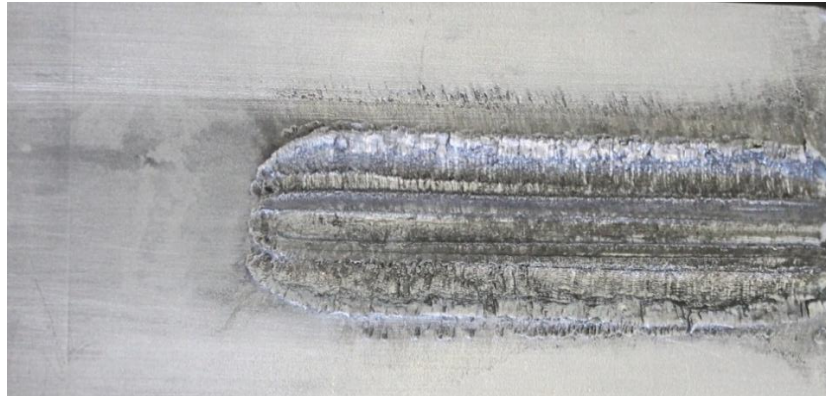


Figure 7.14: Filled booster casing indentation profile



Figure 7.15: Reference RXKF charge on top of witness plate

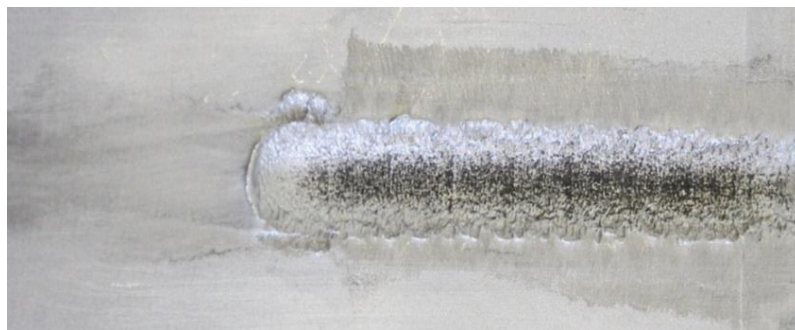


Figure 7.16: Reference RXKF charge indentation profile

It was observed that the side wall thickness of the booster casing was not consistent. Wall thickness varied from a thick side measuring 1.14 mm to a thin side measuring 0.32 mm. This is evident in Figure 7.17.

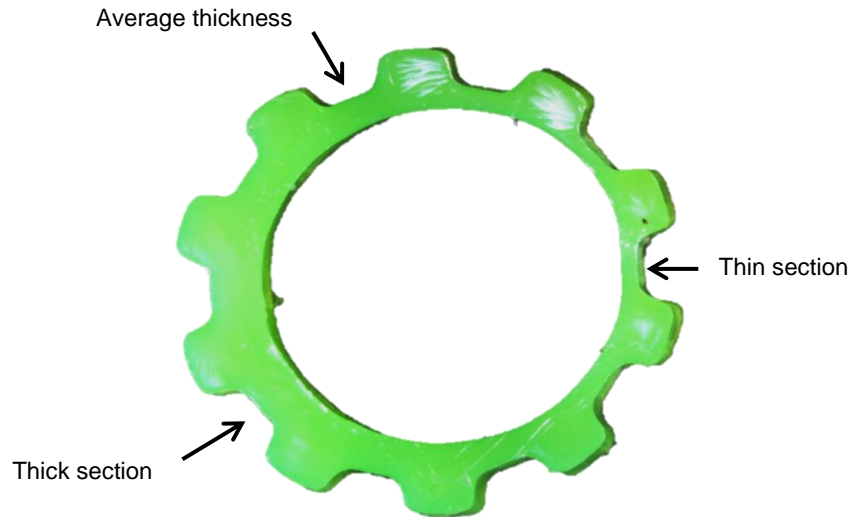


Figure 7.17: Sectioned booster casing showing thin and thick sections

Variations in the wall thickness can influence the energy transfer generated by the reacting explosives formulation to the witness plate. The influence is notable on the indentation depth as indicated by Figure 7.18.

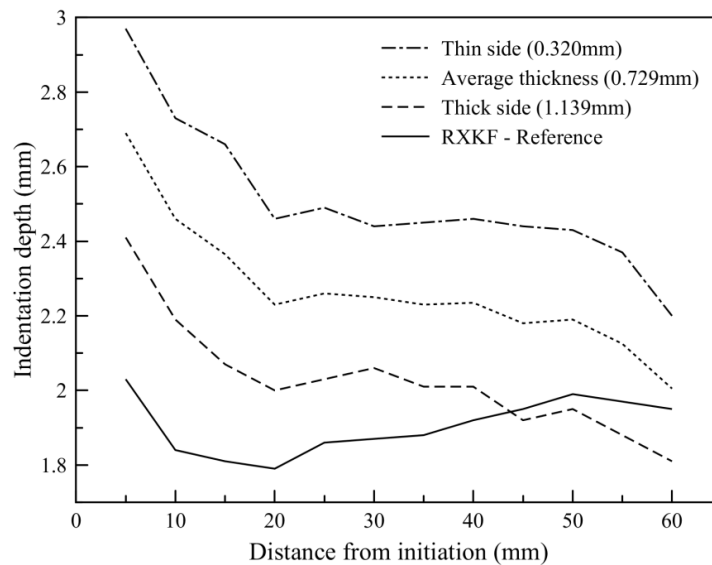


Figure 7.18: Indentation profile results for various thicknesses of sleeves

Consistency in the wall thickness of the booster casing is important to ensure constant energy focusing of a detonating booster.

7.3.6.2 Indentation profile

This section focussed on quantifying the indentation profile obtained in an aluminium witness plate. Again the booster casing was placed so that the cavity of the shape was facing the plate. Nine RXKF booster pellets were used.

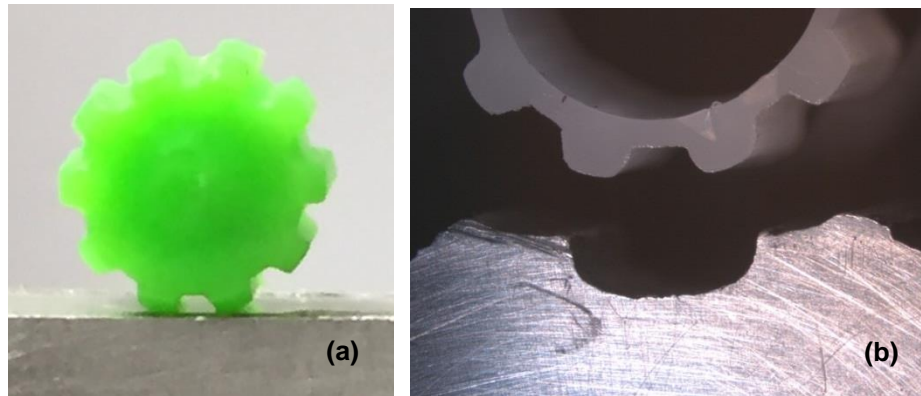


Figure 7.19: Indentation profile set-up (a) and a typical result (b)



Figure 7.20: Wide angle depiction of the result. Reference result (a) and profiled result (b)

Comparing the results obtained from the reference to those of the booster profile shot, it is evident that there is a definite difference in the shape. The reference profile seems to be deeper than the booster profile. The booster profile, on the other hand, seems to be wider than the reference profile. This is in line with the observation made from the large-scale evaluations conducted in Section 7.3.3. The actual measurements taken are reported in Tables 7.7 and 7.8.

Table 7.7: Indentation width / depth comparison

	Booster (mm)	Reference (mm)
Maximum depth	3.15 ^{±0.09}	2.85 ^{±0.08}
Width	22.75 ^{±0.11}	13.80 ^{±0.08}

Table 7.8: Indentation profile compared with ribbed profile

	Coordinates Witness plate	Witness plate	Coordinates Booster shape	Booster shape
Angle (°)	WX∠XY	114.62 ^{±2.36}	AB∠BC	126.79 ^{±1.03}
Top gap (mm)	WZ	3.51 ^{±0.31}	AD	2.09 ^{±0.12}
Rib top width (mm)	ZT	2.91 ^{±0.28}	DF	1.33 ^{±0.10}
Rib height (mm)	XV	3.15 ^{±0.26}	BE	0.78 ^{±0.12}
Width of bottom gap (mm)	XY	2.68 ^{±0.21}	BC	1.17 ^{±0.09}

Figure 7.21 depicts the profile of results reported in Table 7.8 (average of ten measurements). It goes further in finding relations between the original booster profile and the profile obtained in the aluminium witness block. The relations obtained are given in Table 7.9.

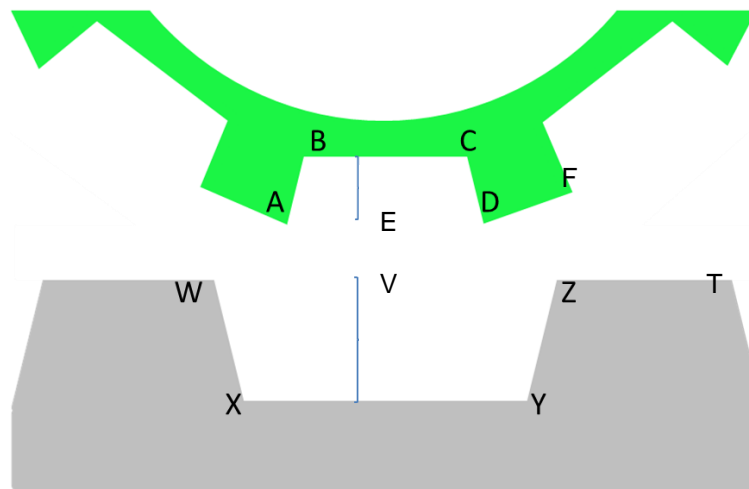


Figure 7.21: Depiction of indentation measurements (A to F represent the gap profile in the booster and T to Z represent the indentation in the witness block)

Table 7.9: Observations from profile measurements

Witness block dimension	Operator	Booster casing dimension	Operator	Angle
WZ	=	~1.7*AD		
VX	=	~4.0*BE		
XY	=	~2.3*BC		
AB	∠	BC	=	127°
WX	∠	XY	=	115°

7.3.7 Mathematical derivation

EXPLO 5 is a detonation code used to determine the detonation characteristics of the RXKF 9501 explosive formulation. The original detonation characteristics of EXPLO 5 are given in Table 7.10.

In order to understand why a larger indentation was obtained in the witness block underneath the original cavity in the witness block, detonation principles need to be applied. Without derogating a highly complex science, this can only be looked at from a one-dimensional perspective. The process followed started with the detonation of the explosives used inside the booster casing. A shock wave was generated as part of the detonation process. The shock wave then progressed through the materials surrounding the explosives. The EXPLO 5 detonation modelling code was used to obtain initial data presented in Table 7.10. In order to use Hugoniot planes, an empirical constant 's' needed to be determined. This 's' is specific for the explosive material used, in this case RXKF 9501.

Table 7.10: EXPLO 5 characteristics for RXKF 9501

Characteristic	Unit	Value
Detonation pressure	GPa	28.507
Detonation velocity	m.s ⁻¹	8217.49
Particle velocity	m.s ⁻¹	2089.82
Sound velocity	m.s ⁻¹	6127.67
Density of reaction products	g.cm ⁻³	2.226
Specific volume of product	cm ³ .g ⁻¹	0.449
Density of explosives	g.cm ⁻³	1.66

$$P_1 = \rho\mu_1(C_o + s\mu_1) \quad \text{Equation 7.5}$$

P_1 = Pressure
 ρ = Density
 μ = Particle velocity
 C_o = Bulk sound speed

Equation 7.5 then equates 's' to be 1.002. 's' is unitless.

The shock now moves into the HDPE casing. As the shock moves into the HDPE, pressure (P) and particle velocity (μ) stay the same. This is valid on the interface. As the shock moves into the HDPE, (P_1) and (μ_1) are expected to change. To determine the new particle velocity (μ_2), the original pressure is kept the same.

The particle velocity at the interface is then determined by setting Equation 7.6 equal to Equation 7.7.

For the explosives, the following parameters are valid:

$$P = \rho_0 C_0 (\mu_1 - \mu_2) + \rho_0 s_0 (\mu_1 - \mu_2)^2 \quad \text{Equation 7.6}$$

ρ_0 = 1.66 g.cm⁻³
 μ_1 = 2.086 km.s⁻¹
 C_o = 6.127 km.s⁻¹
 s_0 = 1.0026

For the HDPE sleeve, the following parameters are valid:

$$P = \rho_1 C_1 (\mu_2 - \mu_b) + \rho_1 s_1 (\mu_2 - \mu_b)^2 \quad \text{Equation 7.7}$$

ρ_1 = 0.915 g.cm⁻³
 μ_b = 0.000 km.s⁻¹
 C_1 = 2.901 km.s⁻¹
 s_0 = 1.481

thus:

$$\rho_0 C_0 (\mu_1 - \mu_2) + \rho_0 s_0 (\mu_1 - \mu_2)^2 = \rho_1 C_1 (\mu_2 - \mu_b) + \rho_1 s_1 (\mu_2 - \mu_b)^2 \quad \text{Equation 7.8}$$

The following calculations show μ_2 to be 1.4755 km.s^{-1} . Upon substituting μ_2 into Equation 7.6, the new pressure is calculated to be 6.87 GPa. This denotes a substantial drop from 28.5 GPa. The wave is still moving forward.

The HDPE sleeve is touching the aluminium witness plate on both sides and has an air gap in the middle. To obtain the pressure when the wave enters the aluminium, Equation 7.6 is adapted to form Equation 7.9. Equation 7.9 is now set equal to Equation 7.10.

For the wave exiting the HDPE sleeve, the following parameters are valid:

$$P = \rho_1 C_1 (\mu_2 - \mu_3) + \rho_1 s_1 (\mu_2 - \mu_3)^2 \quad \text{Equation 7.9}$$

$$\begin{aligned} \rho_1 &= 0.915 \text{ g.cm}^{-3} \\ \mu_2 &= 1.476 \text{ km.s}^{-1} \\ C_1 &= 2.901 \text{ km.s}^{-1} \\ s_1 &= 1.481 \end{aligned}$$

For the aluminium witness block, the following parameters are valid:

$$P = \rho_2 C_2 (\mu_3 - \mu_c) + \rho_2 s_2 (\mu_3 - \mu_c)^2 \quad \text{Equation 7.10}$$

$$\begin{aligned} \rho_2 &= 2.785 \text{ g.cm}^{-3} \\ \mu_c &= 0.000 \text{ km.s}^{-1} \\ C_2 &= 5.328 \text{ km.s}^{-1} \\ s_2 &= 1.338 \end{aligned}$$

thus:

$$\rho_1 C_1 (\mu_2 - \mu_3) + \rho_1 s_1 (\mu_2 - \mu_3)^2 = \rho_2 C_2 (\mu_3 - \mu_c) + \rho_2 s_2 (\mu_3 - \mu_c)^2 \quad \text{Equation 7.11}$$

The following calculations show μ_3 to be 0.309 km.s^{-1} . Upon substituting μ_3 into Equation 7.9, the new pressure is found to be 4.93 GPa. This is a noticeable drop from 6.87 GPa. The HDPE sleeve touching the aluminium witness plate has now been determined and the air gap in the middle can now be quantified.

$$P = \rho_1 C_1 (\mu_2 - \mu_3) + \rho_1 s_1 (\mu_2 - \mu_3)^2 \quad (\text{Equation 7.9})$$

$$\begin{aligned} \rho_1 &= 0.915 \text{ g.cm}^{-3} \\ \mu_2 &= 1.476 \text{ km.s}^{-1} \\ C_1 &= 2.901 \text{ km.s}^{-1} \\ s_1 &= 1.481 \end{aligned}$$

The air parameters are as follows:

$$P = \rho_3 C_3 (\mu_3 - \mu_d) + \rho_3 s_3 (\mu_3 - \mu_d)^2 \quad \text{Equation 7.12}$$

$$\begin{aligned} \rho_3 &= 2.030 \text{ g.cm}^{-3} \text{ (new air density at pressure exiting the HDPE)} \\ \mu_d &= 0.000 \text{ km.s}^{-1} \\ C_3 &= 0.899 \text{ km.s}^{-1} \\ s_3 &= 0.939 \end{aligned}$$

thus:

$$\rho_1 C_1 (\mu_2 - \mu_3) + \rho_1 s_1 (\mu_2 - \mu_3)^2 = \rho_3 C_3 (\mu_3 - \mu_d) + \rho_3 s_3 (\mu_3 - \mu_d)^2 \quad \text{Equation 7.13}$$

The following calculations show μ_4 to be 0.77 km.s^{-1} . Upon substituting μ_4 into Equation 7.9, a pressure of 2.54 GPa is found. This is a noticeable drop from 6.87 GPa. The wave is still moving forward. Two shock waves merged in the gap.

Two shock waves then approach, colliding with each other. They have equal amplitude, and when they meet a much higher pressure shock is reflected in both directions. Because these two waves are equal in many ways (except for their direction) their original particle velocity remains constant.

After the interaction of the shock waves there will again be a right-moving wave and a left-moving wave. These waves should be equal. If the left-moving Hugoniot is set equal to the right-moving Hugoniot, a '0' (zero) value is obtained as shown by Equation 7.14.

$$\rho_3 C_3 (2\mu_3 - \mu) + \rho_3 s_3 (2\mu_3 - \mu)^2 = \rho_3 C_3 (\mu - 2\mu_3) + \rho_3 s_3 (\mu - 2\mu_3)^2 \quad \text{Equation 7.14}$$

The solution to the particle velocity after the interaction is used to determine the pressure. By equating the zero particle velocity into one of the Hugoniot's, the pressure

is 7.35 GPa (one of the equations refers to either the equation to the right of the equal sign or to the left of the equal sign in Equation 7.14). This is more than twice the pressure of the wave in air and more than the original pressure in the HDPE.

This pressure then moves into the aluminium. In order to calculate the pressure moving into the aluminium, the initial particle velocity must first be determined. This is done by keeping the density of air as the shock wave exits the HDPE into the air, constant. The air density is calculated to be 2.03 g.cm⁻³. From Equation 7.5, the particle velocity is calculated to be 1.54 km.s⁻¹.

The air parameters are as follows:

$$P = \rho_3 C_3 (\mu_5 - \mu_6) + \rho_3 s_3 (\mu_5 - \mu_6)^2 \quad \text{Equation 7.15}$$

$$\rho_3 = 2.030 \text{ g.cm}^{-3} \text{ (new air density at pressure exiting the HDPE)}$$

$$\mu_5 = 1.540 \text{ km.s}^{-1}$$

$$C_3 = 0.899 \text{ km.s}^{-1}$$

$$s_3 = 0.939$$

For the aluminium witness block, the same parameters are used as given earlier. Equation 7.10 is re-written as Equation 7.16 to accommodate μ_6 . The following parameters are valid:

$$P = \rho_2 C_2 (\mu_6 - \mu_c) + \rho_2 s_2 (\mu_6 - \mu_c)^2 \quad \text{Equation 7.16}$$

$$\rho_2 = 2.785 \text{ g.cm}^{-3}$$

$$\mu_c = 0.000 \text{ km.s}^{-1}$$

$$C_2 = 5.328 \text{ km.s}^{-1}$$

$$s_2 = 1.338$$

thus:

$$\rho_3 C_3 (\mu_5 - \mu_6) + \rho_3 s_3 (\mu_5 - \mu_6)^2 = \rho_2 C_2 (\mu_6 - \mu_c) + \rho_2 s_2 (\mu_6 - \mu_c)^2 \quad \text{Equation 7.17}$$

The following calculations show μ_6 to be 1.54 km.s⁻¹. Upon substituting μ_6 into equation 7.16, a pressure of 5.54 GPa is found. This is a noticeable drop from 7.35 GPa.

The actual calculations are shown in Appendix 7H.

7.4 Discussion

In this section, a shock wave simulator was successfully developed and used to demonstrate wave profiles generated from different shapes. From simulator data, selected shapes were used to evaluate the effect of the focused shock wave on steel witness plates. Marginal differences were noted. A prototype booster casing was designed and manufactured using injection moulding techniques. This produced booster casing with symmetrical defects. It was demonstrated that such defects could severely influence the focusing of the shock wave and hence the pressure focus point.

Indentation profiles obtained from shaped booster bodies on aluminium witness blocks showed that the indentation depth in the witness block can be expected to be four times the depth of the rib used. The inside width also increases to about twice its original value. This clearly demonstrated that shock focusing could be achieved.

Particle velocity, density, shock velocity, and pressure are all parameters influenced when a shock wave passes through different materials. When shock moves across a material interface from one medium (having low impedance) to another medium (having high impedance), the shock pressure increases. This has been demonstrated by the profile obtained in the aluminium witness block when evaluating the shaped booster. From the calculation presented, the changing shock wave can be shown as follows:

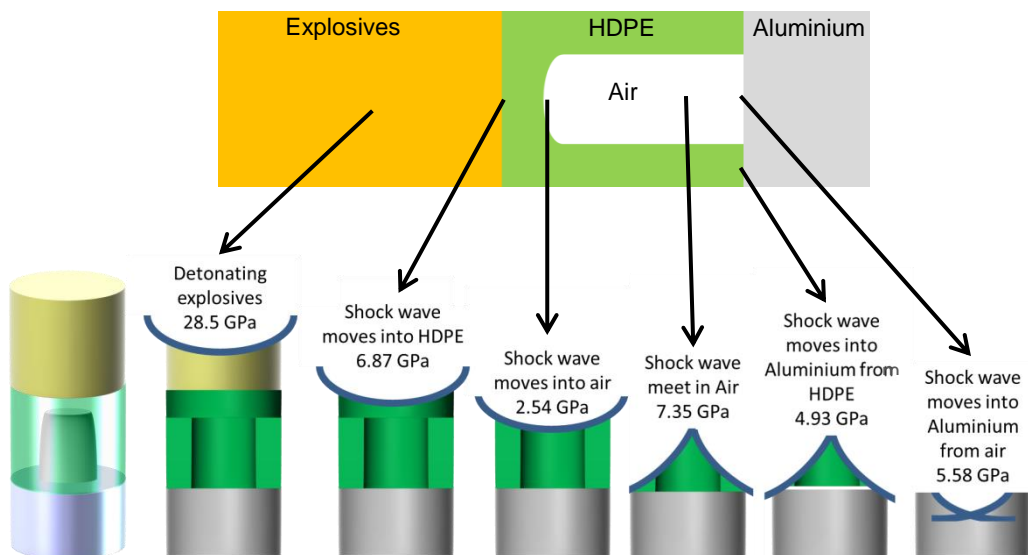


Figure 7.22: Shock wave pressure variances through different materials

When a plane shock wave reflects from a concave wall, a converging shock arises, resulting in a locally high pressure. This is shown when shock waves meet and collide (Figure 7.22).

Cooper (1996:198) suggested the pressure to cause incipient melting of the aluminium to be 0.6 Mbar and the pressure to cause complete melting to be 0.9 Mbar. The difference in pressures as well the difference of barrier material resulted in a difference in shock impedance. The difference in pressure when the shock wave exits the HDPE into the aluminium compared to when the pressure from the combined shock waves enters the aluminium, explains the indentation profile in the aluminium.

Incorporating ribs on the side of the casing can increase the shock pressure and in turn assist with better initiation of an explosives acceptor charge.

7.5 Summary

This chapter detailed the identification of a desired shape for optimal shock wave focusing and described the interaction of these waves. The augmentation of the waves has also been shown. A new booster casing design is proposed and validated mathematically.

CHAPTER 8

EVALUATION OF TENSILE PERFORMANCE AND TRACIBILITY OF NON-METALLIC CASING

8.1 Introduction

Initiating systems are unique blends of chemical explosive formulations in combination with encapsulating materials. The detonator/booster casing keeps the explosive train in position and prevents the explosives from being exposed to the environment. A compromise in the integrity of the casing or casing material can result in system failure as well as unsafe conditions. The mechanical properties of the casing material are important in that it must be able to keep its integrity in harsh conditions on a mine bench. Typical initiating systems are assembled through crimping techniques. Ultrasonic welding has been incorporated in this design to better accommodate the non-metallic body. Mechanical strain testing was conducted to evaluate the overall structural integrity of the assembled system.

The shock tube, shock tube holder, main body and the shock tube connector clip or booster casing were secured in their positions by using an ultrasonic welding technique. Certain organic polymers are not ideally suited to function under all conditions (Nicholson, 1991:130). Nicholson (1991:130) stated that on exposure to outdoor conditions (especially sunlight), the polymers undergo certain reactions that can lead to a loss of their desirable properties. The biggest factor influencing the integrity of the design is ageing. Weathering is a broad term that is applied to the changes that take place in a polymer on exposure to climate conditions, e.g., hot and cold temperatures, humidity, and ultraviolet light, assisted by contributions from visible and near-infrared portions of the electromagnetic spectra. During detonator application solar radiation is minimal and polymers can be marginally exposed to direct sunlight for only several days (rarely exceeding 30 days). Therefore solar radiation is not considered as a mechanism for weathering of polymers. Temperature fluctuations are more applicable to this area of design.

This chapter concludes by evaluating the assembled non-metallic initiator casing's compatibility with a wireless radio frequency identification detection (RFID) system.

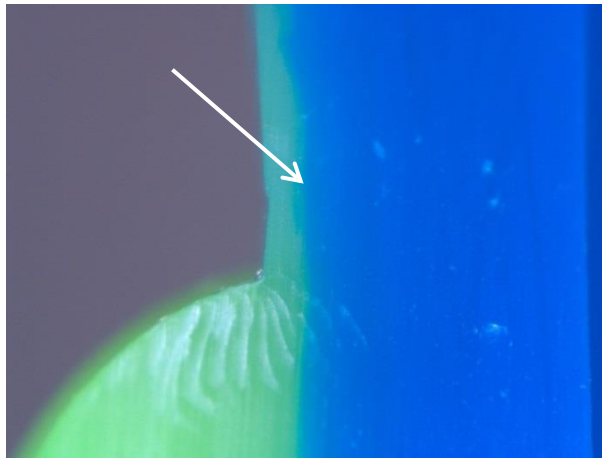


Figure 8.1: Typical ultrasonic weld interface

8.2 Test and Evaluation of the Proposed Design

To have a detonating system certified and fit for purpose is a tedious process involving numerous tests against international standards. It is not intended to demonstrate the conformance of this proposed design to such standards. The intention is rather to determine the material strength at different temperatures involving tensile tests. The test items were also subjected to thermal ageing that simulated a time span of 10 years. Current customer requirements stipulate a temperature range of 50 °C to 20 °C. Test samples were manufactured as per the specifications shown in Appendices 8A – 8D.

8.2.1 Detonator component tensile test

This test was conducted by conditioning the test items at the set temperature for three hours and then determining the tensile strength of the sample using a Shimadzu AGSX 20kN tensile tester fitted with a 5-kiloNewton (kN) loadcell. All tests were conducted using a travel speed of 10 mm/min.

8.2.1.1 Tensile tests conducted at different temperatures

The test samples consisted of the following components:

- a) Shock tube and shock tube holder
- b) Shock tube holder and main body
- c) Main body and booster casing

The tests were conducted at 50 °C, ambient (20 °C) and -20 °C. The test items were conditioned at each temperature for 3 hours (h). The test items were positioned inside the tensile tester and secured to top and bottom clamps.

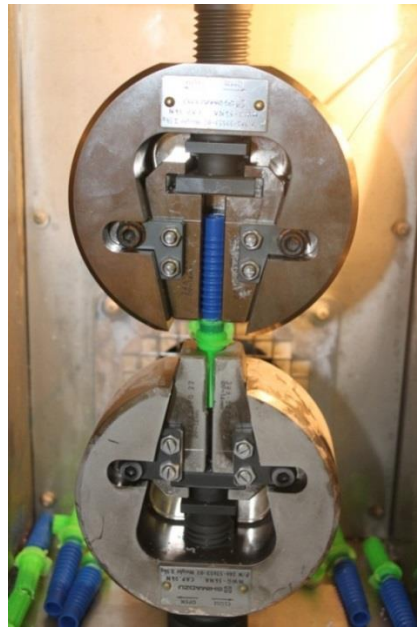


Figure 8.2: Typical set-up of clamped in position on tensile tester

A climatic control cabinet (Figure 8.3) connected to the tensile tester ensured that the test was conducted at the above-mentioned selected temperatures.



Figure 8.3: Sample inside climatic chamber on tensile tester

Test samples were placed inside the conditioning chamber and subjected to a 14-day diurnal temperature cycle test at a relative humidity (RH) of 95%. The tests items were then subjected to pull-tests as described in Section 8.2.1.1.



Figure 8.6: Test items inside climatic chamber

8.2.1.3 Results

Figures 8.7, 8.9 and 8.11 show the test items before they were subjected to the tensile test. The results obtained are shown in Figures 8.8, 8.10 and 8.12.



Figure 8.7: Shock tube (a) and shock tube holder (b) interface

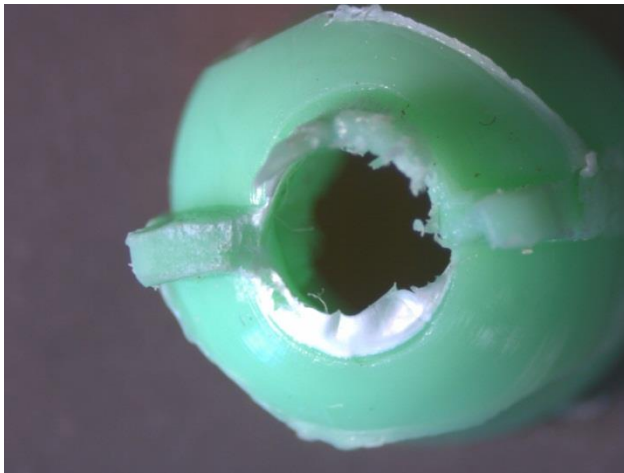


Figure 8.8: Shock tube and shock tube holder interface failure



Figure 8.9: Shock tube holder (a) and main body (b) interface

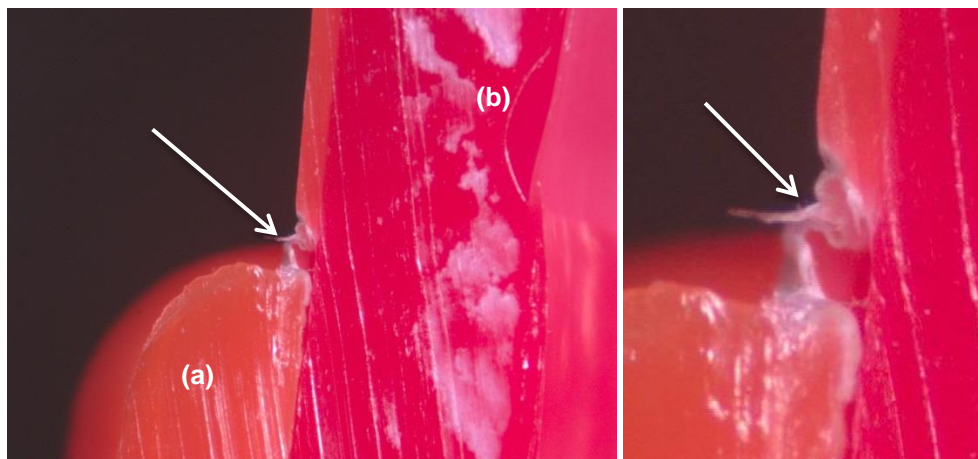


Figure 8.10: Shock tube holder (a) and main body (b) interface failure



Figure 8.11: Main body (a) and booster (b) body interface

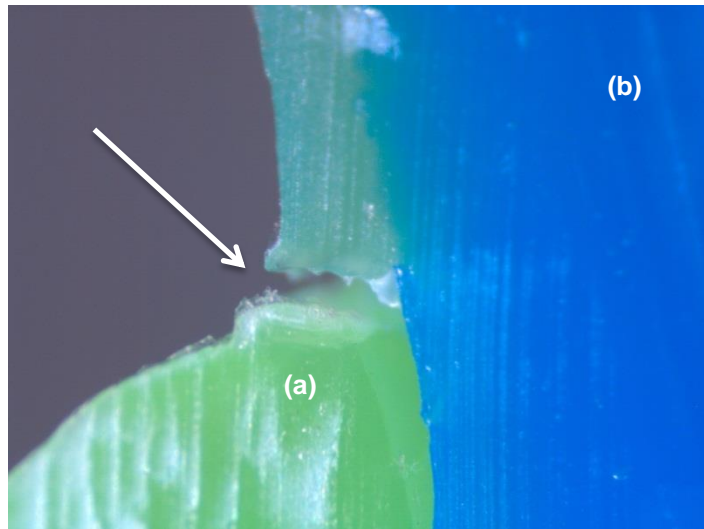


Figure 8.12: Main body (a) and booster body (b) interface failure

Table 8.1: Pull-out results – Shock tube and shock tube holder interface

Newton (N)	Shock tube and shock tube holder interface		
	50 °C	20 °C	-20 °C
Average force	125.6	184.5	219.0
Standard deviation	5.1	9.3	35.3
Range	20.1	31.8	130.7
Travel (mm)			
Average travel	216.5	162.1	43.2
Standard deviation	12.0	32.9	25.5
Range	55.0	107.5	91.85

Table 8.2: Pull-out results – Shock tube holder and main body interface

	Shock tube holder and main body interface		
Newton (N)	50 °C	20 °C	-20 °C
Average force	239.5	306.2	381.3
Standard deviation	47.4	95.3	108.9
Range	192.6	352.7	506.0
Travel (mm)			
Average travel	1.59	1.9	1.3
Standard deviation	0.5	0.9	0.6
Range	1.7	3.1	2.9

Table 8.3: Pull-out results – Main body and booster body interface

	Main body and booster body interface		
Newton (N)	50 °C	20 °C	-20 °C
Average force	448.6	716.5	1073.2
Standard deviation	41.4	64.4	83.6
Range	148.4	251.9	293.4
Travel (mm)			
Average travel	7.8	7.7	5.2
Standard deviation	2.3	1.3	1.5
Range	8.1	5.0	5.4

Table 8.4: Pull-out results – Shock tube and shock tube holder interface (aged)

	Shock tube and shock tube holder interface		
Newton (N)	50 °C	20 °C	-20 °C
Average force	128.3	186.5	270.0
Standard deviation	9.6	9.7	34.1
Range	32.9	33.8	119.4
Travel (mm)			
Average travel	243.8	162.13	85.8
Standard deviation	17.5	32.9	40.0
Range	69.8	107.5	141.5

Table 8.5: Pull-out results – Shock tube holder and main body interface (aged)

	Shock tube holder and main body interface		
Newton (N)	50 °C	20 °C	-20 °C
Average force	232.3	306.0	483.0
Standard deviation	41.0	43.6	126.7
Range	166.2	179.0	490.0
Travel (mm)			
Average travel	2.5	1.5	2.0
Standard deviation	0.7	0.4	0.7
Range	2.5	2.1	2.4

Table 8.6: Pull-out results – Main body and booster body interface (aged)

	Main body and booster body interface		
Newton (N)	50 °C	20 °C.	-20 °C
Average force	446.6	734.0	1020.1
Standard deviation	77.1	103.7	165.0
Range	221.8	414.1	448.1
Travel (mm)			
Average travel	5.8	4.0	3.6
Standard deviation	2.3	1.2	1.7
Range	8.1	4.5	5.9

8.2.1.4 Discussion

The tensile test results show that the force required to pull the parts apart increases with a decrease in temperature. Greater standard deviations and ranges are also noted. Stress-strain behaviour is notably different for the interfaces tested (Appendices 8E to 8J). Shock tube to shock tube holder interface shows to be more ductile compared with both shock tube holder to main body interface and main body to booster body interface. This is mainly due to the material characteristics of shock tubes that tend to stretch more. The larger surface area of the weld securing the shock tube holder to the main body and the larger thickness of these parts result in a more brittle profile. Comparable behaviour is noted for the main body to booster body interface. Here the booster stretched during the test, influencing the stress-strain profile to represent a more ductile profile. The minimum force required to break the weld (considering all tests) was 110 N. This is significantly more than the 80 N considered the minimum force required pull shock tube from a metallic detonator assembly.

8.3 Tracking and Tracing

The compatibility of RFID tracking systems with the item intended for use is important to ensure proper effectiveness. Preceding chapters discussed non-metallic initiator

casing design and showed that the proposed casing design is an effective means to encase explosives. However, to conclude the feasibility of a non-metallic initiator casing, the proposed design should not compromise the effective functioning of RFID tags.

8.3.1 RFID detection testing

A Motorola MC9 19ZEU handheld RFID scanner was used to detect AZ-9620 RFID tags. The scanner has a Marvell PXA320 processor (@806 MHz). An integrated, linearly polarised antenna operates at frequencies of 865–868 MHz and 902–928 MHz. A nominal read range of 9.14 m can be achieved with a 1.22 m write range. AZ-9620 tags are passive, item-level tags that operate at a frequency of 860–960 MHz. The actual label dimension is 31 mm x 14.7mm with the antenna dimension 27 mm x 9.7 mm. An Alien Higgs®-3 IC type chip is used on the tags. The tags have a 10-year data retention capability with a write endurance of 100 000 cycles. RFID tags were placed in aluminium detonator shells and HDPE detonator parts. The following configurations were evaluated:

- One hundred (100) RFID tag placed inside 100 aluminium shells. The shells containing the tags were placed in a cardboard box in a 10 x 10 orientation.
- One RFID was positioned inside an aluminium shell. The RFID-containing shell was then placed in the middle of the cardboard box containing aluminium shells in a 10 x 10 orientation (none of the other shells contained RFID tags).
- One RFID tag was placed next to an aluminium shell (not inside the aluminium shell) inside the cardboard box containing aluminium shells in a 10 x 10 orientation. The tag was positioned in the middle of the box and on the outer side of the box.
- One RFID tag was placed inside the HDPE shock tube holder, HDPE body, HDPE clip and HDPE booster body. These components were scanned individually.
- The HDPE components were assembled and scanned (assembled units separately).
- Thirty (30) HDPE bodies containing RFID tags were placed inside a cardboard box.

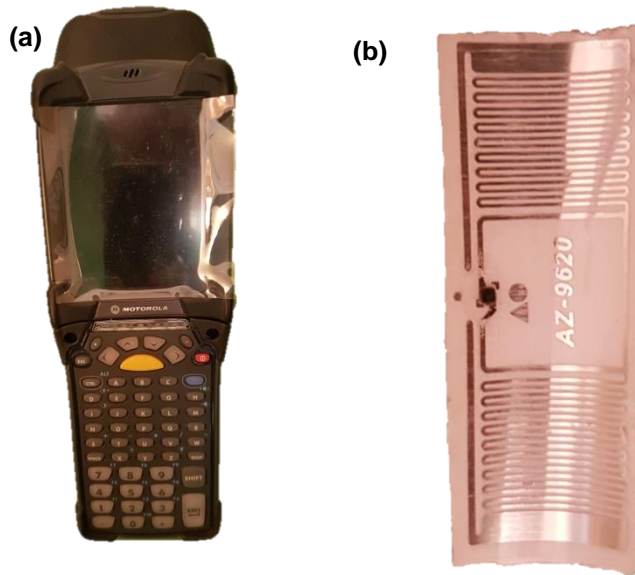


Figure 8.13: Motorola RFID scanner (a) and an RFID tag (b)



Figure 8.14: RFID tag inside aluminium shell positioned in the middle off 100 aluminium shells

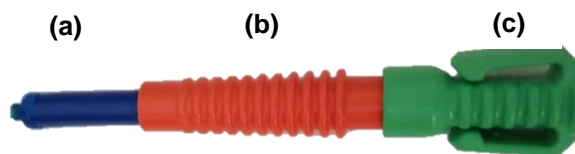


Figure 8.15: RFID tags positioned inside the shock tube holder (a), body (b) and the clip (c)

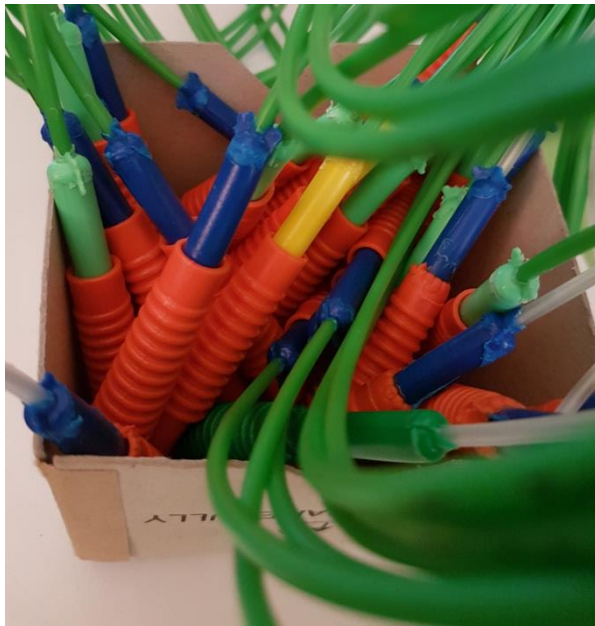


Figure 8.16: 30 HDPE bodies containing 30 RFID tags

8.3.1.1 Results

Results obtained are presented in Table 8.7.

Table 8.7: RFID tag detection results

Description	Number of RFID tags scanned	Number of RFID tags detected by scanner
RFID tags inside aluminium shells.	100	0
One RFID tag surrounded by aluminium shells.	1	0
One RFID placed next to aluminium shells.	1	0 (for all positions tested)
One RFID tag placed inside non-metallic components.	10 shock tube holders 10 bodies 10 clips 10 booster bodies	10 10 10 10
RFID tags placed inside non-metallic components and assembled.	3 tags per unit 10 units tested	3 tags were detected for all 10 units tested
30 non-metallic bodies containing RFID tags were placed inside a cardboard box.	30	30

8.3.1.2 Discussion

The RF detection system functions with a receiver and a transmitter. The transmitter uses a modulation technique to encode data that is then sent to a receiver. An antenna, attached to the receiver, obtains and translates the modulated signal. Data can then be stored on the receiver (tag). The transmitter also determines the power level or signal strength of the system which can further be enhanced through active receiver systems. Applying receivers in high noise environments can adversely affect the signal, resulting in poor signal-to-noise ratios. High noise environments cause reflection, scattering, refraction and diffraction of the signal. Metallic surroundings cause reflection of the radio wave and hence shield the signal from reaching the receiver, compromising the effectiveness of the RF system. HDPE provides a solution in that the signal is not reflected. Test results showed 100% detection of RFID tags used in HDPE detonator parts.

8.4 Summary

The actual design details of the different components are given in Appendices 8A–8D. These parts were ultrasonically welded together and subjected to tensile testing at different temperatures. Samples were also artificially aged after which these samples were also subjected to tensile testing at different temperatures. Different stress-strain behaviours were noted with distinctive differences in elastic and plastic regions between the samples evaluated. A minimum force at break was measured to be 110 N. This is above the 80 N accepted as benchmark.

Complete assemblies were populated with RFID tags and tested for functionality. All the tags were detected when used in combination with HDPE components.

CHAPTER 9

SUMMARY AND CONCLUSIONS

9.1 Summary

Current initiators consist of a timing delay segment, and a primary explosive component on top of a secondary explosive component. Metal confinement is used as an outer casing to hold all the components of the initiator together. International law has emphasised the importance of a greener and safer initiator design. Lead azide is the primary explosive used in initiators, due to ease of manufacture and relative low cost. However, lead azide is a heavy metal salt and not environmentally acceptable. Poor traceability of initiators post manufacturing is a challenge and poses both safety and security risks. 2D barcoding is a solution, but has limitations owing to the shape of the initiator. RFID is a more feasible track and trace solution, but the metallic initiator casing can compromise the effectiveness of such system. Identifying RFID as the way forward for track and trace systems implies moving away from metal encapsulation of initiator.

Finding a replacement for the current lead azide primary explosive is the first step towards a greener initiating system. Changing explosive formulations to fulfil a specific task is an involved process and requires a great deal of understanding of energetic materials' behaviour. It is challenging to prove experimentally and to evaluate every factor that might have an influence on explosive performance. Selected parameters were identified in an attempt to evaluate the performance of the explosives developed in this study. Such parameters laid the foundation for exploring nano-porous silicon as a base that could be used to develop an alternative explosive formulation to lead azide, as well as contributing to intermediary explosives development.

Dissolution chemistry was used to prepare nano-porous silicon. Nano-porous silicon was evaluated and characterised by evaluating samples of different surface areas. It was shown that the surface area and pore volume of the nano-porous silicon samples changed with time. The drift in reaction was explored and shown to be related to oxidation of the silicon samples. Methods of preparation of 5-nitriminotetrazole and 5-nitrotetrazole were developed for using the components as oxidisers in combination with nano-porous silicon.

Nano-porous silicon and PBX explosive formulations were also developed in this work. Organic and inorganic oxidisers were used and characterised. By using the R_r test method, the reactivity between samples of different particle size, pore volume, density

and composition was successfully quantified. Chemical reactions were determined and heat of reactions calculated. Stoichiometric ratio determinations had shown Si/NaClO₄ (2 : 1) to be the most reactive (from R_r test). It was found that optimal stoichiometric ratios did not necessarily produce the optimal reaction. npSi explosive formulations prepared from PETN were shown to be the least affected by storage compared with SP oxidizers. npSi/NT produced the highest R_r values at a density of 2.5 g.cm⁻³. The fastest burning speeds were obtained from npSi/HNS explosives mixtures with npSi / NT mixtures only 0.05 m.s⁻¹ slower. The reaction rate was also faster for higher surface area formulations. Formulations subjected to a closed vessel pressure test had shown the peak pressures to be related to surface area. NT/npSi with high surface area was identified as a suitable replacement for LA based on reactivity.

A manufacturing method for a PBX formulation that can be used as a suitable intermediary charge with the new primary explosive formulation was developed. Castable and pressable PBX formulations were prepared using different particle size PETN and different binders. The PBX formulations were evaluated using the SSGT. The formulations were also evaluated using impact and friction tests. The pressable PBX formulation BMW111-I was selected as the intermediary charge.

In this work the development of the explosives train was also dealt with. The approach considered that the explosives ought to be sensitive enough to pick up from the input stimuli and should produce enough output to initiate the next explosives. npSi/NT explosive formulation in combination with clean nitriminotetrazole explosive was developed as a primary initiator composition. Developing the explosive train entailed the pick-up explosives to be able to initiate from various signals. It was found that the pick-up ability in the small geometry was related to the density of the formulations. The power output of the explosives was quantified by using the newly developed BBI test. The explosives train developed could be used in a casing, and reliable pick-up and initiation of the intermediary charge could thus be expected. This development was published in the *International Journal of Applied Engineering Research* (Bezuidenhout & Mukhopadhyay, 2016).

Confinement plays a major role in the performance characteristics of explosives. In short, confinement increases the VoD of an explosive formulation and hence the power output. Non-metallic confinement can behave differently. Explosives' length and confinement are two parameters explored while dealing with non-metallic encapsulation. VoD is influenced/determined by column diameter. It was shown that column length also influenced the VoD of the explosives. A new approach was

proposed where explosive length was used to determine the length of the reaction zone. Further to this, a novel equation was developed to determine the VoD of an explosive from witness block indentation diameter and explosive column height.

A design entailing longitudinal ribs on the outside of the explosives initiator would likely to result in a compensation of the detonation pressure. The optimal angle between the ribs was demonstrated using an experimental set-up specifically designed for this study. This was mathematically analysed and validated.

The mechanical integrity of the design was demonstrated through tensile testing. All samples were conditioned at different environmental temperatures and tested. Non-metallic casing had shown superior performance to the specified criteria. The capability of track and trace through a radio frequency identification device was successfully illustrated. The development methodology can be visually summarised as shown in Figure 9.1.

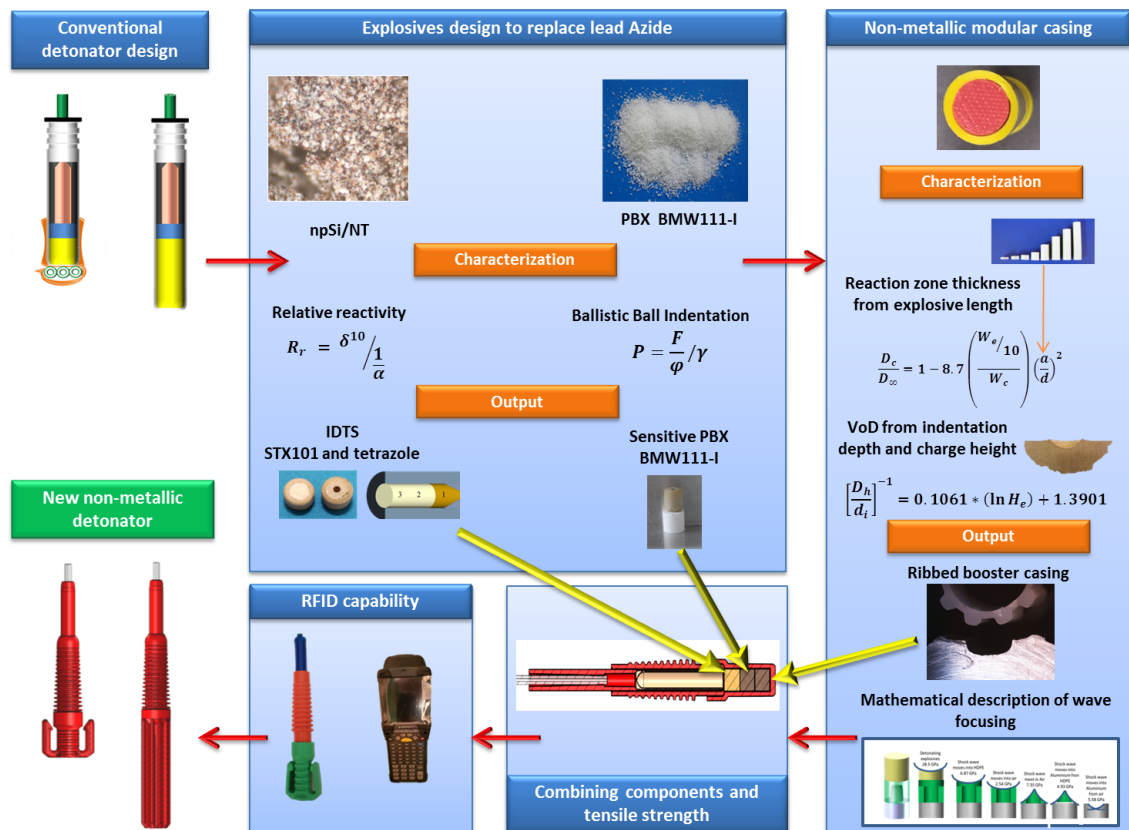



Figure 9.1: Graphical representation of the output of this research leading to the development of a new lead free and non-metallic detonator

Final assembled product specifications are shown in Table 9.1.

Table 9.1: Non-metallic assembly configuration

Non-metallic initiator assembly	Casing	Raw material	Explosives
	<p>Shock tube holder Material: HDPE Dimensions: Appendix 8A</p> <p>Main body Material: HDPE Dimensions: Appendix 8B</p> <p>Booster casing Material: HDPE Dimensions: Appendix 8C–8D</p>	<p>npSi Manufacturing process: dissolution chemistry Pore volume: $0.39 \pm 0.05 \text{ cm}^3 \cdot \text{g}^{-1}$ Surface area: $175 - 185 \text{ m}^2 \cdot \text{g}^{-1}$ % Oxidation: $\leq 1.3 \%$</p>	<p>Lead-free primary explosives STX101 Density: $1.50 - 1.60 \text{ g} \cdot \text{cm}^{-3}$ Explosive's mass: $0.023 - 0.024 \text{ g}$ Tetrazole 1 Density: $1.45 - 1.50 \text{ g} \cdot \text{cm}^{-3}$ Explosive's mass: $0.075 - 0.076 \text{ g}$ Tetrazole 2 Density: $2.10 - 2.20 \text{ g} \cdot \text{cm}^{-3}$ Explosive's mass: $0.050 - 0.060 \text{ g}$</p> <p>PBX base charge PETN 97.5 % Kraton 2.5 % Graphite 0.5 %</p> <p>Explosive pellet dimensions Diameter: $6.40 - 6.50 \text{ mm}$ Length : $6.40 - 6.50 \text{ mm}$ Density: $1.55 - 1.66 \text{ g} \cdot \text{cm}^{-3}$</p>

9.2 Concluding Remarks

From the study conducted, the following conclusions can be made:

- Nano-porous silicon with well-defined pores in the nanometre range was reproducibly manufactured by dissolution chemistry. Nano-porous silicon with a surface area of $107 - 180 \text{ m}^2 \cdot \text{g}^{-1}$ showed pore volumes of $0.21 - 0.39 \text{ cm}^3 \cdot \text{g}^{-1}$. npSi with surface area of $290 - 305 \text{ m}^2 \cdot \text{g}^{-1}$ showed pore volumes of $0.918 - 0.982 \text{ cm}^3 \cdot \text{g}^{-1}$. The relation of surface area to pore volume was found to be linear.

- The level of oxidation influenced the reactivity of explosive formulation prepared by mixing an oxidiser with nano-porous silicon. Data presented showed that 1.3% oxidation could be advantageous in terms of reactivity. This was shown for both organic (PETN) and inorganic (SP) oxidisers. The reactivity of the explosive formulation prepared using an organic oxidiser was more affected by the percentage oxidation of the npSi than the SP mixtures. The SP mixtures however, showed a sudden decline in reactivity when oxidation reaches 23%.
- Mixtures of nano-porous silicon and oxidisers in stoichiometric ratios produced high reactivity reactions. It was shown that higher reactivity reactions could only be obtained if the mixture ratios were non-stoichiometric with more oxidiser in the mixture than needed. This was shown for both organic and inorganic oxidisers.
- Nano-porous silicon / nitriminotetrazole mixtures increased in reactivity with an increase in density. The optimal density was shown to be 2.5 g.cm^{-3} . As the density of the mixture reached 2.0 g.cm^{-3} , a precipitous increase in reactivity was observed.
- The R_r test method established in this study proved to be a reliable method to evaluate the thermal reactivity of explosive formulations. This method distinguished between density effects, mixture ratios and the effect of particle size on the reactivity of formulations.
- Nano-porous silicon / nitriminotetrazole mixtures prepared with high surface area silicon produced the fastest reactions. A decrease in reaction pressure with a decrease in surface area of the nano-porous silicon was noticeable.
- Nano-porous silicon / NT mixtures could be used as a suitable replacement for lead azide.
- STX101 reliably initiated when exposed to the heat produced from a burning delay element and the heat produced from the flame of a fuse head, as well as the shock and heat produced from a shock tube.
- PBX formulations based on PETN and Kraton were successfully manufactured and evaluated. These formulations were prepared to be sensitive enough to

pick up from the npSi/NT mixtures and strong enough to initiate the main explosive charge.

- PBX formulations with different pick-up sensitivities were formulated based on particle size of the PETN as well as the solid content of the mixture.
- BMW111-I was be reliably initiated by STX101. In turn the output of BMW111-I was enough to reliably initiate the main explosive charge.
- The output pressure related to detonation pressure was successfully measured using the Ballistic Ball Indentation test.
- Reaction zone thickness was successfully calculated using explosive length instead of explosive diameter. Mathematical derivation in proving this concept was developed.
- The detonation velocity was calculated using explosive height and the diameter of the indentation on a witness plate. This was mathematically proven.
- Non-metallic confinement in small diameter applications only marginally affected the performance of explosive formulations. The plastic confinement did not significantly increase the VoD of explosives formulation as in the case of metallic confinement. The VoD of explosives confined by lightweight casing (polymeric) was mathematically explored.
- To accommodate improved explosive performance, a ribbed design was incorporated in the non-metallic booster part of the initiating system. This ensured shaping of the detonation wave enhancing the blast effect. The lost detonation energy (due to poor confinement) was recovered by wave-shaping techniques.
- The shaped design produced an indentation profile of approximately four times the depth of the rib height and twice the width of the outside edge. This profile was valid for indentations produced on an aluminium witness plate.
- The non-metallic design of an initiator was accomplished involving a non-metallic detonator casing, a delay element, LA replacement primary explosives and base charge explosives. The components were secured to one another

using ultrasonic welding. The use of this technique in the explosives industry to manufacture an explosives initiator was not known.

- The capability of track and trace for non-metallic initiating systems using RFID was demonstrated.

9.3 Recommendations for Future Research

A number of areas have been identified as possible future research initiatives as a consequence of this study:

- Developing a theoretical model for the BBI test.
- Building a thorough mathematical model demonstrating the interaction of the blast waves on an aluminium witness plate.
- Expanding the npSi manufacture to such an extent that it makes financial sense to manufacture npSi on mega production scale.
- Optimising the manufacture of tetrazole salts in order for it to be produced in large quantities.
- Develop an alternative to shock tube as a signal carrier.

BIBLIOGRAPHY

- Abraham, A., Piekel, N.W., Morris, C.J. & Dreizin, E.L. 2016. Combustion of energetic porous silicon composites containing different oxidizers. *Propellants, Explosives, Pyrotechnics*, 41(1):179-188.
- Agrawal, J.P. 2010. *High energy materials: propellants, and pyrotechnics*. Weinheim: Wiley-VCH.
- Akhavan, J. 1998. *The chemistry of explosives*. Cambridge: Royal Society of Chemistry.
- Akhavan, J. 2011. *The chemistry of explosives*. 3rd edition. Cambridge: Royal Society of Chemistry.
- Allongue, P. 1997. Porous silicon formation mechanisms. In Canham, L.T. (ed.). *Properties of porous silicon*. London: Institution of Electrical Engineers: 3-11.
- Ang, H.G. & Pisharath, S. 2012. *Energetic polymers: binders and plasticizers for enhancing performance*. Weinheim: Wiley-VCH.
- Arbestain, M.C., Rodríguez-Lado, L., Bao, M. & Macías, F. 2009. Assessment of mercury-polluted soils adjacent to old mercury-fulminate production plant. *Applied and Environmental Soil Science*, Article ID 387419, 8 pages. doi:10.1155/2009/387419
- Barbato, G. & Desogus, S. 1986. Problems in the measurements of Vickers and Brinell indentations. *Measurement*, 4(4):137-147.
- Bailey, A. & Murray, S.G. 2000. *Explosives, propellants and pyrotechnics*. London: Brassey's.
- Batchelor, L. & Loni, A. 2010. Stain etched silicon for primary explosives: preliminary batch preparation with AEL feedstocks. Farnborough: Intrinsic Materials.
- Becker, C.R., Apperson, S., Morris, C.J., Gangopadhyay, S., Currano, L.J., Churaman, W.A. & Stoldt, C.R. 2011. Galvanic porous silicon composites for high-velocity nanoenergetics. *Nona Letters*, 11(2):803-807.
- Becker, C.R., Currano, L.J., Churaman, W.A. & Stoldt, C.R. 2010. Thermal analysis of the exothermic reaction between galvanic porous silicon and sodium perchlorate. *ACS Applied Materials & Interfaces*, 2(11):2998-3003.
- Berger, B.P., Haas, B., Folly, P., Mathieu, J., Vine, T. & Griffiths, T.T. 2006. Pyrotechnic compositions containing nanometric silicon. *Proceedings of the 33rd International Pyrotechnics Seminar, Fort Collins, CO, 16–21 July*, 81-92.

- Bezuidenhout, H.C. 2009. Progress report on the development of a detonating porous silicon matrix. Modderfontein: AEL Mining Services.
- Bezuidenhout, H.C. & Mukhopadhyay, S. 2016. Nanoporous silicon based formulations for use in explosions initiating system. *International Journal of Applied Engineering Research*, 11(21):10465-10471.
- Blasting Cap. 2013. Blasting cap: definition. <http://www.answers.com/topic/blasting-cap-2> [19 March 2013].
- Bouma, R.H.B., Hordijk, A.C., Van der Steen, A.C, Halvorsen, T. & Skjold, E. 2001. Influence of RDX crystal quality and size on the sensitivity of RDX based PBXs. In *Insensitive Munitions and Energetic Materials Technology Symposium: EUROMURAT 2001, Bordeaux, France, 8–11 October*. 454-458.
- Brown, G I. 2010. *Explosives: history with a bang*. Stroud: History Press.
- Canham, L.T. 1997a. Chemical composition of 'ages' porous silicon. In Canham, L.T. (ed.). *Properties of porous silicon*. London: Institution of Electrical Engineers: 154-157.
- Canham, L.T. 1997b. Pore type, shape, size, volume and surface area in porous silicon. In Canham, L.T. (ed.). *Properties of porous silicon*. London: Institution of Electrical Engineers: 83-87.
- Canham, L.T. 1997c. Storage of porous silicon. In Canham, L.T. (ed.). *Properties of porous silicon*. London: Institution of Electrical Engineers: 44-49.
- Catholic Encyclopedia. 2012. Berthold Schwarz. <http://www.newadvent.org/cathen/13593b.htm> [19 March 2013].
- Charsley, E.L., Markham, H.M. & Rooney, J.J. 2006. Preliminary investigation of pyrotechnic incendiary compositions. *Proceedings of the 33rd International Pyrotechnics Seminar, Fort Collins, CO, 16–21 July*, 249-259.
- Chavez, D.E. & Parrish, D. A. 2010. Synthesis and characterization of 1-nitroguanyl-3-nitro-5-amino-1,2,4-triazole. *Propellants, Explosives, Pyrotechnics*, 35(1):1-4.
- Churaman, W.A. & Currano, L. 2007. Preparation of nanoporous silicon. ARL-TR-4306. Adelphi, MD: Army Research Laboratory.
- Churaman, W., Currano, L. & Becker, C. 2010. Initiation and reaction tuning of nanoporous energetic silicon. *Journal of Physics and Chemistry of Solids*, 71(2):69-74.

- Churaman, W., Currano, L., Singh, A.K., Rai, U.S., Dubey, M., Amirtharaj, P. & Ray, P.C. 2008. Understanding the high energy behaviour of nano-energetic porous silicon. *Chemical Physics Letters*, 464(4-6):198-201.
- Churaman, W.A., Morris, C.J., Ramachandran, R. & Bergbreiter, S. 2015. The effect of porosity on energetic porous silicon solid propellant micro-propulsion. *Journal of Micromechanics and Microengineering*, 25(11):1-5.
- Clément, D., Diener, J., Gross, E., Künzner, N., Timoshenko, V.Y. & Kovalev, D. 2005. Highly explosive nanosilicon-based composite materials. *Physica Status Solidi (a)* 202(8):1357-1364.
- Coffer, J.L. 1997. Porous silicon formation by stain etching. In Canham, L.T. (ed.). *Properties of porous silicon*. London: Institution of Electrical Engineers: 23-29.
- Conkling, J.A. 1985. *Chemistry of pyrotechnics: basic principles and theory*. Baton Roca, FL: CRC Press.
- Cooper, P.W. 1996. *Explosives engineering*. New York, NY: Wiley-VCH.
- Department of Labour. 2006. *Occupational health and Safety act and regulations*. Pietermaritzburg, KZN: Interpak Books.
- Dobratz, B.M. & Crawford, P.C. 1985. *LLNL explosives handbook: properties of chemical explosives and explosive simulants*. Livermore, CA: Lawrence Livermore National Laboratory, University of California.
- Dozolme, P. 2013. Different types of detonators. <http://mining.about.com/od/surfacemining101/a/Different-types-of-detonators.htm> [20 March 2013].
- Du Plessis, M. 2007. Properties of porous silicon nano-explosive devices. *Sensors and Actuators A*, 135(2):666-674.
- Du Plessis, M. 2008. Nanoporous silicon explosive devices. *Materials Science and Engineering B*, 147(2-3):226-229.
- Dubey, R.S. & Gautam, D.K. 2009. Synthesis and characterization of nanocrystalline porous silicon layer for solar cells application. *Journal of Optoelectronic and Biomedical Materials*, 1(1):8-14.
- Duguet, J.R. 2009. *Initiation of explosives and pyrotechnic materials: chemicals, components, processes*. Port-des-Barques: Cultures et Techniques.

- Ernst, S. 2009. *Advances in nanoporous materials*. Amsterdam: Elsevier Science.
- Ervin, M.H., Issacson, B. & Levine, L.B. 2015. Process for integration of energetic porous silicon devices. *Journal of Physics: Conference Series*, 660:1-5. doi:10.1088/1742-6596/660/1/012067
- Eyring, H., Walker, F.E., Ma, S. & Coon, N. 1980. Similarity and differences between condition for initiation and failure of detonation. *Proceedings of the National Academy of Sciences of the United States of America*, 77(5):2358-2361.
- Explosives.org. 2009. History of explosives and blasting. <http://www.explosives.org/index.php/component/content/article?id=69> [11 March 2013].
- Federation of European Explosives Manufacturers (FEEM). 2009. Guidance note on the FEEM European Explosives Code structure. Commission Directive 2008/43/EC of 4 April 2008 & Commission Directive 2012/4/EU of 22 February 2012 amending Directive 2008/43/EC on Identification & Traceability of Explosives for Civil Uses.
- Fickett, W. & Davis, W.C. 2000. *Detonation: theory and experiment*. Mineola, NY: Dover.
- First Foot Guards. 2013. History of black powder. http://footguards.tripod.com/06ARTICLES/ART28_blackpowder.htm [12 March 2013].
- Föll, H., Carstensen, J. & Frey, S. 2006. Porous and nanoporous semiconductors and emerging applications. *Journal of Nanomaterials*, Article ID 91635, doi 10.1155/JNM/2006/91635
- Fowler, T. 2008. A brief history of lead regulation. <http://scienceprogress.org/2008/10/a-brief-history-of-lead-regulation.htm> [23August 2017].
- Fronabarger, J.W., Williams, M.D., Sanborn, W.B., Bragg, J.G., Parrish, D.A. & Bichay, M. 2011. DBX-1 – A lead free replacement for lead azide. *Propellants, Explosives, Pyrotechnics*, 36(1):541-550.
- Gagliardi, F.J., Chambers, R.D. & Tran, T.D. 2005. Small-scale performance testing for studying new explosives. Paper presented at the 6th VACETS Technical Information Conference (VTIC'05), Milpitas, CA, 3–4 June. <https://e-reports-ext.llnl.gov/pdf/319763.pdf>
- Gale encyclopedia of science*. 2nd edition. 2001. Explosives. Detroit, MI: Gale.

- Gharbi, A., Remaki, B., Halimaoui, A., Bensahel, D. & Souifi, A. 2011. P-type silicon doping profiling using electrochemical anodization. *Journal of Applied Physics*, 109(2): 023715-1 – 023715-5. doi:10.1063/1.3534005
- Gleason, K.K., Wu, Q. & Ross, A. 2006. Porous material formation by chemical vapor deposition onto colloidal crystal templates. US 7112615 B2.
- GlobalSecurity.org. 2006. Primary explosives.
<http://www.globalsecurity.org/military/systems/munitions/explosives-primary.htm> [25 April 2014].
- Gräf, D., Grundner, M., Schultz, R. & Mühlhoff, L. 1990. Oxidation of HF-treated Si water surfaces in air. *Journal of Applied Physics*, 68(10):5155-5161.
- Halimaoui, A. 1997. Porous silicon formation by anodisation. In Canham, L.T. (ed.). *Properties of porous silicon*. London: Institution of Electrical Engineers: 12-22.
- Haskins, P.J., Cook, M.D. & Wood, A.D. 2006. On the dependence of critical diameter and velocity decrement at failure on the burn law. *Proceedings of the 33rd International Pyrotechnics Seminar, Fort Collins, CO, 16–21 July*.
- Held, M. 1989. Corner-turning distance and retonation radius. *Propellants, Explosives, Pyrotechnics*, 14(4):153-161.
- Helmenstine, A.M. 2013. Gunpowder facts and history.
<http://chemistry.about.com/od/historyofchemistry/a/gunpowder.htm> [11 March 2013].
- Henrino, R. 1997. Pore size distribution in porous silicon. In Canham, L.T. (ed.). *Properties of porous silicon*. London: Institution of Electrical Engineers: 89-96.
- Henry, M.D., Welch, C. & Scherer, A. 2009. Techniques of cryogenic reactive ion etching in silicon for fabrication of sensors. *Journal of Vacuum Science and Technology*, A27(5):1221-1216.
- Huynh, M.H.V., Coburn, M.D., Meyer, T.J. & Wetzler, M. 2006. Green primary explosives: 5-nitrotetrazolato- N^2 -ferrate hierarchies. *Proceedings of the National Academy of Sciences of the United States of America*, 103(27):10322-10327.
- Insight Bulletins. 2015. EU-REACH annex XVII: Regulation on lead restrictions in consumer products published. <http://www.Intertek.com/consumer/insight-bulletins/regulation-on-lead-restrictions-in-customer-products.htm> [23 August 2015].
- Johansson C.H. & Persson P.A. 1970. *Detonics of high explosives*. London: Academic Press.

- Johnson, N.C. 2001. CL-20 sensitivity testing and the development of a CL-20 database. In *Insensitive Munitions and Energetic Materials Technology Symposium: EUROMURAT 2001, Bordeaux, France, 8–11 October*. 743-744.
- Kapil, A. 2015. Passive vs active RFID: advantages and disadvantages. <http://blog.mainspringhealth.com/passive-active-rfid-advantages-and-disadvantages.htm> [23 August 2015].
- Kaur, M., Sandhu, M., Mohan, N. & Sandhu, P.S. 2011. RFID technology principles, advantages, limitations and its application. *International Journal of Computer and Electrical Engineering*, 3(1):1739-8163.
- Kellerman, F. 2013. A short history of explosives: mystery author at first look at the crime. http://www.mysterynet.com/kellerman_faye/explosives.shtml [11 March 2013].
- Kent, J.A. (ed.). 2003. *Riegel's handbook of industrial chemistry*. 10th edition. New York, NY: Kluwer Academic/Plenum.
- Klapötke, T.M., Karaghiosoff, K., Mayer, P., Penger, A. & Welch, M. 2006. Synthesis and characterization of 1,4-dimethyl-5-aminotetrazolium 5-Nitrotetrazolate. *Propellants, Explosives, Pyrotechnics*, 31(3):188-195.
- Klapötke, T.M., Laub, H.A. & Stierstorfer, J. 2008. Synthesis and characterization of a new class of energetic compounds-ammonium nitrotetrazolate. *Propellants, Explosives, Pyrotechnics*, 33(3):421-430.
- Klapötke, T.M. 2011. *Chemistry of high-energy materials*. Berlin: De Gruyter.
- Kloppers, P.H. 1987. *Statistiek vir technikon studente*. 3e uitgawe. Pretoria: MK Uitgewers.
- Lamy-Bracq, P., Regis, M., Roger, M. & Fedou, H.F. 2007. Research of the contribution of nano particles in pyrotechnics. *Proceedings of the 34th International Pyrotechnics Seminar, Beaune, France, 8–11 July*.
- Lee, J.H.S. 2008. *The detonation phenomenon*. Cambridge: Cambridge University Press.
- Lehmann, V. & Gösele, U. 1991. Porous silicon formation: a quantum wire effect. *Applied Physics Letters*, 58(8):856-858.
- Lindahall.org. 2013. The use of black powder and nitroglycerine on the transcontinental railroad. <http://railroad.lindahall.org/essays/black-powder.html> [11 March 2013].

- Loboiko, B.G. & Lubyatinsky, S.N. 2000. Reaction zones of detonating solid explosives. *Combustion, Explosion and Shock Waves*, 36(6):716-733.
- Logistics and Materials Handling Blog. 2012. RFID vs Barcodes: Advantages and disadvantages comparison. http://www.aalhyesterforklifts.com.au/index.php/about/blog-post/rfid_vs_barcodes_advantages_and_disadvantages_comparison.htm [23 August 2017].
- Loni, A. 1997. Capping of porous silicon. In Canham, L.T. (ed.). *Properties of porous silicon*. London: Institution of Electrical Engineers: 51-57.
- Loni, A. & Canham, L.T. 2011. Initiators using porous silicon: Phase One report. Farnborough: Intrinsic Materials.
- Malec, C.D., Voelcker, N.H., Shapter, J.G. & Ellis, A.V. 2010. Carbon nanotubes initiate the explosion of porous silicon. *Materials Letters*, 64:2517-2519.
- Mehta, N., Damavarapu, R., Cheng, G., Dolch, T., Rivera, J., Duddu, R. & Yang, K. 2009. Alternates to lead azide and lead based materials – green replacement. *Proceedings of the 36th International Pyrotechnics Seminar, Rotterdam, Netherlands, 23–28 August*.
- Mikulec, F.V., Kirtland, J.D. & Sailor, M.J. 2002. Explosive nanocrystalline porous silicon and its use in atomic emission spectroscopy. *Advanced Materials*, 14(1):38-41.
- MIL-STD-331C. 2005. Department of Defense test method for standard: fuze and fuze components environmental and performance tests.
- Molecular Expressions™: Science, Optics and You. 2013. Rodger Bacon (1214–1294). <http://micro.magnet.fsu.edu/optics/timeline/people/bacon.html> [12 March 2013].
- Morgan, M.G., Pietrobon, R.A., Stringer, M.B. & Provatas, A. 2008. Preliminary results of an investigation into the use of polymeric binders in pyrotechnics (PBP). *Proceedings of the 35th International Pyrotechnics Seminar, Fort Collins, CO, 13–18 July*.
- Nassiopoulos, A. G. 1997. Local formation and patterning of porous silicon. In Canham, L.T. (ed.). *Properties of porous silicon*. London: Institution of Electrical Engineers: 51-57.
- Needham, C.E. 2010. *Blast waves*. Heidelberg: Springer.
- Nicholson, J.W. 1991. *The chemistry of polymers*. Cambridge: Royal Society of Chemistry.

- Nitroglycerin. 2013. Nitroglycerin.
http://www.ch.ic.ac.uk/rzepa/mim/environmental/html/nitroglyc_text.htm
 [19 March 2013].
- Once Upon A Time. 2013. World famous and infamous – Alfred Bernhard Nobel.
<http://www.jcs-group.com/once/famous/nobel.html> [11 March 13].
- Owen, D. 2006. Scientists target greener, safer primary explosives. *Chemistry and Industry Magazine*, 8:9, April 17.
- Parimi, V.S., Lozda, A.B., Tadigadapa, S.A. & Yetter, R.A. 2014. Reactive wave propagation in energetic porous silicon composites. *Combustion and Flame*, 161(11):2991-2999.
- Parimi, V.S., Tadigadapa, S.A. & Yetter, R.A. 2015. Reactive wave propagation mechanisms in energetic porous silicon composites. *Combustion Science and Technology*, 187(1-2):249-268.
- Parson, J., Dickens, J.C., Walter, J. & Neuber, A.A. 2010. Pulsed magnetic field excitation sensitivity of match-type electric blasting caps. *Review of Scientific Instruments*, 81(10):105115.
- Philbin, S.P. 2000. Current strands of research in DERA on the chemistry of energetic materials and insensitive munitions. *2000 Insensitive Munitions & Energetic Materials Technology Symposium: IM/EM Technology Implementation in the 21st Century, San Antonio, TX, 27–30 November*. 208-210.
- Piekel, N.W., Morris, C.J., Churaman, W.A., Cunningham, M.E., Lunking, D.M. & Currano, L. J. 2015. Combustion and material characterization of highly tunable on-chip energetic porous silicon. *Propellants, Explosives, Pyrotechnics*, 40(1):16-26.
- Plummer, A., Coa, H., Dawson, R., Lowe, R., Shapter, J. & Voelcker, N.H. 2008. The influence of pore size and oxidising agent on the energetic properties of porous silicon. In Voelcker, N.H & Thissen, H.W. (eds). *Smart Materials V: Proceedings of SPIE, Melbourne, Australia, 10–12 December, Vol. 7267*. Bellingham, WA: SPIE: 1-9.
- Price, D. 1981. Critical parameters for detonation propagation and initiation of solid explosives. NSWC TR 80-339. Silver Spring, MD: Naval Surface Weapons Center.
- Price, D. 1982. The detonation velocity-loading density relation for selected explosives and mixtures of explosives. NSWC TR 82-298. Silver Spring, MD: Naval Surface Weapons Center.
- Ramachandran, R.R., Churaman, W., Lunking, D. & Morris C.J. 2014. Characterization of energetic porous silicon for microelectromechanical system (MEMS)-based solid propellant microthruster. ARL TR-7087. Adelphi, MD: Army Research Laboratory.

- Redner, P. (2010). The history, chemistry, and physics of energetic materials. In Boddu, V. & Redner, P. (eds). 2010. *Energetic materials: thermophysical properties, predictions, and experimental measurements*. Boca Raton, FL: CRC Press: 7-36.
- Regulations. 2015. Commission regulation (EU) 2015/628 of 22 April 2015. 2015. *Official Journal of the European Union*, OJL 396:1.
- Rhodes, M. (ed.). 2008. *Introduction to particle technology*. 2nd edition. Chichester: John Wiley.
- Richmond, O., Morrison, H.L. & Devenpeck, M.L. 1974. Sphere indentation with application to the Brinell hardness test. *International Journal of Mechanical Sciences*, 16(1):75-82.
- RSA-MIL-STD-153. 1992. Kwalifisering van sekondêre springstowwe vir aanwending in aanjaer ladings. Pretoria: Armscor.
- Sabatini, J.J. & Oyler, K.D. 2016. Recent advances in the synthesis of high explosives materials. *Crystals*, 6(5):1-22. doi:10.3390/cryst6010005
- Sailor Research Group. 2003. Sailor Research Group, Department of Chemistry and Biochemistry, University of California, San Diego, CA. http://sailorgroup.ucsd.edu/research/porous_Si_intro.html [16 August 2010].
- Sailor, M.J., Mikulec, F.V. & Kirtland, J.D. 2004. Porous silicon-based explosive. US 20040244889 A1 9 12 2004.
- Science Clarified. n.d. <http://www.scienceclarified.com/Ex-Ga/Explosives.html> [24 June 2011].
- Science Daily*. 2002. Computer chips found to possess explosive properties useful for chemical analysis and nanoscale sensors. January 10. <https://www.sciencedaily.com/releases/2002/01/020110074039.htm>. [11 April 2006].
- Shugaev, F.V. & Shtemenko, L.S. 1998. *Propagation and reflection of shock waves*. River Edge, NJ: World Scientific.
- Sirius Analytical. 2017. Dissolution definitions. <http://www.sirius-analytical.com/science/dissolution/dissolution-definitions> [5 January 2015].
- Souers, P.C. 1997. Size effect and detonation front curvature. *Propellants, Explosives, Pyrotechnics*, 22(4):221-225.

- Souers, P.C. 1998. *A library of prompt detonation reaction zone data*. Livermore, CA: National Technical Information Service, Lawrence Livermore National Laboratory.
- Souers, P.C. 1999. Measuring explosive non-ideality. Report number UCRL-JC-132499. Paper presented at the International Workshop on the Modeling of Non-Ideal Explosives, Energetic Materials Research and Testing Center, New Mexico, Institute of Mining and Technology, Socorro, NM, 16–18 March.
- Souers, P.C., Vitello, P., Esen, S., Kruttschnitt, J. & Bilgin, H.A. 2004. The effects of confinement on detonation velocity. *Propellants, Explosives, Pyrotechnics*, 29(1):19-26.
- Spitzer, D., Comet, M., Baras, C., Pichot, V. & Piazzon, N. 2010. Energetic nano-materials: opportunities for enhanced performances. *Journal of Physics and Chemistry of Solids*, 71(2):100-108.
- Subramanian, S. & Santosh, L. 2008. Nanoporous silicon for energetic applications. Monmouth Junction, NJ: Vesta Sciences.
- Subramanian, S., Tiegs, T., Limaye, S., Kapoor, D. & Redner, P. 2009. *Nanoporous silicon based energetic materials*. Fort Belvoir, VA: Defense Technical Information Center.
- Szendrei, T. 2010. Prediction of the blast noise levels from Ash Dump 5. Johannesburg: Dynamic Physics Consultants.
- Teipel, U. (ed.). 2005. *Energetic materials: particle processing and characterization*. Weinheim: Wiley-VCH.
- Thiruvengadathan, R., Bezmelnitsyn, A., Apperson, S.J., Tappmeyer, D., Redner, P., Balas, W.A., Nicolich, S., Kapoor, D., Gangopadhyay, K. & Gangopadhyay, S. 2010. Combustion behavior of nanoenergetic material systems. In Boddu, V. & Redner, P. (eds). 2010. *Energetic materials: thermophysical properties, predictions, and experimental measurements*. Boca Raton, FL: CRC Press: 221-262.
- Tillotson, T.M., Gash, A.E., Simpson, R.L., Hrubesh, L.W., Satcher, J.H. & Poco, J.F. 2001. Nanostructured energetic materials using sol-gel methodologies. *Journal of Non-Crystalline Solids*, 285(1-3):338-345.
- Torres-Costa, V. & Martín-Palma, R.J. 2010. Application of nanostructured silicon in the field of optics. A review. *Journal of Materials Science*, 45(11):2823-2838.
- Van der Heijden, A.E.D.M., Creyghton, Y.L.M., Van de Peppel, R.J.E. & Adadjieva, E. 2010. Modification and characterization of (energetic) nanomaterials. *Journal of Physics and Chemistry of Solids*, 71(2):59-63.
- Virginia Semiconductor, Inc. 2003. Wet-chemical etching and cleaning of silicon. Fredericksburg, VA: Virginia Semiconductor, Inc.

Wikipedia. 2011. Detonator. http://en.wikipedia.org/wiki/Blasting_cap [20 June 2011].

White, R. 2007. Isotropic silicon etching using HF/nitric/acetic acid (HNA): standard operating procedure. Department of Mechanical Engineering, School of Engineering, Tufts University, Medford, MA.
<https://www.seas.upenn.edu/~nanosop/documents/IsotropicSiliconEtch.pdf> [19 March 2013].

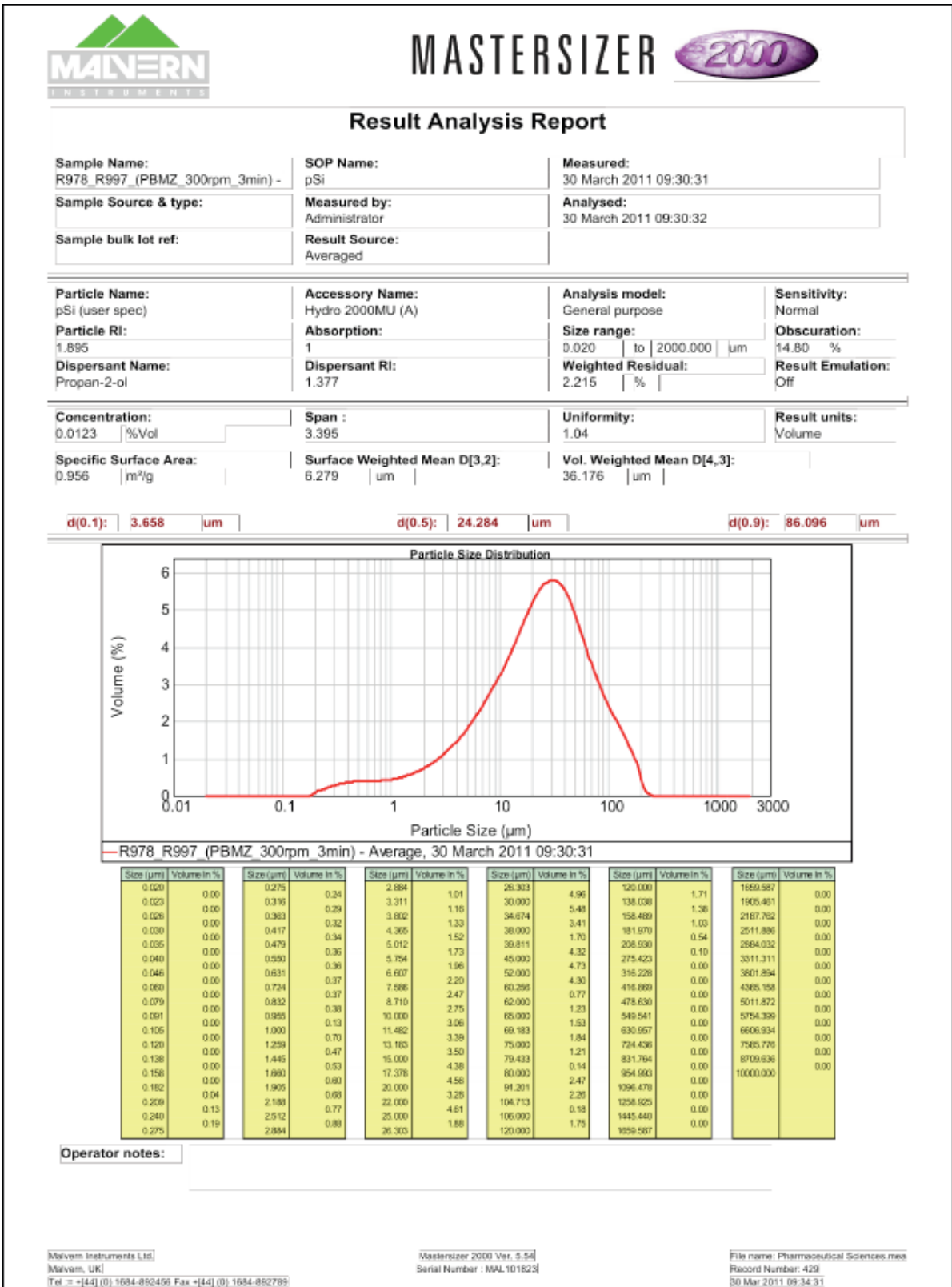
Zandipour, S. 2014. States of matter project – explosives.
<http://Prezi.com/m/j0ca8s7rxqwh/states-of-matter-project-explosives/> [15 February 2014].

Zel'dovich, Y.B. & Raizer, Y.P. 2002. *Physics of shock waves and high-temperature hydrodynamic phenomena*, edited by W.D. Hayes & R.F. Probstein. Mineola, NY: Dover.

Zukas, J.A. & Walters, W. (eds). 1998. *Explosive effects and applications*. New York, NY: Springer.

APPENDICES

APPENDIX 3A: npSi particle size distribution



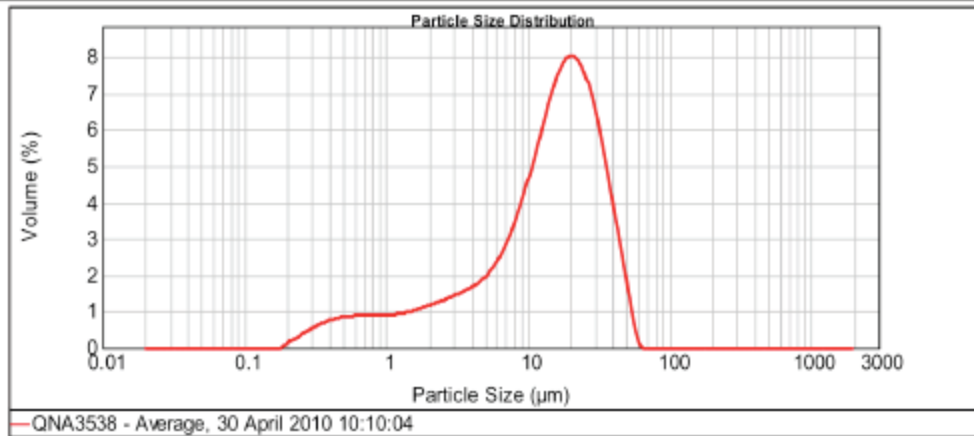
Result Analysis Report

Sample Name: QNA3538 - Average	SOP Name: pSi	Measured: 30 April 2010 10:10:04
Sample Source & type:	Measured by: Administrator	Analysed: 30 April 2010 10:10:05
Sample bulk lot ref:	Result Source: Averaged	

Particle Name: pSi (user spec)	Accessory Name: Hydro 2000MU (A)	Analysis model: General purpose	Sensitivity: Normal
Particle RI: 1.991	Absorption: 1	Size range: 0.020 to 2000.000 μm	Obscuration: 10.72 %
Dispersant Name: Propan-2-ol	Dispersant RI: 1.377	Weighted Residual: 1.151 %	Result Emulation: Off

Concentration: 0.0050 %Vol	Span : 2.197	Uniformity: 0.669	Result units: Volume
Specific Surface Area: 1.61 m^2/g	Surface Weighted Mean D[3,2]: 3.715 μm	Vol. Weighted Mean D[4,3]: 16.795 μm	

d(0.1): 1.534 μm **d(0.5):** 14.991 μm **d(0.9):** 34.474 μm



Size (μm)	Volume In %	Size (μm)	Volume In %	Size (μm)	Volume In %	Size (μm)	Volume In %	Size (μm)	Volume In %	Size (μm)	Volume In %
0.020	0.00	0.275	0.47	2.884	1.31	26.303	6.00	120.000	0.00	1699.587	0.00
0.023	0.00	0.315	0.58	3.311	1.41	30.000	5.60	136.038	0.00	1905.461	0.00
0.026	0.00	0.363	0.67	3.802	1.53	34.674	5.00	156.489	0.00	2187.762	0.00
0.030	0.00	0.417	0.74	4.365	1.68	38.000	2.91	181.970	0.00	2511.886	0.00
0.035	0.00	0.479	0.78	5.012	1.89	39.811	1.28	206.930	0.00	2894.032	0.00
0.040	0.00	0.550	0.80	5.754	2.19	45.000	2.06	275.423	0.00	3311.311	0.00
0.046	0.00	0.631	0.80	6.607	2.58	52.000	2.74	316.228	0.00	3801.894	0.00
0.060	0.00	0.724	0.80	7.586	3.11	60.256	0.78	416.869	0.00	4365.158	0.00
0.079	0.00	0.832	0.80	8.710	3.76	62.000	0.02	476.630	0.00	5011.872	0.00
0.091	0.00	0.955	0.27	10.000	4.53	65.000	0.00	549.541	0.00	5754.369	0.00
0.105	0.00	1.000	1.38	11.482	5.34	69.183	0.00	630.957	0.00	6606.594	0.00
0.120	0.00	1.259	0.87	13.183	5.71	75.000	0.00	724.436	0.00	7585.776	0.00
0.138	0.00	1.445	0.93	15.000	7.20	79.433	0.00	831.794	0.00	8709.636	0.00
0.158	0.00	1.660	0.99	17.378	7.30	80.000	0.00	954.993	0.00	10000.000	0.00
0.182	0.07	1.905	1.07	20.000	5.02	91.201	0.00	1096.478	0.00		
0.209	0.21	2.188	1.15	22.000	6.56	104.713	0.00	1258.025	0.00		
0.240	0.36	2.512	1.23	25.000	2.49	106.000	0.00	1445.440	0.00		
0.275	0.36	2.884	1.23	26.303	2.49	120.000	0.00	1658.587	0.00		

Operator notes:

APPENDIX 3B: HF specification

ANYLSPEC hydrofluoric acid (www.omqi.com)

Issue No: B-001
Issue Date: 12.02.08
Code: SHF40

CODE: SHF40

Assay min. 40%
Residue after Ignition max. 20 ppm
Chloride max. 5 ppm

TRACE ELEMENTS

Fe Iron
Pb Lead
Na Sodium

ISSUE NO: A-001

max. 1.0 ppm
max. 1.0 ppm
max. 1.0 ppm

APPENDIX 3C: Methanol specification

ISOCLEAN methanol (www.omqi.com)

Issue No: B-001
 Issue Date: 12.02.08
 Code: IMETH

	Trace Elements
Assay (CH ₃ OH)	min. 99.9 %
Colour	max. 10 Hazen
Free Acid (HCOOH)	max. 10 ppm
Free Alkali (NH ₃)	max. 1 ppm
Substance reducing	
Potassium permanganate	max 2.5 ppm
Water	max. 0.1 %
Nonvolatile substance	max. 5 ppm

PARTICLE CONCENTRATION

> 0.5u	max. 1500	per 10ml
> 1.0u	max. 300	per 10ml
> 2.0u	max. 70	per 10ml
> 5.0u	max. 10	per 10ml
>10.0u	max. 2.5	per 10ml

Ag	Silver	max.	0.01	ppm
Al	Aluminium	max.	0.05	ppm
As	Arsenic	max.	0.01	ppm
Au	Gold	max.	0.01	ppm
Ba	Barium	max.	0.01	ppm
Be	Beryllium	max.	0.01	ppm
Bi	Bismuth	max.	0.01	ppm
B	Boron	max.	0.02	ppm
Ca	Calcium	max.	0.1	ppm
Cd	Cadmium	max.	0.01	ppm
Co	Cobalt	max.	0.01	ppm
Cr	Chromium	max.	0.01	ppm
Cu	Copper	max.	0.01	ppm
Fe	Iron	max.	0.1	ppm
Ga	Gallium	max.	0.01	ppm
K	Potassium	max.	0.05	ppm
Li	Lithium	max.	0.01	ppm
Mg	Magnesium	max.	0.05	ppm
Mn	Manganese	max.	0.01	ppm
Mo	Molybdenum	max.	0.01	ppm
Na	Sodium	max.	0.2	ppm
Ni	Nickel	max.	0.01	ppm
Pb	Lead	max.	0.01	ppm
Sb	Antimony	max.	0.01	ppm
Sn	Tin	max.	0.01	ppm
Sr	Strontium	max.	0.01	ppm
Ti	Titanium	max.	0.01	ppm
Tl	Thallium	max.	0.01	ppm
V	Vanadium	max.	0.01	ppm
Zn	Zinc	max.	0.02	ppm
Zr	Zirconium	max.	0.01	ppm

APPENDIX 3D: Acetone specifications

AnalaR NORMAPUR grade acetone (www.uk.vwr.com)

Assay (on anhydrous substance)	Min. 99.8 %
Aqueous solution	Passes test
IR Spectrum	Passes test
Acidity	Max. 0.0003 meq/g
Alkalinity	Max. 0.0003 meq/g
Colouration	Max. 10 APHA
Density (20/4)	0.790 to 0.792
Distillation range	56 to 57 °C
Aldehydes (as HCHO)	Max. 10 ppm
Ethanol	Max. 100 ppm
Evaporation residue	Max. 5 ppm
Methanol	Max. 0.05 %
Propan-2-ol	Max. 100 ppm
Substances reducing KMnO ₄ (as O)	Max. 2 ppm
Water	Max. 0.2 %
Ba (Barium)	Max. 0.05 ppm
Al (Aluminium)	Max. 0.1 ppm
Cd (Cadmium)	Max. 0.01 ppm
Ca (Calcium)	Max. 0.5 ppm
Cr (Chromium)	Max. 0.02 ppm
Co (Cobalt)	Max. 0.01 ppm
Fe (Iron)	Max. 0.05 ppm
Cu (Copper)	Max. 0.01 ppm
Mg (Magnesium)	Max. 0.05 ppm
K (Potassium)	Max. 0.1 ppm
Na (Sodium)	Max. 0.5 ppm
Mn (Manganese)	Max. 0.01 ppm
Pb (Lead)	Max. 0.01 ppm
Ni (Nickel)	Max. 0.01 ppm
Sr (Strontium)	Max. 0.02 ppm
Sn (Tin)	Max. 0.1 ppm
Zn (Zinc)	Max. 0.01 ppm

APPENDIX 4A: Heat of formation of elements and bonds

Heat of formation of elements and bonds

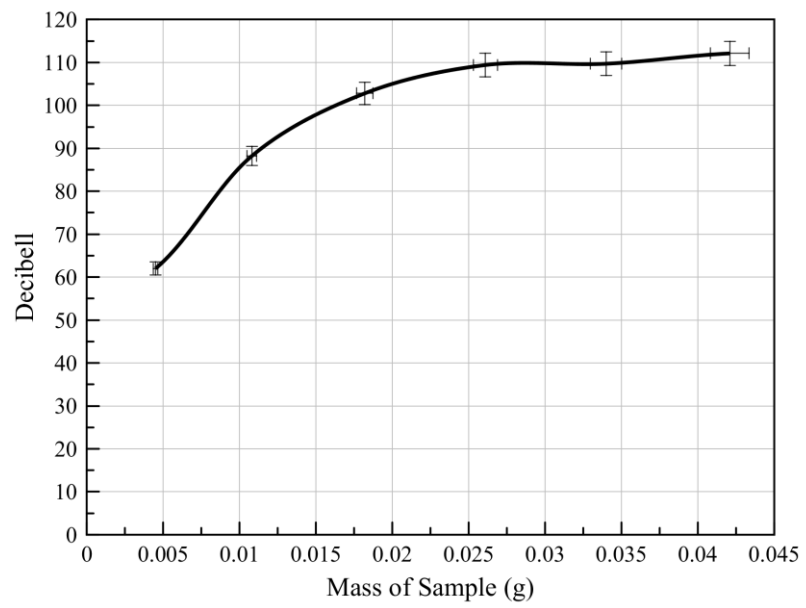
Elements and bonds	State	ΔH_f^0 kJ.mol ⁻¹
N ₂	gas	0
H ₂	gas	0
C	gas	0
O	gas	0
Si	solid	0
SiO ₂	solid	-910.7
NaClO ₄	solid	-384.2
NaCl	solid	-411.2
LiClO ₄	solid	-382.2
LiCl	solid	-408.6
Ba(ClO ₄) ₂	solid	-809.8
BaCl ₂	solid	-858.6
H ₂ O	gas	-241.8
CO	gas	-110.5
CO ₂	gas	-393.5
PETN [#]	solid	-128.7
NT [^]	solid	111
HNS [#]	solid	18.7

ΔH_f^0 values obtained from the *Handbook of Chemistry and Physics*, 73rd edition, 1992–1993: 5-1 to 5-50.

[#] ΔH_f^0 values obtained Cooper (1996:125)

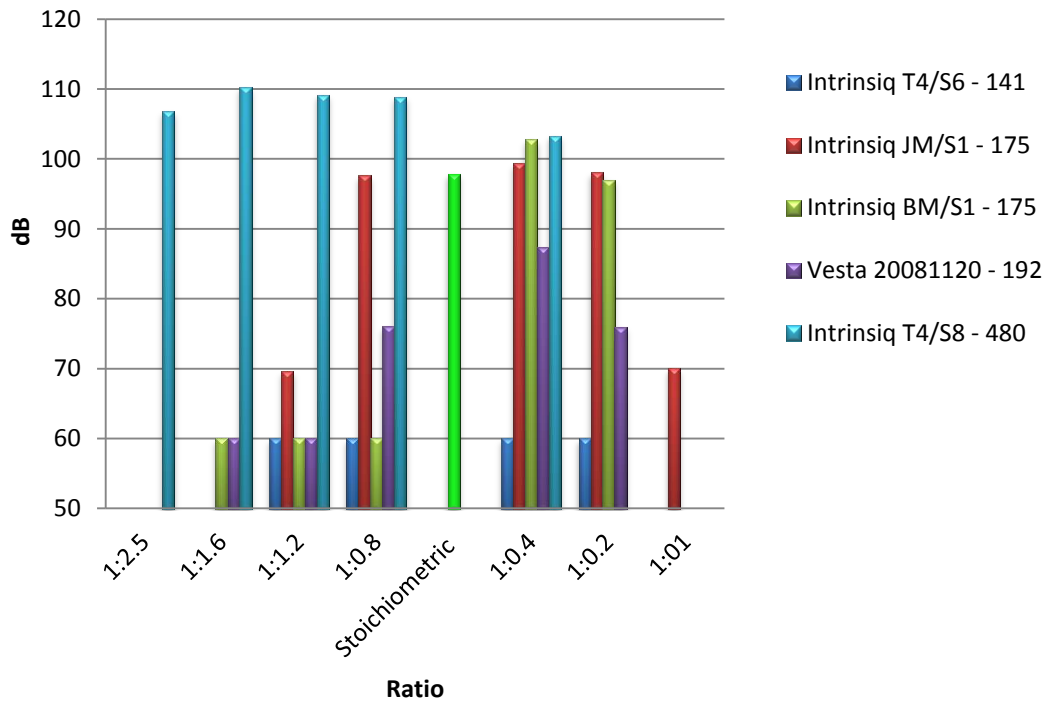
[^] ΔH_f^0 values obtained from *Klapötke et al. (2008:428)*

APPENDIX 4B: Noise generation related to sample mass

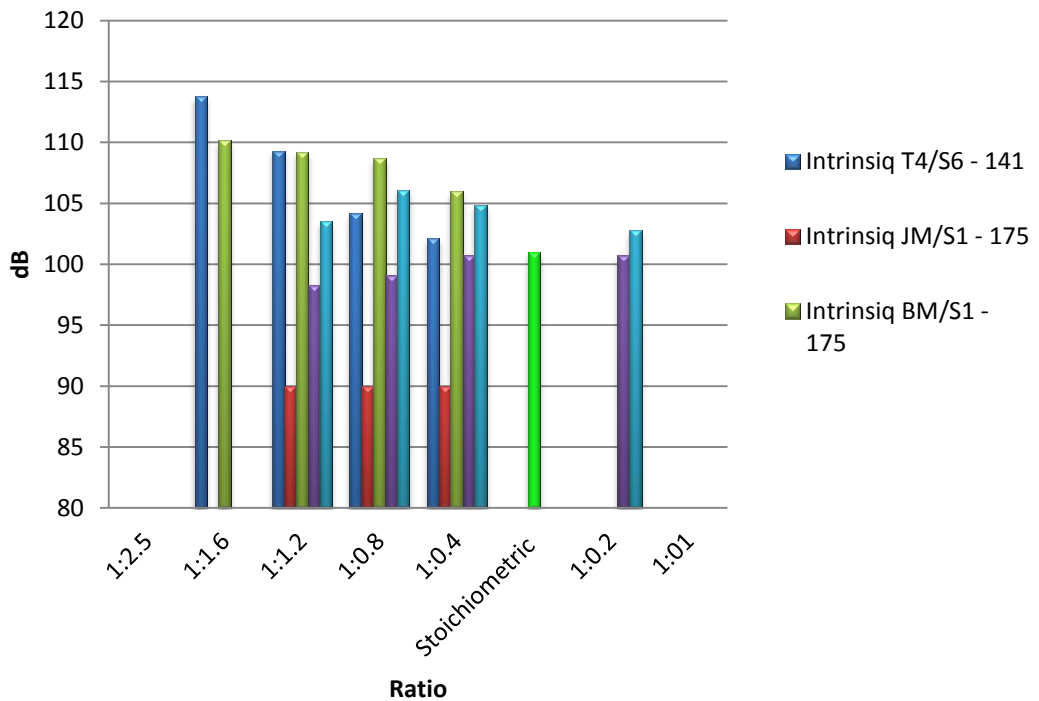


Noise generation related to sample mass

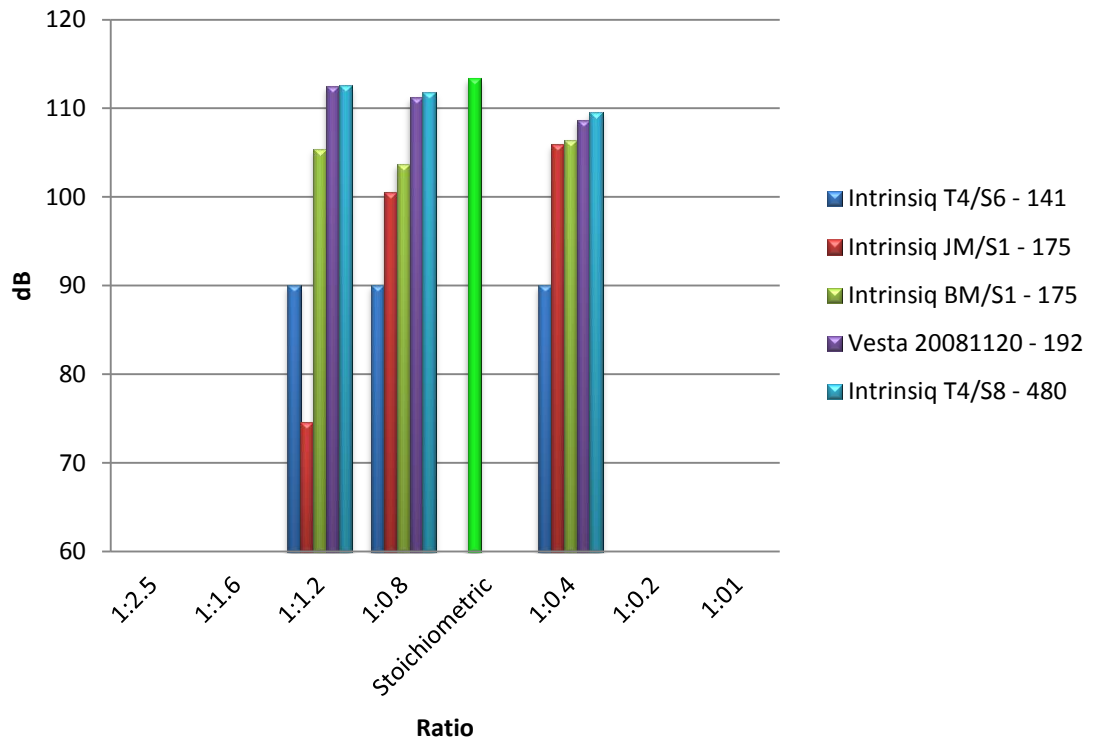
APPENDIX 4C: Reactivity of npSi explosives manufactured from different oxidisers and various surface areas



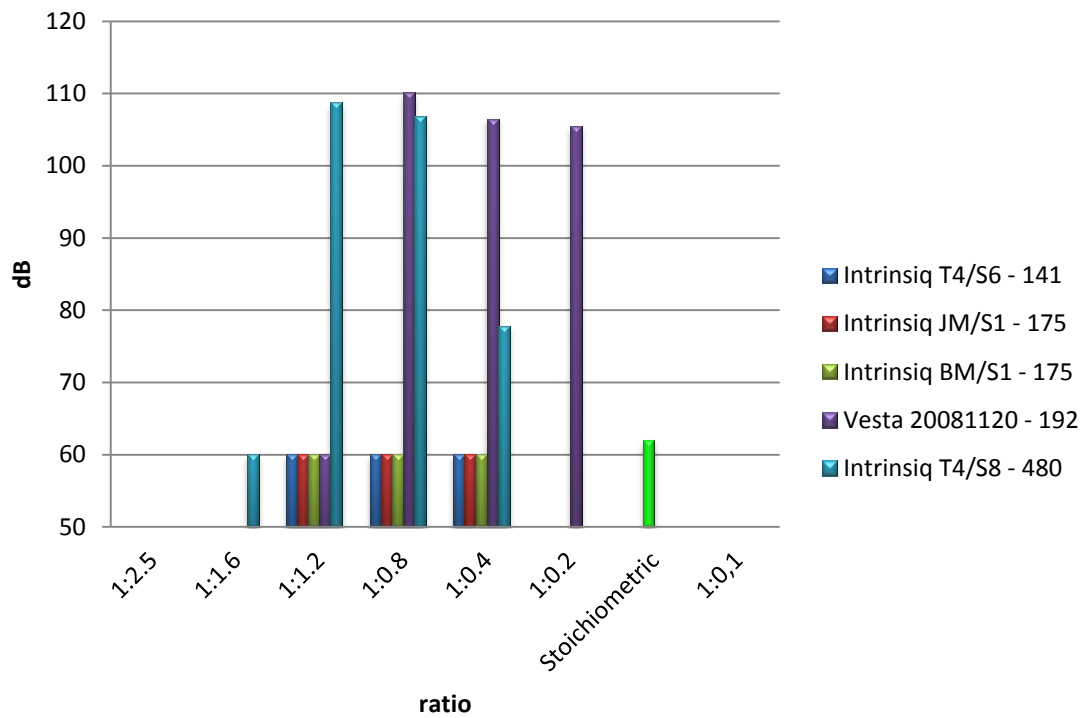
Schematic depiction of the reactivity of Si/lithium perchlorate mixtures



Schematic depiction of the reactivity of barium perchlorate/Si mixtures



Schematic depiction of the reactivity of sodium perchlorate/Si mixtures



Schematic depiction of the reactivity of PETN/Si mixtures

APPENDIX 4D: SSG test results

SSG test results of PBX explosive formulations

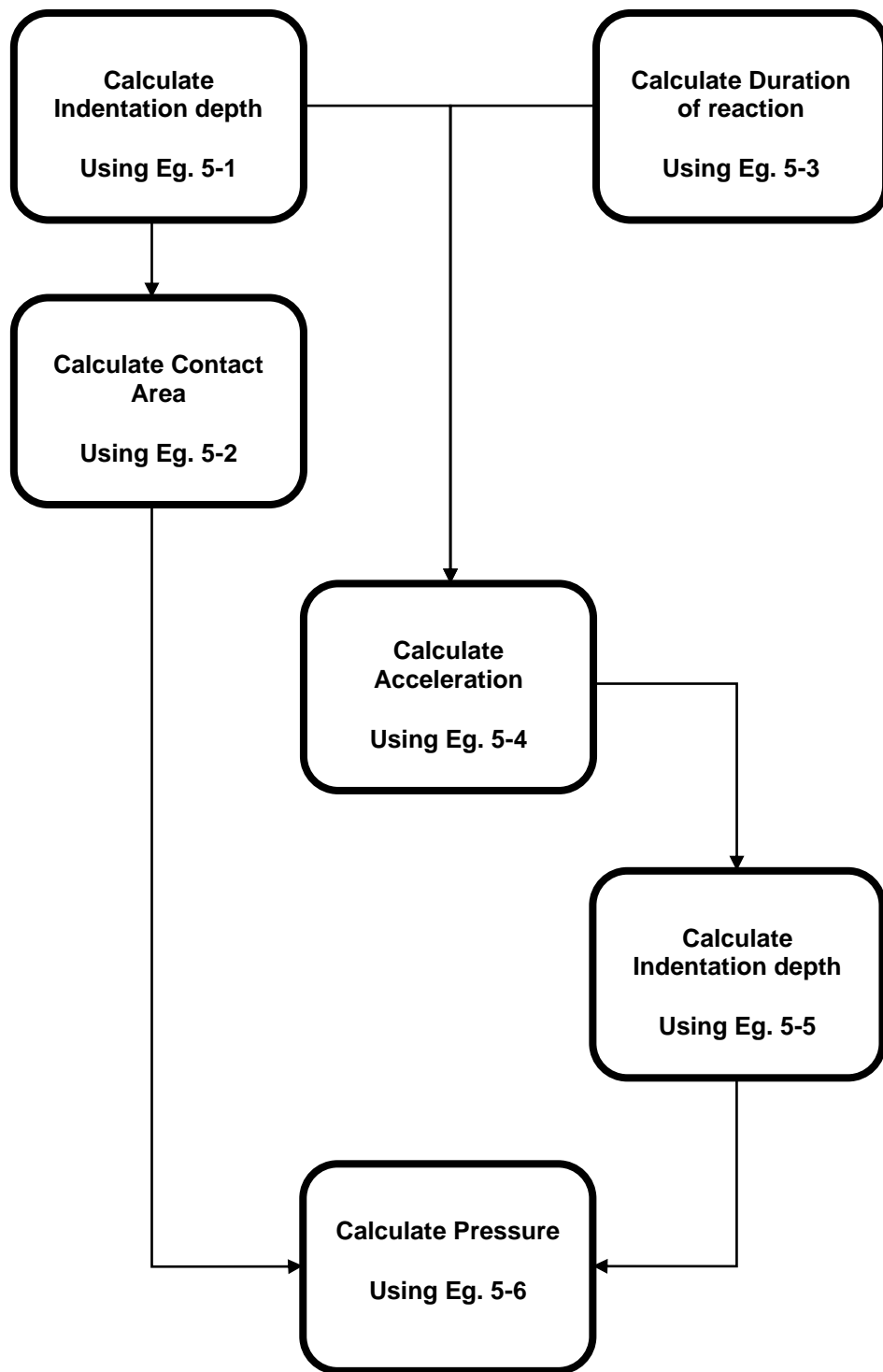
	Formulation	mm
1	BMW 101	0.125
2	BMW 111 - A	1.049
3	BMW 111 - B	0.936
4	BMW 111 - C	0.880
5	BMW 111 - D	0.814
6	BMW 111 - E	1.337
7	BMW 111 - F	1.431
8	BMW 111 - G	1.491
9	BMW 111 - H	1.602
10	BMW 111 - I	1.720
11	BMW 111 - J	1.697
12	BMW 130	0.686
13	BMW 212	1.670
14	BMW 211 - A	1.266
15	BMW 211 - B	1.359
16	THR 211 at density	0.786
17	THR 211	0.944
18	THR 211 - A	0.888
19	THR 211 - B	0.771
20	THR 211 - C	0.462
21	THR 211 - D	0.585
22	THR 211 - E	0.861
23	THR 211 - F	0.923
24	THR 212	0.380
25	THR 280	1.450
26	THR 287 - A	1.432
27	THR 287 - B	0.895
28	THR 287 - C	0.934
29	THR 313	0.259
30	THR 416	0.430
31	PETN	1.150
32	RXKF 9501	0.272
33	Tetrazole	1.391

APPENDIX 4E: Impact and friction sensitivity results of different PBX explosive formulations

Impact and friction sensitivity results

Formulation	Friction N	Impact		
		Height (cm)	F of I	J
THR 211 Fine PETN	54	9.2	33.45	4.5
THR 211 Coarse PETN	36	7.3	26.55	3.6
THR 211 - A	48	8.1	29.45	4
THR 211 - B	54	9.4	34.18	4.6
THR 211 - C	56	8.1	29.45	4
THR 211 - D	42	7.9	28.73	3.9
THR 211 - H	36	7.9	28.73	3.9
THR 211 - E	54	9.1	33.09	4.5
BMW 111 - E	32	7.9	28.73	3.9
BMW 111 - F	42	6.7	24.36	3.3
BMW 111 - G	40	9.6	34.91	4.7
BMW 111 - H	42	7.9	28.73	3.9
BMW 111 - J	48	9	32.73	4.4
BMW 111 - I	42	9.2	33.45	4.5
Fine PETN	24	9.4	34.18	4.6
Coarse PETN	40	14.2	51.64	7
Tetrazole	2	20.8	7.56	1

APPENDIX 5A: Mathematical evaluation logic flow diagram

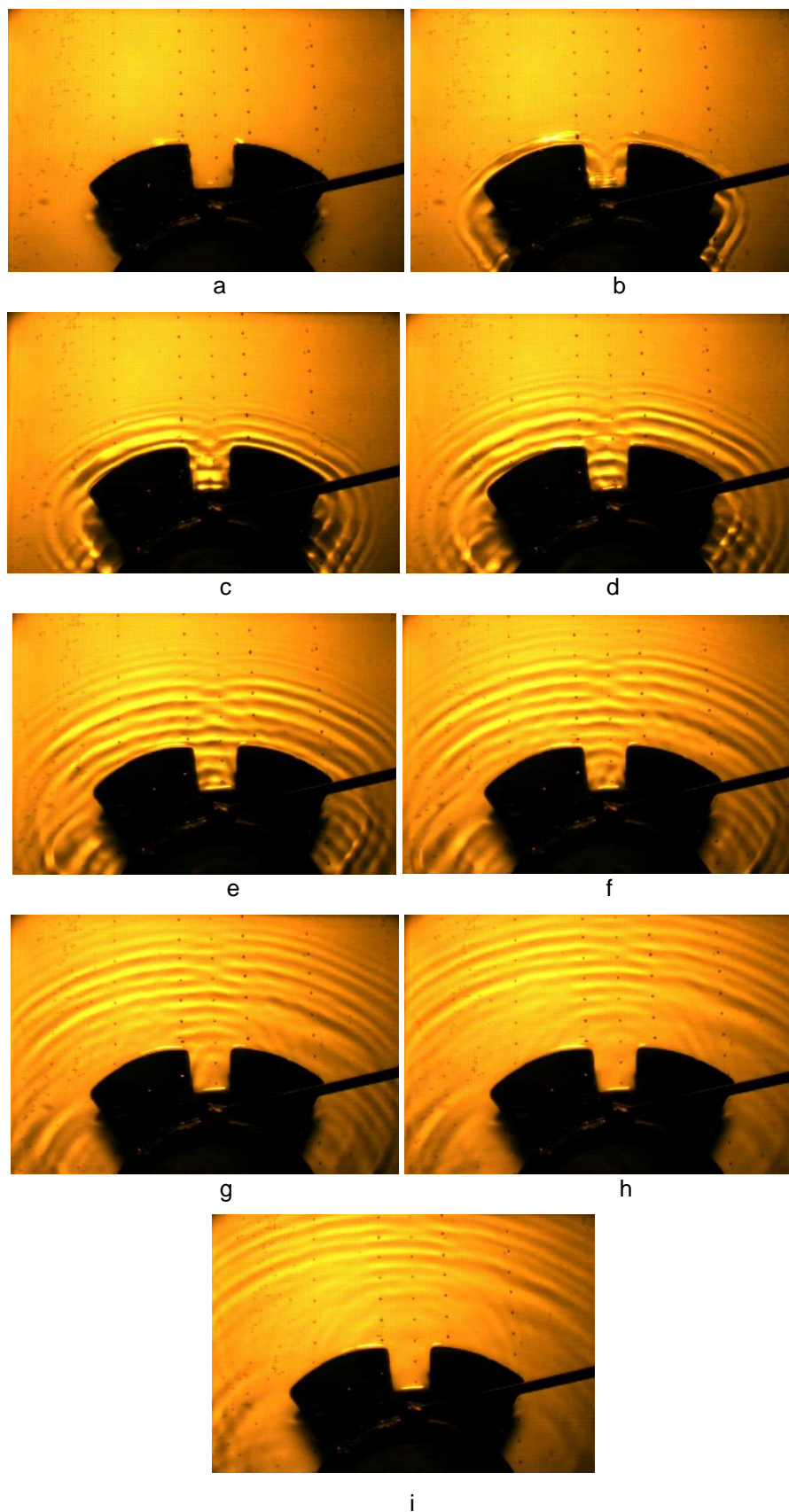


APPENDIX 5B: PETN indentation diameters at different densities

PETN in copper shell indentation at different densities

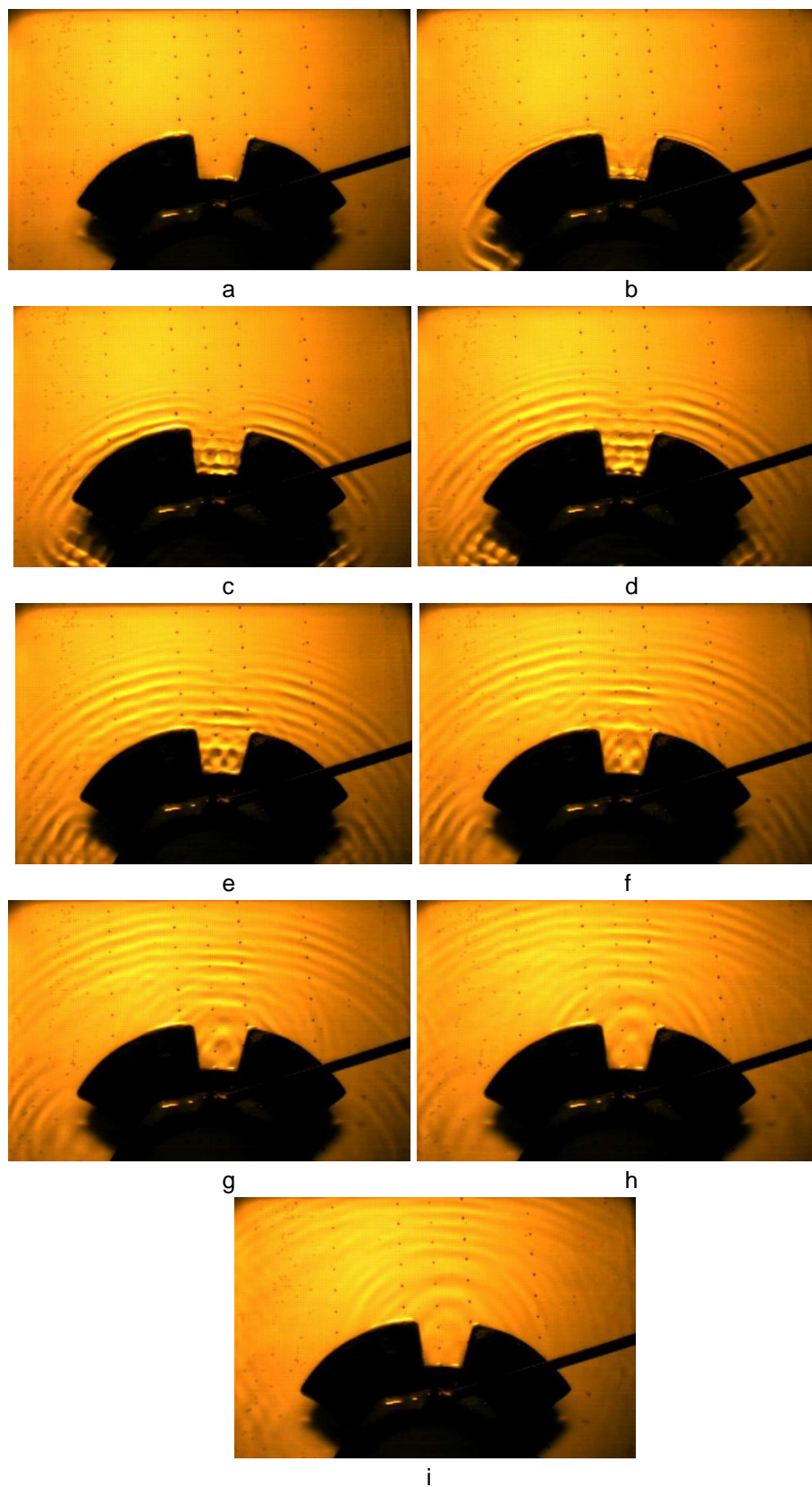
Repetition no	Density (g.cm ⁻³)					
	1.03	1.21	1.3	1.33	1.51	1.66
	Diameter (mm)					
1	5.51	5.64	5.87	5.91	6.21	6.38
2	5.52	5.62	5.9	5.92	6.23	6.42
3	5.55	5.63	5.81	5.91	6.28	6.49
4	5.48	5.69	5.85	5.91	6.29	6.45
5	5.49	5.68	5.86	5.91	6.2	6.45
6	5.52	5.64	5.84	5.93	6.25	6.41
7	5.52	5.62	5.84	5.93	6.23	6.4
8	5.51	5.6	5.87	5.99	6.25	6.39
9	5.49	5.62	5.89	5.98	6.24	6.37
10	5.49	5.64	5.86	5.97	6.29	6.35
11	5.48	5.65	5.86	5.95	6.2	6.42
12	5.5	5.65	5.84	5.91	6.34	6.39
13	5.51	5.68	5.86	5.96	6.21	6.42
14	5.53	5.69	5.89	5.86	6.29	6.42
15	5.52	5.67	5.92	5.9	6.25	6.48
16	5.51	5.66	5.93	5.84	6.24	6.42
17	5.47	5.66	5.9	5.87	6.28	6.43
18	5.51	5.63	5.82	5.89	6.21	6.47
19	5.52	5.65	5.87	5.84	6.25	6.38
20	5.49	5.62	5.86	5.89	6.32	6.39
21	5.49	5.69	5.87	5.86	6.25	6.42
22	5.47	5.68	5.89	5.89	6.17	6.37
23	5.52	5.63	5.9	5.92	6.18	6.38
24	5.51	5.61	5.91	5.93	6.21	6.42
25	5.49	5.62	5.85	5.95	6.21	6.48
26	5.52	5.64	5.86	5.94	6.15	6.45
27	5.52	5.62	5.89	5.96	6.24	6.4
28	5.54	5.52	5.89	5.9	6.15	6.43
29	5.52	5.68	5.87	5.97	6.23	6.38
30	5.51	5.68	5.87	5.92	6.2	6.39
31	5.49	5.61	5.88	5.93	6.21	6.41
32	5.48	5.63	5.89	5.96	6.22	6.4
33	5.48	5.64	5.81	5.94	6.21	6.38
34	5.47	5.67	5.91	5.89	6.21	6.34
35	5.49	5.67	5.91	5.96	6.15	6.44
Ave	5.50	5.64	5.87	5.92	6.23	6.41
STD dev	0.02	0.03	0.03	0.04	0.05	0.04

APPENDIX 7A: Result of 90° shock wave simulation



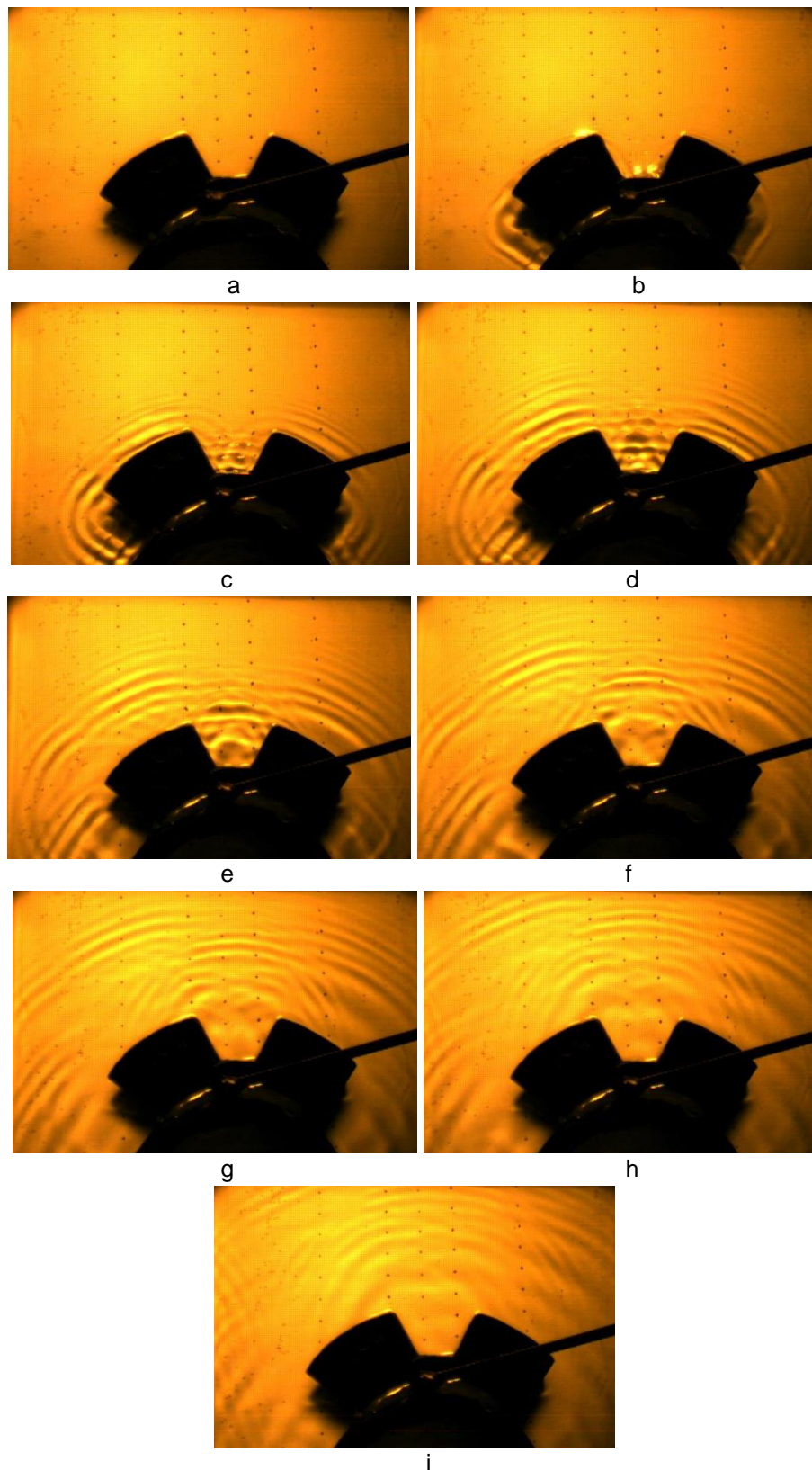
90° wave shapes from shock wave simulator. a) $t = 0.000$, b) $t = 0.02$, c) $t = 0.04$, d) $t = 0.06$, e) $t = 0.08$, f) $t = 0.10$, g) $t = 0.12$, h) $t = 0.14$, i) $t = 0.16$. Time (t) in seconds.

APPENDIX 7B: Results of 75° shock wave simulation



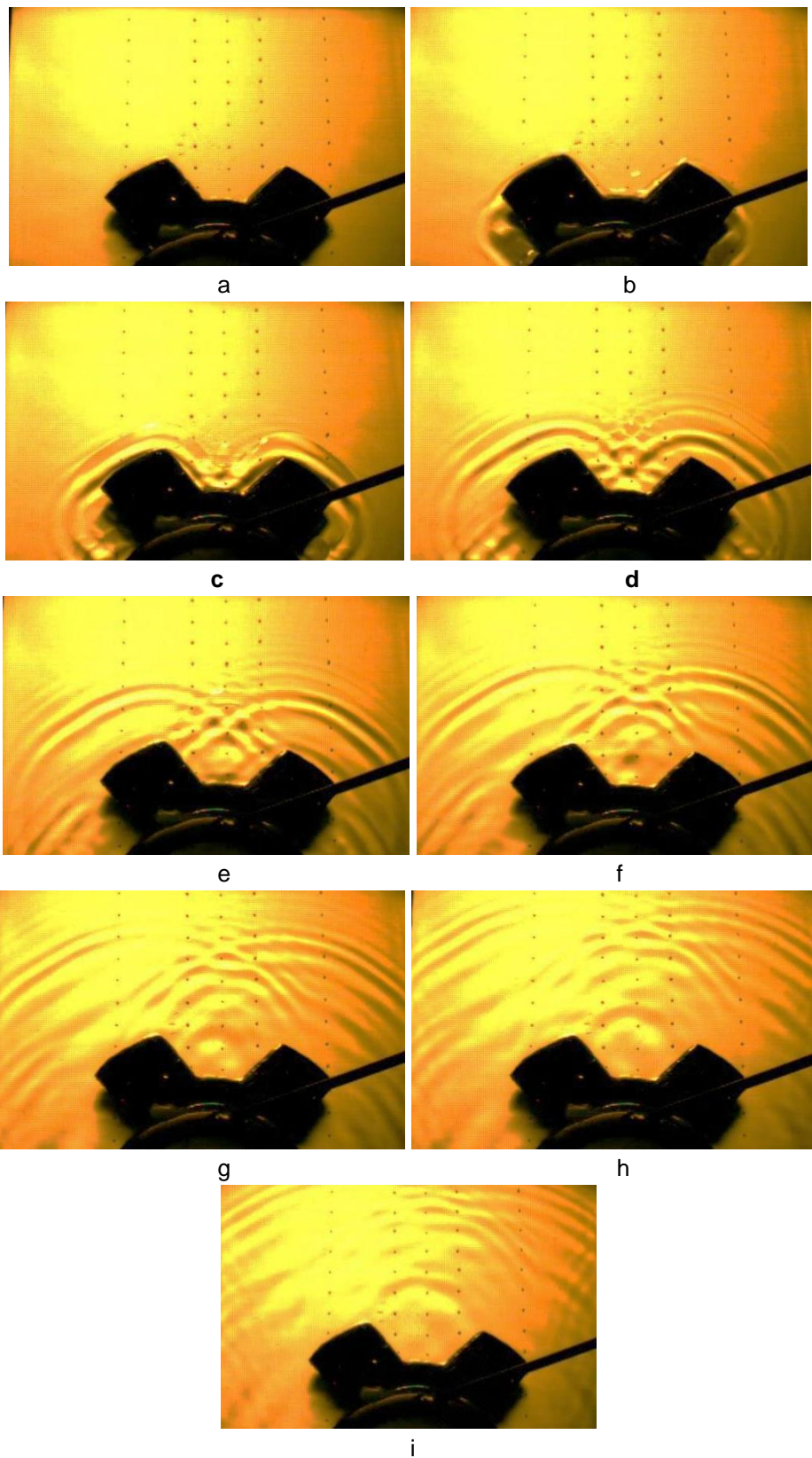
75° wave shapes from shock wave simulator a) $t = 0.000$, b) $t = 0.02$, c) $t = 0.04$, d) $t = 0.06$, e) $t = 0.08$, f) $t = 0.10$, g) $t = 0.12$, h) $t = 0.14$, i) $t = 0.16$. Time (t) in seconds.

APPENDIX 7C: Results of 60° shock wave simulation



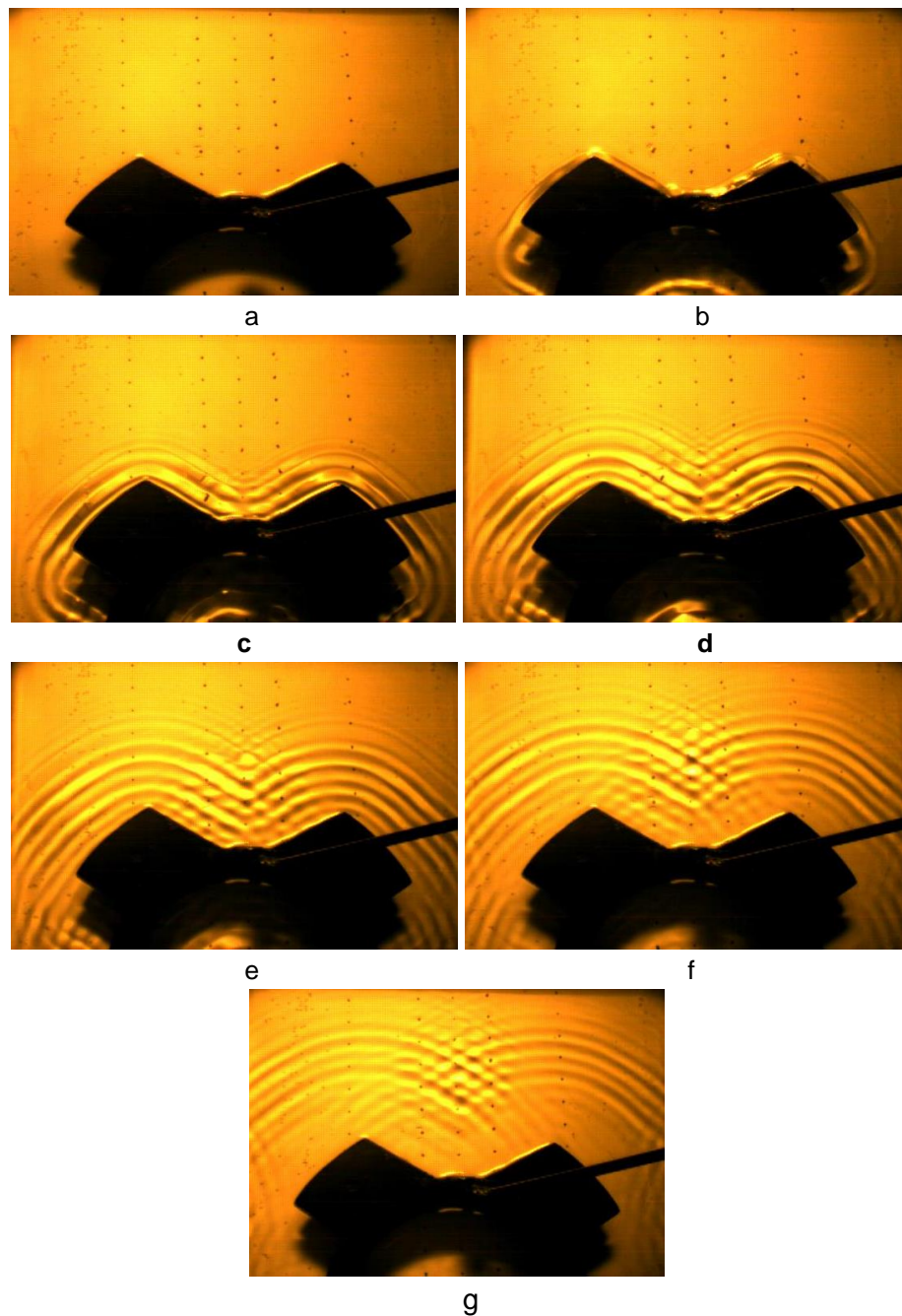
60° wave shapes from shock wave simulator. a) $t = 0.000$, b) $t = 0.02$, c) $t = 0.04$, d) $t = 0.06$, e) $t = 0.08$, f) $t = 0.10$, g) $t = 0.12$, h) $t = 0.14$, i) $t = 0.16$. Time (t) in seconds.

APPENDIX 7D: Results of 45° shock wave simulation



45° wave shapes from shock wave simulator. a) $t = 0.000$, b) $t = 0.02$, c) $t = 0.04$, d) $t = 0.06$, e) $t = 0.08$, f) $t = 0.10$, g) $t = 0.12$, h) $t = 0.14$, i) $t = 0.16$. Time (t) in seconds.

APPENDIX 7E: Results of 30° shock wave simulation



30° wave shapes from shock wave simulator a) $t = 0.000$, b) $t = 0.02$, c) $t = 0.04$, d) $t = 0.06$, e) $t = 0.08$, f) $t = 0.10$, g) $t = 0.12$. Time (t) in seconds.

APPENDIX 7F: Large-scale plate dent test results – outside profile

Large-scale plate dent test results – outside profile

Distance	Booster	Booster spaced	45°	60°	75°
mm	mm	mm	mm	mm	mm
20	0.00	0.00	0.00	0.00	0.00
40	5.11	3.61	4.04	3.56	3.86
45	10.89	7.84	9.17	8.93	8.97
50	14.28	10.30	12.00	11.84	11.86
55	16.46	11.68	13.60	13.34	13.38
60	18.15	12.72	14.86	14.67	14.65
65	20.23	14.33	16.52	16.07	16.09
70	22.30	15.84	18.10	17.74	17.49
75	24.67	17.31	19.75	19.16	19.10
80	27.04	18.55	21.37	20.95	20.57
85	29.45	20.38	22.85	21.99	22.03
90	31.95	22.14	24.14	23.38	23.30
95	33.84	23.76	25.06	24.25	24.11
100	34.66	24.91	25.54	24.60	24.56
105	35.26	25.47	25.75	24.71	24.71
110	35.69	26.10	25.66	24.52	24.57
115	34.62	26.17	25.23	23.92	24.03
120	32.96	25.98	24.53	23.20	23.32
125	31.26	25.18	23.35	21.85	21.94
130	28.92	24.05	21.81	20.36	20.68
135	26.94	22.40	20.44	18.72	18.96
140	23.99	21.08	18.96	17.34	17.69
145	21.92	19.19	17.16	15.90	15.87
150	19.87	17.45	15.68	14.35	14.71
155	17.31	15.54	14.17	12.70	13.21
160	15.57	13.92	12.58	11.36	11.82
165	13.40	12.32	11.33	10.04	10.49
170	11.87	10.66	10.04	8.66	9.41
175	5.81	5.53	5.01	3.59	4.93
180	0.17	1.27	0.20	0.38	0.46

APPENDIX 7G: Large-scale plate dent test results – inside profile

Large-scale plate dent test results – inside profile

	Reference spaced	45°	60°	75°
mm from edge	mm	mm	mm	mm
0	0.01	0.01	0.01	0.01
20	2.69	2.75	2.44	2.31
40	5.89	5.95	5.54	5.28
45	6.79	6.67	6.3	6.01
50	7.74	7.71	7.2	6.88
55	8.74	8.58	8.04	7.70
60	9.72	9.56	9.02	8.60
65	10.61	10.5	9.92	9.46
70	11.69	11.47	10.9	10.49
75	12.9	12.66	12.07	11.51
80	14.04	13.65	13.09	12.61
85	15.41	15.11	14.61	14.13
90	16.45	15.71	15.57	14.97
95	17.25	16.2	16.61	15.88
100	17.59	15.88	17.54	16.71
105	17.23	16.63	17.22	16.22
110	16.39	14.81	16.81	15.59
115	15.15	13.18	16.21	14.98
120	13.79	12.34	15.08	13.66
125	12.5	10.87	13.37	12.20
130	11.04	9.85	12.11	10.84
135	9.84	8.76	10.8	9.61
140	8.59	7.18	9.69	8.52
145	7.41	6.97	8.65	7.50
150	6.32	5.89	7.59	6.41
155	5.19	5.1	6.6	5.38
160	4.01	4.17	5.56	4.36
180	0.05	1.02	1.97	1.31
200	-3.19	-1.52	-1.4	0.00

APPENDIX 7H: Pressure calculations

Equation 7.5	
Input	$\text{solve}(28.507 = 1.66 \cdot (2.089) (6.127 + x \cdot (2.089)), x)$
Solution 1	$x = \frac{363007851}{362205443} \approx 1.002215339431$

From RXKF to HDPE (Equation 7.8)	
Input	$\text{solve}(1.66 \cdot (6.127) (2.089 - x) + 1.66 \cdot (1.0026) (2.089 - x)^2 = 0.915 \cdot (2.901) x + 0.915 \cdot (1.481) x^2, x)$
Solution 1	$x = -\frac{\sqrt{22246114043089409785}}{154600500} + \frac{1236171703}{38650125} \approx 1.4754685435493$
Solution 2	$x = \frac{\sqrt{22246114043089409785}}{154600500} + \frac{1236171703}{38650125} \approx 62.4918124419585$

Equation 7.6	
Input	$0.915 \cdot (2.901) \cdot (1.4755) + 0.915 \cdot (1.481) \cdot (1.4755)^2$
Output	6.86681053777875
Decimal Output	6.8668105377787

From HDPE to Aluminum (Equation 7.11)	
Input	$\text{solve}(0.915 (2.901) (1.4755 - x) + 0.915 (1.481) (1.4755 - x)^2 = 2.785 (5.328) x + 2.785 (1.338) x^2, x)$
Solution 1	$x = \frac{-\sqrt{2342355092836976702} - 1432789291}{316162000} \approx -9.3726151076428$
Solution 2	$x = \frac{\sqrt{2342355092836976702} - 1432789291}{316162000} \approx 0.3089750054167$

Equation 7.9	
Input	$2.785 \cdot (5.328) \cdot (0.3089) + (2.785 \cdot (1.338) \cdot (0.3089)^2)$
Output	4.9391699367993

From HDPE to AIR (Equation 7.13)	
Input	$\text{solve}(0.915 (2.901) (1.4755 - x) + 0.915 (1.481) (1.4755 - x)^2 = 2.03 (0.899) x + 2.03 \cdot (0.939) (x)^2, x)$
Solution 1	$x = \frac{-\sqrt{3480721197800159182} - 1695665873}{220422000} \approx -16.1568943885104$
Solution 2	$x = \frac{\sqrt{3480721197800159182} - 1695665873}{220422000} \approx 0.7712625278068$

Equation 7.9 (second calculation)	
Input	$2.03 \cdot (0.899) \cdot (0.7712) + 2.03 \cdot (0.939) (0.771262)^2$
Output	2.54129269612181348
Decimal Output	2.5412926961218

From Air to Air (Equation 7.14)	
Input	$\text{solve}(2.03 (0.899) (2 (0.77) - x) + 2.03 (0.939) (2 (0.77) - x)^2 = 2.03 (0.899) (x + 2 (0.77)) + 2.03 (0.939) (x + 2 (0.77))^2, x)$
Solution 1	$x = 0$

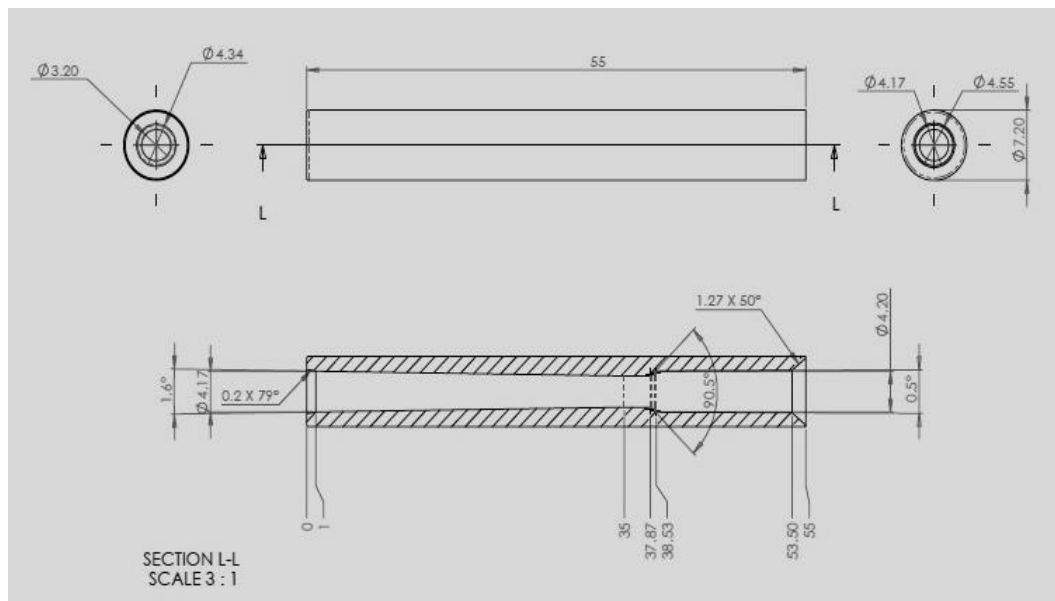
Left side of Equation 7.14	
Input	$2.03 (0.899) (2 (0.77126) - 0) + 2.03 (0.939) (2 (0.77126) - 0)^2$
Output	7.350532530413968
Decimal Output	7.350532530414

Particle velocity from equation 7.5	
Input	$\text{solve}(7.35 = 2.03 x (0.899 + 0.939 x), x)$
Solution 1	$x = -\frac{\sqrt{12116717041}}{54462} - \frac{899}{1878} \approx -2.4998523800606$
Solution 2	$x = \frac{\sqrt{12116717041}}{54462} - \frac{899}{1878} \approx 1.5424508891128$

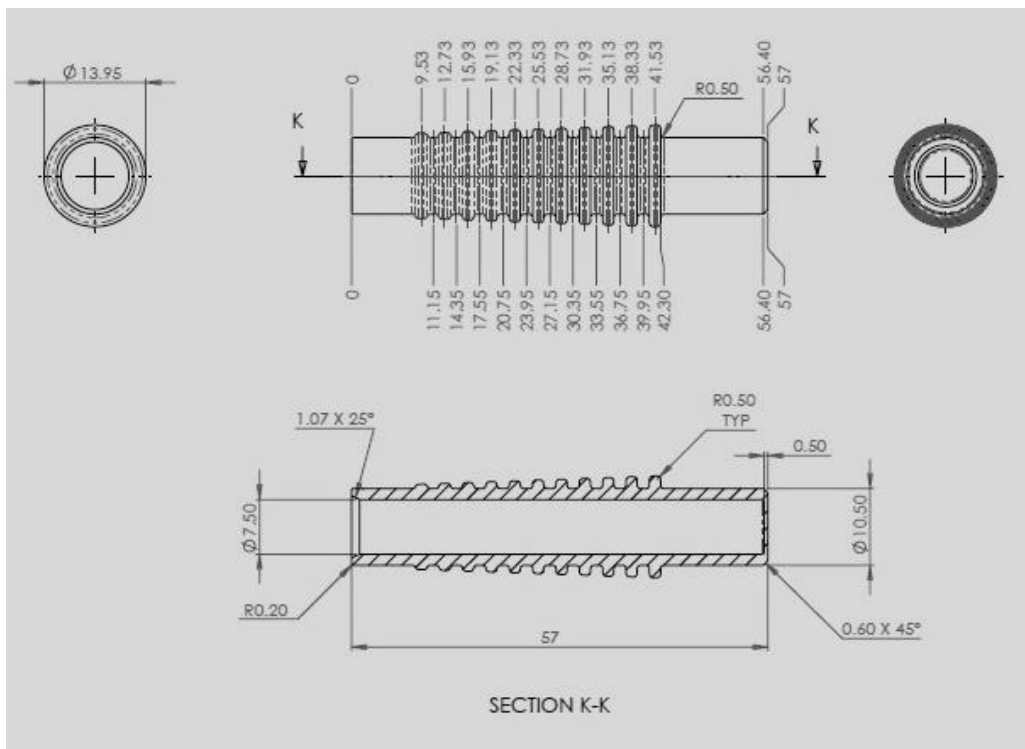
Air to Aluminium (combined waves) (Equation 7.17)	
Input	$\text{solve}(2.03 (0.899) (1.54) + 2.03 (0.939) (1.54 - x)^2 = 2.785 (5.328) (x - 0) + 2.785 (1.338) (x - 0)^2, x)$
Solution 1	$x = \frac{-\sqrt{334901391905441} - 17257903}{3033600} \approx -11.7214577569884$
Solution 2	$x = \frac{\sqrt{334901391905441} - 17257903}{3033600} \approx 0.3436208635285$

Left side of Equation 7.17	
Input	$\text{solve}(x = 2.785 \cdot (5.328) (0.3436 - 0) + 2.785 \cdot (1.338) (0.3436 - 0)^2, x)$
Solution 1	$x = \frac{3461522390673}{625000000000} = 5.5384358250768$

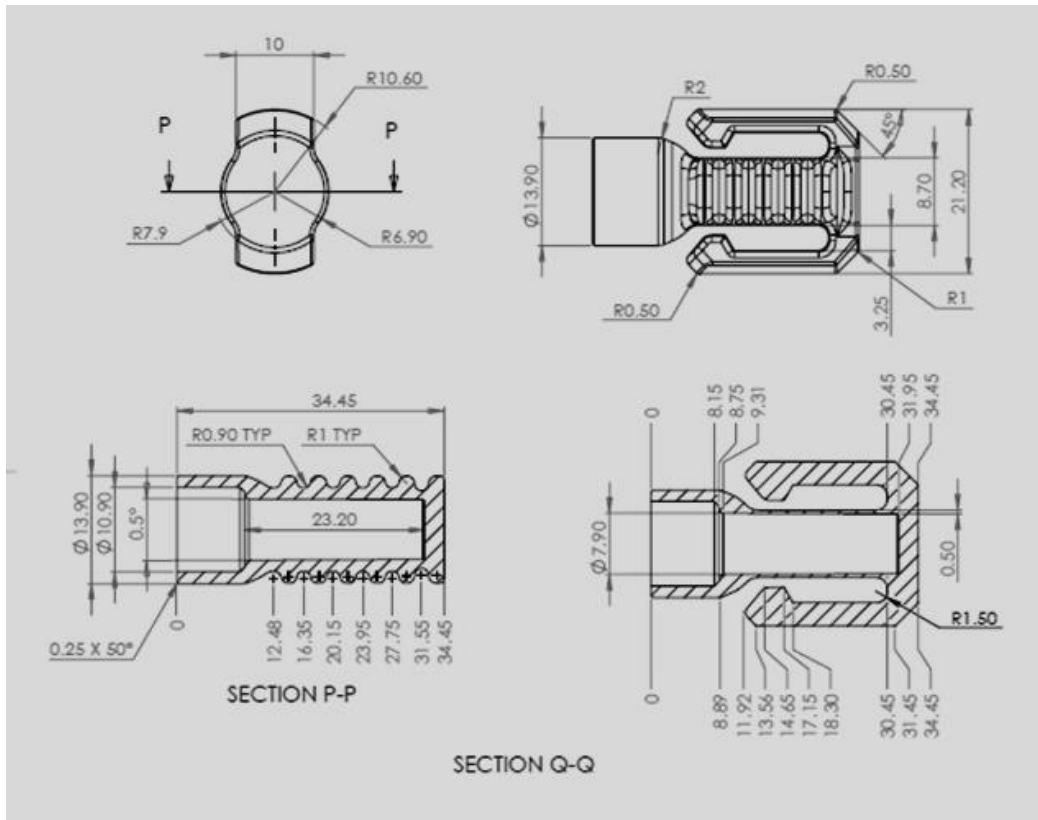
APPENDIX 8A: Shock tube holder design



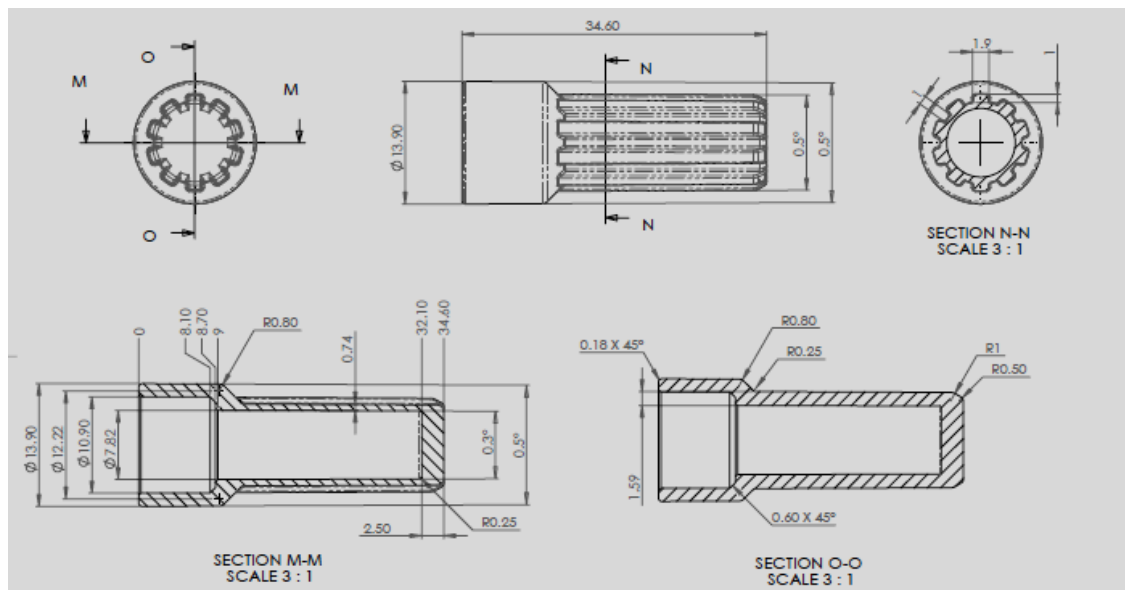
APPENDIX 8B: Main body design



APPENDIX 8C: Shock tube connector clip design

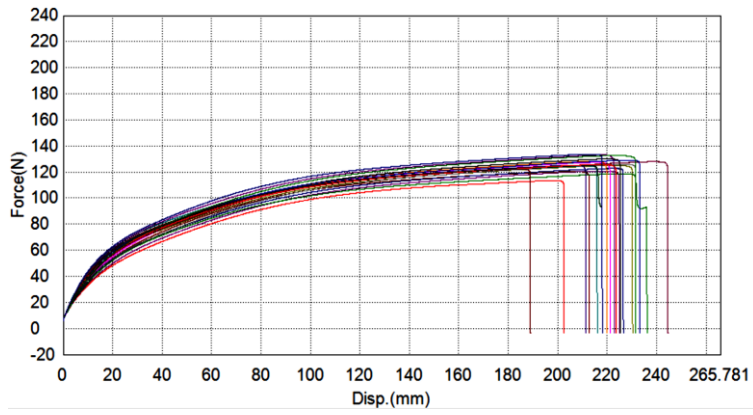


APPENDIX 8D: Booster casing design

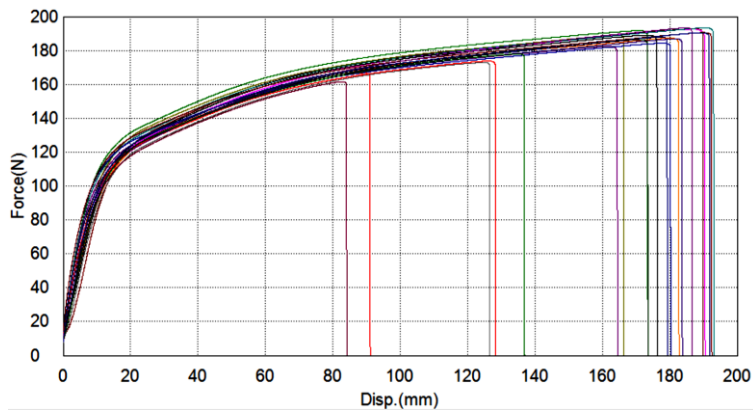


APPENDIX 8E: Actual pull-strength results – shock tube to shock tube holder

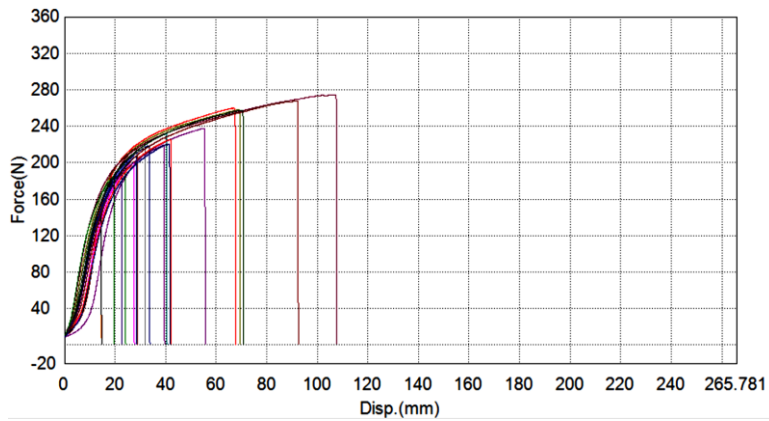
Interface: Shock tube to shock tube holder – 50 °C



Interface: Shock tube to shock tube holder – 20 °C

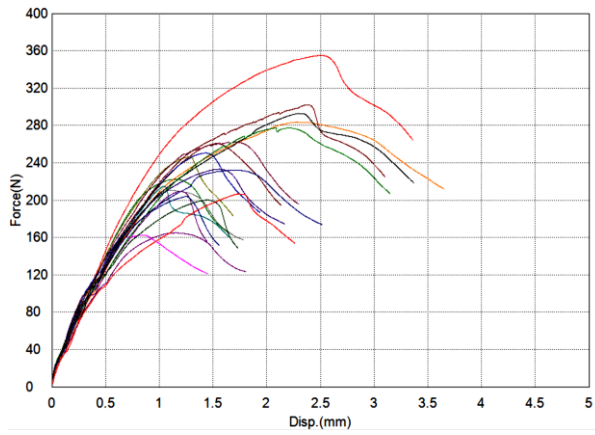


Interface: Shock tube to shock tube holder – -20 °C

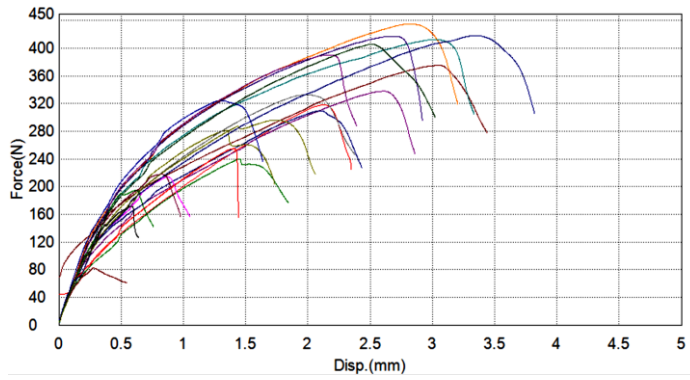


APPENDIX 8F: Actual pull-strength results – shock tube holder to body

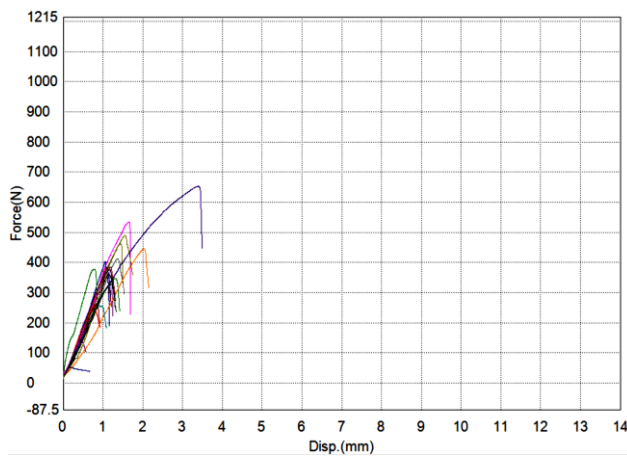
Interface: Shock tube holder to body – 50 °C



Interface: Shock tube holder to body – 20 °C

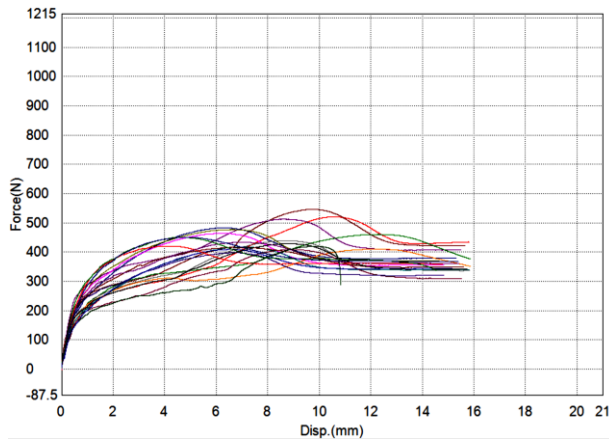


Interface: Shock tube holder to body – -20 °C

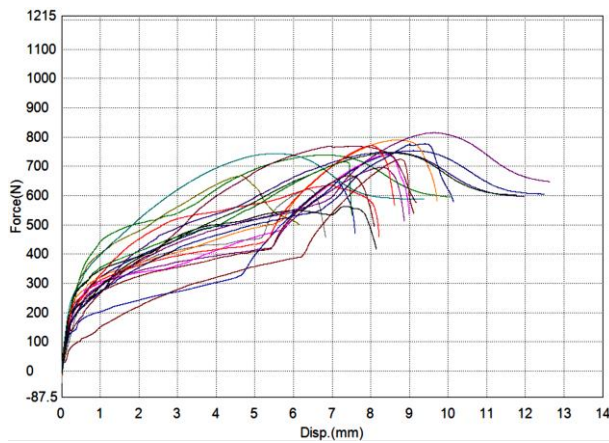


APPENDIX 8G: Actual pull-strength results – body to base

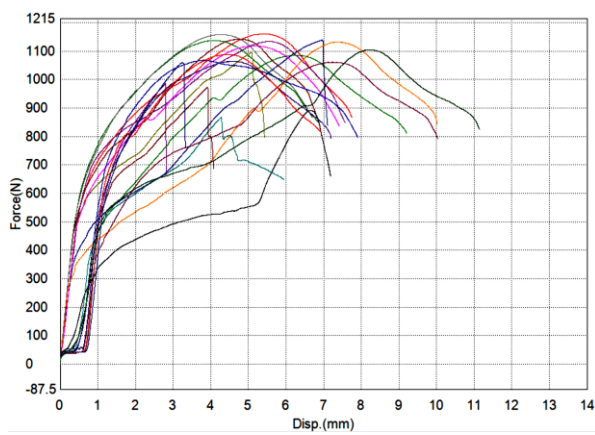
Interface: Body to base – 50 °C



Interface: Body to base – 20 °C

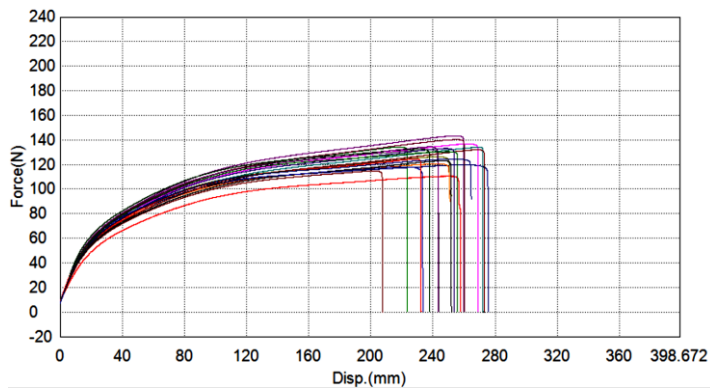


Interface: Body to base – -20 °C

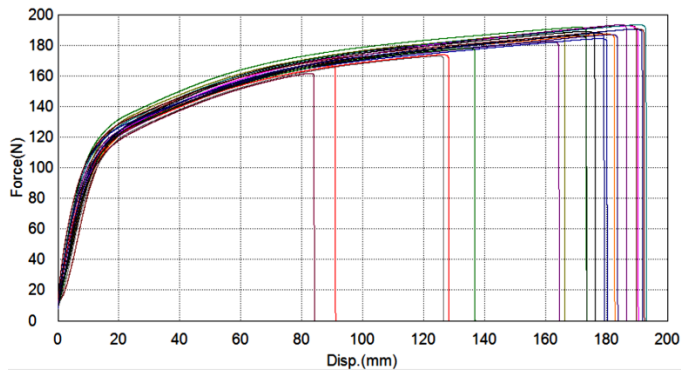


APPENDIX 8H: Actual pull-strength results (aged) – shock tube to shock tube holder

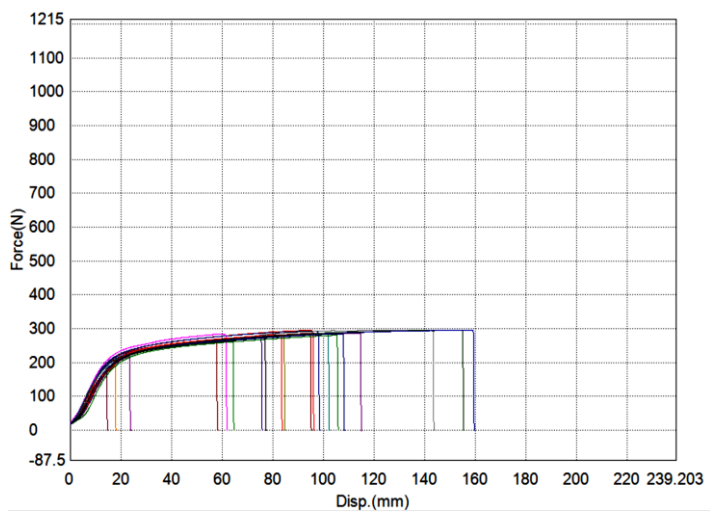
Interface: Shock tube to shock tube holder – 50 °C



Interface: Shock tube to shock tube holder – 20 °C

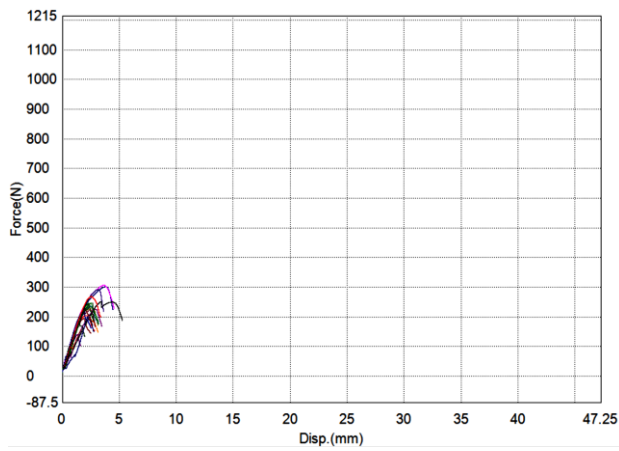


Interface: Shock tube to shock tube holder – -20 °C

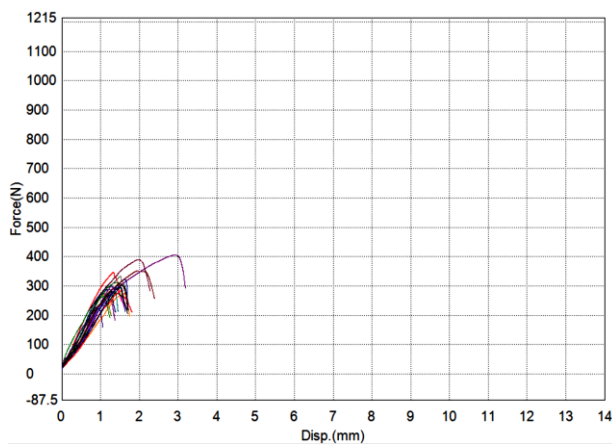


APPENDIX 8I: Actual pull-strength results (aged) – shock tube holder to body

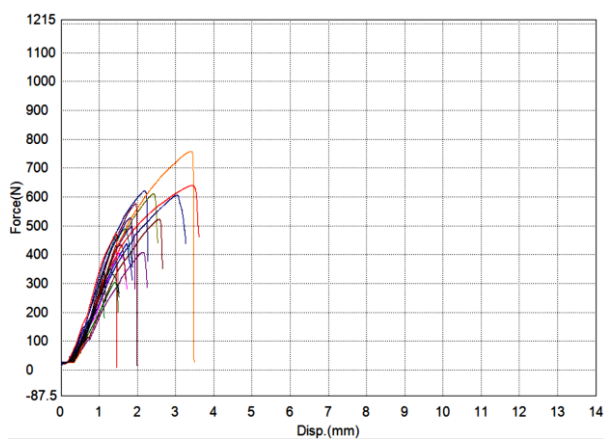
Interface: Shock tube holder to body – 50 °C



Interface: Shock tube holder to body – 20 °C

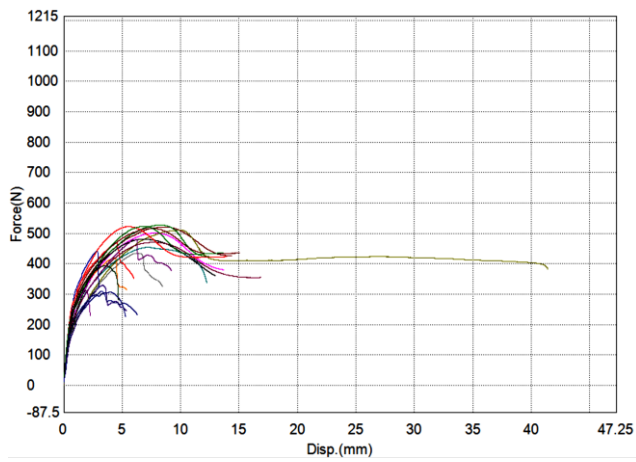


Interface: Shock tube holder to body – -20 °C

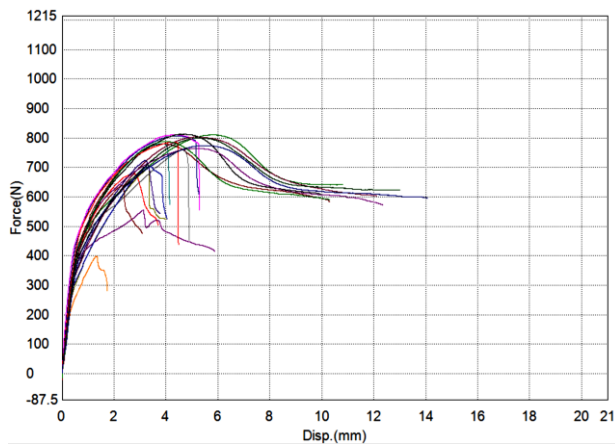


APPENDIX 8J: Actual pull-strength results (aged) – body to base

Interface: Body to base – 50 °C



Interface: Body to base – 20 °C



Interface: Body to base – -20 °C

